METAL EMBEDDED ARTIFICIAL GRID DIELECTRIC RESONATOR ANTENNA ARRAYS AND SIW FEEDING MECHANISMS FOR MM-WAVE APPLICATIONS

A Thesis Submitted to the College of

Graduate and Postdoctoral Studies

In Partial Fulfillment of the Requirements

For the Degree of Doctor of Philosophy

In the Department of Electrical and Computer Engineering

University of Saskatchewan

Saskatoon

By

Waqas Mazhar

Permission to Use

In presenting this thesis in partial fulfillment of the requirements for a Postgraduate degree from the University of Saskatchewan, I agree that the Libraries of this University may make it freely available for inspection. I further agree that permission for copying of this thesis in any manner, in whole or in part, for scholarly purposes may be granted by the professor or professors who supervised my thesis work or, in their absence, by the Head of the Department or the Dean of the College in which my thesis work was done. It is understood that any copying or publication or use of this thesis or parts thereof for financial gain shall not be allowed without my written permission. It is also understood that due recognition shall be given to me and to the University of Saskatchewan in any scholarly use which may be made of any material in my thesis.

Requests for permission to copy or to make other use of the material in this thesis in whole or part should be addressed to:

Head of the Electrical and Computer Engineering

57 Campus Drive

University of Saskatchewan

Saskatoon, Saskatchewan S7N 5A9 Canada

OR

Dean

College of Graduate and Postdoctoral Studies

University of Saskatchewan

116 Thorvaldson Building, 110 Science Place

Saskatoon, Saskatchewan S7N 5C9   Canada

Abstract

One of the major challenges in deploying future millimeter-wave, wideband communication systems is the designing of wide impedance bandwidth, high gain and high efficiency front end antennas. Conventional metal antennas have disadvantages like narrow frequency bandwidth, high conductor loss, and low radiation efficiency which make them inadequate for such systems. Therefore, this thesis investigates the future potentials of the low loss (i.e., no conductor loss) and high efficiency artificial grid dielectric resonator antennas for millimeter-wave applications using deep X-Ray lithography (DXRL).

In the first section, a new design approach is introduced, to enhance the feed versatility and design characteristics of the previously explored grid dielectric resonator antennas (GDRAs). For instance, the implementation of the multi-layer GDRAs technique has improved the impedance bandwidth performance of normal GDRAs from 5.5% to $\geq$12%. Secondly, the integration of the various feeding techniques such as conventional coplanar waveguide (CPW), capacitive CPW and inductive CPW feeds are successfully applied to GDRAs for mm-wave applications, which was previously limited to microstrip feed-line only due to grid to feed-line shorting issues.

The power distribution networks are always very crucial in defining antenna array performance. The feed structures like microstrip corporate feed and series feed are not practical at millimeter-wave frequencies due to the high conductor and radiation losses. Therefore, in the second section, the substrate integrated waveguide (SIW) feeding mechanisms for one-dimensional (1D) and two-dimensional (2D) planar arrays are explored. Various wide-band, low amplitude and phase imbalance, SIW parallel feed networks are developed at 24 and 60 GHz for the large GDRA arrays integration.

In the third section, the X-ray lithographic procedure for the development of two different monolithic GDRA array layers is described: i) solid template frame GDRA array layer; ii) and strip template frame GDRA array layer. All design steps from the DXRL mask fabrication to sample exposure, sample development and electroplating are thoroughly investigated.

In the fourth and the final section, the performance of the two proposed GDRA array approaches using SIW feed mechanism is evaluated. Contrary to ordinary large DRA arrays these monolithic GDRA array designs greatly help in mitigating the GDRAs to a feedline alignment problem, which

may result in distorted radiation pattern and significant impedance mismatch. Furthermore, the use of thin rectangular micro-inclusions over more complicated I-beam structures has reduced the fabrication complexities as well as has enhanced the effective permittivity of the newly developed GDRAs up to 22.5 which results in compact and low-profile structures. The performance of the rectangular grid based monolithic GDRAs is characterized in two steps. In a first step, low profile single channel series fed 1×4, and 1×8 GDRA arrays are implemented using SIW longitudinal slot feed topology at 32 GHz with a maximum impedance bandwidth of 12% and a realized gain of 11.9 dBi. Moreover, the effect of the template frame thickness, frame permittivity and the inclusion heights on the antenna array performance is discussed in detail. While, in a second step, subarrays of 1×4 and 1×8 GDRA elements are further extended to 4×4 and 8×8, 2D-monolithic GDRA arrays with SIW parallel feed networks and which have successfully demonstrated an impedance bandwidth up to 18% and a peak realized gain of 19.8 dBi at 60 GHz.

The proposed GDRAs offer exciting features such as wide impedance bandwidth, high gain and low cross polarization and are a promising alternative at mm-wave frequencies to conventional metallic patch antennas antennas which suffer from low impedance bandwidth and high conductor losses, as well as an alternative to high permittivity, conventional ceramic DRAs which are narrow band and hard to machine at mm-wave frequencies where fabrication tolerances become comparable with the operating frequency wavelength. Lastly, the high permittivity GDRAs are low profile antennas which can be easily integrated in compact mm-wave devices.

Acknowledgment

Table of Contents

List of Tables

List of Figures

xiv

List of Abbreviations

BW	bandwidth
cIoT	customer Internet of thing
CLS	Canadian light source
CST	computer simulation technology
dB	decibel
DNG	double negative
DPD	double positive dielectrics
DRA	dielectric resonator antenna
DWM	dielectric waveguide model
DXRL	deep X-ray lithography
FDTD	finite difference time domain
FEM	finite element method
FIT	finite integration technique
FNBW	first null beamwidth
GCPW	grounded coplanar waveguide
GDRA	grid dielectric resonator antenna
GHz	gigahertz
HFSS	high frequency structure simulator
HPBW	half power beamwidth
iIoT	industrial Internet of thing
IoT	internet of thing
LCP	liquid crystal polymer
LMDN	local multi-point distributed networks
MEMS	micro-electro-mechanical systems
mm	millimeter
MMA	methyl methacrylate
MoM	method of moment
PDMS	polydimethylsiloxane
PGMEA	propylene glycol monomethyl acetate
PMMA	polymethylmethacrylate
PTH	plated through hole
Q-factor	quality factor
SEM	scanning electron microscope
SIIG	substrate integrated insular guide
SINRD	substrate integrated non-radiating dielectric
SiP	system in package
SISW	substrate integrated slab-waveguide
SIW	substrate integrated waveguide
SoS	system on substrate
TE	transverse electric
TEM	transverse electromagnetic
TM	transverse magnetic

TORR	triangular open ring resonator
UV	ultraviolet

Chapter 1 : Introduction

1.1.   Background and Motivation

The field of wireless communication has witnessed tremendous development in recent years, making it the fastest growing segment of telecommunication technology [1]. The wireless revolution is touching and reshaping many aspects of our daily life. The terms Internet of Things (IoT) [2], [3] and 5G [4] are becoming hot topics among many researchers presenting new challenges and problems [5] for future communications. These challenges stem from the growing network traffic generated by high throughput mobile applications. Growing trends of the wireless connectivity with increased user expectations are the key indicators of this wireless boom [6]. It is forecasted that wireless traffic volume would grow by 1000 times in the year 2020 in comparison to 2010 [7].

The expansion of mobile phones in last two decades along with the success of 3G cellular communication services has motivated the development of wideband 4G and 5G cellular technologies as well as many other wireless protocols like Bluetooth, Wi-Gig (802.11ad), Wireless-HD and Local Multi-point Distributed Networks (LMDN) [8]. High throughput of the 5G wireless networks [9] has driven the usage of millimeter-wave (mm-wave) spectrum into practical applications [10]. These networks are targeted to provide data rates of 1000 fold higher than the 4G networks [11], [12]. Diverse application domains such as healthcare, automotive and energy industries are going to have extensive usage of 5G technologies. For instance, in telecommunication, the wearable smart devices, and sensors are continuously revolutionizing the current healthcare sector. This sector is readily exploring and adopting new devices and technologies for its daily practices, and patient care. More than 96 percent of the hospitals in North America have electronic medical records in place, and the use of connected devices is on the rise as the global Internet of Things (IoT) healthcare market is expected to reach $410 billion by 2022 [13]. Similarly, according to a study conducted by Qualcomm, UC Berkeley and IHS Markit on future of the 5G economy, it is predicted that 5G will enable more than US$2.4 trillion in total economic output across the automotive industry [14]. Cumulatively, 5G economic impact in the automotive sector represents nearly 20% of the global 5G economic effect.

Furthermore, in the coming years, IoT will be the foundation for building a smart city and related applications such as wearable computing, multiple personal devices, smart and remote healthcare, and lifeline systems. IoT is broadly classified into two categories [15]: i) Consumer IoT (cIoT); and ii) industrial IoT (iIoT) [16], [17]. Consumer IoT involves the interconnection of, not only all electronic devices belonging to the user, but also virtually anything else in the user environment, such as homes, offices, and cities. In contrast, Industrial IoT focuses on the integration between Operational Technology (OT) and Information Technology (IT). It is estimated that over 50 billion devices will be connected to the internet by 2020 and IoT will account for over 75% of the traffic [18].

Such a dramatic shift in capacity and user requirement is the continuous source of motivation for many researchers to explore the potential of the millimeter wave bands for future wireless system and applications. The radio frequency (RF) devices are the backbone of the wireless communication systems architecture. The transmitter, receiver, modulation, and demodulation within different devices revolve around the RF technology. Personal communication systems are now shifting toward higher frequencies to meet the requirements of different bandwidth-intensive services like e-gaming, video conferencing, hi-definition data streaming [19] and other online services.

This shift in the frequency paradigm is due to overcrowding and high interference in the sub-6GHz frequency band, which has been shared by all previous and current generations of commercial mobile communication. High frequencies have several advantages such as less interference, huge bandwidth, i.e., 1.3 GHz at 28 GHz and 14 GHz at 60 GHz, that enables high data rates and thus paves the way for new human-centric and machine type communication applications that have not been possible to date [20]. The frequency allocation of the mm-wave spectrum is shown in Figure 1.1. Due to smaller wavelength, mm-waves allow small size antennas and miniaturization of other microwave components for more compact and smart devices, enabling high speed digital signal processing and data transmission.
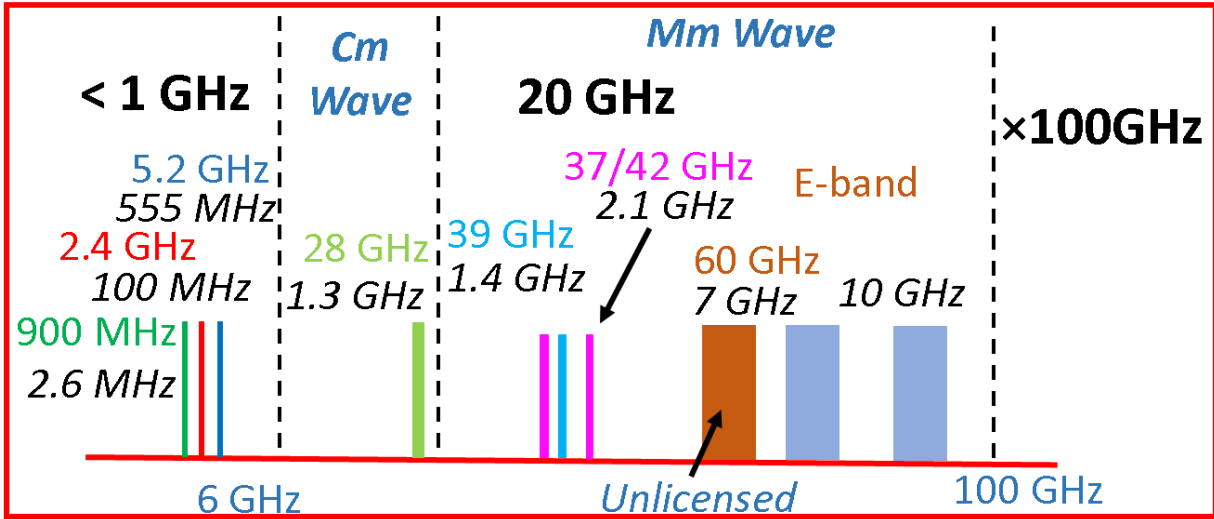
Figure 1.1 Frequency allocation of the mm-wave spectrum

However, microwave devices and circuits at higher frequencies require special consideration in term of design, fabrication, material selection, and high accuracy in structural dimensions on the order of microns. The demand for smart and compact devices is one of the major factors of the growing need for microfabrication and nanotechnologies in RF and microwave applications.

Micro/Nanofabrication applications include MEMS, micro-optics, integrated circuits, nanotechnology, and many more. Microfabrication has slightly different considerations for each of these applications, i.e., electroplating is a vital process for deep submicron IC metallization and LIGA microstructures [21], deep–RIE (reactive ion etching) is a key technology in trench DRAM and MEMS [22], imprint lithography is used in micro fluids where typical dimensions are 100μm as well in nanotechnology where feature size is condensed within 10nm. Deep X-ray lithography [23] is one of the emerging technologies used in the fabrication of microwave and millimeter wave structures, which are very difficult to synthesize with other techniques. It is capable of fabricating structures with high aspect ratios and with lateral dimensions ranging from millimeter to micron scales.

Antennas as a front-end element always have a pivotal role in defining the performance of the wireless communication system. In recent years, a substantial boom in high-frequency antenna design has been witnessed, mainly due to high gain and broad impedance bandwidth requirements for the future 5G applications such as mm-wave automotive radars, high definition video transmission, and cellular and satellite communication systems [24]. Traditionally printed circuit

board (PCB) based antenna solutions have been preferred for sub-6 GHz communication due to their simple fabrication and ease of integration with other RF circuit components [25], [26]. Conventional antennas including leaky wave antennas [27], patch antennas [28], dipole antennas [29] and slotted antennas [30] are types of metal printed antennas where the radiation explicitly comes from the metal surface. However, these metal antennas can suffer from low radiation efficiency [31], [32] at mm-wave frequencies due to high conductor losses generated by the metal surface currents. Secondly metal antennas also inherit low impedance bandwidth as they radiate through two-dimensional planar surfaces, which limits their operation for future wide band mm-wave applications.

Dielectric resonator antennas (DRA), on the other hand comprised of ceramics can offer wide impedance bandwidth and higher efficiency due to the absence of conductor losses and simple coupling schemes to different transmission line configurations, thus they can easily be integrated with planar structures [33]–[35]. The DRAs are also advantageous over conventional patch antenna arrays by offering smaller size, i.e. proportional to the square root of the dielectric constant of the material making them suitable for mm-wave devices. As compared to microstrip antennas, medium permittivity DRAs can have much wider bandwidth (~10% for dielectric resonator $\varepsilon_r \sim 10$) and this is because they radiate through the whole 3D surface except the grounded part. However, they also have some limitations such as higher permittivity DRAs i.e., $\varepsilon_r > 10$, which normally result in low impedance bandwidth [36]. Secondly, placing and aligning individual DRA elements over feed network for large arrays also presents a significant fabrication challenge.

Besides conventional dielectrics, artificial dielectrics that mimic the properties of natural dielectrics or even manifest properties that cannot generally occur in nature have been widely studied and applied to microwave devices [37], [38]. An artificial dielectric can be envisioned as a large scale model of an actual dielectric, built by embedding small conducting structures in a regular pattern. The material response is strictly dependent on the size of the embedded inclusions at a given wavelength. Generally, the inclusion size is required to be much smaller than the incident wavelength to make them non-resonant structures. Antennas made from artificial dielectrics possess characteristics similar to conventional dielectric material like low conductor loss, and high radiation efficiency [39]. More importantly they provide more design freedom as the

electromagnetic properties of the artificial material can be engineered by changing the size, shape, and spatial density of the metal inclusions.

Gridded dielectrics are recently discovered under the category of double positive artificial dielectrics (DPD). More details about grid dielectrics are provided in Chapter 2. In [40], they are used to build antennas named as "metal grid dielectric resonator antennas" (GDRAs). They provide an exciting alternative to the conventional metallic patch antennas (MPAs) and DRAs, where high effective permittivity is achieved artificially by embedding micro-inclusions in a low permittivity host material. They offer several promsing features for mm-wave antennas like high effective permitivity, wide impedance bandwidth, high gain and low cross polarization [41]. They are called DRAs because they most closely resemble DRA behavior than other types of antennas, and have similar properties like compact structure, light weight, radiation patterns similar to magnetic dipoles, and high radiation efficiency due to the absence of surface waves and resonant mettalic losses [40]. They can generally be fed using similar mechanisms to DRAs [33]–[35]. Also, the material functions as a permittivity magnifier, so they also work similar to higher permittivity homogeneous classic ceramic-type DRAs.

However, there are considerable differences between GDRAs and regular DRAs. Firstly, the GDRAs are made only of low-permittivity polymer dielectrics, and embedded metal structures.This could be advantageous from a fabrication point of view for emerging commercial applications since they do not require hard fired ceramic materials. Another unique feature of the approach is an extension to arrays, which can be fabricated as a single monolithic piece. Unlike the homogenous ceramic type DRAs [36], the dielectrics in the GDRAs are non-resonant structures, so the metal vertical grid structures rather act like miniature waveguides to steer the fields in the desired direction to make a radiating structure with similar near-field patterns to a conventional DRA. There are also various unique and controllable non-isotropic modes [40] present in the GDRAs that could be advantageous for various applications, where feeding position and orientation changes the generated modes.

A single element GDRA with an effective permittivity of 14.6, an impedance bandwidth of 6%, and a realized gain of 7.6 dBi has been demonstrated in [40]. Futher improvement in the impedance bandwidth of I-beam embedded GDRAs has been made in [41] by using different coplanar waveguide (CPW) feeds. The antennas proposed in that work have wide impedance bandwidth of

16.26% and high radiation efficiency of 90% and are an excellent choice for high performance mm-wave antennas. However, considerable work remains to make a feasible next-generation technology, including reducing the fabrication complexity of the embedded inclusions by decreasing the grids height (i.e, low-profile) and using simple grid structures such as square and rectangles. Lastly, arraying the GDRA elements effectively to provide high gain, which involves developing viable high-frequency feed and signal distribution networks is required.

Feeding networks are also an important building block of many high performance microwave and mm-wave devices, especially for antennas [42], [43]. The high-power handling and low loss feature of a rectangular waveguide makes it an ideal candidate for the power dividing applications. However, conventional rectangular waveguides are bulky, expensive, and difficult to integrate with planar microwave and mm-wave structures thus limiting their widespread usage. On the other hand, planar transmission lines such as microstrip-line, co-planar line etc. have been used primarily in lower frequency microwave applications, providing low cost fabrication and easy integration with other circuits. Microstrip-line, however, is not an ideal candidate for higher frequencies because of dispersion, mutual coupling, high transmission losses, and high radiation losses especially at line discontinuities [44], [45].

The substrate integrated waveguide (SIW) [46], [47] has high performance at mm-wave frequencies and can be realized using conventional printed circuit board (PCB) techniques. Like microstrip-line and other planar feed technologies, SIW is not only compatible with printed circuit board (PCB) techniques, but also has "waveguide-like" performance at higher frequencies, e.g. low loss, high Q, compact size, and allows integration with planar structures. SIW virtually eliminates radiation losses and undesirable back radiations typical of conventional feed structures at high frequencies. An SIW feeding mechanism has been reportedly used up to 101.8 GHz [48] for exciting antenna arrays.

In conclusion, some of the major challenges for deploying future mm-wave mobile communication devices are the designing of high performance antennas, i.e., high gain and high radiation efficiency to mitigate the effect of the severe free space path loss [49] at certain frequencies due to atmospheric absorption i.e., 4 dB/km at 60 GHz. Front-ends capable of operating in a large frequency bandwidth to meet the increasing demand of bandwidth-hungry applications such as high-definition video streaming, strict fabrication tolerances due to relatively small operating

wavelength which requires special fabrications techniques for developing the antennas for the emerging millimeter wave RF transceivers, and low loss signal distribution networks for feeding the large antenna arrays are required for next generation systems.

A more detailed description of current DRAs, GDRAs and ultra-high precision X-ray lithographic fabrication techniques are provided in the coming sections for giving better insight into the current and the future requirements for high-performance mm-wave antennas.

1.2. Comments on Conventional and Artificial Dielectric Resonator (DR) Antennas and Arrays

Following are the important conclusions extracted from the past literature published on traditional and artificial DRAs:

1. Conventional low permittivity DRAs are not only difficult to excite but their large size makes them impractical to be integrated into compact devices.

2. Most of the high permittivity DRA structures are composed of hard ceramic material which is difficult to machine with high precisions especially for mm-wave applications, where the fabrication tolerances become comparable to the operating wavelength.

3. Ceramic DRAs with high material constant have low operational bandwidth due to high-Q factor, limiting their use for wideband applications.

4. In comparison to ceramic DRAs, artificial DRAs have more freedom in antenna design, i.e., material characteristics can be altered by using various shape metallic inclusions as well as their inter-element spacing, size, etc.

5. Dielectric permittivity of most of the previously discovered artificial dielectrics is found to be in the range of 4-10 as discussed in [50], [51]. However, for more compact designs structures with a higher dielectric constant such as $\epsilon_r > 10$ are required.

6. The artificial dielectrics provide more flexibility to antenna designers as compared to the conventional high permittivity substrates such as optimizing the proposed dielectric in simulation software prior to utilizing them in practical antennas.

7. Excitation of new modes is possible by using artificial dielectric resonators as mentioned in [40], which have more focused broadband radiation patterns than the simple dielectric resonator antennas.

8. The impedance bandwidth of artificial dielectric resonator antennas discussed in [40] of 6% still needs to be improved for wideband applications with stable radiation patterns.

9. Recent several research publications have used SIW feed technology in DR arrays [52]-[57]. However, SIW arrays using artificial polymer-based dielectric resonators are still to be explored.

1.3. X-Ray Lithography

During the last decade, there has been tremendous progress in the field of microfabrication, driven by the market need for compact, precise, and low-cost micro-components and microsystems required in portable telecommunication equipment, computers, and healthcare diagnostics. For instance, micro components are needed in healthcare for implantable medical devices, microreactors for bioprocessing, fiber optical alignment systems in communication, and mechanical parts such as nozzles, gears, and actuators. The rapid pace towards the miniaturization of new devices and systems is demanding new microfabrication techniques. Since the discovery of the fact that the processes used for designing silicon microchips can be extended towards the manufacturing of microstructures in other materials, the semiconductor-based industries have activated several research and developments programs in microtechnology. Generally, these methodologies produce two-dimensional structures, which then further required other processes to make three-dimensional (3D) structures. For instance, in micromechanical systems components are developed by wet chemical anisotropic etching of single crystal silicon. Additional improvements can be achieved by using dry etching using ions and plasma. Further developments regarding very deep microstructures have been made by using X-ray lithography using synchrotron radiation. The most prominent microfabrication technologies available in the market are isotropic and anisotropic etching, surface and bulk micromachining and a process known as LIGA, which allows the development of microstructures with the lateral dimension in the microns and aspect ratio up to 200 [59].

LIGA is an acronym for Lithography (Lithographie), electroplating (Galvanoformung), molding (Abformung). It was first reported at Karlsruhe Nuclear research laboratory in Germany in the 1980s while developing small slotted nozzles for separating uranium isotopes. Since then, various research groups have been working to develop a range of innovative high precision components such as microfluid devices, micro-reactors, and micro-spectrometers. The unique process of LIGA allows direct fabrication of high-quality 3D microstructures.

The core process of the LIGA is deep-X-ray lithography (D-XRL), which permits deep structures with submicron features using intense and highly collimated beam of X-Ray radiations. A detailed description of the fabrication process is discussed in Chapter 5.

Recently, there has been considerable interest in polymer-based antennas especially at millimeter-wave frequencies, where design dimensions are in millimeters. Therefore, deep X-ray lithography technology with characteristics of sub-micron features sizes and aspect ratio ~ 50 could be an excellent option for fabricating these microwave and millimeter structures in polymers.

1.4. Thesis Objective and Challenges

The research is aimed at demonstrating the potential of high permittivity micro-structured artificial grid dielectrics in designing compact and high-performance antenna arrays at millimeter-wave (mm-wave) frequencies. Polymer based antennas have emerged as a strong candidate for future mm-wave applications due to their wide bandwidth and high radiation efficiency [59]. But low permittivity DRAs of 2-3 are not only challenging to excite but also have large size and high resonance frequency [60]. Alternatively, ceramic dielectrics with high permittivity can be compact, but are typically narrowband and hard to fabricate. The concept of metal embedded artificial dielectrics provides an interesting alternative for attaining high permittivity dielectrics for building compact size, while maintaining wide bandwidth and high gain.

This thesis demonstrates several mm-wave GDRA examples fed through coplanar waveguide (CPW) and substrate integrated waveguide feeding mechanisms. The proposed antennas exhibit wide impedance bandwidth, high gain, high radiation efficiency and stable radiation pattern over the designed frequency bandwidth.

In the view of the proceeding background and the importance of high-performance mm-wave antennas, this research will address the following key objectives:

- The first objective of this research is to investigate the different shape metal inclusions such as rectangle and square to reduce the design complexities of previously explored I-beam GDRAs [40] as well as further enhancing the effective permittivity.
- The second objective is to improve the performance characteristics of the GDRAs e.g., enhancing the impedance bandwidth, making it compatible with different feed techniques such as coplanar-waveguide and aperture feeding for high-frequency applications.

- The third objective of this research is to extend the GDRAs concept to antenna arrays as a thin monolithic polymer layer with all the GDRA elements embedded inside to remove the requirement to assemble and align individual GDRA elements to the feed structure.

- The fourth objective is to develop a viable deep X-ray lithography-based fabrication procedure for building large-scale monolithic GDRA arrays at K_u and V-band. The fabricated structures will be measured to both structurally and functionally. This will include performing an optical microscope and a scanning electron microscope (SEM) inspection of the fabricated devices to ensure the structure quality and lateral dimension tolerances.

- The fifth objective is to design feasible high frequencies signal distribution networks using substrate integrated waveguide (SIW) technology for feeding single channel and multichannel GDRA arrays at 32 and 60 GHz.

- Finally, the frequency response and radiation patterns of all fabricated prototypes will be measured and discussed.

1.5.   Thesis Outline

The organization of the thesis is as follows: Chapter 2 discusses the electromagnetic wave propagation, antenna theory, and the literature review relevant to the scope of this thesis. Chapter 3 presents the implementation of multi-layer GDRAs integrated with the coplanar feedlines to enhance the impedance bandwidth and feed diversity. Furthermore, it provides the design and development of newly proposed monolithic rectangular grid based GDRAs. Chapter 4 describes a complete design procedure for building 1×8 SIW power splitter at 24 GHz along with in-depth parametric analysis of different design stages involved during the process. Chapter 5 provides a fabrication procedure for building GDRA array layers using deep X-ray lithography (DXRL). Chapter 6 provides single channel 4- element and 8-element series fed monolithic GDRA arrays at 32 GHz. In Chapter 7, the monolithic GDRA arrays concept is further extended to 2-dimensional multi-channel 4×4 and 8×8 GDRAs arrays at 60 GHz. Chapter 8 summarizes the thesis work by highlighting the key details and contributions made through this research work as well as the recommendations for the future work.

1.6. Publications

1. *W. Mazhar, D. Klymyshyn, and A. A. Qureshi, "Design and analysis of wideband eight-way SIW power splitter for mm-wave applications," Int. J. RF Microw. Comput. Eng., vol. 28, no. 2, 2018.*

W. Mazhar is the main author of this paper. This paper presents his original Ph.D. research work. The concept and design of the devices is completely developed by Waqas Mazhar. He also drafted the text of this paper documenting important research. The contribution of various other authors listed on the paper is given below:

D. Klymyshyn is the supervisor of this research activity and provided detailed insight and thorough revisions for the paper edits.

A. A. Qureshi assisted in preparing the PCB layouts for the fabricated devices.

2. *W. Mazhar, D. Klymyshyn, M. Tayfeh Aligodarz, S. Ganguly, A. A. Qureshi, and M. Boerner, "CPW fed grid dielectric resonator antennas with enhanced gain and bandwidth," Int. J. RF Microw. Comput. Eng., vol. 29, no. 3, p. e21639, Mar. 2019.*

W. Mazhar is the main author of this paper. This paper documents a part of his Ph.D. research work. He originally proposed the concept of multi-segment GDRA along with CPW feeding mechanism. The devices used to demonstrate this multi-segment and feeding concepts were previously designed and fabricated by the various authors on the paper during Dr. Klymyshyn's previously supervised research work, however these devices were never tested or fed in this manner. W. Mazhar also drafted the text of this paper documenting his specific contribution to this larger research.

D. Klymyshyn is the supervisor of this research activity and provided detailed insight and thorough revisions for the paper edits.

S. Ganguly designed the GDRA elements reported in this paper.

M. Tayfeh Aligodarz was one of the primary authors on a previous paper [40] involving the single element GDRA and provided layout tips for device fabrication.

A. A. Qureshi assisted in preparing the layouts for fabrication.

M. Boerner arranged fabrication of the devices at KIT.

3. W. Mazhar, D. Klymyshyn, G. Wells, A. A Qureshi, M. Jacobs, and S. Achenbach, "Low profile artificial grid dielectric resonator antenna arrays for mm-wave applications," IEEE Trans. Antennas Propag., vol. 67, no. 07, 2019.

W. Mazhar is the main author of this paper. The paper presents his original Ph.D. research work. The fabricated devices are completely developed by W. Mazhar. He also drafted the text of this paper documenting important research. The contribution of various other authors listed on the paper is mentioned below:

D. Klymyshyn is the supervisor of this research activity and provided detailed insight and thorough revisions for the paper edits.

G. Wells is the beamline scientist at CLS and assisted/advised on various fabrication steps at CLS including setting up the XRL exposures, sample development bath and the electroplating bath.

A. A Qureshi assisted in preparing the PCB layouts for the feed circuits.

Michael Jacobs is an associate scientist at CLS and helped in making the carbon mask required for XRL exposures.

S. Achenbach is the beam team lead at CLS. He offered useful suggestions for improving the development procedure for the thick exposed resists as well as for the microscopic inspection of the exposed samples.

4. W. Mazhar, D. Klymyshyn, G. Wells, A. A Qureshi, and, M. Jacobs "60 GHz Substrate Integrated Waveguide Fed Monolithic Grid Dielectric Resonator Antenna Arrays," accepted in IEEE antennas and wireless propagation letters, vol. 18, no. 06 April 2019.

W. Mazhar is the main author of this paper. The paper presents his original Ph.D. research work. The fabricated devices are completely developed by W. Mazhar. He also drafted the text of this paper documenting important research. The contribution of various other authors listed on the paper is mentioned below:

D. Klymyshyn is the supervisor of this research activity and provided detailed insight and thorough revisions for the paper edits.

G. Wells is the beamline scientist at CLS and assisted/advised on various fabrication steps at CLS including setting up the XRL exposures, sample development bath and the electroplating bath.

A. A Qureshi assisted in preparing the PCB layouts for the feed circuits.

Michael Jacobs is an associate scientist at CLS and helped in making the carbon mask required for XRL exposures.

References

[1] Y. Zou, J. Zhu, X. Wang, and L. Hanzo, "A Survey on Wireless Security: Technical Challenges, Recent Advances, and Future Trends," *Proc. IEEE*, vol. 104, no. 9, pp. 1727–1765, Sep. 2016.

[2] M. Huang and Y. Chen, "Guest Editorial: Internet of things and intelligent devices and services," *CAAI Trans. Intell. Technol.*, vol. 3, no. 2, pp. 73–74, Jun. 2018.

[3] R. Ranjan *et al.*, "The Next Grand Challenges: Integrating the Internet of Things and Data Science," *IEEE Cloud Comput.*, vol. 5, no. 3, pp. 12–26, May 2018.

[4] S. Mumtaz, A. Bo, A. Al-Dulaimi, and K.-F. Tsang, "Guest Editorial 5G and Beyond Mobile Technologies and Applications for Industrial IoT (IIoT)," *IEEE Trans. Ind. Informatics*, vol. 14, no. 6, pp. 2588–2591, Jun. 2018.

[5] M. Guizani, H. Chen, and C. Wang, *The Future of Wireless Networks:Architectures, Protocols and Services*, Ist Edt. CRC Press, Taylor and Francis Group, 2015.

[6] F. Hu, *Opportunities in 5G networks : a research and development perspective*, 1st ed. 2016.

[7] G. Liu and D. Jiang, "5G: Vision and Requirements for Mobile Communication System towards Year 2020," *Chinese J. Eng.*, vol. 2016, pp. 1–8, Apr. 2016.

[8] J. Andrusenko, J. L. Burbank, and F. Ouyang, "Future Trends in Commercial Wireless Communications and Why They Matter to the Military," *Johns Hopkins APL Tech. Dig.*, vol. 33, pp. 6–15, 2015.

[9] S. Kumar, G. Gupta, and K. R. Singh, "5G: Revolution of future communication technology," in *2015 International Conference on Green Computing and Internet of Things (ICGCIoT)*, 2015, pp. 143–147.

[10] Zizheng Cao *et al.*, "Advanced Integration Techniques on Broadband Millimeter-Wave Beam Steering for 5G Wireless Networks and Beyond," *IEEE J. Quantum Electron.*, vol. 52, no. 1, 2016.

[11] W. Tong and Z. Peiying, "5G: A technology vision-Huwawei," hw_329327, 2014. https://www.huawei.com/ilink/en/download/HW_314849

[12] Q. C. Li, H. Niu, A. T. Papathanassiou, and G. Wu, "5G Network Capacity: Key Elements and Technologies," *IEEE Veh. Technol. Mag.*, vol. 9, no. 1, pp. 71–78, Mar. 2014.

[13] Verizon, "The Journey to 5G | Healthcare IT News," 2018. [Online]. Available: https://www.healthcareitnews.com/news/journey-5g. [Accessed: 16-Jul-2018].

[14] D. J. Teece, "5G Mobile: Disrupting the Automotive Sector," 2017.

[15] D. Bandyopadhyay and J. Sen, "Internet of Things: Applications and Challenges in Technology and Standardization," *Wirel. Pers. Commun.*, vol. 58, no. 1, pp. 49–69, May 2011.

[16] M. R. Palattella, P. Thubert, X. Vilajosana, T. Watteyne, Q. Wang, and T. Engel, "6TiSCH Wireless Industrial Networks: Determinism Meets IPv6," in *Internet of things*, Cham: Springer, 2014, pp. 111–141.

[17] L. J. Poncha, S. Abdelhamid, S. Alturjman, E. Ever, and F. Al-Turjman, "5G in a Convergent Internet of Things Era: An Overview," in *2018 IEEE International Conference on Communications Workshops (ICC Workshops)*, 2018, pp. 1–6.

[18] "Cisco Visual Networking Index: Forecast and Trends, 2017–2022 White Paper - Cisco," c11-741490, 2019. https://www.cisco.com/c/en/us/solutions/collateral/service-provider/visual-networking-index-vni/white-paper-c11-741490.html

[19] H. Peng, Y. Xiao, Y. Ruyue, and Y. Yifei, "Ultra Dense Network: Challenges, Enabling Technologies and New Trends," *China Commun.*, vol. 13, no. 2, pp. 30–40, 2016.

[20] I. Ndip, T. H. Le, O. Schwanitz, and K.-D. Lang, "A comparative analysis of 5G mmWave antenna arrays on different substrate technolgies," in *2018 22nd International Microwave and Radar Conference (MIKON)*, 2018, pp. 222–225.

[21] A. del Campo and E. Arzt, "Fabrication Approaches for Generating Complex Micro- and Nanopatterns on Polymeric Surfaces," *Chem. Rev*, vol. 108, no. 3, p. 911−945, 2008.

[22] T. G. Sun, X. Z. Gao, and H. Zhang, "Fabrication of micro/nano dual-scale structures by improved deep reactive ion etching," *J. Micromech. Microeng*, vol. 20, no. 7, p. 075028, 2010.

[23] H. Guckel, "High-aspect-ratio micromachining via deep X-Ray lithography," in *Proc. IEEE*, 1998, pp. 1586–1593.

[24] W. Hong, K. H. Baek, Y. Lee, Y. Kim, and S.-T. Ko, "Study and prototyping of practically large-scale mmWave antenna systems for 5G cellular devices," *IEEE Commun. Mag.*, vol. 52, no. 9, pp. 63–69, Sep. 2014.

[25] K.-L. Lau, K.-M. Luk, and K.-F. Lee, "Design of a Circularly-Polarized Vertical Patch Antenna," *IEEE Trans. Antennas Propag.*, vol. 54, no. 4, pp. 1332–1335, Apr. 2006.

[26] Y. P. Zhang and J. J. Wang, "Theory and Analysis of Differentially-Driven Microstrip Antennas," *IEEE Trans. Antennas Propag.*, vol. 54, no. 4, pp. 1092–1099, Apr. 2006.

[27] Y. B. Nechaev, D. N. Borisov, A. I. Klimov, and I. V. Peshkov, "Planar center-fed leaky-wave antenna arrays for millimeter wave systems," in *2015 International Conference on Antenna Theory and Techniques (ICATT)*, 2015, pp. 1–3.

[28] H. Liu, Y. He, H. Wong, and Z. Shen, "Printed J-slot patch antenna for millimeter-wave applications," in *2016 International Wireless Communications and Mobile Computing Conference (IWCMC)*, 2016, pp. 794–799.

[29] H. Chu, Y.-X. Guo, and Z. Wang, "60-GHz LTCC Wideband Vertical Off-Center Dipole Antenna and Arrays," *IEEE Trans. Antennas Propag.*, vol. 61, no. 1, pp. 153–161, Jan. 2013.

[30] K. Sakakibara, Y. Ikeno, N. Kikuma, and H. Hirayama, "Millimeter-wave slotted waveguide planar array using partially-parallel feeding with travelling-wave excitation," in *2010 IEEE Antennas and Propagation Society International Symposium*, 2010, pp. 1–4.

[31] J. Navarro, "Wide-band, low-profile millimeter-wave antenna array," *Microw. Opt. Technol. Lett.*, vol. 34, no. 4, pp. 253–255, Aug. 2002.

[32] D. Liu, *Advanced millimeter-wave technologies : antennas, packaging and circuits*. J. Wiley & Sons, 2009.

[33] M. Mrnka and Z. Raida, "Enhanced-Gain Dielectric Resonator Antenna Based on the Combination of Higher-Order Modes," *IEEE Antennas Wirel. Propag. Lett.*, vol. 15, pp.

710–713, 2016.

[34] K. Gong, X. H. Hu, P. Hu, B. J. Deng, and Y. C. Tu, "A Series-Fed Linear Substrate-Integrated Dielectric Resonator Antenna Array for Millimeter-Wave Applications," *Int. J. Antennas Propag.*, vol. 2018, pp. 1–6, Apr. 2018.

[35] R. Cicchetti, A. Faraone, E. Miozzi, R. Ravanelli, and O. Testa, "A High-Gain Mushroom-Shaped Dielectric Resonator Antenna for Wideband Wireless Applications," *IEEE Trans. Antennas Propag.*, vol. 64, no. 7, pp. 2848–2861, Jul. 2016.

[36] S. Keyrouz and D. Caratelli, "Dielectric Resonator Antennas: Basic Concepts, Design Guidelines, and Recent Developments at Millimeter-Wave Frequencies," *Int. J. Antennas Propag.*, vol. 2016, pp. 1–20, Oct. 2016.

[37] M. R. Hidayat, A. D. Setiawan, S. Basuki, and A. Munir, "Artificial dielectric material and its implementation for TE10 mode waveguide filter," in *2017 11th International Conference on Telecommunication Systems Services and Applications (TSSA)*, 2017, pp. 1–4.

[38] R. C. Jain, "Artificial Dielectrics and Some of their Applications," *IETE J. Educ.*, vol. 47, no. 2, pp. 67–77, Apr. 2006.

[39] K. Wu, "Integration and interconnect techniques of planar and non-planar structures for microwave and millimeter-wave circuits," in *Asia-Pacific Microwave Conference (APMC) Proceedings*, 2001, pp. 411–416.

[40] M. T. Aligodarz, D. M. Klymyshyn, Atabak Rashidian, M. Borner, L. Shafai, and J. Mohr, "Investigations on Photoresist-based Artificial Dielectrics with Tall Embedded Metal Grids and Their Resonator Antenna Application," *IEEE Trans. Antennas Propag.*, vol. 63, no. 9, pp. 3826–3838, 2015.

[41] W. Mazhar, D. M. Klymyshyn, M. Tayfeh Aligodarz, S. Ganguly, A. A. Qureshi, and M. Boerner, "CPW fed grid dielectric resonator antennas with enhanced gain and bandwidth," *Int. J. RF Microw. Comput. Eng.*, vol. 29, no. 3, p. e21639, Mar. 2019.

[42] *Microwave filters impedance-matching network and coupling structures*. New York: McGraw-Hill, 1964.

[43] J. Hirokawa and M. Ando, "Single-layer feed waveguide consisting of posts for plane TEM wave excitation in parallel plates," *IEEE Trans. Antennas Propag.*, vol. 46, no. 5, pp. 625–630, May 1998.

[44] K. Wu, "Substrate integrated circuits (SICs) for low-cost high-density integration of millimeter-wave wireless systems," in *IEEE Radio and Wireless Symposium (RWS) Proceedings*, 2008, pp. 683–686.

[45] C. Wood *et al.*, "Radiation conductance of open-circuit low dielectric constant microstrip," *Electron. Lett.*, pp. 121–123, 1978.

[46] K. Wu, D. Desiandes, and Y. Cassivi, "The substrate integrated circuits - a new concept for high-frequency electronics and optoelectronics," in *6th International Conference on Telecommunications in Modern Satellite, Cable and Broadcasting Service, 2003. TELSIKS 2003.*, vol. 1, p. P-III-P-X.

[47] F. Xu and K. Wu, "Guided-wave and leakage characteristics of substrate integrated waveguide," *IEEE Trans. Microw. Theory Tech.*, vol. 53k, no. 1, pp. 66–73, Jan. 2005.

[48] N. Ghassemi, K. Wu, S. Claude, X. Zhang, and J. Bornemann, "Low-Cost and High-Efficient W-Band Substrate Integrated Waveguide Antenna Array Made of Printed Circuit Board Process," *IEEE Trans. Antennas Propag.*, vol. 60, no. 3, pp. 1648–1653, Mar. 2012.

[49] J. G. Andrews *et al.*, "What Will 5G Be?," *IEEE J. Sel. Areas Commun.*, vol. 32, no. 6, pp. 1065–1082, Jun. 2014.

[50] C. C. Njoku, W. G. Whittow, and J. C. Vardaxoglou, "Simulation Methodology for Synthesis of Antenna Substrates With Microscale Inclusions," *IEEE Trans. Antennas Propag*, vol. 60, no. 5, pp. 2194–2202, 2012.

[51] I. Awai, Y. Maegawa, and T. Ishizaki, "Measurement of effective material constants of artificial dielectrics made of spherical metal particles," in *Asia Pacific Microwave Conference*, 2009, p. 1655–1658.

[52] W. M. Abdel Wahab, S. S-Naeini, and D. Busuioc, "Low cost low profile dielectric resonator antenna (DRA) fed by planar waveguide technology for millimeter- wave frequency applications," in *2009 IEEE Radio and Wireless Symposium*, 2009, pp. 27–30.

17

[53] W. M. Abdel-Wahab, D. Busuioc, and S. S-Naeini, "Millimeter-Wave High Radiation Efficiency Planar Waveguide Series-Fed Dielectric Resonator Antenna (DRA) Array: Analysis, Design, and Measurements," *IEEE Trans. Antennas Propag.*, vol. 59, no. 8, pp. 2834–2843, Aug. 2011.

[54] A. Sharma, A. Sarkar, A. Biswas, and M. J. Akhtar, "Substrate integrated waveguide fed dual-frequency dual-linearly-polarized dielectric resonator antenna," *Int. J. Microw. Wirel. Technol.*, vol. 10, no. 04, pp. 505–511, May 2018.

[55] K. Gong, X. H. Hu, P. Hu, B. J. Deng, and Y. C. Tu, "A Series-Fed Linear Substrate-Integrated Dielectric Resonator Antenna Array for Millimeter-Wave Applications," *Int. J. Antennas Propag.*, vol. 2018, pp. 1–6, Apr. 2018.

[56] Z. Hao, W. Hong, A. Chen, J. Chen, and K. Wu, "SIW fed dielectric resonator antennas (SIW-DRA)," in *2006 IEEE MTT-S International Microwave Symposium Digest*, 2006, pp. 202–205.

[57] N. Ashraf, H. Vettikalladi, and M. A. S. Alkanhal, "A DR Loaded Substrate Integrated Waveguide Antenna for 60 GHz High Speed Wireless Communication Systems," *Int. J. Antennas Propag.*, vol. 2014, pp. 1–9, Jun. 2014.

[58] S. K. Griffiths, "Fundamental limitations of LIGA x-ray lithography: sidewall offset, slope and minimum feature size," *J. Micromechanics Microengineering*, vol. 14, no. 7, pp. 999–1011, Jul. 2004.

[59] A. A. Qureshi, D. M. Klymyshyn, M. Tayfeh, W. Mazhar, M. Borner, and J. Mohr, "Template-Based Dielectric Resonator Antenna Arrays for Millimeter-Wave Applications," *IEEE Trans. Antennas Propag.*, vol. 65, no. 9, pp. 4576–4584, Sep. 2017.

[60] K. M. Luk and K.W. Leung, *Dielectric resonator antennas*. Research Studies Press, 2003.

0

Chapter 2 : Background and Theory

2.1.   Electromagnetic Wave Theory

In general, electric, and magnetic fields are complex vector quantities having magnitude, phase and direction. The connection between the electric and magnetic fields, charges and currents associated with them are governed by physics laws known as Maxwell's equations, which set the foundation of classical electromagnetic theory. This group of well-defined equations is achieved through a series of experimental observations made by different scientists. These equations can either be written in differential or in integral form. However, the differential form of Maxwell's equations is the most commonly used representation to solve the boundary value of electromagnetic problems.

2.1.1. Maxwell's Equations in Differential Form

These expressions are used to describe and relate field vectors, charges densities and current densities in the space at any time. For these expressions to be valid, it is required that the field vectors are single-valued, bounded, and continuous functions of the space and time, i.e., exhibit continuous derivatives. In most cases, the field vectors associated with the electromagnetic waves possess these characteristics except in cases where abrupt changes in the current and charge density occur. This discontinuous distribution usually occurs at the interface between two media, where there are distinct variations in the electrical parameters across the interface. Therefore, a complete description of the field vectors at a time and at any point requires not only the Maxwell's equations in differential form, but also well-defined boundary conditions associated with them. The Maxwell's equations in the differential form can be written as:

$$\Delta \times \boldsymbol{E} = -\boldsymbol{M} - \frac{\partial \boldsymbol{B}}{\partial t} \tag{2.1}$$

$$\Delta \times \boldsymbol{H} = \boldsymbol{J} + \frac{\partial \boldsymbol{D}}{\partial t} \tag{2.2}$$

$$\nabla . \boldsymbol{D} = \rho_e \tag{2.3}$$

$$\nabla . \boldsymbol{B} = \rho_m \tag{2.4}$$

$$\boldsymbol{D} = \varepsilon \boldsymbol{E} \tag{2.5}$$

$$\boldsymbol{B} = \mu \boldsymbol{H} \tag{2.6}$$

$$\boldsymbol{J} = \sigma \boldsymbol{E} \tag{2.7}$$

All the above field variables are time-varying quantities, with each as a function of time and space coordinates such as $E = E(x, y, z; t)$. These variables can be defined as

E = electric field intensity (V/m)

H = magnetic field intensity (A/m)

D = electric flux density (C/m^2)

B = magnetic flux density (Weber/ m^2)

ρ_e = electric charge density (C/ m^3)

ρ_m = magnetic charge density (Weber/ m^3)

whereas J is electric current density (A/ m^2), M is the magnetic current density (V/ m^2) and ε, μ and σ are the permittivity, permeability and conductivity of the medium. For free space $\varepsilon = \varepsilon_0 = 8.85 \times 10^{-12} \left(\frac{farads}{meter}\right)$; $\mu = \mu_0 = 4\pi \times 10^{-7} \left(\frac{henries}{meter}\right)$ and $\sigma = 0$.

Eq. (2.5)-(2.7) are the constitutive relations for the Maxwell's equation. They are needed to illustrate the general nature of the electric and magnetic fields; how they are coupled and depend on each other.

In a quick summary, equation (2.1) is Faraday's law, that describes that time-varying magnetic field creates a circulating electric field. The second equation (2.2) is the Maxwell's Amperes law, which describes the creation of circulating magnetic fields (2.6) by currents of electric charges (2.7) and by time-varying electric fields (2.5). Equation (2.3) is Gauss's law of electricity which states that electric field originates from electric charges contained in a closed surface, while equation (2.4) is Gauss's law of magnetism which states that magnetic fields do not originate at points or there are no magnetic charges in nature but can be visualized as loops that have no beginning or end point. Faraday's law and Maxwell's Ampere law describe how the time-varying electric field produces a time-varying magnetic field and vice versa. Once there is a change in one quantity (electric field), a change in other quantity (magnetic field) occurs, and these changes continue to "propagate" in time.

For the first two equations (2.1) and (2.2), E and H-fields are confined together. However, for most of the electromagnetic problems decoupling of both E and H fields is required to determine

solutions to EM problems, such as antenna power pattern. This can be done by taking time derivates on both sides of (2.1) and (2.2), which result in following 2nd order equations:

$$\Delta \times \frac{\partial \boldsymbol{B}}{\partial t} = \mu_o \frac{\partial \boldsymbol{J}}{\partial t} + \mu_o \varepsilon_o \frac{\partial^2 \boldsymbol{E}}{\partial t^2} \tag{2.8}$$

$$\Delta \times \Delta \times \boldsymbol{E} = \mu_o \frac{\partial \boldsymbol{J}}{\partial t} + \mu_o \varepsilon_o \frac{\partial^2 \boldsymbol{E}}{\partial t^2} \tag{2.9}$$

By using the vector identity

$$\Delta \times (\Delta \times \boldsymbol{A}) = \nabla(\nabla.\boldsymbol{A}) - \nabla^2 \boldsymbol{A} \tag{2.10}$$

The equation (2.9) can be written as

$$\nabla(\nabla.\boldsymbol{E} - \nabla)^2 \boldsymbol{E} = \mu_o \frac{\partial \boldsymbol{J}}{\partial t} + \mu_o \varepsilon_o \frac{\partial^2 \boldsymbol{E}}{\partial t^2} \tag{2.11}$$

The above expression is the differential equation involving E-field and known sources. The electric fields have been mathematically decoupled from the magnetic field. By repeating a similar process for equation (2.2) gives us:

$$\nabla(\nabla.\boldsymbol{B} - \nabla)^2 \boldsymbol{B} = \mu_o \Delta \times \boldsymbol{J} - \frac{1}{c^2}\frac{\partial^2 \boldsymbol{B}}{\partial t^2} \tag{2.12}$$

In summary, Maxwell equations in wave form can be expressed as follows:

$$\nabla(\nabla.\boldsymbol{E} - \nabla)^2 \boldsymbol{E} = \mu_o \frac{\partial \boldsymbol{J}}{\partial t} + \mu_o \varepsilon_o \frac{\partial^2 \boldsymbol{E}}{\partial t^2} \tag{2.13}$$

$$\nabla(\nabla.\boldsymbol{B} - \nabla)^2 \boldsymbol{B} = \mu_o \Delta \times \boldsymbol{J} - \frac{1}{c^2}\frac{\partial^2 \boldsymbol{B}}{\partial t^2} \tag{2.14}$$

$$\nabla.\boldsymbol{E} = \frac{\rho_o}{\varepsilon_o} \tag{2.15}$$

$$\nabla.\boldsymbol{B} = 0 \tag{2.16}$$

One of the most important parameters to characterize the antenna performance is the radiation behavior. The usual method for analyzing any radiation problem is to specify the sources first and then acquire the field radiated by those sources. Generally, there are two approaches which could be used for acquiring the antenna radiated field as shown in Figure 2.1. In most of the practical problems, a one-step procedure is preferred; as the electric and magnetic field intensities are both physically measurable quantities, whereas the two-step procedure using potentials is preferred for analytical analysis. The two step procedures relate electric potential and magnetic potential to $\boldsymbol{J}$ and $\boldsymbol{M}$ by integral relations. The $\boldsymbol{E}$ and $\boldsymbol{H}$ fields are then determined by simply differentiating electric potential $\boldsymbol{A}$ and magnetic potential $\boldsymbol{F}$. Although the two-step procedure involves both

integration and differentiation in comparison to a one step procedure involving integration only, the integrands in two-step procedures are much simpler. In the next section, we will demonstrate the radiated fields computation for an infinitesimal dipole using the vector potential approach.
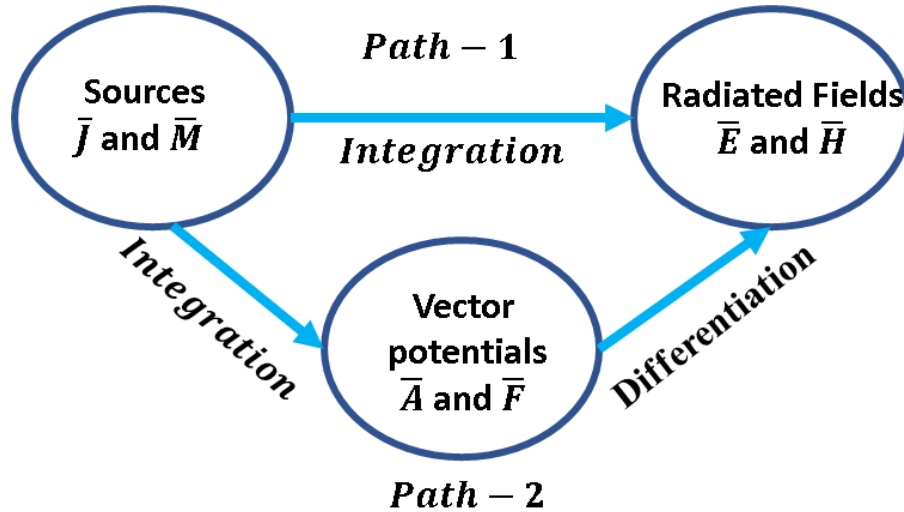
Figure 2.1 Block diagram for computing fields from electric and magnetic sources

2.1.2. Radiation from Infinitesimal Dipole (Hertzian dipole)

2.2.1.1.   Infinitesimal Dipole

An infinitesimal linear wire ($l \ll \lambda$) placed symmetrically at the origin of the coordinate system along the z-axis is shown in Figure 2.2. The infinitesimal dipole is usually not practical; however, it is mostly utilized as a building block for analyzing complex antennas. The two plates shown on the top and bottom of the dipole are used to provide capacitive loading for maintaining uniform current distribution along the wire. The spatial variation of the current is supposed to be constant as the wire radius is assumed very thin ($a \ll \lambda$). The current distributing along the wire is given by the following equation:

$$I(z') = \widehat{a_z} I_o \ \text{(A)} \tag{2.17}$$

2.2.1.2.   Radiated Fields

Since the source shown in Figure 2.2a carries only electric current I_e, while other entities like current I_m and magnetic vector potential are zero. Therefore, the electric vector potential $\boldsymbol{A}$ can be written as [1]:

$$\mathbf{A}(x,y,z) = \frac{\mu}{4\pi} \oint I_e(x',y',z') \frac{e^{-jkR}}{R} dl' \ \text{(V)} \tag{2.18}$$
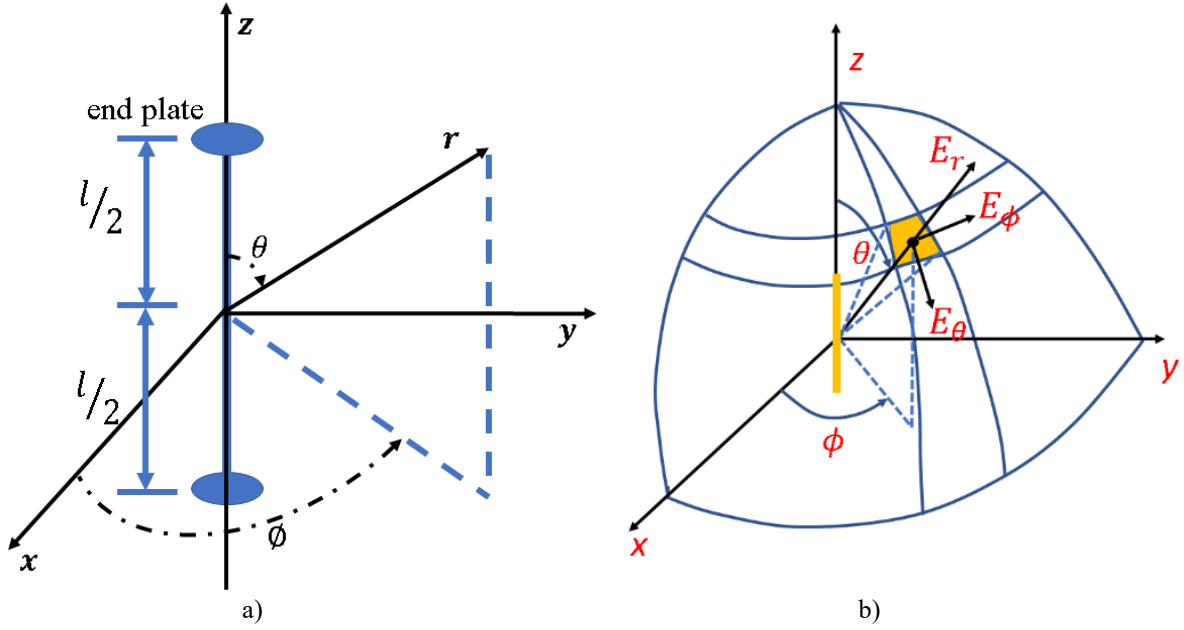
Figure 2.2 a) Infinitesimal dipole; b) Electric field orientation[1] © 2016 Wiley. Reprinted with permission

where (x, y, z) represents the observation point coordinates and (x', y', z') represents the source coordinates, R is the distance from any point on the source to an observation point. For the given problem, we can write the following conventions:

$$I_e(x', y', z') = \widehat{a_z} I_o \tag{2.19}$$

$$x' = y' = z' = 0 \tag{2.20}$$

$$R = \sqrt{(x - x') + (y - y') + (z - z')} = \sqrt{x^2 + y^2 + z^2} \tag{2.21}$$

$$dl' = dz' \tag{2.22}$$

$$k = \omega^2 \varepsilon \mu \tag{2.23}$$

By using the above equations, we can rewrite the equation (2.18) as follow:

$$\mathbf{A}(x, y, z) = \widehat{a_z} \frac{\mu I_o e^{-jkr}}{4\pi r} \int_{-l/2}^{+l/2} dz' = \widehat{a_z} \frac{\mu I_o l e^{-jkr}}{4\pi r} \tag{2.24}$$

$$\mathbf{H} = \widehat{a_\Phi} \frac{1}{\mu} (\vec{\nabla} \times \vec{A}) = \widehat{a_\Phi} \frac{1}{\mu r} \left[\frac{\partial(r A_\theta)}{\partial r} - \frac{\partial(A_r)}{\partial \theta} \right] \tag{2.25}$$

---

[1] Reprinted with permission from [1] C.A Balanis, *Antenna theory: analysis and design*, 2016.

For antennas, the radiated fields are generally expressed in spherical coordinates. Therefore, the spherical transformation of $\mathbf{A}(x, y, z)$ for the above expression can be written as

$$\begin{bmatrix} A_r \\ A_\theta \\ A_\phi \end{bmatrix} = \begin{bmatrix} \sin\theta\cos\phi & \sin\theta\sin\phi & \cos\theta \\ \cos\theta\cos\phi & \cos\theta\sin\phi & -\sin\theta \\ -\sin\phi & \cos\phi & 0 \end{bmatrix} \begin{bmatrix} A_x \\ A_y \\ A_z \end{bmatrix}$$

$$A_r = A_z \cos\theta = \frac{\mu I_o e^{-jkr}}{4\pi r}\cos\theta \tag{2.26}$$

$$A_\theta = A_z \cos\theta = -\frac{\mu I_o e^{-jkr}}{4\pi r}\sin\theta \tag{2.27}$$

$$A_\phi = 0 \tag{2.28}$$

$$H_r = H_\theta = 0 \tag{2.29}$$

$$H_\phi = j\frac{\mu I_o l \sin\theta}{4\pi r}\left[1 + \frac{1}{jkr}\right]e^{-jkr} \tag{2.30}$$

$$\mathbf{E} = \mathbf{E}_A = -j\omega\mathbf{A} - j\frac{1}{\omega\mu\varepsilon}\nabla(\nabla.A) = \frac{1}{j\omega\varepsilon}\nabla\times\mathbf{H} \tag{2.31}$$

$$E_r = \eta\frac{I_o l \cos\theta}{2\pi r^2}\left[1 + \frac{1}{jkr}\right]e^{-jkr} \tag{2.32}$$

$$E_\theta = j\eta\frac{kI_o l \sin\theta}{4\pi r}\left[1 + \frac{1}{jkr} - \frac{1}{(kr)^2}\right]e^{-jkr} \tag{2.33}$$

$$E_\phi = 0 \tag{2.34}$$

$$\eta = \frac{E_\theta}{H_\phi} \quad (\Omega) \tag{2.35}$$

As per our initial assumption $dl \ll r$ for far-field, therefore terms $\frac{1}{jkr}$, $\frac{1}{(kr)^2}$ can be approximated to be zero in the above E and H-field equations.

In the far-field case with $kr \gg 1$, E and H-fields in spherical coordinates can be expressed as follows:

$$\mathbf{H} = H_\phi = j\frac{k\mu I_o l \sin\theta}{4\pi r}\left[1 + \frac{1}{jkr}\right]e^{-jkr}.\hat{\phi} \tag{2.36}$$

$$\mathbf{E} = E_\theta = j\eta\frac{kI_o l \sin\theta}{4\pi r}e^{-jkr}.\hat{\theta} \tag{2.37}$$

$$E_r \approx E_\phi = H_r = H_r = H_\theta = 0 \quad \text{for } kr \gg 1$$

For electromagnetic waves, the magnitude and direction of the energy flow is described by a quantity known as a Poynting vector "S" which is equal to the cross product of the electric and magnetic field. Hence, for an infinitesimal dipole, the complex Poynting vector can be written as follows:

$$< S >= \frac{1}{2}\mathbf{E}\times\mathbf{H}^* \tag{2.38}$$

24

$$< S >= \frac{1}{2}\left(\frac{I_o l}{4\pi}\right)^2 k^2 \frac{\eta_o}{r^2} \sin^2 \theta . \hat{r} \quad (W/m^2) \tag{2.39}$$

$$\eta_o = \sqrt{\frac{\mu_0}{\varepsilon_0}} \quad (\Omega)$$

The following conclusions can be extracted from the above Poynting vector expressions:

i)   More input current means more radiated power.

ii) The smaller the length of the antenna, the lower is the radiated power.

iii) Power density is decreasing with the factor of r^2 of distance.

iv) Radiated power is dependent on angular distribution.

Total power radiated per unit solid angle is given by:

$$\frac{dP}{d\Omega} = r^2 < S >. \hat{r} \tag{2.40}$$

$$P = \int_0^{2\pi} \int_0^{\pi} \frac{dP}{d\Omega} \sin \theta d\theta d\phi \tag{2.41}$$

$$P = \frac{1}{2}\left(\frac{I_o l}{4\pi}\right)^2 k^2 \eta_o 2\pi \int_0^{\pi} \sin^3 \theta \, d\theta \tag{2.42}$$

$$P = \frac{1}{12\pi} I_o{}^2 l^2 k^2 \eta_o \quad (W) \tag{2.43}$$

Since the antenna radiates real power, therefore its radiation resistance can be given by an expression:

$$P = \frac{1}{2} I^2 R_{rad} \tag{2.44}$$

By comparing (2.43) and (2.44), the radiation resistance can be expressed as:

$$R_{rad} = \eta_o \left(\frac{2\pi}{3}\right)\left(\frac{dl}{\lambda}\right)^2 \quad (\Omega) \tag{2.45}$$

The infinitesimal dipole is not a good example of an efficient antenna due to small radiation resistance. For instance, in above expression (2.43) for $dl = 0.01\lambda$, i.e. $(l \ll \lambda)$; $R_{rad} = 0.08$. In general practice, large radiation resistance is required for antennas for efficient radiation; otherwise, most of the energy will be dissipated into the physical resistance as heat dissipation.

2.2 Antenna Fundamental Design Parameters

2.2.1. Radiation Pattern

The antenna radiation pattern is defined as a *mathematical function or graphical representation of the radiation properties of the antenna as a function of the space coordinates* [1]. In most cases, the antenna pattern is determined in the far-field region and represented as a function of the spherical coordinates. A series of electric or magnetic field values at a constant radius from the antenna is called the antenna amplitude pattern or field pattern. Another way of representing an antenna pattern is the power pattern, which is the square of the magnitude of the electric or magnetic field as a function of angular space. For example, a polar plot of field pattern and power pattern for a 10-element linear array of isotopic sources with an inter-element spacing of 0.25λ is shown in Figure 2.3a&b. Moreover, a linear plot of power pattern in a cartesian plane is also presented in Figure 2.3c for defining the important antenna pattern terms such as major/main-lobe, minor-lobes, back-lobes, half-power beamwidth (HPBW), and first null beamwidth (FNBW).

a)   b)

26
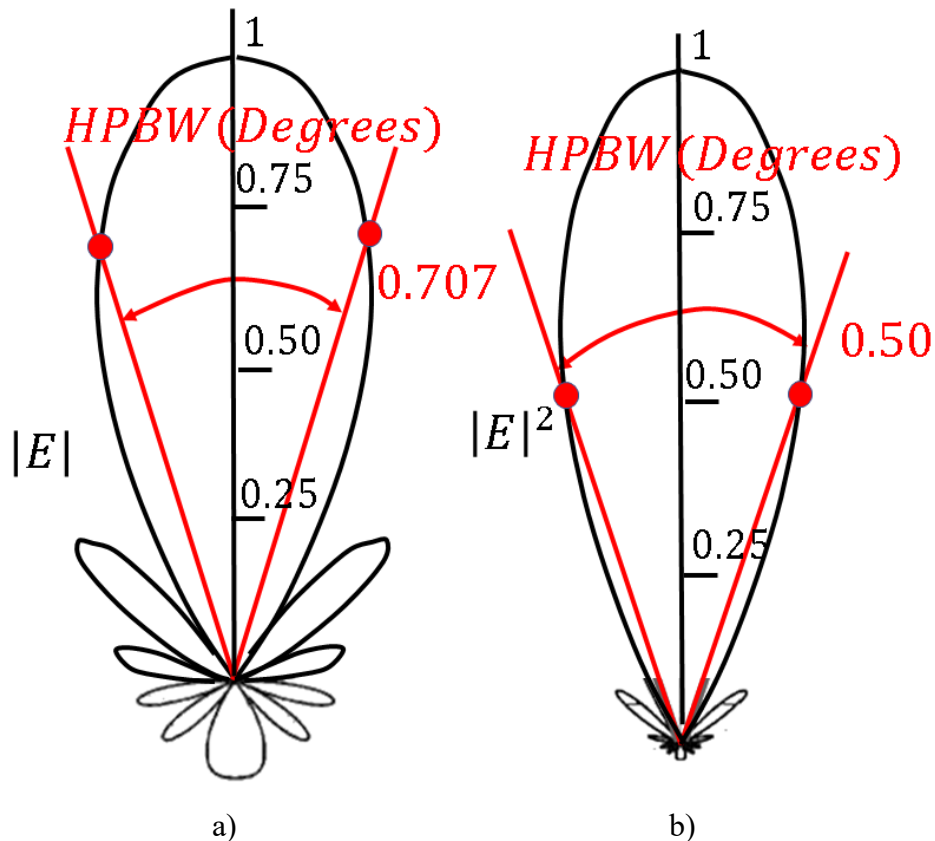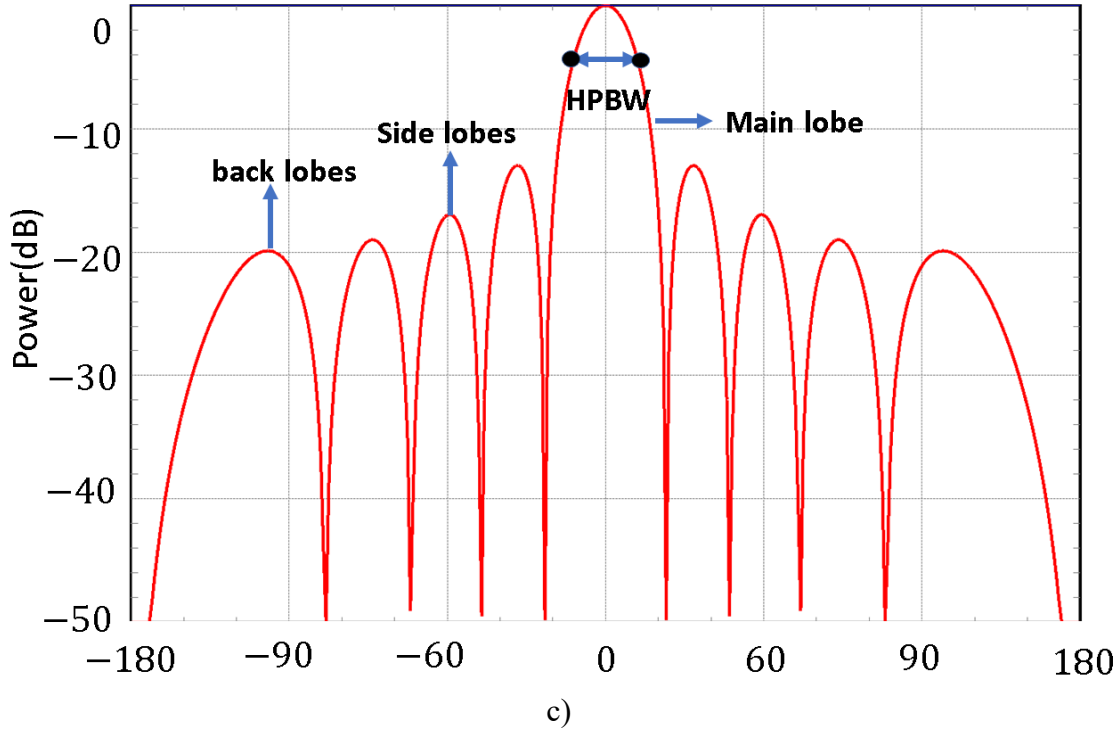
Figure 2.3 Two-dimensional a) normalized field pattern (in linear scale); b) normalized power pattern (in linear scale); c) normalized power pattern (in dB)

HPBW = half power beamwidth

FNBW = first null beamwidth

Main lobe: The antenna lobe containing the direction of maximum radiation

HPBW: Angular separation between two half power points on the main lobe is called half power beamwidth. For instance, in Figure 2.3c HPBW= 42^0

FNBW: Angular separation between two first nulls of the antenna pattern are called first null beamwidth. For instance, in Figure 2.3c FNBW= 60^0

2.2.2. Directivity

The directivity of the antenna is defined as *the ratio of radiation intensity in a given direction from the antenna to the radiation intensity averaged in overall directions* [1]. The radiation intensity in a given direction is a power radiated by an antenna per unit solid angle whereas the average radiation intensity is equal to total power radiated by antenna divided by 4π. In mathematical form, directivity can be written as:

$$D = \frac{U}{U_o} = \frac{4\pi U}{P_{rad}} \quad \text{(dB)} \tag{2.46}$$

$$U = r^2 W_{rad} \quad \text{(W)} \tag{2.47}$$

27

where U= radiation intensity, P_{rad}= total radiated power and W_{rad}= radiation density.

2.2.3. Antenna Efficiency

There are several types of efficiency that can be related to an antenna. The overall antenna efficiency e_o considers losses at the input terminal and within the structure of the antenna. Such losses are mainly due to impedance mismatch between the antenna and transmission line, or conduction and dielectric losses (I^2R) as illustrated in Figure 2.4.
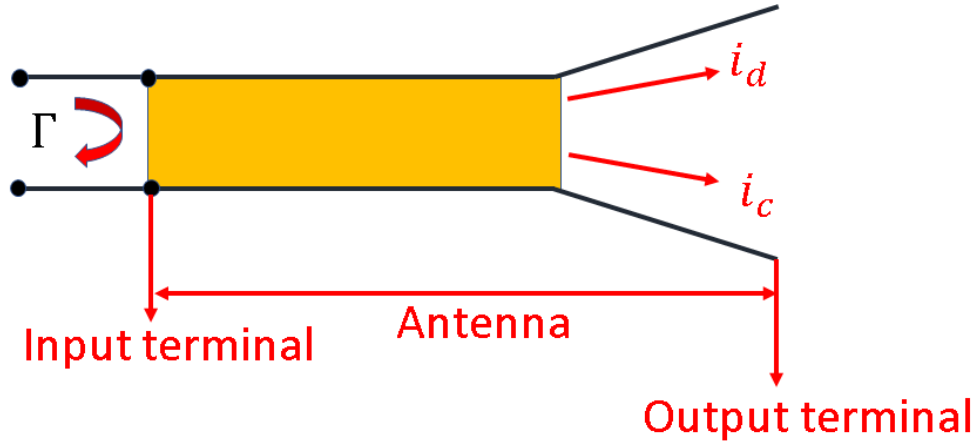
Figure 2.4 Reference terminal and losses of an antenna

In general, the total antenna efficiency can be written as:

$$e_o = e_r e_c e_d \tag{2.48}$$

e_o = antenna total efficiency

e_d = dielectric efficiency

e_r = reflection efficiency= $(1-|\Gamma|^2)$

e_c = conduction efficiency

whereas Γ = voltage reflection coefficient of an antenna and is defined as

$$\Gamma = \frac{(Z_{in} - Z_0)}{(Z_{in} + Z_0)} \tag{2.49}$$

Z_{in} = input impedance of an antenna

Z_0 = characteristic impedance of the transmission line

Generally, it is complicated to compute e_c and e_d. However, they can be determined experimentally as a single value. Therefore, we can rewrite the equation (2.48) as

$$e_o = e_{cd}(1\text{-}|\Gamma|^2)$$
$$\text{(2.50)}$$

whereas the term e_{cd} is referred to radiation efficiency, which is also often used to relate antenna gain and directivity.

2.2.4. Gain
i)   Relative Gain

The relative gain of the antenna is defined as a *ratio of the power gain in a given direction to the power gain of a reference antenna in its reference direction*. For correct measurement, the input power should be kept the same for both antennas. The reference antenna is usually a dipole antenna, horn antenna, or any antenna that gain is known or can be calculated. The mathematical expression for antenna gain can be written as:

$$G = \frac{4\pi U(\theta, \phi)}{P_{in}(reference\ antenna)}$$
$$\text{(2.51)}$$

where $U(\theta, \phi)$ = radiation intensity

ii)   Realized Gain

According to the definition of IEEE standards [2], an antenna gain does not include the losses resulting from impedance mismatches and dissipative losses as defined in Section 2.2.3. The term "realized gain" which is also referred to an absolute gain takes account of all mismatch/reflection losses represented in equation (2.48) as:

$$G(\theta, \phi) = e_o \left(\frac{4\pi U(\theta, \phi)}{P_{rad}} \right)$$
$$\text{(2.52)}$$

The expression (2.50) can also be related to directivity as:

$$G(\theta, \phi) = e_o D$$
$$\text{(2.53)}$$

2.2.5. Impedance Bandwidth
Impedance bandwidth and pattern bandwidth are the most common bandwidths, which are usually employed to characterize antennas. The impedance bandwidth is the *range of the frequencies for which the return loss (i.e. $S_{11}(dB)$) of an antenna lies below -10dB (VSWR ≤ 2)* as shown in Figure 2.5. Since the return loss and VSWR are measurements of how much power is reflected by the antenna from the transmission line, the input impedance of the antenna must be matched with the impedance of transmission line for maximum power transfer over a given frequency range. The

mathematical expression for VSWR, reflection coefficient and return loss are given in equation 2.54, 2.55 and 2.56.

$$\text{VSWR} = \frac{1 + |\Gamma|}{1 - |\Gamma|} \qquad (2.54)$$

$$\Gamma = \frac{(Z_{in} - Z_0)}{(Z_{in} + Z_0)} \qquad (2.55)$$

$$S_{11}(dB) = 20 \log |\Gamma| \qquad (2.56)$$

The bandwidth is expressed in percentage of the frequency difference of upper minus lower frequency over the center frequency. For example, a 10% bandwidth indicates that the frequency difference of the acceptable operation is 10% of the center frequency. The analytical relation for percentage bandwidth can be written as:

$$\% \text{ bandwidth} = \frac{f_h - f_l}{f_c} \qquad (2.57)$$

The pattern bandwidth is associated with gain, side lobe level, beamwidth, polarization and beam direction over certain range of frequency where an acceptable level of these parameters is maintained.
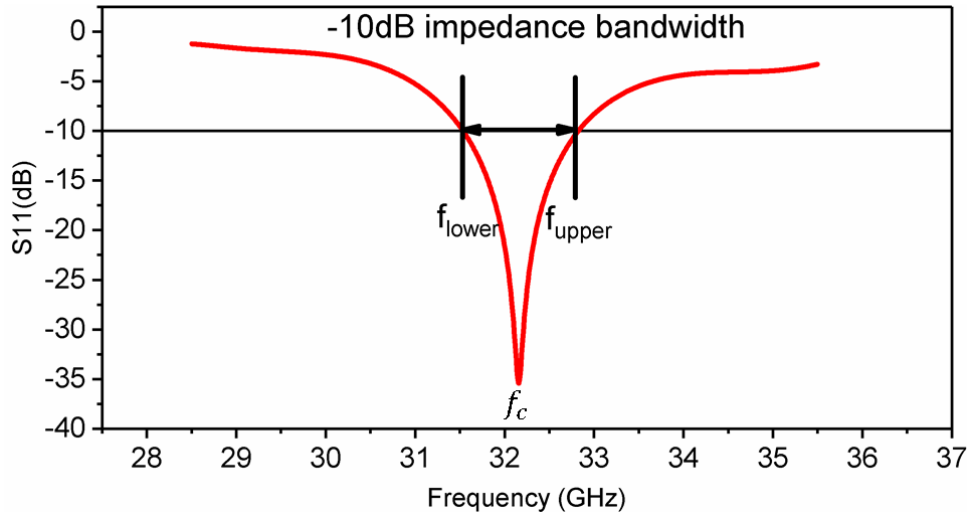
Figure 2.5 S-parameter plot for visualizing impedance bandwidth

f_{lower}, f_{upper}, and f_c are the lower, upper, and center frequency of the response

2.3   Planar Transmission Lines

Most electronic circuits, and especially high frequency digital, RF, and microwave circuits, employ transmission lines. Among these, printed circuit structures known as planar transmission lines are the most useful in modern electronics. They are used in microwave not only as interconnects for carrying signals between different components but also to develop various

matching networks, baluns, couplers, hybrids, filters, etc. Microstrip line, coplanar waveguide (CPW), strip line, coplanar strip line (CPS), finline, slot line, and substrate integrated waveguide (SIW) are some of the common planar transmission lines. This section describes three types of planar lines: i) microstrip line; ii) coplanar waveguide; and iii) substrate integrated waveguide.

2.3.1. Microstrip Line

The microstrip line was proposed by a group of engineers from the Federal Communications Research Laboratories in December 1952 [3]. It is one of the most popular planar transmission lines primarily due to its simple structure, ease of fabrication and direct integration with both active and passive microwave circuits [4]–[6]. The geometry of the microstrip line is provided in Figure 2.6. It consists of a metallic strip of width "w" on a grounded dielectric substrate of height "d" and relative permittivity ε_r. The microstrip line does not support the propagation of transverse electromagnetic mode (TEM) since the top metallic strip of width "w" is exposed to air. As a result, the signal in the microstrip line travels with two different phase velocities; outside the substrate and inside the substrate.

Hence, the actual mode of propagation inside the microstrip line is the hybrid mode between TE and TM mode. Field distribution for microstrip line is illustrated in Figure 2.6b. However, in most practical applications, the dielectric substrates are extremely thin as compared to the operating wavelength of the propagating signal, which allow them to be treated as a quasi-TEM mode. Therefore, good approximations for phase velocity, propagation constant, and characteristic impedance can be derived from the quasi-static solution. Given the design dimensions, the characteristic impedance of the microstrip line can be calculated by the following expressions [7]:

$$Z_o = \begin{cases} \dfrac{60}{\sqrt{\varepsilon_e}} \ln\left(\dfrac{8d}{W} + \dfrac{W}{4d}\right) & for\ W/d \leq 1 \\[3ex] \dfrac{120\pi}{\sqrt{\varepsilon_e \left[W/d + 1.393 + 0.667 \ln\left(W/d + 1.444\right)\right]}} & for\ W/d \geq 1 \end{cases} \qquad (2.58)$$

where W is the width of the microstrip line, d is the height of the substrate, and ε_e is the effective permittivity of the dielectric substrate, which accounts for the fact that fields around the microstrip line are partly in the air and partly in the dielectric substrate. The effective dielectric constant of the microstrip line can be approximated by:

$$\epsilon_e = \frac{\varepsilon_r + 1}{2} + \frac{\varepsilon_r - 1}{2} \frac{1}{\sqrt{1 + 12d/W}} \qquad (2.59)$$

a)   b)
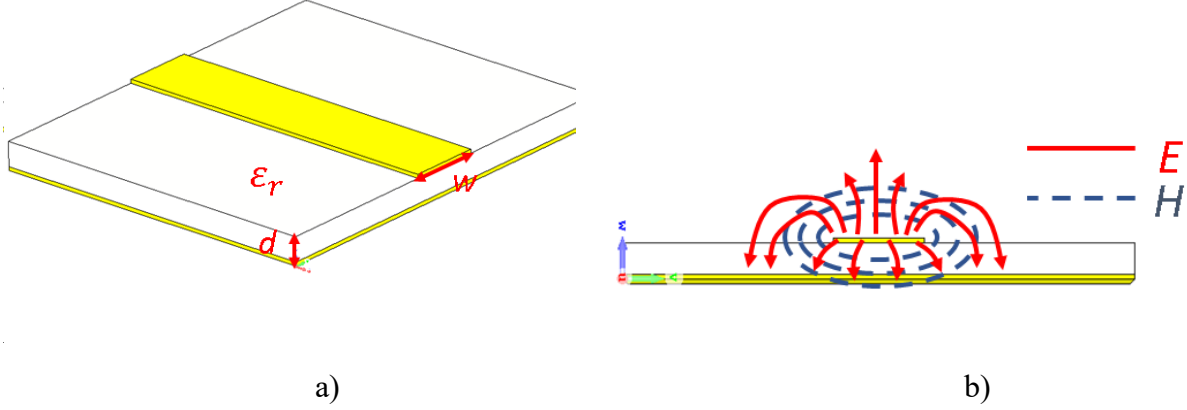
Figure 2.6 a) Geometry of microstrip line; b) Field distribution

There are three primary losses related to the microstrip line; conductor loss, dielectric loss, and radiation loss. The relation for the dielectric losses approximated in [8] is provided in (2.60). Similarly, the expression for ohmic loss is also given in (2.61). The radiation loss usually appears at high frequencies. This loss has been studied in [9], and the relation for radiation loss corresponding to the matched microstrip line is provided in (2.62). By looking at this equation, the radiation loss can be reduced by using a thin conductor strip or high permittivity substrate.

$$a_d = \frac{k_o \varepsilon_e (\varepsilon_r - 1) \tan \delta}{2 \sqrt{\varepsilon_e} (\varepsilon_r - 1)}; \; k_o = \frac{2\pi}{\lambda_o}; \; \tan \delta = \frac{\varepsilon_r (imginary)}{\varepsilon_r (real)}$$
$$\varepsilon_r = \varepsilon_r (real) - j\varepsilon_r (imaginary) \qquad (2.60)$$

$$a_c = \frac{R_s}{Z_o W}; \; R_s = \sqrt{\frac{\omega \mu_o}{2\sigma}} \qquad (2.61)$$

$$a_r = 60 \left(\frac{(2\pi t)}{\lambda_o}\right)^2 \left(1 - \frac{\varepsilon_e - 1}{2\sqrt{\varepsilon_e}} \log\left(\frac{\sqrt{\varepsilon_e + 1}}{\sqrt{\varepsilon_e - 1}}\right)\right) \qquad (2.62)$$

t= thickness of the conductor

2.3.2. Co-planar Waveguide

The coplanar waveguide (CPW) was proposed by Wen [10] in 1969. It consists of a strip of metallic conductor on a dielectric substrate with two ground planes running adjacent and parallel to the strip on the same surface. Since the dominant mode is quasi-TEM, there is ideally no cut off frequency in CPW. The presence of three separate conductors on the same surface makes it suitable

for integration with external passive and active devices. A useful relation for finding the characteristic impedance of CPW [11], [12] is provided in equation (2.63). The geometry of simple coplanar waveguide with design variables is given in Figure 2.7a.

a)   b)
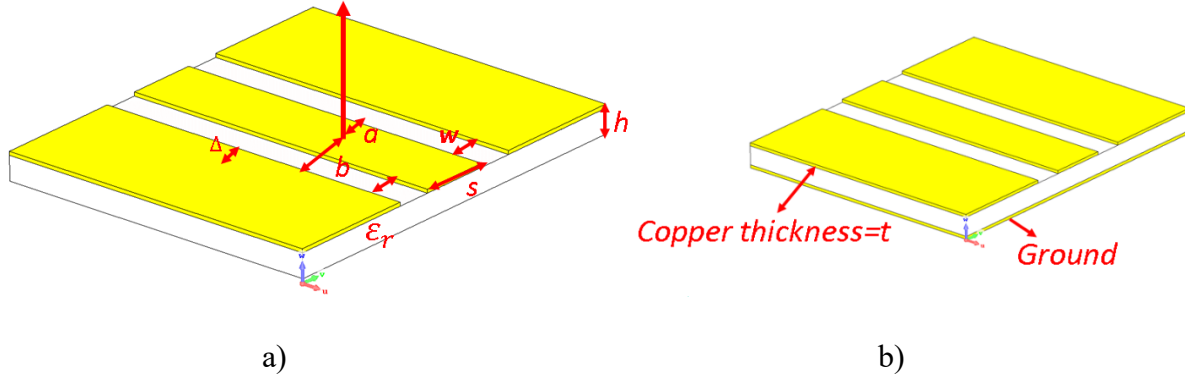
Figure 2.7 Geometry of a) coplanar waveguide; b) grounded coplanar waveguide

$$Z_o = \frac{30\pi K(k'_o)}{\sqrt{\varepsilon_e} K(k_o)} \qquad (2.63)$$

where

$$k_o = \frac{S}{S + 2W} \qquad (2.64)$$

$$k'_0 = \sqrt{1 - k_0^2} \qquad (2.65)$$

where $K(k_o)$ is the elliptical integral of first kind. More details in this regards are available in [13]. There are several configurations of coplanar waveguide discussed in [11]. One of the most common is the grounded CPW, which has an additional ground plane beneath the dielectric substrate. This configuration is used, for instance, for high power applications requiring heat dissipation as the back conductor allows a body contact to a heat sink. The design geometry for this configuration is given in Figure 2.7b. Like CPW, GCPW supports quasi TEM mode of propagation. The loss in CPW is generally dominated by conductor and dielectric loss, whereas the radiation loss is almost negligible at high frequencies due to tight E-fields confinement between the adjacent ground planes. The dielectric loss related to the quasi-TEM mode is given by equation (2.66) [13].

$$a_d = 27.29 \frac{\epsilon_r}{\sqrt{\varepsilon_{eff}}} \frac{[\varepsilon_{eff} - 1]}{[\varepsilon_r - 1]} \frac{\tan\delta}{\lambda_0} \text{ (dB/unit length)} \qquad (2.66)$$

where λ_0, $\tan \delta$, ε_r and ε_{eff} are the free space wavelength, loss tangent, relative permittivity and effectivity permittivity of the substrate. The mathematical expression for conductor loss computed by perturbation method can be written as [14] :

$$a_c = \frac{R_s}{16K^2(k)(1-k^2)Z_o} \times \left\{ \left[\frac{1}{a}\ln\left(\left(\frac{2a}{\Delta} - 1\right)\left(\frac{b-a+\Delta}{b+a+\Delta}\right)\right) \right] + \left[\frac{1}{b}\ln\left(\left(\frac{2b}{\Delta} - 1\right)\left(\frac{b-a+\Delta}{b+a+\Delta}\right)\right) \right] \right\} \quad (2.67)$$

where $K(k)$ is the complete elliptical integral of first kind, Δ is the small distance from edges of the conductor, $k = \frac{a}{b}$, $a = \frac{S}{2}$, $b = w + \frac{S}{2}$ and R_s are the series resistance of the center conductor in ohm per unit length.

2.3.3. Substrate Integrated Waveguide

For many years, conventional transmission lines such as microstrip lines have been used for transporting electromagnetic energy between different microwave devices due to their low cost, simple fabrication, and full-scale integration with planar structures. However, their performance at mm-wave frequencies is less acceptable due to various transmission losses such as conductor loss, dielectric loss, and the radiation loss [7] which not only degrades their performance but also enables strong coupling between adjacent devices.

In contrast, classical metallic waveguides are well known for their low loss and high-power handling for mm-wave frequencies. However, the problems like the large size and weight, high-cost fabrication [15] and incompatibility for direct integration with planar structures makes them undesirable for compact and low-profile mm-wave circuits. To address, the above-mentioned problems, an alternative to metallic waveguide has been developed called substrate integrated waveguide (SIW) [16], also known as a laminated waveguide [17]. It combines the advantages of both the planar circuits and the metallic waveguide such as compact size, low loss, high-quality factor, shielding, and high power handling [15]. SIW can be realized with a set of two arrays of metallic posts implanted in the substrate parallel to each other as shown in Figure 2.8 whereas the top and bottom copper cladding act as PEC (perfect electric conductor) sheets or waveguide electric walls. The array of the metallic post/plated through holes (PTH) with a set of two conducting sheets on the same substrate provide the attributes of waveguide in a planar form. The SIW technology is employed in various microwave and millimeter-wave circuits including directional couplers [18], cavity-filters [19], oscillators [20], and power amplifiers [21], as well as antenna feed and distribution structures. SIW components with the ease of planar integration

can be designed on a single printed board, however, generally require a transition to a planar topology such as microstrip to launch signals. This offers a viable solution for mm-wave applications such as wireless networks, automotive radars, and biomedical devices.

2.3.3.1. Working Principle

Substrate integrated waveguides have propagation and dispersion characteristics similar to rectangular metallic waveguides, provided that the metallic wall posts/vias are placed close enough for the radiation leakage to be minimal. However, they are dielectric filled rather than air filled waveguides. This can make SIW more lossy than rectangular waveguide especially at mm-wave frequencies due to dielectric loss.
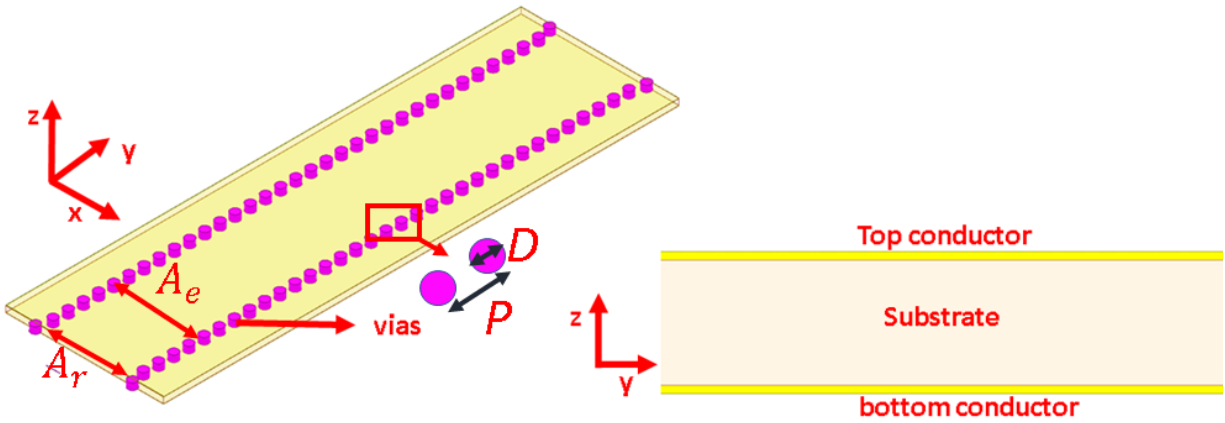
Figure 2.8 Simulated model for an SIW define variables

Additionally, the SIW structures do not permit TM modes due to discontinuous side walls. The mathematical expression for the cut off frequency of the fundamental mode TE_{10} and the second mode in SIW is given below [22].

$$
\begin{cases}
f_c(TE_{10}) = \dfrac{c}{2\sqrt{\varepsilon_r}}\left(A_r - \dfrac{D^2}{0.95P}\right)^{-1} \\[3mm]
f_c(TE_{20}) = \dfrac{c}{2\sqrt{\varepsilon_r}}\left(A_r - \dfrac{D^2}{1.1P} - \dfrac{D^2}{1.1P^2}\right)^{-1}
\end{cases}
\tag{2.68}
$$

$$
A_e = A_r - \frac{D^2}{0.95P}
\tag{2.69}
$$

$$\lambda_g = \frac{2\pi}{\sqrt{\frac{\varepsilon_r(2\pi f)^2}{c^2} - \left(\frac{\pi}{A_e}\right)^2}} \tag{2.70}$$

where A_r is the width of the SIW waveguide, A_e is the equivalent width in a normal dielectric filled rectangular waveguide D is the diameter of vias and P is the longitudinal spacing between adjacent vias. The relation (2.69) is further refined in [22] which takes into account dispersion effects and can be re-written as:

$$A_e = A_r - 1.08\frac{D^2}{P} + 0.1\frac{D^2}{A_r} \tag{2.71}$$

2.3.3.2.   Loss Mechanism

A key issue in designing SIW structures is the minimization of the losses, especially at mm-wave frequencies. There are three main loss mechanisms which need to be considered in designing SIW structures: i) the dielectric loss [23], ii) the conductor loss [23], and iii) the radiation loss [24]. The mathematical expressions for these losses are given below:

$$\alpha_c = \sqrt{\frac{\omega\mu_o}{2\sigma}} \times \frac{\left(2h\pi^2 + A_e{}^3 k^2\right)}{A_e{}^3 h\beta k\eta}$$

h = height of the substrate; β = phase constant = $\frac{2\pi}{\lambda}$ $\qquad\qquad$ (2.72)

η = intrinsic impedance = $\sqrt{\frac{\mu_o}{\varepsilon_r \varepsilon_o}}$; σ = conductivity of the metal

$$\alpha_d = \frac{k^2 \tan\delta}{2\beta} \tag{2.73}$$

$\tan\delta$ = dielectric loss tangent

$$\alpha_R = \frac{\frac{1}{A_e}\left(\frac{D}{A_e}\right)^{2.84}\left(\frac{P}{D} - 1\right)^{6.28}}{4.85\sqrt{\frac{2A_e}{\lambda_g} - 1}} \tag{2.74}$$

where α_c is the conduction loss, α_d is the dielectric loss, and α_R is the radiation loss. SIW conductor loss is similar to metallic waveguides and is primarily affected by the substrate thickness, as the conductor losses depend on the surface current integral $|J|^2$ on the metal surface. Furthermore, the attenuation constant is inversely proportional to the height of the substrate, which implies that conductor loss can be reduced by increasing the height of the substrate. Conversely the dielectric losses depend on the dielectric material only, not on the shape of the SIW. Therefore,

it can be reduced by using better quality, low loss dielectric materials. Lastly, the radiation loss can be kept within acceptable limits by adopting the criteria $D = \lambda_g/5$ and $P \leq 2d$ mentioned in [25]. Larger spacing between the SIW vias results in high lateral radiation leakage, which would cause high coupling or crosstalk between adjacent SIW channels. The insertion loss of the SIW, which generally accounts for the conductor, dielectric and radiation losses can be significantly increased by the effect of the conductor surface roughness. Over the years, various analytical models for the conductor surface roughness have been developed for the metallic surfaces and incorporated in commercial electromagnetic software for conducting their design study. For illustration purpose, the effect of the surface roughness on the insertion loss of 40mm long SIW is simulated and provided in Figure 2.9, which clearly indicates the high insertion loss with increased surface roughness.

A comprehensive study on the losses in SIW, microstrip lines, and coplanar waveguides is provided in [26], which supports the fact that the losses in the SIW structures are smaller than the microstrip lines. Furthermore, it is important to notice here that reducing the substrate thickness also makes the metal surface roughness effect more prominent on the SIW performance.

2.3.3.3. Size and Bandwidth

Another important factor to be considered before designing SIW structures is their size and operational bandwidth. The width of the SIW defines the cut off frequency of the fundamental mode TE_{10} and is usually more compact than the metallic waveguides due to factor $\varepsilon_r > 1$. Various techniques have been proposed to reduce the size of the conventional SIW structures. In [27] substrate integrated folded waveguide is proposed with a metal septum which reduces the size of the waveguide by a the factor of 2 with slightly larger losses. Half mode substrate integrated waveguide based on a virtual magnetic wall are presented in [28], and offer nearly 50% size reduction of the SIW structure. On a similar note, several topologies of SIW structures are also developed to enhance its operational bandwidth. For instance, in [29] substrate integrated slab waveguide is proposed, where the dielectric medium of the waveguide is periodically perforated with air holes along the lateral portion of the waveguide. This strategy permits mono-modal bandwidth from 7.5 to 18 GHz. In another study [30], the deployment of ridge waveguide in SIW can improve the mono-modal bandwidth up to 73% from 4.9 to 13.39 GHz. In [31], the performance of the ridge waveguide is further improved by placing a row of the partial height metallic cylinders in the middle of the SIW, with metal plate connected at the bottom of the

cylinders. This approach can further enhance the operational bandwidth of SIW up to 168% from 6.8 to 25GHz. Other SIW structures have also been described in the literature and are summarized in [32], including substrate integrated slab-waveguide (SISW), substrate integrated non-radiating dielectric (SINRD) guide, substrate integrated image dielectric guide (SIJDG), substrate integrated inset dielectric guide, and substrate integrated insular guide (SIIG).
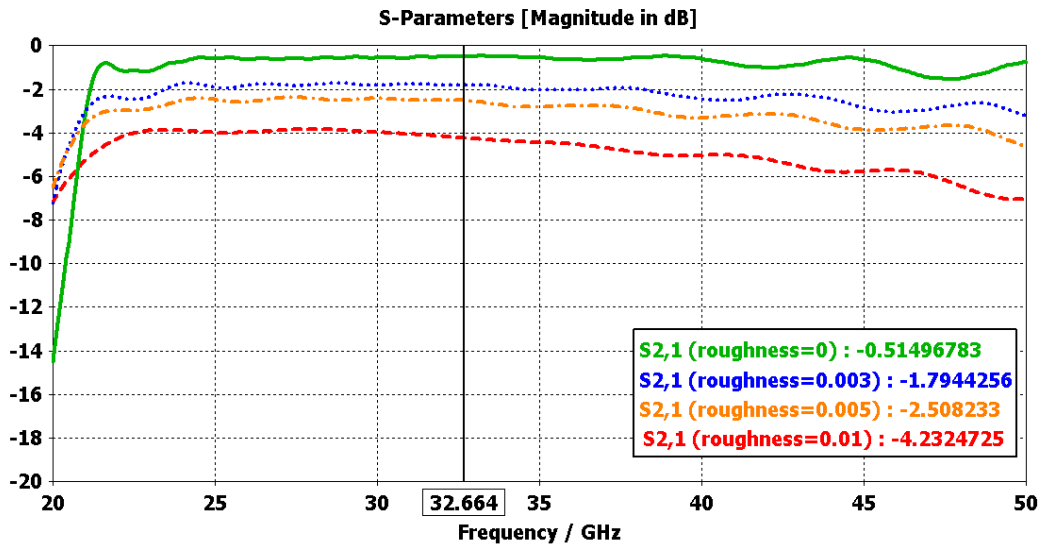
Figure 2.9 Simulated SIW insertion loss study for difference values of the mean copper surface roughness in mm

2.4. Conventional Dielectric Resonator Antennas

The GDRAs in this work present some similar behavior to classic homogenous DRAs. This section gives some background of conventional DRAs to provide a better understanding for comparison.

Since the 1960s, dielectric resonators have been used as high-Q-factor elements in the microwave applications. They offer a compact and viable alternative to waveguide cavity resonators with easier integration to printed board circuits. They can perform various functions such as filters and oscillators and are often found enclosed in metal shielding to avoid any radiation.

By removing the metal shielding and with an appropriate way of excitation, it was found that the same dielectric resonator could become an efficient radiator. Additionally, by using lower permittivity dielectric material, this radiation behavior could be extended to a wide range of frequencies. In the 1980s, Long, McAllister, and Shen conducted a systematic study on dielectric resonators as a radiating elements [33]–[35]. Their research examined various shapes such as

38

spherical, cylindrical, and rectangular dielectric resonator antennas and found that they could be utilized as an attractive substitute to traditional low gain antennas such as monopoles, dipoles, and microstrip patches.

Dielectric resonator antennas have been considered an important alternative to the conventional antennas since their discovery. The key performance parameters which made them much more popular and technically acceptable are the wide impedance bandwidth, low loss, high radiation efficiency, and their compact size. All these characteristics are directly related to the physical geometry of the DRA. For instance, they offer low loss and high radiation efficiency due to lack of conduction and surface wave loss as there are no metal surfaces involved. This merit could be very useful for application at high frequencies such as in the range from 30GHz to 300GHz, where the conduction loss is proportional to the design frequency.

Similarly, the wide bandwidth feature is related to the 3D surface of the DRA, whereas the conventional patch antennas radiate energy through a 2D surface only. The compact size of the dielectric resonator antenna is linked with the relative permittivity of the design material. The size of the DRA is proportional to $\frac{\lambda_o}{\sqrt{\varepsilon_r}}$ with $\lambda_o = \frac{c}{f_o}$, where f_o is the resonant frequency and ε_r is the relative permittivity of the material forming the radiating structure. By using the DRAs at high permittivity, the physical size of the antenna could be shrunk by an approximate factor of $\sqrt{\varepsilon_r}$.

2.4.1. Working Principle

The term dielectric resonator emanates from the concept of dielectric material having the ability to resonate at certain frequencies. It is commonly treated as an energy storing device due to it inherit high-Q-factor. However, it was observed that by lowering the Q-factor, DRs could be used as a resonator as well as an effective radiating source at certain frequencies. This phenomenon can be explained as follows: The high Q-factor dielectric material cannot radiate much energy irrespective of any coupling mechanism as the fields are tightly confined within the structure. Whereas, reducing the Q-factor, allows the excited radio waves to move back and forth inside the resonator walls forming standing waves and, hence storing electrical energy. Oscillating current introduces oscillating electric fields (E) and oscillating magnetic fields (H). The time-varying fields radiate away from the antenna into space due to accelerating currents, provided the resonator is excited at proper mode. Some common radiating modes for standard shaped DRAs are TE_{111}^z, TE_{113}^z (for rectangular DRA) where subscript z shows the number of E-field cycles along

the height of the DRA i.e., z-axis, TE_{111}, TE_{101} (for hemispherical), TE_{01}, TM_{01}, and HE_{11}/EH_{11} (for cylindrical). For demonstration purpose, the working principle of rectangular DRAs is discussed here as the general function is somewhat comparable to aid in the understanding of the GDRAs.

2.4.2. Rectangular DRA

The three-dimensional cross-sectional view of the rectangular DRA (RDRA) is shown in Figure 2.10. The design parameters for rectangular DRA are $a \times d \times b$ (width×length×height) and the relative dielectric constant is ε_r. The major design advantage of the rectangular DRA is its three independent geometrical dimensions, which allows more design flexibility as compared to other shapes of DRAs. For any given resonant frequency and fixed dielectric constant, two out of the three dimensions of the rectangular DRA can be chosen independently. In contrast, the cylindrical DRA has only one degree of freedom while the hemisphere has none. The dielectric waveguide model (DWG) [36] is normally used to predict the resonant frequency and radiation Q-factor of an isolated rectangular DRA.
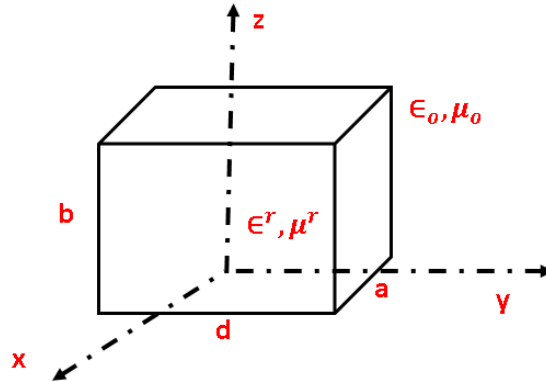
Figure 2.10 Rectangular DRA with dimensions a, d and b

The dielectric waveguide model was first proposed by Marcatili [36] to determine the guided wavelength in rectangular dielectric guides. Figure 2.11a shows the model of the dielectric waveguide with the width "a" in the y-direction, height "b" in the z-direction and the wave propagation in the x-direction. The field modes inside the waveguide can be classified into TE_{mn}^z and TM_{mn}^z where m and n denotes the number of field extrema in the y and z-directions inside the guide. Moreover, the fields inside the guide are assumed to vary sinusoidally, whereas the outside fields are expected to decay exponentially as shown in Figure 2.11b [36].
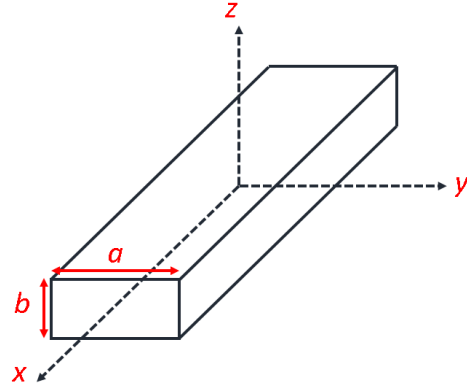
a)
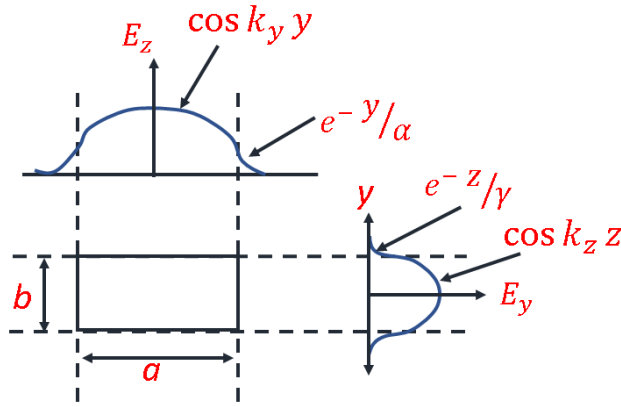
b)

Figure 2.11 a) Dielectric guide; b) Cross-sectional field distribution

The wave propagation numbers k_x, k_y and k_z for $|y| \leq {}^a/_2$ and $|z| \leq {}^b/_2$ and the attenuation constant in the y and z-axis can be determined by matching the fields at boundary conditions as given below [37]:

$$k_x^2 = \varepsilon_r k_o^2 - k_y^2 - k_z^2 \tag{2.75}$$

$$k_y = \frac{m\pi}{a}\left(1 + \frac{2}{ak_o\sqrt{\varepsilon_r - 1}}\right)^{-1} \tag{2.76}$$

$$k_z = \frac{n\pi}{b}\left(1 + \frac{2}{bk_o\sqrt{\varepsilon_r - 1}}\right)^{-1} \tag{2.77}$$

$$\alpha = \frac{1}{\sqrt{(\varepsilon_r - 1)k_o^2 - k_y^2}} \tag{2.78}$$

$$\gamma = \frac{1}{\sqrt{(\varepsilon_r - 1)k_o^2 - k_z^2}} \tag{2.79}$$

where k_o is free space wavenumber given by:

41

$$k_o = \frac{2\pi}{\lambda_o} = \frac{2\pi f_o}{c} \qquad (2.80)$$

and where f_o is the operating frequency, λ_o is free space wavelength and c is the speed of light. For well guided modes, fields are confined within the guide, which allows a further approximation of wave propagation numbers k_y and k_z.

$$k_y = \frac{m\pi}{a} \qquad (2.81)$$

$$k_z = \frac{n\pi}{b} \qquad (2.82)$$

This approximation is similar to considering magnetic walls boundary at $y = \pm\,^a/_2$ and $z = \pm\,^b/_2$.

2.4.2.1. Resonant Frequency and Q-Factor

To build an RDRA, the dielectric waveguide is truncated along $x = \pm\,^d/_2$ with magnetic walls as shown in Figure 2.12b. This results in an isolated RDRA model in free space with dimensions $a, b,$ and d. However, for practical applications, this model can be replaced with an RDRA with dimensions $a, h = \frac{b}{2}$ and d mounted on a ground plane as shown in Figure 2.12c.

a)   b)

42

c)
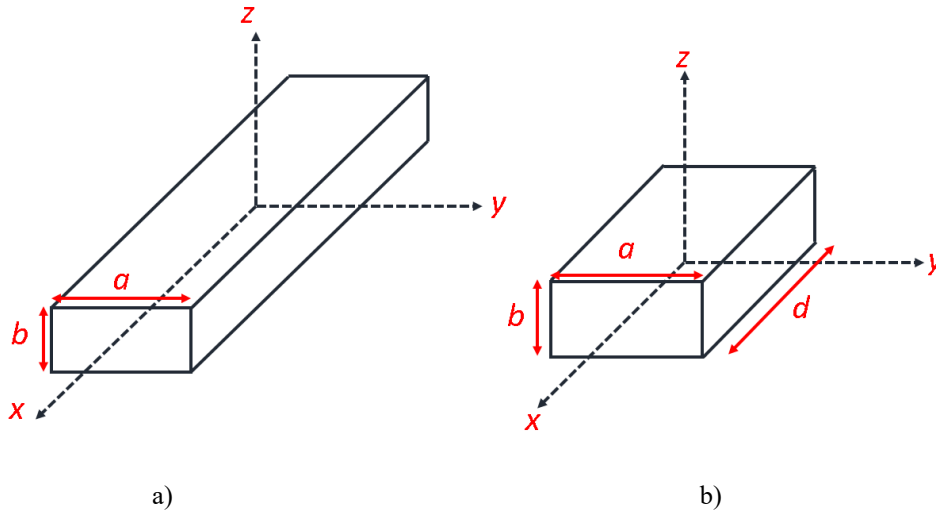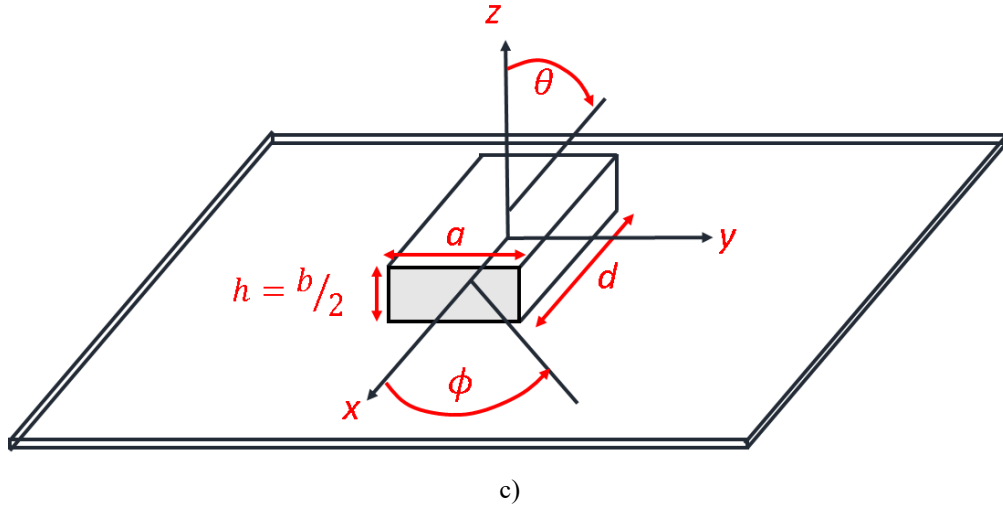
Figure 2.12 Dielectric waveguide model (DWM) for rectangular DRAs a) Infinite dielectric waveguide; b) Truncated dielectric waveguide; c) DRA on a ground plane

If the rectangular DRA has dimensions such as $a, b > d$, the lowest order mode will be $TE^z_{\delta 11}$ (subscript z shows the number of E-field cycles along the height of the DRA i.e., z-axis) By applying the dielectric waveguide model (DWM), the mode field components inside the DRA can be written as follows [38]:

$$E_x = 0 \tag{2.83}$$

$$E_y = A\,k_z\cos(k_x x)\begin{Bmatrix}\cos(k_y y)\\\sin(k_y y)\end{Bmatrix}\begin{Bmatrix}\sin(k_z z)\\\cos(k_z z)\end{Bmatrix} \tag{2.84}$$

$$E_z = -A\,k_y\cos(k_x x)\begin{Bmatrix}\sin(k_y y)\\\cos(k_y y)\end{Bmatrix}\begin{Bmatrix}\cos(k_z z)\\\sin(k_z z)\end{Bmatrix} \tag{2.85}$$

$$H_x = A\frac{(k_y^2 + k_z^2)}{j\omega\mu_o}\cos(k_x x)\begin{Bmatrix}\sin(k_y y)\\\cos(k_y y)\end{Bmatrix}\begin{Bmatrix}\cos(k_z z)\\\sin(k_z z)\end{Bmatrix} \tag{2.86}$$

$$H_y = A\frac{(k_x k_y)}{j\omega\mu_o}\sin(k_x x)\begin{Bmatrix}\sin(k_y y)\\\cos(k_y y)\end{Bmatrix}\begin{Bmatrix}\cos(k_z z)\\\sin(k_z z)\end{Bmatrix} \tag{2.87}$$

$$H_z = A\frac{(k_x k_z)}{j\omega\mu_o}\sin(k_x x)\begin{Bmatrix}\sin(k_y y)\\\cos(k_y y)\end{Bmatrix}\begin{Bmatrix}\cos(k_z z)\\\sin(k_z z)\end{Bmatrix} \tag{2.88}$$

whereas by using equation (2.75), we have $k_x^2 + k_y^2 + k_z^2 = \varepsilon_r k_o^2$

$$k_z \tan\left(\frac{k_x d}{2}\right) = \sqrt{(\varepsilon_r - 1)k_o^2 - k_z^2} \tag{2.89}$$

43

By plugging the values from (2.81), (2.82) and (2.75) into a transcendental equation (2.89) and solving it for k_z, the resonant frequency of rectangular DRA can be defined as follows:

$$f_o = \frac{c}{2\pi\sqrt{\varepsilon_r}}\sqrt{k_x^2 + k_y^2 + k_z^2} \qquad (2.90)$$

The radiation Q-factor of the rectangular DRA can be described by a relation [37] given below:

$$Q = \frac{2\omega W_e}{P_{rad}} \qquad (2.91)$$

where W_e is the energy stored in the DRA and P_{rad} is the radiated power. These quantities can be further defined as [37]:

$$W_e = \frac{\varepsilon_o \varepsilon_r abd}{32}\left(1 + \frac{\sin(k_z d)}{k_z d}\right)(k_x^2 + k_y^2) \qquad (2.92)$$

$$P_{rad} = 10 k_o^4 |p_m|^2 \qquad (2.93)$$

$$p_m = \frac{-8j\omega\varepsilon_o(\varepsilon_r - 1)}{k_x k_y k_z}\sin\left(\frac{k_z d}{2}\right)\hat{z} \qquad (2.94)$$

p_m = magnetic dipole moment of the DRA

Moreover, the impedance bandwidth of the DRA can be estimated form the radiation Q-factor by using the following relation:

$$BW = \frac{S - 1}{Q\sqrt{S}} \qquad (2.95)$$

where S is the maximum acceptable voltage standing wave ratio, which is usually considered VSWR = 2. Additionally, it can be concluded from the above-mentioned relation that the DRAs with higher Q-factor offers narrow impedance bandwidth as the fields get more confined inside the DRA structure.

2.4.2.2. Radiation Model

The radiation phenomena in an RDRA can be explained with the help of modes, which are the E and H-fields distributions inside the RDRA. Having prior knowledge of E and H-field distributions inside the isolated RDRA not only helps to predict the radiation characteristics of the antenna but also in choosing an appropriate feed type for maximum coupling between the source and the DRA. However, here the lower order modes in the RDRA have been presented.

The E and H field distributions for lowest mode order mode $TE^z_{\delta 11}$ (subscript z denotes number E-field extrema along z-axis) in RDRA mounted on an infinite ground plane are shown in Figure

2.13. These field distributions have close resemblance with the magnetic dipole along the z-axis. This observation consolidates the fact that radiation pattern generated by DRA can be approximated by the short magnetic dipole. Furthermore, H-fields for higher order modes such as $TE_{\delta 13}^z$ and $TE_{\delta 15}^z$ are also presented in Figure 2.13d along with equivalent magnetic dipole model and corresponding radiation patterns. These modes also radiate like the dominant mode of the RDRA, however, for higher order modes, the antenna radiations get highly concentrated in broadside direction with an increased number of side lobes.

E-field ─── H-field

a)   b)

θ (degrees)

xz-Plane   yz-Plane

$TE_{\delta 13}$ $TE_{\delta 15}$

c)   d)

Short magnetic dipole

$TE_{\delta 13}$ $TE_{\delta 15}$

e)

45

$$TE_{\delta13}\text{……….………………………………………..….}TE_{\delta15}$$

f)
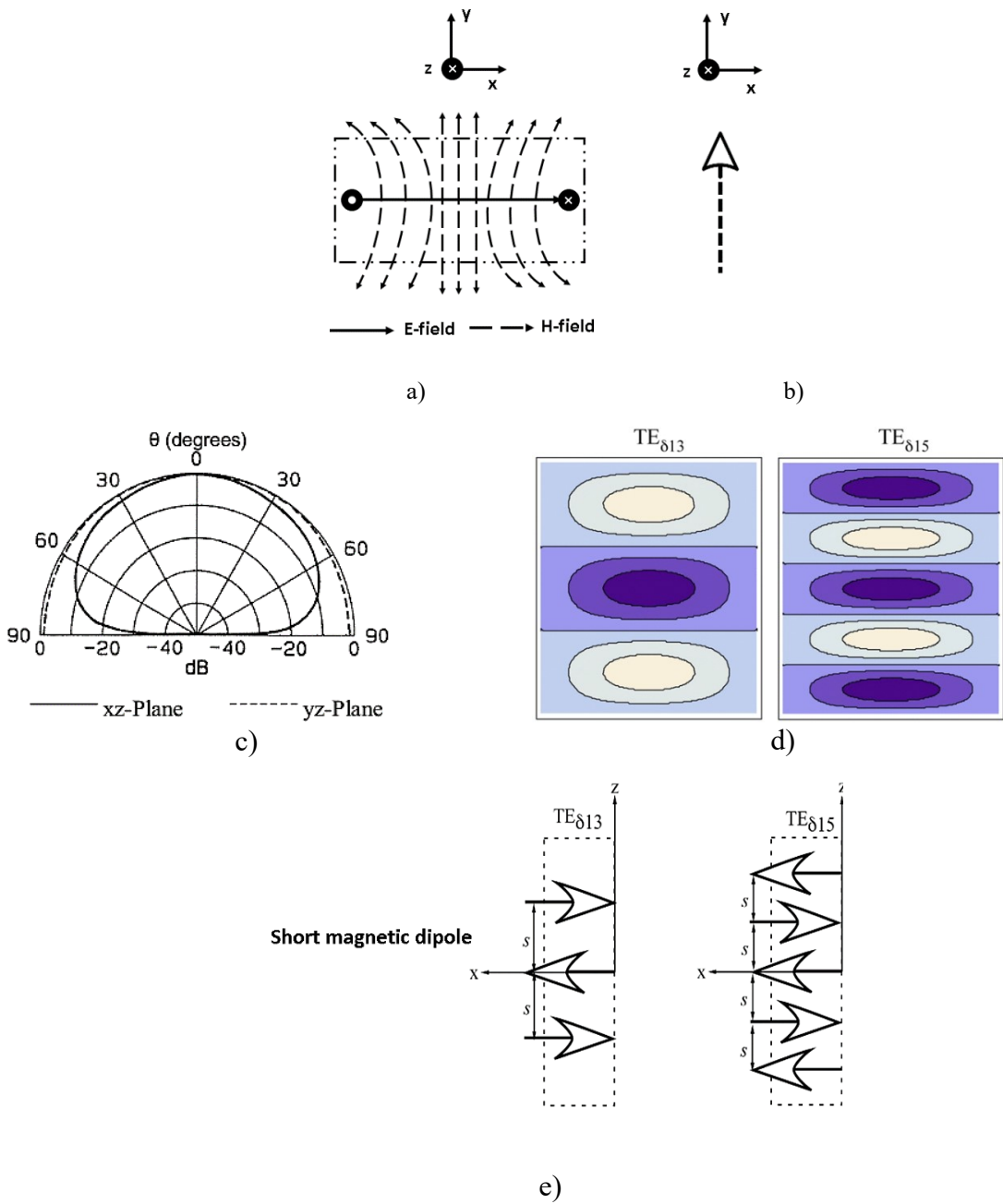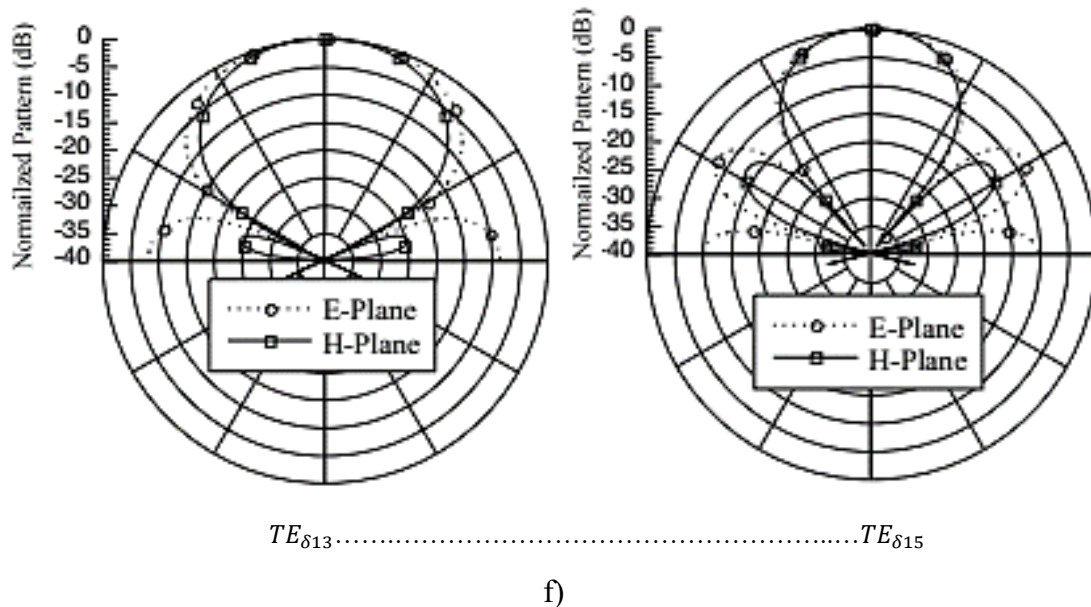
Figure 2.13 EM-field distributions of $TE^z_{\delta11}$ mode in the isolated rectangular dielectric resonator; b) Equivalent short magnetic dipole model; c) Ideal far-field patterns above an infinite ground plane d) H-field distributions for higher order modes in RDRA [38]; e) Magnetic dipole model for higher order modes in RDRA; f) Far-field patterns for higher order modes in RDRA [2] (d-f)

2.5.   Comparison of DRAs with Metal Patch Antennas

DRAs have no conductor loss, no surface-wave loss [39], narrow bandwidth and high radiation efficiency making them an excellent candidate for future mm-wave wireless applications [40]. In contrast, the surface and conductor loss become severe at high frequencies for traditional microstrip patch antennas (MPAs), which significantly reduce their radiation efficiency and make them more impractical for mm-wave applications. Typical MPAs are also comparatively narrowband. A comparison of the characteristics of DRA and MPA is presented in Table 2.1.

A wideband strip fed DRA at 60-GHz is proposed in [41]. An impedance bandwidth of 7.5% with broadside gain of 7.1 dBi is achieved by using tapered microstrip open stub as the excitation and the impedance transformer. In [42] stacked DRAs were designed to achieve good radiation characteristics where a gain of 6 dBi is realized. In [43], a DRA was fed by coplanar waveguide to excite $HE_{\delta11}$ mode, however radiation efficiency was low and a peak realized gain was 3.2 dBi only. In [44], a DRA antenna built from high resistivity silicon wafer via micromachining at 58 GHz had reasonable gain and radiation efficiency of 7 dBi and 79%, however, it has narrow

impedance bandwidth of only 3.8%. A broadband dual resonance slot couple DRA is proposed in [45], where the slot resonance and DRA resonance are merged to achieve broad impedance bandwidth characteristics. A brief summary of some of mm-wave dielectric resonator antennas is provided in Table 2.2.

Table 2.1 Comparison of DRA and MPA

Parameter	*Dielectric resonator antenna*	*Microstrip patch antenna*
Dimension	Maximum dimension, $D = \dfrac{\lambda_o}{\sqrt{\varepsilon_r}}$	Resonant length, L=0.49λ_e
Radiation efficiency	High as there are no conductor losses	Poor due to surface waves
Gain	Low	High
Bandwidth	High	Low
Power handling	High	Low
Conductor loss	Minimum because of absence of conductor	Exist due to conducting patch
Polarization purity	Easily achieved	Difficult to achieve
Resonant mode	*TE, TM, HEM*	*TE, TM*
Waves	Standing waves are formed due abrupt change in permittivity	Surface waves are excited due to thicker dielectric substrate

Table 2.2 Recent dielectric resonator antennas for millimeter applications

Reference	DRA type	Relative permittivity	Feeding mechanism	Frequency (GHz)	Impedance bandwidth (%)	Gain (dBi)
[46]	Rectangular	10	Coupling slot	24	3.8	6.3
[47]	Rectangular	48	CPW	60	2.8	3.2
[48]	Rectangular	38	H-slot	35	12	0.5
[49]	Rectangular	10	Meander slot	130	11	4.7
[50]	Rectangular	12.6	Coupling slot	60.5	6.1	6.0
[51]	Circular	42	Folded dipole	27.7	9.8	1

2.6.   Artificial Dielectrics

Artificial dielectrics were first introduced in [52] as a lightweight substitute to real-dielectric materials, for developing microwave lenses [53]. The difference between the natural and artificial

dielectric is that atoms and molecules in artificial material are constructed artificially by humans. The term "artificial dielectric" came into use because they have macroscopic analogies to naturally existing dielectrics. An artificial dielectric can be realized by embedding small conducting structures in the host material in a regular pattern. These tiny structures cause the scattering of the electric field, when exposed to incident waves and thus create an effective equivalent delay [54]. The artificially engineered dielectrics can be considered as a homogeneous dielectric for frequencies at which the embedded structures are much smaller than the incident wavelength. The effective permittivity (ε_{eff}) and permeability (μ_{eff}) are the two important constituent parameters to define the characteristics of any material. They describe the response of a material to an incident electromagnetic wave. The material permittivity corresponds to the reaction of the electric field whereas permeability corresponds to how materials react and behave towards the applied magnetic field. Depending upon the type of the materials, the incident electromagnetic waves may cause increased electric or magnetic polarization in the material. The type of the induced polarization in a material depends upon the embedded particle shapes. For instance, particle shapes like square, rectangle or sphere produce electric dipole moment and hence cause electric polarization in the material whereas particles such as split rings generate circulating currents and enhances the magnetic polarization of the material.

For most materials the electromagnetic properties can be characterized by a set of three Maxwell constitutive relations as given below:

$$\boldsymbol{D} = \varepsilon\boldsymbol{E} = \varepsilon_o\boldsymbol{E} + \boldsymbol{P} \tag{2.96}$$

$$\boldsymbol{B} = \mu\boldsymbol{H} = \mu_o(\boldsymbol{H} + \boldsymbol{M}) \tag{2.97}$$

$$\boldsymbol{J} = \sigma\boldsymbol{E} \tag{2.98}$$

where $\boldsymbol{D}$ is an electric displacement vector, $\boldsymbol{P}$ is an electric polarization and $\boldsymbol{M}$ is a magnetic polarization (magnetization). These equations support the fact that the permittivity and the permeability of the medium/material can be engineered by controlling the degree of electric or magnetic polarization.

An influx of research has been conducted to miniaturize antennas using artificial magnetic materials [55], [56] which are used as a substrate for low profile antennas while maintaining the same performance matrix [56]. Microstrip patch antenna mounted on the magneto-dielectric substrate at 600 MHz is discussed in [57]. Double-negative (DNG) (with negative permeability

and negative permittivity), is another artificial material explored extensively in recent years. Since, the first DNG material [58] reported by Shelby et al. [59] great progress has been made in searching new DNG materials and their potential applications [60], [61]. DNG materials composed of split-ring resonators (SRRs) and conducting wires rely on the microstructure suggested by Pendry et al. [62].

The DNG materials have been used for designing small antennas [63], sub wavelength cavities, and waveguides [64]. Investigation of DNG media, based on a mixture of spherical particles embedded in a host dielectric has been discussed and demonstrated in [65].

Multiband material based on concentric resonant inclusions has been discussed in [66]. Triangular open ring resonator (TORR) inclusions described in [67]–[69], have excellent performance as magnetic ring resonators in the microwave region. The increased effective permittivity of the host dielectric material through the addition of dielectric inclusions has been presented in [70]. The effective permittivity achieved with a different number of layers of spherical inclusions. In [71] the resonant cavity thickness has been reduced up to $\lambda/60$ for ultra-thin directive antennas using artificial composite materials made up of capacitive and inductive grids. In [72] the author presented a highly efficient, compact, and wideband antenna by using an artificial substrate having equal permittivity and permeability. Texture dielectrics have been utilized for reducing the size of the antenna without degrading the bandwidth and efficiency by introducing lower permittivity in regions of higher current density and higher permittivity elsewhere [73].

The effect of the volume fraction of the cubic inclusions to the electromagnetic (EM) properties of the artificial heterogeneous medium has been studied in [74].

Spheres [75], [76] are one of the most commonly used shapes for making artificial heterogeneous substrates because they offer equal size in three dimensions and have a relatively easy analysis as the induced field is uniform in all directions [77], [78]. Discs [79], cubes [80], ellipsoids, rectangular strips, and I-shaped elements are other inclusions that have been discussed in the literature for making artificial heterogeneous substrates [81].

2.6.1. Gridded Dielectrics

Gridded dielectrics [82] are recently discovered under the category of double positive artificial dielectrics (DPD). Gridded dielectrics can be conceptualized as an artificial dielectric material

composed of small metal inclusions arranged periodically in a host material to enhance the electric polarization. The polymer base dielectrics normally offer permittivity of 2-3 and are difficult to excite. On the other hand, ceramic dielectrics usually have high permittivity and narrow bandwidth. The concept of gridded dielectric provides an exciting alternative to high permittivity dielectrics, where the designer has more freedom in attaining the desired material characteristics by introducing metal embodiments of different shape and size in the host material. The design material can be optimized upfront in simulation software such as ANSYS HFSS and CST Microwave Studio before experimental validation and applied in the design of GDRAs as shown in the following chapters.

Figure 2.14 provides the typical geometry of the gridded dielectric material. The material is comprised of low permittivity host dielectric and the tall metal grid embodiments. The dielectric body is made up of X-ray sensitive polymer PMMA. Deep micro-scale cavities are made in a PMMA resist through X-ray exposure. These exposed cavities are then developed and electroplated in metal using an electroforming process to create the inclusions.
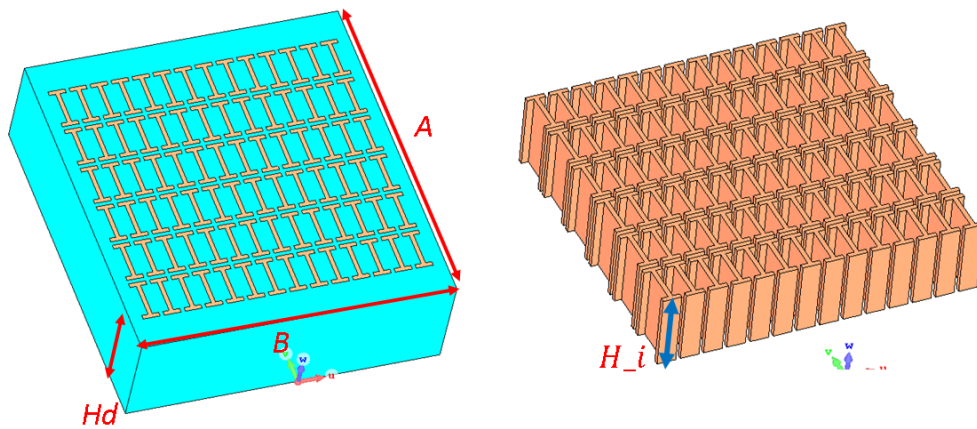
Figure 2.14 Geometry of gridded dielectric material

The physical parameters such as shape, size, and spacing between the metal inclusions have a significant effect on the properties of the gridded dielectrics. Metallic inclusion size should be kept in order of $\frac{\lambda_0}{10}$, so they will not be self-resonant structures at the operating frequencies. Usually, large inclusions produce strong interaction with the incident electromagnetic waves whereas the smaller features appear more homogeneous to electromagnetic waves. Reducing the grids thickness and gap between the adjacent elements increases the electric flux density inside the grid structures which increases the electric permittivity of the host dielectric material.

References

[1]   C. A. Balanis, *Antenna theory : analysis and design*. Wiley, 2016.

[2]   "IEEE standard definitions of terms for antennas," *IEEE Trans. Antennas Propag.*, vol. 17, no. 3, pp. 262–269, May 1969.

[3]   R. M. Barrett, "Microwave Printed Circuits--The Early Years," *IEEE Trans. Microw. Theory Tech.*, vol. 32, no. 9, pp. 983–990, Sep. 1984.

[4]   E. Bogatin, "A closed form analytical model for the electrical properties of microstrip interconnects," *IEEE Trans. Components, Hybrids, Manuf. Technol.*, vol. 13, no. 2, pp. 258–266, Jun. 1990.

[5]   E. Yamashita and K. Atsuki, "Analysis of Thick-Strip Transmission Lines (Correspondence)," *IEEE Trans. Microw. Theory Tech.*, vol. 19, no. 1, pp. 120–122, Jan. 1971.

[6]   H. R. Kaupp, "Characteristics of Microstrip Transmission Lines," *IEEE Trans. Electron. Comput.*, vol. EC-16, no. 2, pp. 185–193, Apr. 1967.

[7]   D. M. Pozar, *Microwave engineering*. Wiley, 2012.

[8]   E. J. Denlinger, "Losses of Microstrip Lines," *IEEE Trans. Microw. Theory Tech.*, vol. 28, no. 6, pp. 513–522, Jun. 1980.

[9]   M. D. Abouzahra and L. Lewin, "Radiation from Microstrip Discontinuities," *IEEE Trans. Microw. Theory Tech.*, vol. 27, no. 8, pp. 722–723, Aug. 1979.

[10]   C. P. Wen, "Coplanar Waveguide: A Surface Strip Transmission Line Suitable for Nonreciprocal Gyromagnetic Device Applications," *IEEE Trans. Microw. Theory Tech.*, vol. 17, no. 12, pp. 1087–1090, Dec. 1969.

[11]   D. Bhattacharya, "Characteristic impedance of coplanar waveguide," *Electron. Lett.*, vol. 21, no. 13, p. 557, 1985.

[12]   B. C. Wadell, *Transmission line design handbook*. Artech House, 1991.

[13]   B.-T. Lee, "Analysis and Modeling of Coplanar Strip Line," pp. 169–206.

[14]   C. L. Holloway and E. F. Kuester, "A quasi-closed form expression for the conductor loss of CPW lines, with an investigation of edge shape effects," *IEEE Trans. Microw. Theory Tech.*, vol. 43, no. 12, pp. 2695–2701, 1995.

[15]   H. Kumar and R. Jadhav, "A Review on Substrate Integrated Waveguide and its Microstrip Interconnect," *J. Electron. Commun. Eng.*, vol. 3, no. 5, pp. 36–40, 2012.

[16]   K. Wu, "Integration and interconnect techniques of planar and non-planar structures for microwave and millimeter-wave circuits," in *Asia-Pacific Microwave Conference (APMC) Proceedings*, 2001, vol. 2, pp. 411–416.

[17]   H. Uchimura, T. Takenoshita, and M. Fujii, "Development of a laminated waveguide," *IEEE Trans. Microw. Theory Tech.*, vol. 46, no. 12, pp. 2438–2443, 1998.

[18]   K. Wu, "Towards system-on-substrate approach for future millimeter-wave and photonic wireless applications," in *2006 Asia-Pacific Microwave Conference*, 2006, pp. 1895–1900.

[19]   H. J. Tang, W. Hong, Z. C. Hao, J. X. Chen, and K. Wu, "Optimal design of compact millimetre-wave SIW circular cavity filters," *Electron. Lett.*, vol. 41, no. 19, p. 1068, 2005.

[20]   Y. Cassivi and K. Wu, "Low cost microwave oscillator using substrate integrated waveguide cavity," *IEEE Microw. Wirel. Components Lett.*, vol. 13, no. 2, pp. 48–50, Feb. 2003.

[21]   M. Abdolhamidi and M. Shahabadi, "X-Band Substrate Integrated Waveguide Amplifier," *IEEE Microw. Wirel. Components Lett.*, vol. 18, no. 12, pp. 815–817, Dec. 2008.

[22]   Y. Cassivi, L. Perregrini, P. Arcioni, M. Bressan, K. Wu, and G. Conciauro, "Dispersion characteristics of substrate integrated rectangular waveguide," *IEEE Microw. Wirel. Components Lett.*, vol. 12, no. 9, pp. 333–335, Sep. 2002.

[23]   S. Kumari and S. Srivastava, "Losses in Waveguide and Substrate Integrated Waveguide (SIW) For Ku Band: A Comparison," *Int. J. Mod. Eng. Res. www.ijmer.com*, vol. 3, no. 1, pp. 53–57, 2013.

[24]   M. Pasian, M. Bozzi, and L. Perregrini, "A Formula for Radiation Loss in Substrate

Integrated Waveguide," *IEEE Trans. Microw. Theory Tech.*, vol. 62, no. 10, pp. 2205–2213, Oct. 2014.

[25] Y. J. Cheng, *Substrate integrated antennas and arrays*. CRC Press, 2015.

[26] M. Bozzi, L. Perregrini, and K. Wu, "Modeling of Conductor, Dielectric, and Radiation Losses in Substrate Integrated Waveguide by the Boundary Integral-Resonant Mode Expansion Method," *IEEE Trans. Microw. Theory Tech.*, vol. 56, no. 12, pp. 3153–3161, Dec. 2008.

[27] N. Grigoropoulos, B. Izquierdo, and P. R. Young, "Substrate integrated folded waveguides (SIFW) and filters," *IEEE Microw. Wirel. Components Lett.*, vol. 15, no. 12, pp. 829–831, Dec. 2005.

[28] M. Bozzi, A. Georgiadis, and K. Wu, "Review of substrate-integrated waveguide circuits and antennas," *IET Microwaves, Antennas Propag.*, vol. 5, no. 8, p. 909, 2011.

[29] M. Bozzi, D. Deslandes, P. Arcioni, L. Perregrini, K. Wu, and G. Conciauro, "Efficient analysis and experimental verification of substrate-integrated slab waveguides for wideband microwave applications," *Int. J. RF Microw. Comput. Eng.*, vol. 15, no. 3, pp. 296–306, May 2005.

[30] W. Che, Cuixia Li, P. Russer, and Y. L. Chow, "Propagation and band broadening effect of planar integrated ridged waveguide in multilayer dielectric substrates," in *2008 IEEE MTT-S International Microwave Symposium Digest*, 2008, pp. 217–220.

[31] M. Bozzi, S. A. Winkler, and K. Wu, "Broadband and compact ridge substrate-integrated waveguides," *IET Microwaves, Antennas Propag.*, vol. 4, no. 11, p. 1965, 2010.

[32] K. Wu, D. Desiandes, and Y. Cassivi, "The substrate integrated circuits - a new concept for high-frequency electronics and optoelectronics," in *6th International Conference on Telecommunications in Modern Satellite, Cable and Broadcasting Service, 2003. TELSIKS 2003.*, vol. 1, p. P-III-P-X.

[33] M. W. McAllister and S. A. Long, "Resonant hemispherical dielectric antenna," *Electron. Lett.*, vol. 20, no. 16, p. 657, 1984.

[34] M. W. McAllister, S. A. Long, and G. L. Conway, "Rectangular dielectric resonator antenna," *Electron. Lett.*, vol. 19, no. 6, p. 218, 1983.

[35] S. Long, M. McAllister, and Liang Shen, "The resonant cylindrical dielectric cavity antenna," *IEEE Trans. Antennas Propag.*, vol. 31, no. 3, pp. 406–412, May 1983.

[36] E. A. J. Marcatili, "Dielectric Rectangular Waveguide and Directional Coupler for Integrated Optics," *Bell Syst. Tech. J.*, vol. 48, no. 7, pp. 2071–2102, Sep. 1969.

[37] K. M. Luk and K. W. Leung, *Dielectric resonator antennas*. Research Studies Press, 2003.

[38] A. Petosa, S. Thirakoune, and A. Ittipiboon, "Higher-order modes in rectangular DRAs for gain enhancement," in *2009 13th International Symposium on Antenna Technology and Applied Electromagnetics and the Canadian Radio Science Meeting*, 2009, pp. 1–4.

[39] I. A. Eshrah, A. A. Kishk, A. B. Yakovlev, and A. W. Glisson, "Theory and implementation of dielectric resonator antenna excited by a waveguide slot," *IEEE Trans. Antennas Propag.*, vol. 53, no. 1, pp. 483–494, Jan. 2005.

[40] A. Petosa, *Dielectric resonator antenna handbook*. Artech House, 2007.

[41] X. Liang, D. Yang, R. Jin, and J. Geng, "A 60-GHz wideband dielectric resonator antenna with inclined radiation," in *2012 IEEE International Workshop on Antenna Technology (iWAT)*, 2012, pp. 124–127.

[42] Y. Coulibaly, M. Nedil, L. Talbi, and T. A. Denidni, "Design of a mm-wave broadband CPW-fed stacked dielectric resonator antenna for underground mining communication," in *2010 IEEE Antennas and Propagation Society International Symposium*, 2010, pp. 1–4.

[43] P. V. Bijumon, A. P. Freundorfer, M. Sayer, and Y. M. Antar, "On-Chip Silicon Integrated Cylindrical Dielectric Resonator Antenna for Millimeter Wave Applications," in *2007 International Symposium on Signals, Systems and Electronics*, 2007, pp. 489–492.

[44] M. O. Sallam *et al.*, "Micromachined On-Chip Dielectric Resonator Antenna Operating at 60 GHz," *IEEE Trans. Antennas Propag.*, vol. 63, no. 8, pp. 3410–3416, Aug. 2015.

[45] A. Buerkle, K. Sarabandi, and H. Mosallaei, "Compact slot and dielectric resonator antenna with dual-resonance, broadband characteristics," *IEEE Trans. Antennas Propag.*, vol. 53,

no. 3, pp. 1020–1027, Mar. 2005.

[46]   Y.-M. Pan, K. W. Leung, and K.-M. Luk, "Design of the Millimeter-wave Rectangular Dielectric Resonator Antenna Using a Higher-Order Mode," *IEEE Trans. Antennas Propag.*, vol. 59, no. 8, pp. 2780–2788, Aug. 2011.

[47]   P. Bijumon, Y. M. Antar, A. Freundorfer, and M. Sayer, "Integrated dielectric resonator antennas for system on-chip applications," in *2007 Internatonal Conference on Microelectronics*, 2007, pp. 275–278.

[48]   M.-R. Nezhad-Ahmadi, M. Fakharzadeh, B. Biglarbegian, and S. Safavi-Naeini, "High-Efficiency On-Chip Dielectric Resonator Antenna for mm-Wave Transceivers," *IEEE Trans. Antennas Propag.*, vol. 58, no. 10, pp. 3388–3392, Oct. 2010.

[49]   D. Hou, Y.-Z. Xiong, W.-L. Goh, S. Hu, W. Hong, and M. Madihian, "130-GHz On-Chip Meander Slot Antennas With Stacked Dielectric Resonators in Standard CMOS Technology," *IEEE Trans. Antennas Propag.*, vol. 60, no. 9, pp. 4102–4109, Sep. 2012.

[50]   L. Ohlsson *et al.*, "Slot-Coupled Millimeter-Wave Dielectric Resonator Antenna for High-Efficiency Monolithic Integration," *IEEE Trans. Antennas Propag.*, vol. 61, no. 4, pp. 1599–1607, Apr. 2013.

[51]   P. V. Bijumon, Y. Antar, A. P. Freundorfer, and M. Sayer, "Dielectric Resonator Antenna on Silicon Substrate for System On-Chip Applications," *IEEE Trans. Antennas Propag.*, vol. 56, no. 11, pp. 3404–3410, Nov. 2008.

[52]   W. E. Kock, "Metallic Delay Lenses," *Bell Syst. Tech. J.*, vol. 27, no. 1, pp. 58–82, Jan. 1948.

[53]   S. S. Jones and J. Brown, "Metallic Delay Lenses," *Nature*, vol. 163, no. 4139, pp. 324–325, Feb. 1949.

[54]   R. E. Colli., *Field theory of guided waves*. IEEE Press, 1991.

[55]   P. M. Ikonen, S. I. Maslovski, C. R. Simovski, and S. A. Tretyakov, "On artificial magnetodielectric loading for improving the impedance bandwidth properties of microstrip antennas," *IEEE Trans. Antennas Propag*, vol. 54, no. 6, pp. 1654–1662, 2006.

[56]   Y. Lee and Y. Hao, "Characterization of microstrip patch antennas on metamaterial substrates loaded with complementary split-ring resonator," *Microw. Opt. Technol. Lett.*, vol. 50, no. 8, pp. 2131–2135, 2000.

[57]   A. Kabiri1, L. Talbi1, and O. M. Ramahi, "A Super-miniaturized Low Profile Antenna on a Substrate of Rose Curve Resonators," in *PIERS Proceedings*, 2011, pp. 106–109.

[58]   V. G. Veselago, "The electrodynamics of substances with simultaneously negative values of ε and μ," *Sov. Phys.*, vol. 10, no. 4, pp. 509–514, 1968.

[59]   R. A. Shelby, D. R. Smith, and S. Schultz, "Experimental verification of a negative index of refraction," *Sci. Magz.*, vol. 292, pp. 77–79, 2001.

[60]   A. Alú and N. Engheta, "Achieving transparency with plasmonic and metamaterial coatings.," *Phys. Rev. E. Stat. Nonlin. Soft Matter Phys.*, vol. 72, 2005.

[61]   J. B. Pendry, D. Schurig, and D. R. Smith, "Controlling electromagnetic fields.," *Science*, vol. 312, no. 5781, pp. 1780–2, Jun. 2006.

[62]   J. B. Pendry, "Negative Refraction Makes a Perfect Lens," *Phys. Rev. Lett.*, vol. 85, no. 18, pp. 3966–3969, Oct. 2000.

[63]   R. W. Ziolkowaski and A. D. Kipple, "Application of Double Negative Materials to Increase the Power radiated by Electrically Small Antennas," *IEEE Antennas Propag.*, vol. 51, no. 10, pp. 2626–2640, 2003.

[64]   N. Engheta, "Invited - Metamaterials with Negative Permittivity and Permeability: background, Salient Features. and New Trends," *IEEE MTT-S*, vol. 1, pp. 187–190, 2003.

[65]   O. G. Vendik and M. S. Gashinoval, "Artificial Double Negative (DNG) Media Composed by Two Different Dielectric Sphere Lattices Embedded in a Dielectric Matrix," in *34th European Microwave Conference,* 2004, pp. 1209 – 1212.

[66]   C. Sabah, "Multiband Metamaterials Based on Multiple Concentric Open-Ring Resonators Topology," *IEEE J. Sel. Top. Quantum Electron.*, vol. 19, no. 1, 2013.

[67]   C. Sabah, A. O. Cakmak, E. Ozbay, and S. Uckun, "Transmission measurement of a new metamaterial sample with negative refraction index," *Phys. B Condens. Matter,* vol. 405,

pp. 2955–2958, 2010.

[68]   C. Sabah, "Composition of non-concentric triangular split ring resonators and wire strip for dual-band negative index metamaterial," in *IEEE Med. Microw. Symp*, 2010, pp. 303–306.

[69]   C. Sabah, "Multiband planar metamaterials," *Microw. Opt. Technol. Lett.*, vol. 53, pp. 2255–2258, 2011.

[70]   C. C. Njoku, W. G. Whittow, and J. C. Vardaxoglou, "Simulation Methodology for Synthesis of Antenna Substrates With Microscale Inclusions," *IEEE Trans. Antennas Propag*, vol. 60, no. 5, pp. 2194–2202, 2012.

[71]   A. Ourir, A. de Lustrac, and J.-M. Lourtioz, "All-metamaterial-based subwavelength cavities (λ/60) for ultrathin directive antenna," *Appl. Phys. Lett.*, vol. 88, no. 8, pp. 084103-1-08403-3, 2006.

[72]   M. I. Kitra, C. J. Panagamuwa, P. McEvoy, J. C. Vardaxoglou, and J. R. James, "Low SAR ferrite handset antenna design," *IEEE Antennas Propag.*, vol. 55, no. 4, p. 1155–1164, 2007.

[73]   G. Kiziltas *et al.*, "Topology design optimization of dielectric substrates for bandwidth improvement of a patch antenna," *IEEE Antennas Propag.*, vol. 51, no. 10, pp. 2732–2743, 2003.

[74]   C. C. Njoku, W. G. Whittow, and J. C. Vardaxoglou, "Effective Permittivity of Heterogeneous Substrates With Cubes in a 3-D Lattice," *IEEE Ant. Wirel. Propg. Lett*, vol. 10, pp. 1480–1483, 2011.

[75]   I. Awai, O. Mizue, and A. K. Saha, "Artificial Dielectric Resonator Made of Spherical Metal Particles," *IEICE Trans. Electron.*, vol. E92–C, no. 1, pp. 72–76, 2009.

[76]   X. Cai, R. Zhu, and G. Hu, "Experimental study for metamaterials based on dielectric resonators and wire frame," *Metamaterials*, vol. 2, no. 4, pp. 220–226, 2008.

[77]   J. A. Stratton, *Electromagnetic Theory*. New York: McGraw-Hill, 1941.

[78]   J. Avelin, A. Sihvola, R. Sharma, and I. Hanninen, "Modelling of dielectric materials with cubic inclusion shapes," in *EuCAP*, 2007, pp. 36–39.

[79]   N. G. Alexopoulos, C. A. Kyriazidou, and H. F. Contopanagos, "Effective parameters for

metamorphic materials and metamaterials through a resonant inverse scattering approach," *IEEE Trans. Microw. Theory Tech*, vol. 59, no. 2, pp. 254–267, 2007.

[80]   L. Xing, Q. Xu, J. Li, Z. Wei, J. Ding, and C. Guo, "Broaden the bandwidth of patch antenna by using inhomogeneous metamaterial substrate," in *PIERS symb.*, 2010, p. 155–159.

[81]   I. Awai, Y. Maegawa, and T. Ishizaki, "Measurement of effective material constants of artificial dielectrics made of spherical metal particles," in *Asia Pacific Microwave Conference*, 2009, p. 1655–1658.

[82]   M. T. Aligodarz, D. M. Klymyshyn, Atabak Rashidian, M. Borner, L. Shafai, and J. Mohr, "Investigations on Photoresist-based Artificial Dielectrics with Tall Embedded Metal Grids and Their Resonator Antenna Application," *IEEE Trans. Antennas Propag.*, vol. 63, no. 9, pp. 3826–3838, 2015.

Chapter 3 : GDRA Concept-Single Element Design and Feeding

3.1. Introduction

GDRAs were originally proposed in 2015 by our research group as a new double positive dielectric material offering good antenna properties such as mutli-resonance, new resonant modes, broadside radiation patterns and good radiation efficiency. However, the proposed design concept had limited scope for future wideband mm-wave applications as it was restricted to microstrip line edge feeding due to feed line and grid short circuiting, and had relatively low impedance bandwidth i.e., typically<6%.

This chapter[3] presents the new concept for GDRA element feeding to improve performance and practicality. It also compares the original I-beam inclusions to a new rectangular inclusion structure. In the first segment of the chapter, the previously designed I-beam GDRAs fed by microstrip line (developed by S. Ganguly in [1] and fabricated at Karlsruhe Institute of Technology (KIT) Germany) were used to evaluate the potential of new planar feed structures. In this case, two different options for coplanar waveguide (CPW) feeding at 22.6-26.6 GHz and 26.6-29.3 GHz were studied by applying a thin 300μm perforated PMMA layer between the feed layer and metal inclusions of the GDRA to avoid short-circuiting the underneath feed line. This multi-segment approach also results in a GDRA structure that improves the impedance bandwidth up to 16.3%, while providing a maximum realized gain of 7.2 dBi across the frequency band with excellent broadband patterns and -18 dB cross-polarization levels. Moreover, the near-field distributions of the GDRAs with the new feed options are also examined, and their effect on antenna GDRAs radiation pattern is discussed.

In the second segment[4] of the chapter, new rectangular inclusion-based grid GDRAs (fabricated at SyLMAND Canadian Light Source (CLS), Saskatoon) are investigated in detail for reducing the GDRA fabrication complexities and increasing the effective permittivity compared to the previously explored I-beam GDRAs. Lastly, SIW based longitudinal slot coupling is successfully

---

[3]Details including some textual material, some illustrations and some tabular material in Section 3.2-3.5 are published in W. Mazhar, D. M. Klymyshyn, M. Tayfeh Aligodarz, S. Ganguly, A. A. Qureshi, and M. Boerner, "CPW fed grid dielectric resonator antennas with enhanced gain and bandwidth," *Int. J. RF Microw. Comput. Eng.*, *vol. 29, no. 3, p. e21639, Mar. 2019.* © 2019 Wiley. Reprinted with permission.
[4]Details including some textual material, some illustrations and some tabular material in Section 3.5 are accepted in W. Mazhar, D. Klymyshyn, G. Wells, A. A Qureshi, M. Jacobs, and S. Achenbach, "Low profile artificial grid dielectric resonator antenna arrays for mm-wave applications," *IEEE Trans. Antennas Propag., vol. 67, no. 07, 2019* © 2019 IEEE. Reprinted with permission.

demonstrated for exciting the single GDRA element, which results in wide impedance bandwidth of 3.9 GHz from 30.2-34.1 GHz with a peak broadside gain of 6.4 dBi. This type of feeding is suitable for large GDRA arrays, such as SIW series slot fed GDRA arrays, which is demonstrated in the coming chapters.

3.2. I-beam GDRA Concept

The I-beam GDRA is shown in Figure 3.1a, which shows the top view of the overall grid arrangement and details of the lateral cross-section of the embedded metal grid elements. The grid elements and arrangement are similar to the concept presented in [2] , however, in this case, a thin intermediate layer of polymer **Δ**z is introduced underneath the grid structures, as shown in Figure 3.1a.
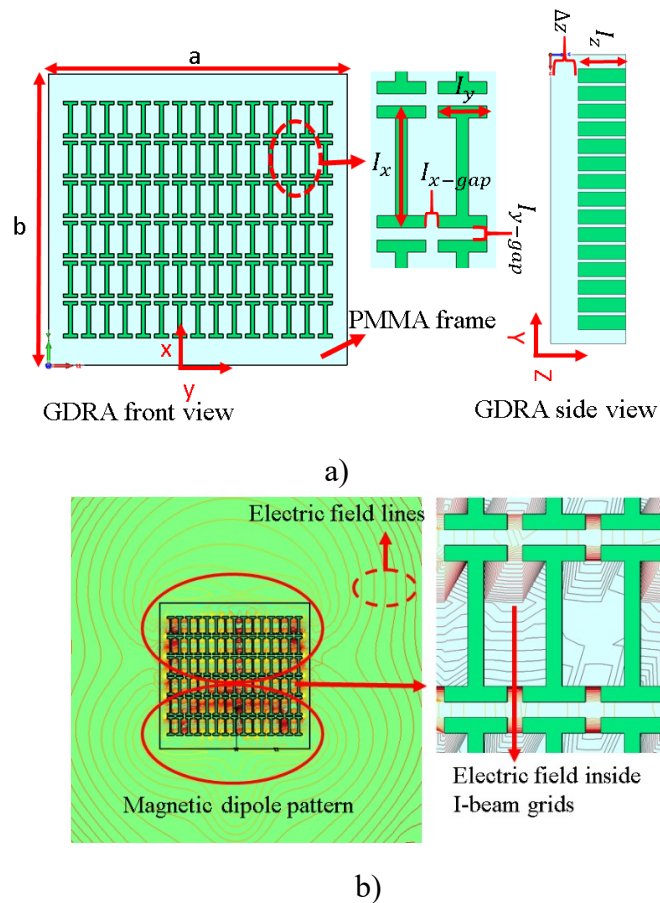
Figure 3.1 a) Model of GDRA with I-beams and the intermediate layer **Δ**z; b) E-field pattern for a sample GDRA fed through GCPW at 24 GHz © 2019 Wiley. Reprinted with permission

Further design details are also available in Table 3.1. The metallic I-beam grid tends to increase the effective relative permittivity of the host material by creating high electric flux density regions

between the small gaps of the adjacent metal grid elements, as seen in the E-field patterns of the GDRA shown in the expanded view of Figure 3.1b. This relates to the increase of electric dipole polarization in the region, which increases the effective permittivity of the host material. This effect can be further described by Maxwell constitutive relations given below:

$$D = \varepsilon_{eff}E = \varepsilon_b E + P \tag{3.1}$$

$$\varepsilon_{eff} = \varepsilon_b + \frac{P}{E} \tag{3.2}$$

where ε_b is the permittivity of the base material, ε_{eff} is the effective permittivity of the artificial engineered material (i.e., in this case GDRA), and P is the electric polarization which is an average electric dipole moment per unit volume of the material. Therefore, it is evident from equation 3.2 that increasing the electric dipole moment in the region enhances the effective permittivity of the material.

3.2.1. Effective Permittivity Estimation

There are several techniques available for retrieving the constitutive parameter of the artificial dielectric materials. However, in this case, the scattering S-parameters technique available in CST Microwave Studio is utilized for estimating the effective permittivity of the grid dielectric material. Closely spaced embedded metal inclusions with I-beam structures are arranged in a square grid to increase the localized electric field intensity inside the grids. The size of the embedded inclusions and separation gaps is chosen to maintain an aspect ratio < 10 for feasible fabrication. Moreover, the lateral dimensions of the inclusions I_x, I_y and spacing in the rectangular grids I_{x-g}, I_{y-g} is kept $<(\frac{\lambda_{eff}}{10})$ to avoid any incident wave scattering or self-resonance of the grid structures. All design variables for this study are provided in Figure 3.1 and Table 3.1. The reflection and transmission coefficients are calculated from an electromagnetic wave incident on a square block of grid dielectric material. The simulation model comprised of two-waveguide ports with a pair of the perfect electric conductor (PEC) and perfect magnetic conductor (PMC) walls as shown in Figure 3.2a. The resulted 2-ports solution is used to estimate the effective permittivity of the grid dielectric material through a set of equations [3] given below:

$$z = \pm \sqrt{\frac{(1 + S_{11})^2 - S_{21}^2}{(1 - S_{11})^2 - S_{21}^2}} \tag{3.3}$$

$$e^{jnk_o d} = X \pm j\sqrt{1 - X^2} \tag{3.4}$$

$$X = \frac{1}{2S_{21}(1 - S_{11}^2 + S_{21}^2)} \tag{3.5}$$

where n and z are the refractive index and impedance of the material under test. Since the grid material under consideration is a passive medium, hence the signs of the equation 3.3 and 3.4 are determined by the following requirement:

$$z' \geq 0 \tag{3.6}$$

$$n'' \geq 0 \tag{3.7}$$

where $(-)'$ and $(-)''$ indicate the real and imaginary parts of the operators, respectively. The refractive index of the material can be determined from equation 3.4 as follows:

$$n = \frac{1}{k_o d}\left\{[\ln(e^{jnk_o d})'' + 2m\pi] - j[\ln(e^{jnk_o d})]'\right\}; \; k_o = \frac{2\pi}{\lambda_0} \tag{3.8}$$

where m is an integer relative to the branch index of n' and d is the thickness of the slab/material under test. The imaginary part of the n can be uniquely decided by using equation 3.7, whereas the real part is complex by the branches of the logarithm function. More detail about this procedure is available in [3]. Once the refractive index n and impedance z of the medium are available, the effective permittivity ϵ of the material can be estimated by the following relation:

$$\epsilon = \frac{n}{z} \tag{3.9}$$

The CST Microwave Studio predicted linear magnitudes of S_{11} and S_{21} de-embedded to the front face of the grid dielectric material are provided in Figure 3.2b. Additionally, the retrieved effective permittivity of the test material along with refractive index n and impedance z are shown in Figure 3.2b, and Figure 3.2c. An effective permittivity of 14.5 is realized at 24 GHz with the element dimensions of 0.2×0.5×0.85 mm ($I_x \times I_y \times I_z$), and grid separation of 0.05mm.
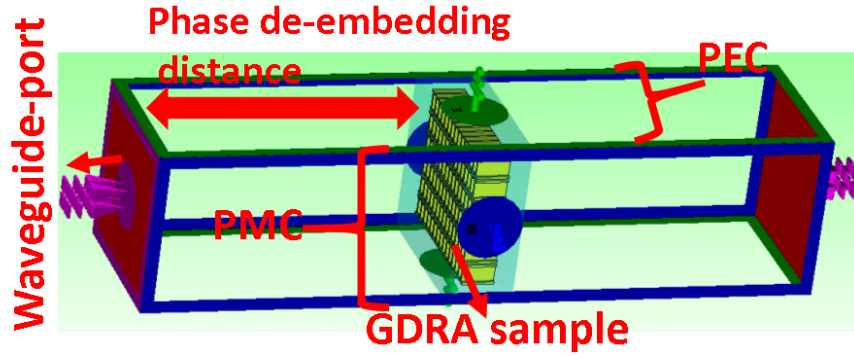
a)
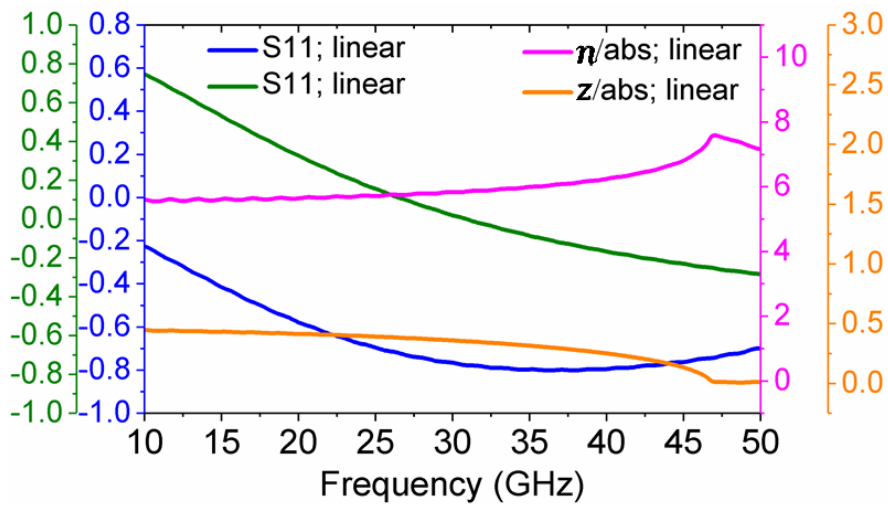
b)
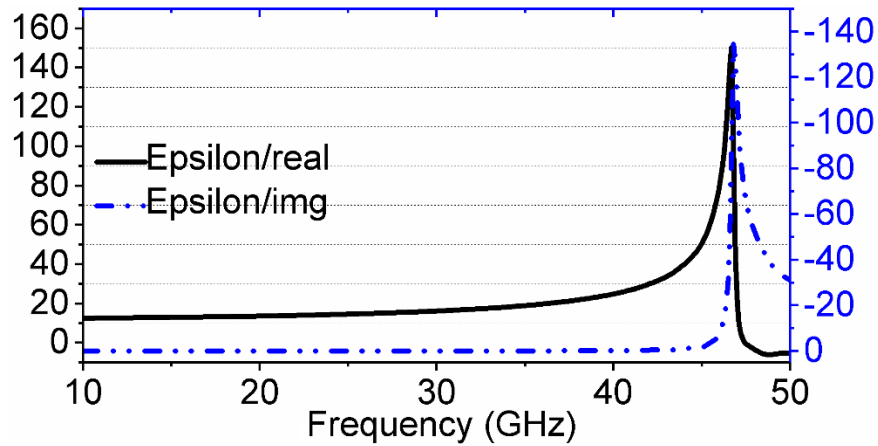
c)

Figure 3.2 a) Simulation setup for the permittivity estimation; b) Simulated reflection and transmission coefficients along with refractive index and impedance of the GDRA sample; b) Real and imaginary permittivity of the GDRA sample

3.2.2. Bandwidth Enhancement with an Intermediate Layer

A thin intermediate layer, **Δ**z, of PolyMethyl-Methacrylate (PMMA) introduced underneath the grid structures produces a multi-layer DRA effect, which lowers the effective permittivity of the GDRA and produces an increase in impedance bandwidth. Figure 3.3a shows the frequency response of a CPW-fed simple GDRA (i.e., **Δ**z = 0) with an effective permittivity of ε_d = 14.4. An impedance bandwidth of 5.6% (i.e., 1.2 GHz at 23.48 GHz) is achieved, for the relatively high permittivity grid resonator. It is important to mention here that the stub length of **Δ**L = 0.3mm as shown in Figure 3.3b is used for exciting the simple GDRA in this case. The further increase in the stub-length (i.e., **Δ**L = 2mm) results in short-circuiting of the feedline and the GDRA grid structures, which limits the functionality of the GDRA due to high input reflections as shown in Figure 3.3b.

The effective permittivity of the multi-layer GDRA is estimated by:

$$\in_{eff} = \frac{\varepsilon_d.I_z + \varepsilon_z.\varDelta z}{I_z + \varDelta z} \tag{3.10}$$

where ε_d is the effective permittivity of the GDRA layer with grids only, ε_z is the permittivity of the thin intermediate layer at the base of the GDRA, and I_z and $\varDelta z$ are the GDRA dimensions given in Table 3.1. Using equation 3.10 the effective permittivity of the multi-layer GDRA is calculated to be 10.8.

From the DWM approximation [4], it is known that the resonance frequency of rectangular DRAs has the following relation with the effective permittivity of the resonator.

$$f_{r,1} \propto \frac{1}{\sqrt{\varepsilon_{eff}}} \tag{3.11}$$

Therefore, the resonance frequency of the multi-layer GDRA with a thin polymer layer can be estimated as:

$$f_{r,2} \cong f_{r,1}\frac{\sqrt{\varepsilon_{eff,GDRA}}}{\sqrt{\varepsilon_{eff,MS-GDRA}}} \tag{3.12}$$

The frequency response of the multi-layer GDRA is presented in Figure 3.3a, which demonstrates the bandwidth enhancement of 14.2%. The resonance frequency is also shifted as shown in Figure 3.3a however, interestingly the change in resonance frequency is not as significant as estimated by equation 3.12, i.e., $f_{r,2} \cong 23.48\frac{\sqrt{14.4}}{\sqrt{10.8}} = 27.1$ GHz. The simulated resonance of the multi-layer GDRA is observed at 25.2 GHz. Hence, adding a thin layer of dielectric under GDRA does not behave quite like a homogenous multi-layer DRA. In fact, the thin layer of the dielectric material

helps in mode matching at the interface between the GDRA and CPW feed line structure along with the slight decrease in the effective permittivity of the GDRA. The H-fields plots shown in Figure 3.4 for both simple GDRA and multi-layer GDRA illustrate this effect.
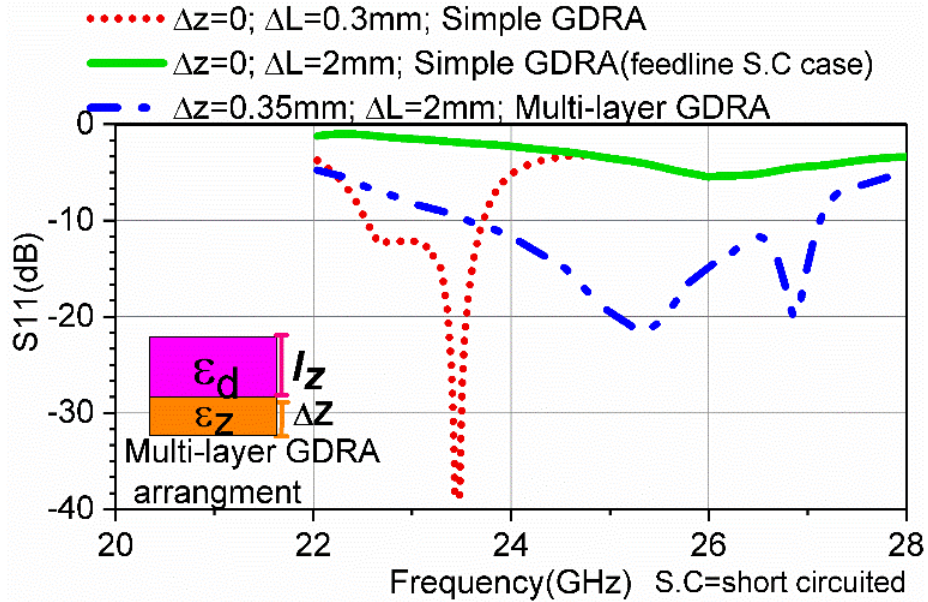
a)
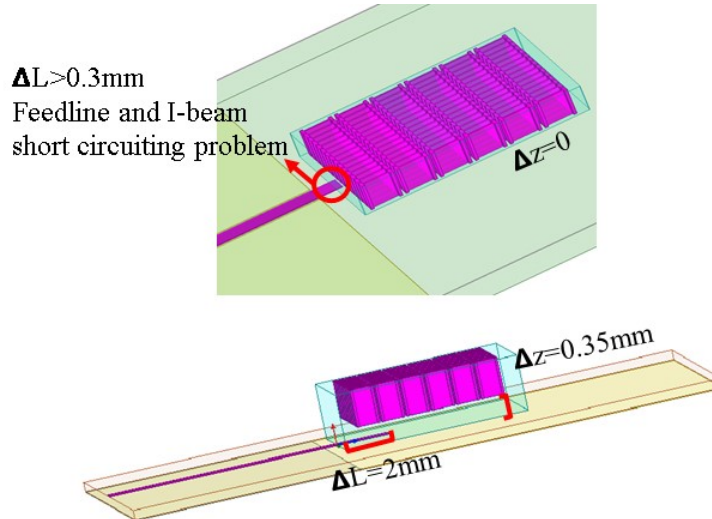
b)

Figure 3.3 a) Effect of permittivity on impedance bandwidth of the normal and multi-layer GDRA fed through open-ended CPW feed; b) GDRA feedline arrangement for simple GDRA, **Δ**z=0 and for multi-layer GDR, **Δ**z=0.35mm © 2019 Wiley. Reprinted with permission.

In comparison to the simple GDRA, a high concentration of H-fields can be seen at the interface between the multi-layer GDRA and the CPW feed line, which then get coupled into the GDRA.

Therefore, the introduction of a thin layer of dielectric under the GDRA results in more efficient coupling/smooth transition of the fields from the CPW line to the GDRA structure and hence produces a wide impedance bandwidth response. The GDRA intermediate layer thickness **Δ**z and, the CPW feed length **Δ**L are the two preliminary design parameters that can be used to maximize the coupling through mode matching.
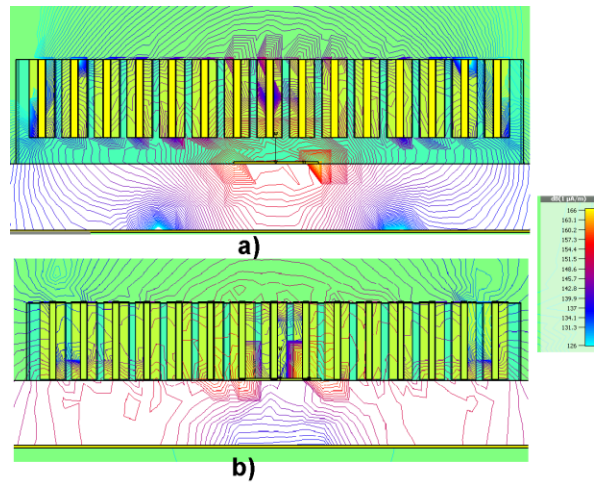
Figure 3.4 H-field distribution in XZ plane of CPW fed GDRA a) with multi-layer approach; b) without multi-layer approach © 2019 Wiley. Reprinted with permission
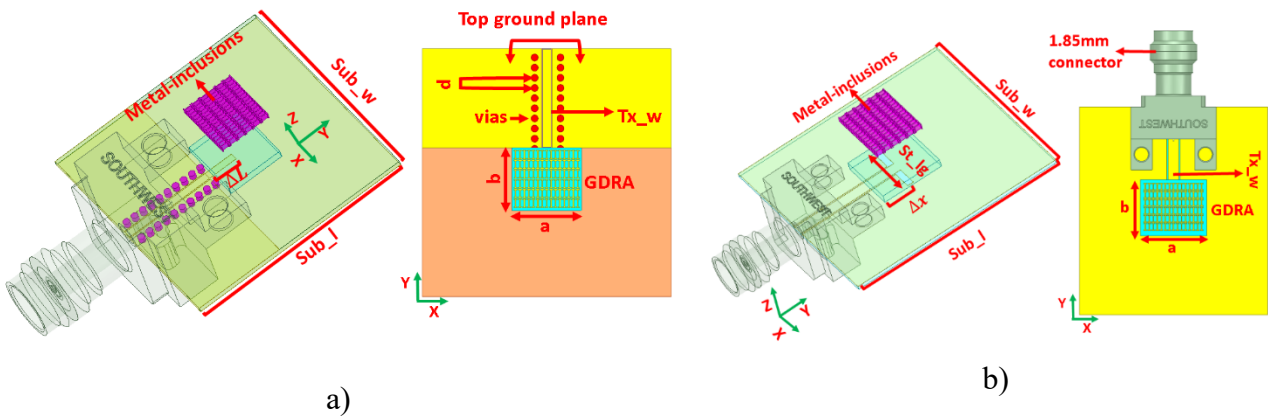
Figure 3.5 Simulated design models a) GCPW fed GDRA; b) CPW inductive fed GDRA © 2019 Wiley. Reprinted with permission

Table 3.1 GDRA design dimensions (mm)

Parmaters	Symbol	Values (mm)
Beam x-gap	I_{x-g}	0.05
Beam y-gap	I_{y-g}	0.05
Beam width	I_x	0.20
Beam length	I_y	0.50
Beam height	I_h	0.85
Beam offset	Δz	0.35
GDRA width	b	4.00
GDRA length	a	4.00
GDRA height	h	1.2
GCPW fed GDRA		
Substrate length	Sub_l	20.0
Substrate width	Sub_w	20.0
Conductor width	Tx_w	0.62
Stub length	ΔL	2.15
Via radius	via_rad	0.20
Vias pitch	d	0.55
CPW inductive fed GDRA		
Substrate length	Sub_l	20.0
Substrate width	Sub_w	20.0
Conductor width	Tx_w	0.80
Slot length	St_lg	3.30
Slot width	-	0.40
GDRA offset	Δx	1.80

3.3.   GDRA CPW Feeding

Coplanar waveguide (CPW) is an effective excitation mechanism for dielectric resonator antennas [5] at millimeter-wave frequencies and system on chip (SoC) applications. It facilitates the

integration of active/passive circuit elements and antennas, has low radiation leakage, and provides minimal surface wave excitation and a wide impedance bandwidth interface compared to microstrip.

Another advantage of CPW is its diversity in providing different feeding mechanisms for DRAs. Two CPW approaches are proposed here for their suitability in feeding multi-layer GDRAs: 1) open-ended grounded CPW (GCPW) stub feed; and 2) CPW inductive feed.

3.3.1. GDRA Fed by GCPW Technique

A multi-layer GDRA fed by an open-ended GCPW is shown in Figure 3.5a. Rogers 6002 substrate with a material thickness of 0.508 mm and dielectric permittivity of 2.94 is assumed for the simulation. Thin substrates typically provide more confined fields for the feed structure and can reduce the adverse effects of leaky modes and surface waves at high frequencies. GCPW employs through hole vias for connecting the top layer ground plane and bottom layer ground plane. The placement of through-hole vias is extremely important in acquiring the desired impedance and low loss characteristics as well as suppressing parasitic modes in the guide. The ground signal ground (GSG) spacing is kept very small to ensure tight E-field confinement at GSG interfaces to avoid radiation losses. Moreover, plated through holes (PTH) are also placed close to the edge of the coplanar ground plane. i.e., 0.2 mm to prevent high parasitic inductance which increases the impedance and conductor losses especially at high frequencies. Due to adjacent via hole loading effects, the trace width of the 50Ω CPW line is only 0.62 mm. This is 15% narrower than simple CPW line which helps in better input impedance match between the feed point and GDRA interface. The feed length ΔL and the intermediate layer thickness Δz are found to be two critical factors in controlling the signal coupling and the impedance bandwidth of the multi-layer GDRA. A parametric study of both Δz and ΔL is provided in Figure 3.6 and Figure 3.7. An initial length of $\Delta L \sim \lambda g/4$ as suggested in [6] is chosen, in this case, 1.65 mm.

At $\Delta z = 0$, the metallic inclusions are short-circuited to the CPW feedline stub, causing high input resistance and reactance which results in high input reflections because of poor input impedance match. The input reactance of the GDRA is found to be predominantly inductive as shown in Figure 3.6. The reason for this inductive behavior is the feed board vias loading and mode mismatch at the GDRA and feed-line interface, which is reduced by introducing a capacitive effect produced by the thin layer of PMMA material underneath the GDRA, which helps in proper mode

field transition. Increasing the intermediate layer thickness Δz helps in decreasing both the resistive and reactive part of the input impedance of the GDRA. At Δz=0.35 mm, the input reactance is reduced to almost zero in the desired frequency band with real impedance at around 50 Ω. The best input impedance is observed for Δz=0.35 mm. However, the matching condition is achieved when the input impedance has only a resistive component. Therefore, further input matching is realized by tuning the length ΔL of the open circuit GCPW line, which acts as an open stub tuner. The effect of ΔL on the impedance bandwidth of the GDRA is presented in Figure 3.7.
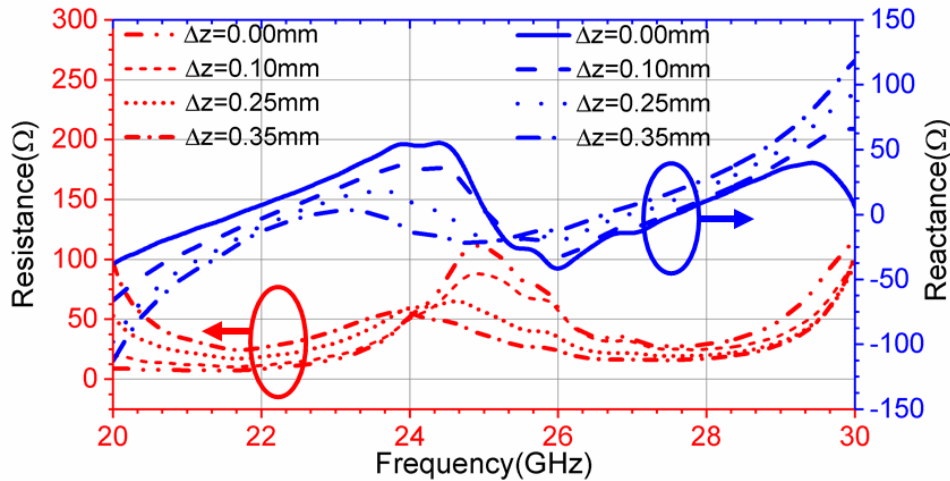
Figure 3.6 Parametric study of real-impedance and reactance of the multi-layer GDRA for intermediate layer thickness Δz in GCPW feed. © 2019 Wiley. Reprinted with permission

Maximum return loss of -30 dB has been achieved for ΔL and Δz of 2.15 mm and 0.35 mm with a 10-dB impedance bandwidth of 3.5 GHz as shown in Figure 3.7. Increasing the length of ΔL moves the GDRA resonance toward higher frequencies. Moreover, the simulated radiation efficiency is found to be above 85% in most of the design bandwidth as shown in Figure 3.10.

The vector field distribution of the GDRA fed by GCPW technique is presented in Figure 3.16. It is important to notice here that the coupling mechanism between the GDRA and GCPW feedline is magnetic in nature. The fields in the GDRA and the GCPW feedline stub are directed in the same direction, which results in low cross polarization values in both E and H-plane as shown in Table 3.2. More detailed analysis of the field vectors and their effect on the GDRA radiation pattern is provided in Section 3.4.3.
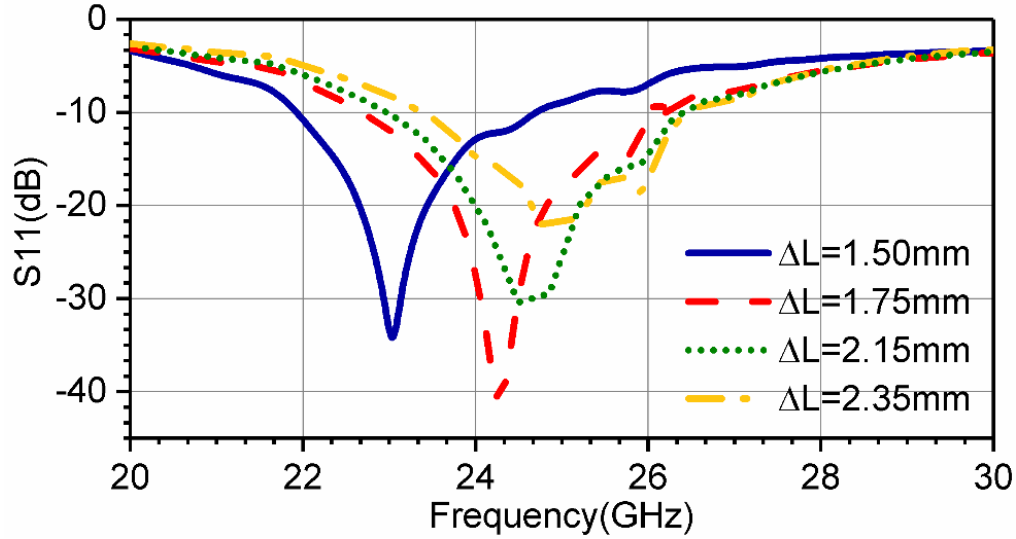
Figure 3.7 Effect of extended open-ended length ΔL on return loss of the GCPW feed. © 2019 Wiley. Reprinted with permission

3.3.2. GDRA Fed by CPW Inductive Feed Technique

The multi-layer GDRA, i.e., (Δz=0.35 mm) fed by a CPW inductive feed is shown in Figure 3.5b. It is emphasized here that the slot is not intended to be an efficient radiator but rather to provide an efficient energy coupling source from CPW to GDRA. For this reason, the slot length is chosen in the proximity of $\lambda_g/2$ at resonance, where λ_g is the effective guided wavelength in the substrate. The resonance frequency is selected at 25 GHz which gives λ_{eff}=7.78 mm. Therefore, the initial length for the non-resonant slot is assumed at 3.52 mm $< \lambda_{eff}/2$. Secondly, the slot width is also selected $< \lambda_{eff}/15$ for avoiding high cross-polarization levels.

The slot length, *slot_lg* and the offset position of the GDRA, Δx are two key design variables that control the impedance match and the resonance frequency. The parametric study of the GDRA position at an initial slot length of 3.52 mm is presented in Figure 3.8. Multiple resonance behavior is observed as both the slot and GDRA are resonant structures. Moreover, these resonances are slightly displaced from the free slot and GDRA resonances, due to the presence of the CPW feed line and metallization in the slot coupling region of the GDRA. In addition, the presence of metallization in the middle of the slot makes this configuration an inductive slot, where the dominant coupling fields are magnetic fields. During, the first design step, the effect of the GDRA offset, Δx, over the fixed slot length is studied. The best impedance bandwidth is achieved for a GDRA position Δx of 1.8 mm with two resonances observed at 26.63 GHz and 28.1 GHz in

70

addition to slot resonance at 24.5 GHz. Further improvement in impedance match and energy coupling is achieved through fine-tuning of the slot length i.e., 3.3 mm, to merge the two resonances of the GDRA at 26.63 GHz and 28.1 GHz as shown in Figure 3.9. This results in a simulated bandwidth of 1.85 GHz, centered at 27.25 GHz with the maximum return loss of -21.2 dB.

The multi-layer GDRA near-field distributions at 27.2 GHz and 28.2 GHz are presented in Figure 3.16. The small inclusion features tend to guide the fields and can be designed to modify the E and H-vector field patterns to generate new resonant modes as shown in Figure 3.16, which are different than the conventional high permittivity DRAs modes. For instance, for CPW inductive case, the E-field patterns are similar to the TE_{111} mode in the normal DRA, i.e., E fields circulating in the YZ plane. However, for H-fields additional field cycles are observed in the XZ plane, i.e., two and three for 27.2 GHz and 28.2 GHz respectively rather than just one H-field cycle as in the TE_{111}^{x} mode of the conventional high permittivity DRA as shown in Figure 3.16. Moreover, the inductive slot configuration results in a coupling mechanism between the slot and a GDRA, which is magnetic in nature [7].
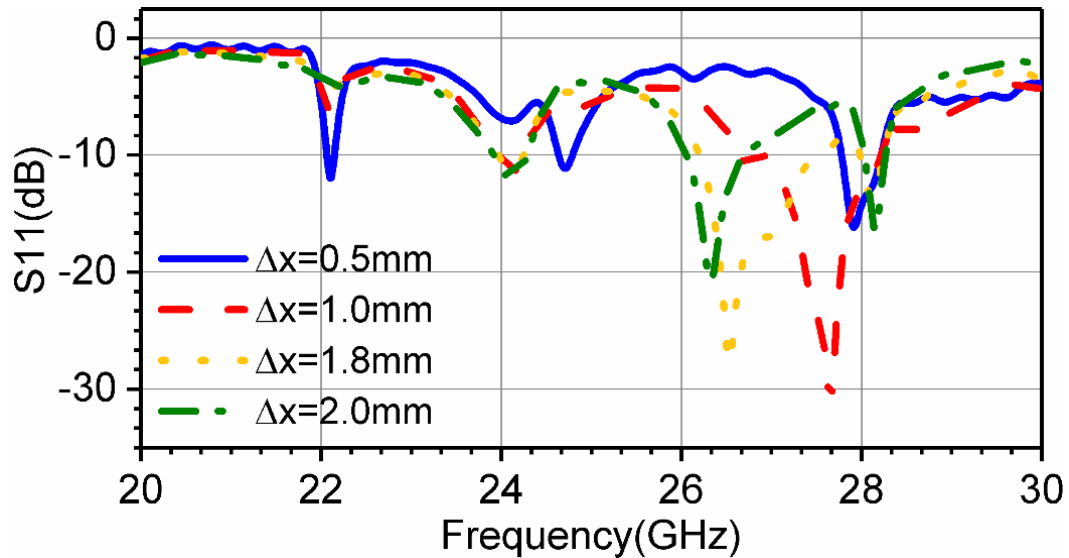
Figure 3.8 Effect of DRA offset on reflection coefficient of the CPW inductive fed GDRA. © 2019 Wiley. Reprinted with permission
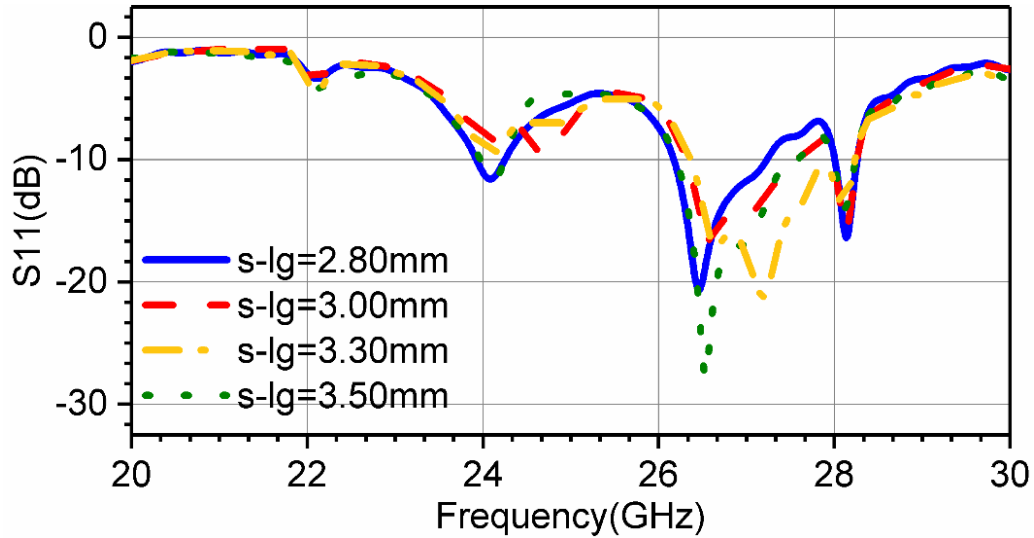
Figure 3.9 Parametric study of frequency response S_{11} (dB) of the slot length in the CPW inductive fed GDRA. © 2019 Wiley. Reprinted with permission

It is also observed that the magnetic fields in the GDRA, the magnetic field due to induced current in the slot coupling region and the magnetic field in the CPW line underneath the GDRA, all are matched and directed in the same direction, which supports the low cross-polarization levels in the CPW inductive fed GDRA. Figure 3.10 shows the simulated radiation efficiency of 84% is achieved across the frequency bandwidth. Additionally, a corresponding simulated performance matrix for all discussed CPW designs is presented in Table 3.2.

Table 3.2 A comparative analysis of GDRA fed through different CPW techniques

Feed Type	Imp. BW (GHz)	Max-R. G(dBi)	Max E-plane Cross-pol(dB)	Max H-plane Cross-pol(dB)	Max Sim. Rad Efficiency%
Open circuit GCPW	23-26.4	7.43	-21	-19	90
CPW inductive	26.3-28.15	5.73	-24	-22	84

Imp=Impedance; R. G= Realized gain; BW=bandwidth; Rad=radiation
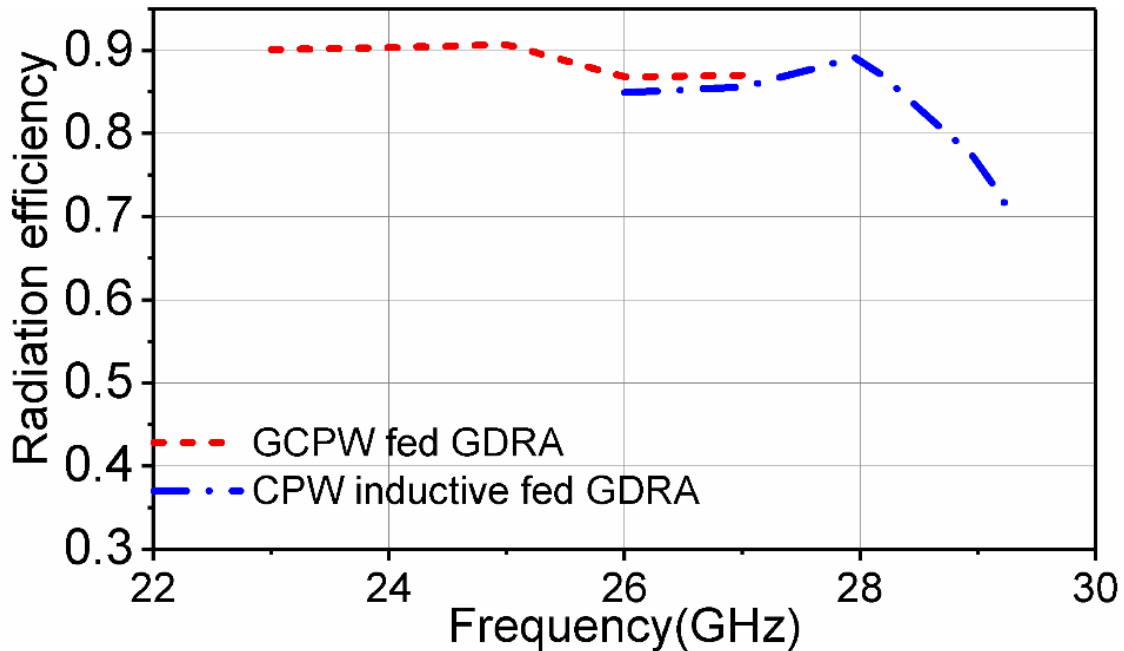
Figure 3.10 Simulated radiation efficiency for CPW fed GDRAs. © 2019 Wiley. Reprinted with permission

3.4. Fabrication and Measured Results

3.4.1. Single Element GDRA Fabrication

Deep X-ray lithography (D-XRL) with metal electroforming was used for precise fabrication of the multi-layer I-beam GDRA structures using the process described in [2]. These GDRA elements are designed and fabricated as a part of Shaon Ganguly's thesis [1] but not experimentally tested, and fed only by microstrip feedline in simulations. All steps in this process were done at KIT, with deep-XRL exposures performed at beamline *Litho-2*. For I-beam inclusions, a maximum filled cavity metal height of 0.85 mm has been considered for fabrication. The gap structures in the PMMA grid have an aspect ratio of 24. Figure 3.11 shows the scanning electron microscope (SEM) image of the plated I-beam inclusions, confirming tall, smooth, vertical side walls with uniform metallization. More information on deep-XRL fabrication is presented in Chapter 5.
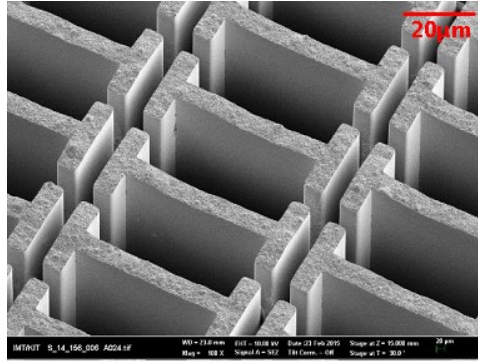
Figure 3.11 SEM image of tall-embedded I-shaped inclusions (PMMA removed for imaging) - (Image courtesy of KIT) © 2019 Wiley. Reprinted with permission

3.4.2. S-Parameters

To validate the performance, the GDRAs have been integrated with the CPW feeds realized on Rogers 6002 substrate with permittivity ϵ_r=2.94 and thickness of 0.508mm. The V-type 1.85mm connector as shown in Figure 3.12a is used for measuring the S-parameters for all circuits. The Agilent vector network analyzer HP8722ES is utilized for conducting this measurement. Comparative analysis of the measured reflection coefficient (S_{11}) for the simulated and measured circuits with both types of CPW feeds is provided in Figure 3.13. For all designs, the GDRA element was mounted on feed circuits using silicone adhesive at the GDRA corners. A wide measured impedance bandwidth up to 4 GHz is observed. The addition of the thin layer of PMMA has removed the limitation of the GDRA inclusions being short-circuited with the input feedline, which causes high input impedance and mode mismatch loss. Moreover, the multi-layer approach has allowed the GDRA to be excited underneath at the point of the best input impedance match for both open-ended microstrip feedline stub and CPW inductive slot feed options. Additionally, the PMMA layer has enhanced the energy coupling by reducing the input impedance of the GDRA. Nonetheless, both measured results are found to have good agreement with the simulation results, as shown in Table 3.3 and Figure 3.13.

Table 3.3 Comparison between the simulated and measured results

Antenna performance parameters	GCPW fed GDRA	CPW inductive fed GDRA
Simulated S11 B.W ≤-10 dB	23-26.4 GHz	26.3-28.15 GHz
Measured S11 B.W ≤-10 dB	22.6-26.6	26.6-29.3 GHz
Measured % B. W	16.26	9.6
Simulated max-R. G (dBi)	7.43	5.73
Measured max- R.G (dBi)	7.2	5.42

*R. G = realized gain

74

<div align="center">a)   b)</div>
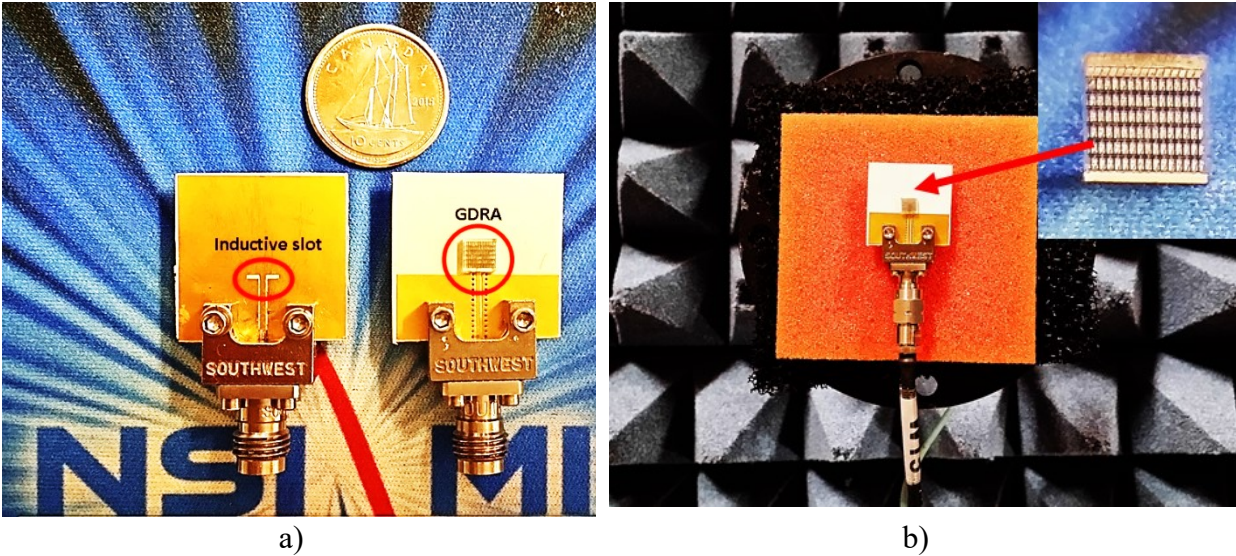
Figure 3.12 Fabricated designs: a) CPW inductive feed on the left, GCPW fed GDRA on the right; b) GCPW fed GDRA on AUT of the scanner for the far-field measurement. © 2019 Wiley. Reprinted with permission
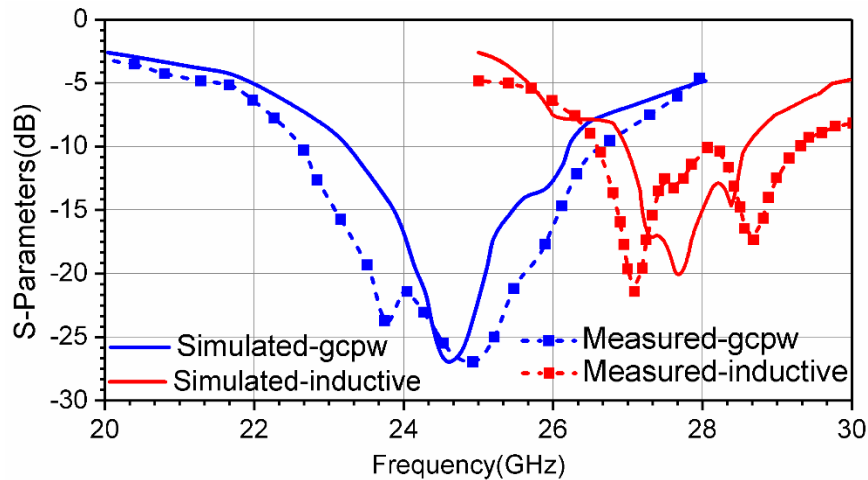
Figure 3.13 Measured S_{11} responses for CPW-fed multi-layer GDRAs. © 2019 Wiley. Reprinted with permission

3.4.3. Radiation Pattern

To characterize the radiation properties of the GDRAs using the CPW feeds, both E and H-plane patterns are measured using the NSI-700S spherical measurement system. Figure 3.12b shows the GCPW fed GDRA mounted on the AUT on spherical far-field system. The simulated and measured radiation patterns are provided in Figure 3.14. Most of the radiation patterns are found to be like ordinary DRAs, i.e., resembling patterns of horizontal magnetic dipoles. The radiation is highly concentrated in the broadside direction resulting in a higher gain. One of the reasons for

this improvement is the presence of the additional H-field cycles generated by the grids of the GDRA structure, which are not present in the conventional DRA [8]. Secondly, the near-field analysis has revealed that the metallic grids inside the PMMA material generate small secondary radiations which combine in phase to enhance the overall radiation performance. For both feeding topologies, E-plane cross-pols are well below -20 dB at broadside. The reason for these low cross pols is the orientation of the E-field vectors at the feeding point along the y-axis of the XY plane in both cases. E-plane cross-pol levels using the GCPW feed technique are found to be even better than the CPW inductive feed because of suppression of surface waves as result of tight E-field confinement between the top and bottom ground planes connected through vias.

On the other hand, H-plane cross-pols for both feeding schemes is observed at around -17 dB, which are slightly higher than the E-plane cross-pol values. The metal grid structures cause the H-field rotations in both XZ and YZ planes which increases the overall H field cross-pol levels. For better visualization, the E-field, and H-field cycles for all feed topologies are presented in Figure 3.16. The realized gain vs. frequency plot is provided in Figure 3.15 to characterize the pattern bandwidth of a GDRA for both feeding schemes. A maximum realized gain of 7.2 dBi is achieved. The performance comparisons between the proposed GDRA and the previously reported DRAs are listed in Table 3.4.

Table 3.4 A comparison table between the proposed design and others

Ref	% BW	Max-Realized. Gain(dBi)	Max Cross-pol(dB)	Max Sim. Rad Efficiency%
This paper	16.26	7.2	-21	90
[2]	6	7.6	-20	88
[9]	12.5	5.5	-19	95
[10]	6.45	10	-20	-
[11]	6	5.05	-21	-
[12]	3.8	6.3	-15	-
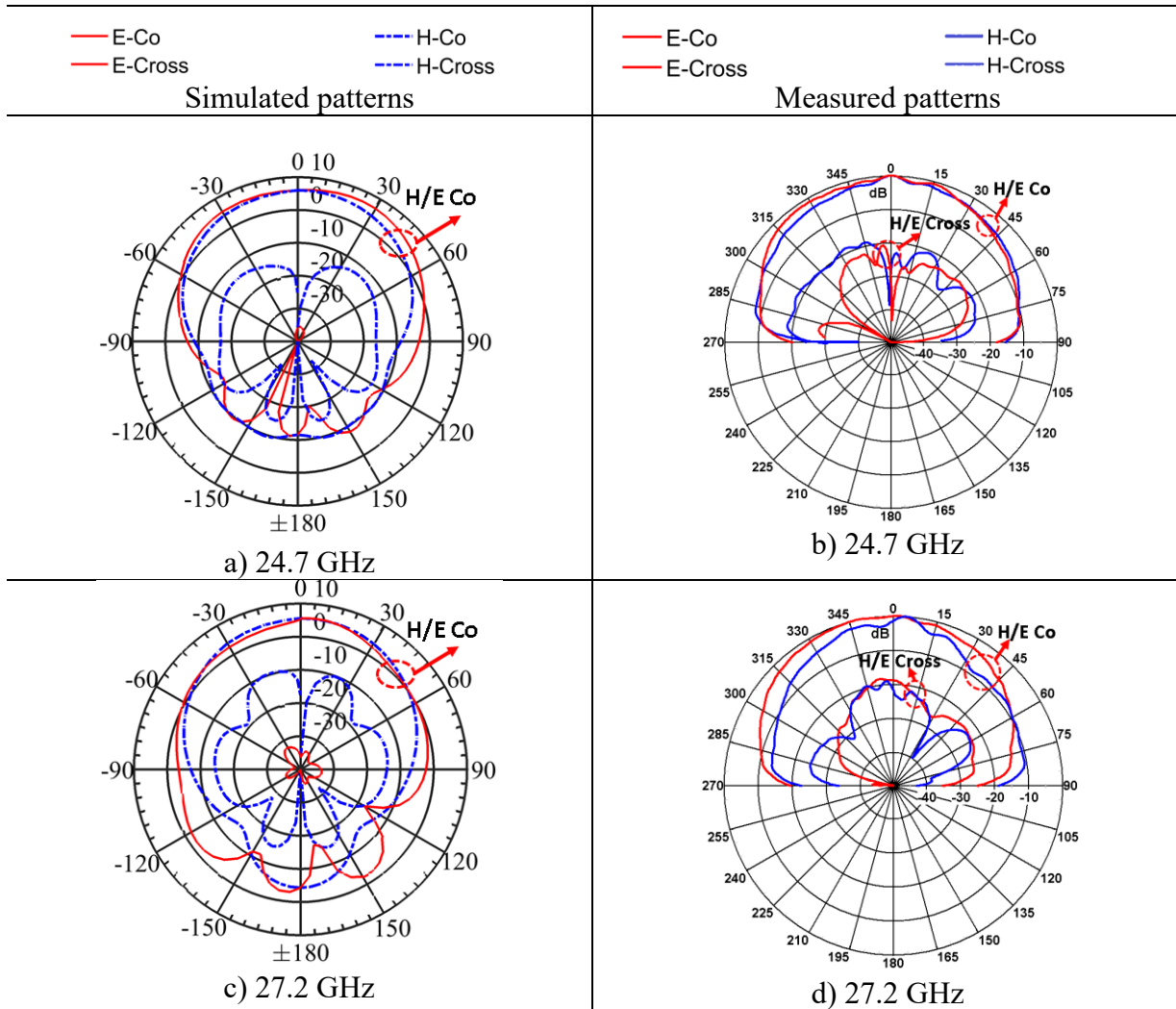
Figure 3.14 Simulated vs. measured radiation patterns: a: b) GCPW feed; c: d) Inductive CPW feed. © 2019 Wiley. Reprinted with permission
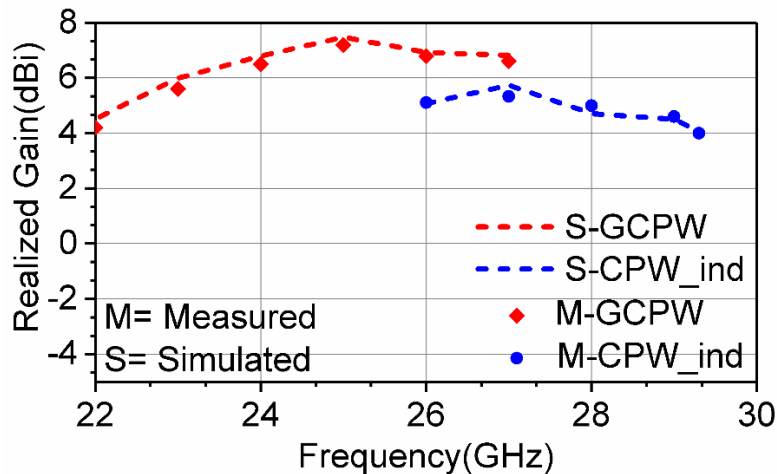
Figure 3.15 Simulated and measured realized gain for proposed CPW feed techniques. © 2019 Wiley. Reprinted with permission
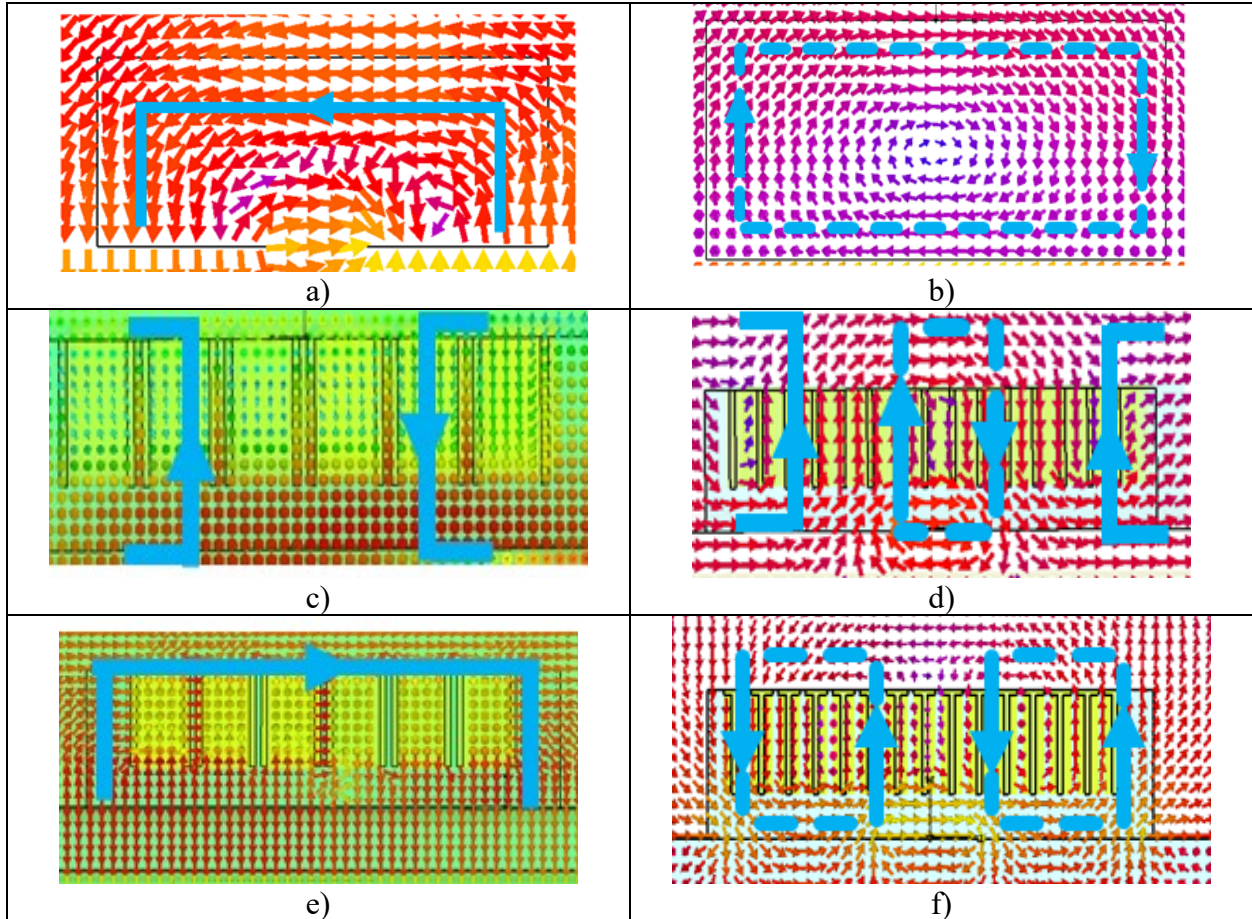
Figure 3.16 a, b) E and H-field pattern for conventional DRA fundamental mode; c, d) E and H-field pattern for GDRA fed by GCPW technique at 24.7 GHz; e, f) E and H-field pattern for GDRA fed by CPW inductive feed at 27.2 GHz. © 2019 Wiley. Reprinted with permission

3.5. Rectangular grids GDRA Design

The CPW fed I-beam GDRA work well for single elements and even better than the previous microstrip fed GDRAs. The addition of a thin perforated layer of polymer between the grids and the feed circuit has allowed the GDRAs to be fed using underneath feed mechanisms like CPW inductive slot feed, which is not possible in the original I-beam GDRA structures due to grids and feed network shorting problems. In addition, this multi-segment GDRA design concept has also improved the GDRAs impedance bandwidth up to 16% making it viable for wideband mm-wave applications.

However, there are number of areas which still require significant development to make the GDRA concept practical for large mm-wave antenna arrays. For instance, adapting feasible feed networks for large GDRA arrays as it is difficult to make compact distribution structures using coplanar waveguide (CPW) feeding due to the requirement for planar top side ground. Secondly, reducing

78

the overall height of the GDRAs to make them suitable for low profile applications. Other problems include reducing the fabrication complexities of the previously explored GDRAs by utilizing other grid structures like rectangular or square grids and investigating the effect of these new grids structures on the material characteristics such as change in effective permittivity. Lastly, developing a viable monolithic template frame approach for precisely aligning the GDRAs over the feed networks especially for large GDRA arrays. All of these issues are addressed in the remainder of the thesis.

3.5.1. Design Consideration

The simulated design model of a GDRA element with rectangular inclusion structures is shown in Figure 3.17. The example element is comprised of a rectangular block of low permittivity polymer (in this case polymethyl methacrylate, PMMA) having a relative permittivity of 2.5 with dimensions $L \times W \times H$ = 2.7mm×2.7mm×0.5mm, and tall rectangular metallic grid structures of embedded nickel. These structures can be realized as uniformly distributed rectangular cavities exposed and developed in PMMA through deep X-ray lithography (DXRL) and filled by electroplated nickel, as described further in Chapter 5.

The material characteristics of the artificial dielectrics are determined by the combination of the electromagnetic properties of both host material and the embedded inclusions. The effective permittivity is related to; 1) the permittivity of host material; 2) the size of metal inclusions; and 3) the lateral spacing between metal inclusions. Obtaining high effective permittivity is possible by increasing the volume fraction of the additive material and more specifically, by decreasing the gaps between elements to increase the localized electric flux density.
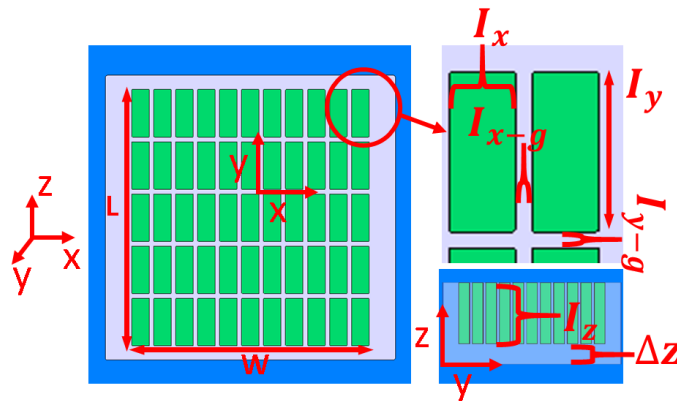
Figure 3.17 Simulated design model of the GDRA element with rectangular inclusion structures. Specific parameters are listed in Table 3.5. © 2019 IEEE. Reprinted with permission.
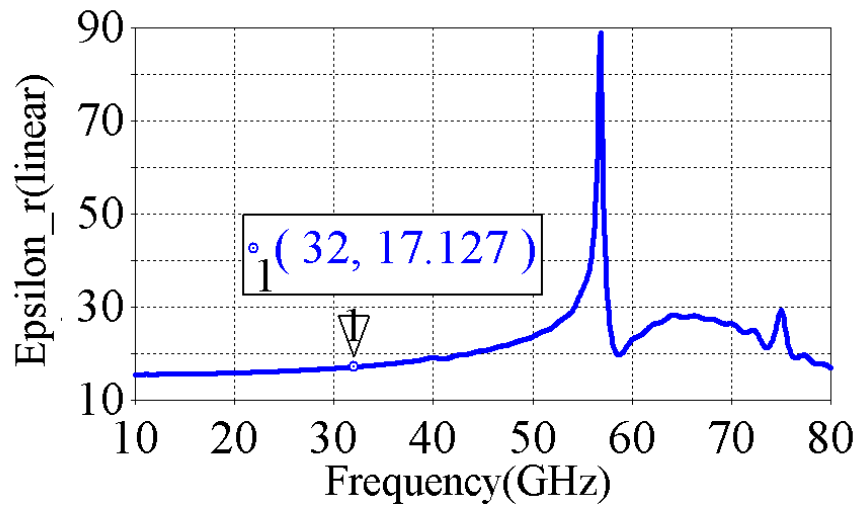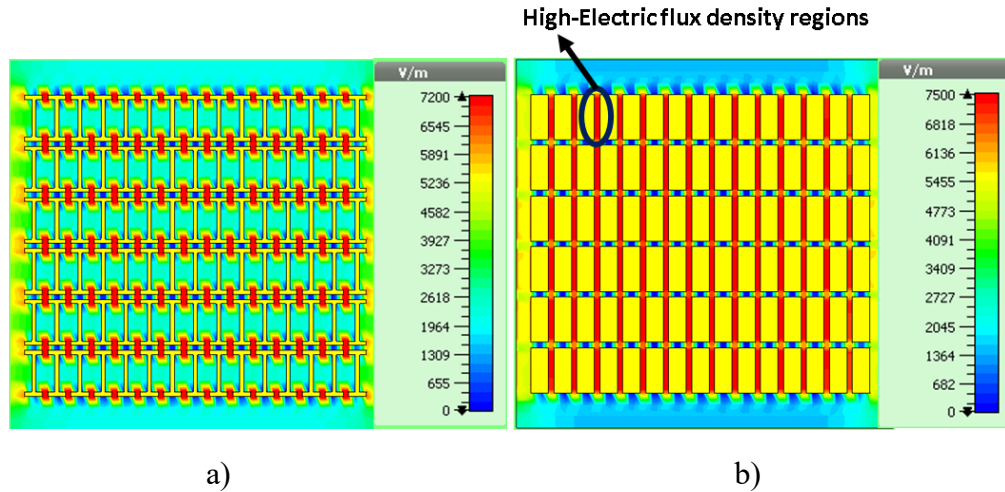
Figure 3.18 Electric field intensity comparison: a) I-beam grids; b) Rectangular grids; c) Estimated permittivity of the grid dielectric material © 2019 IEEE. Reprinted with permission.

Metal embodiments like cubes and rectangles produce large effective permittivity, providing high volume density and large localized capacitive surface density. I-beam structures provide large localized flux density with comparatively low embedded metal volume. However, rectangular structures can create higher and more uniformly distributed flux density than I-beam structures, resulting in larger effective permittivity. Being simpler shapes, they can also reduce fabrication complexity. Figure 3.18a&b compares electric field patterns of I-beam and rectangular GDRAs. The red areas indicate regions of highest electric flux density. An effective permittivity of 17 as shown in Figure 3.18c is estimated at the design frequency of 32 GHz for the rectangular inclusion elements with PMMA base template thickness of 0.5mm, using the simulation technique described

80

in Section 3.2.1. The grid size is constrained by the requirement to keep the dimensions much smaller than the operating wavelength, to avoid the inclusions becoming self-resonant:

$$(I_x, I_y, I_z) \leq \frac{\lambda_g}{10} \tag{3.13}$$

where $I_x, I_y,$ and I_z are the lateral dimensions of the rectangular inclusions in the x, y, and z directions, and λ_g is the guided wavelength at the operating frequency. These dimensions also ensure that the grid structures appear small to the incident wave resulting in minimal increase to material loss. All parameters used for the rectangular GDRA design configurations in this section are given in Table 3.5.

3.5.2. Solid Template Frame Single Element GDRA Design

Figure 3.19 shows the configuration of a single element solid template frame GDRA excited by a longitudinal slot placed in the SIW channel. The SIW parameters are designed using equations 2.68 to 2.71 and are chosen to ensure the propagation of only fundamental mode from 26-40 GHz. A microstrip transition [13], [14] is used to interface to the SIW and excite the GDRA element, bonded to the substrate, through the slot. More detailed discussion about the microstrip to SIW transition is presented in Section 4.2.

Two different GDRA element models are compared: 1) GDRA with a thin PMMA frame only slightly larger than the grid, and only meant to contain the embedded elements; and 2) GDRA with a large PMMA template considerably larger than the grid. The 2nd approach is meant to demonstrate an extension of the GDRA concept to a single piece monolithic array, which can include alignment markers as shown in Figure 3.19b to ensure precise, complete array alignment between the GDRA layer and the SIW feed layer, rather than requiring element-element alignment. Moreover, the performance of the GDRA with a large PMMA template frame and a conventional high permittivity DRA, is compared.

The critical design parameters to control the resonance frequency and the energy coupling in the GDRA are the distance between the longitudinal slot and the SIW short-circuited (SC) wall (W_{sc}), the slot length ($slot\_lg$), and the intermediate layer thickness (Δz). Distance Wsc is an important factor in controlling the input reflection coefficient and standing wave phase at the excitation slot. The initial value of Wsc is λ_g /4 at the longitudinal slot, where λ_g is the guided wavelength. This ensures large current disruption in the slot for excitation described further in Chapter 6. The slot

81

length is chosen in the proximity of $\lambda_{eff}/2$ to make it a non-resonant excitation source for the GDRA element. To avoid shorting the slot and the embedded metal inclusions, an intermediate layer (thickness $\Delta z = 0.2$mm) of perforated PMMA is introduced at the interface, which also helps in improving energy coupling between the slot and the GDRA. More details on the intermediate layer thickness and its effect on the input impedance of the GDRA are discussed in Chapter 6.
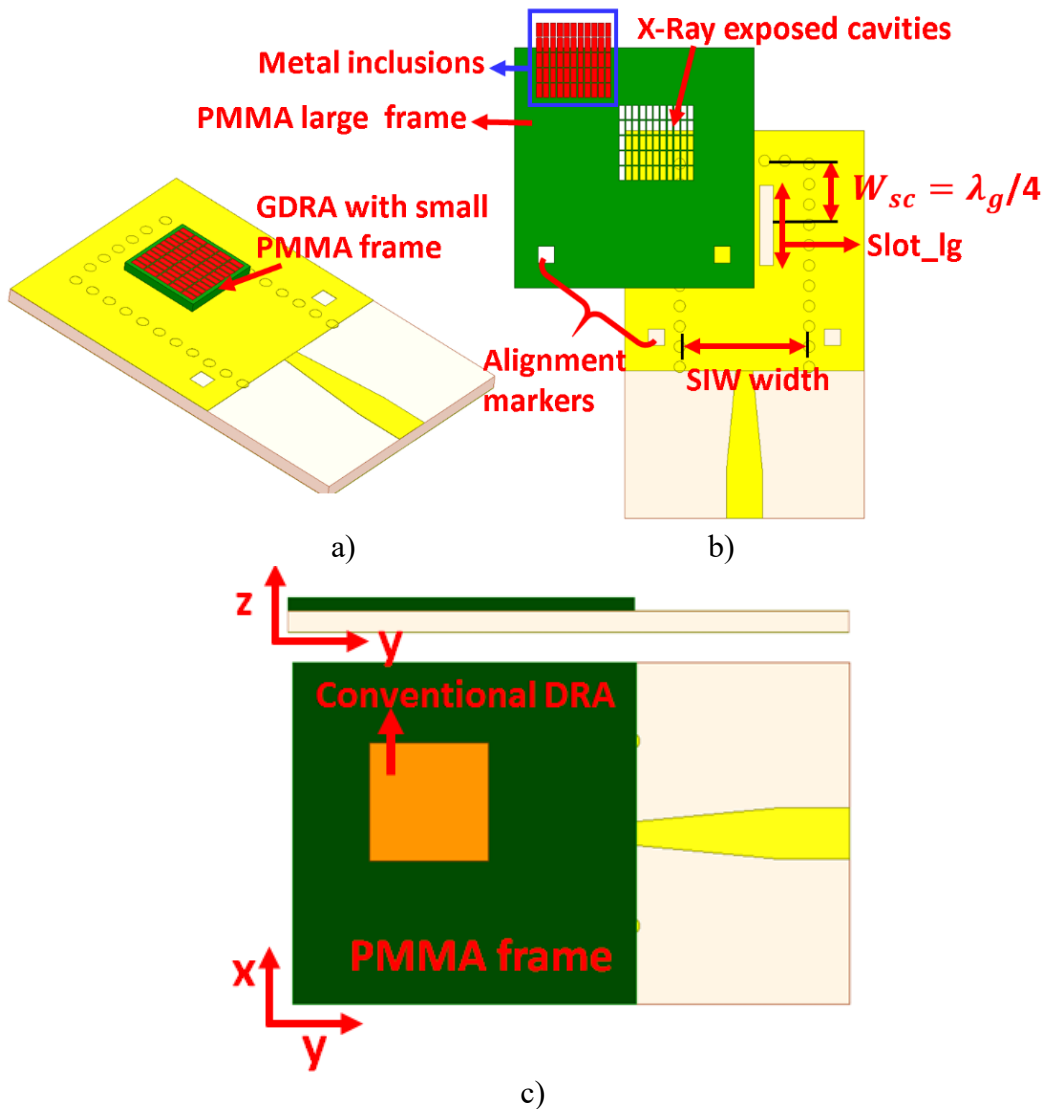
Figure 3.19 Simulation design for GDRA element fed through longitudinal SIW slot; a) with small PMMA frame encapsulating the embedded elements; b) with large PMMA template encapsulating the embedded elements; c) Single element conventional high permittivity DRA with a PMMA template frame © 2019 IEEE. Reprinted with permission.

Table 3.5 SIW and GDRA Design Parameters (Figs. 3.17, 3.19)

Parameters	Symbols	Values(mm)
Grid x-gap	I_{x-g}	0.05
Grid y-gap	I_{y-g}	0.05
Element width	I_x	0.20
Element length	I_y	0.50
Element height	I_z	0.30
Int. layer thickness	Δz	0.20
GDRA length	L	2.70
GDRA width	w	2.70
GDRA height	$I_z + \Delta z$	0.50
SIW width	a	4.30
Slot length	Slot_lg	2.70
Vias gap	d	0.65
Slot gap	Slot_gap	4.30
SC distance for long. slot	W_{sc}	3.20
Conventional DRA		
DRA width	w	2.80
DRA length	L	2.80
DRA height	h	1.00
Permittivity	ϵ_r	17

*long.= longitudinal

A simulated -10 dB bandwidth of 1.7 GHz centered at 32 GHz is shown in Figure 3.20 for the single element large template GDRA with the parameters given in Table 3.5 . It is observed that introducing a large template frame results in a slight lowering of resonant frequency and similar directivity of the GDRA in comparison to the small frame design. The reason for this lower frequency resonance with the large dielectric template is a slight increase in the overall effective volume of the GDRA. These results validate that the large template frame around the GDRA

element does not alter its performance significantly and hence it can be used for building large template based GDRA arrays.

To provide a comparative analysis, a conventional DRA of relative permittivity $\in_r$=17 resonating at 32 GHz is also designed. The antenna dimensions are provided in Table 3.5. The required height of this antenna is two times larger than the GDRA design shown in Figure 3.19b, to make the conventional DRA functional. Similarly, the 10-dB impedance bandwidth of the conventional DRA is half of the high permittivity GDRA design i.e., only 800 MHz as shown in Figure 3.20. S-parameters of a conventional DRA ($\in_r$=17) with the exact dimensions of the GDRA ($2.7mm \times 2.7mm \times 0.5mm$) are also shown in Figure 3.20. The reflection coefficient for this case does not even reach the 10-dB impedance bandwidth reference. Thus, a single element template embedded GDRA outperforms the similar high permittivity DRA both in term of operational bandwidth and the element size making it viable for compact and low-profile design requirements.
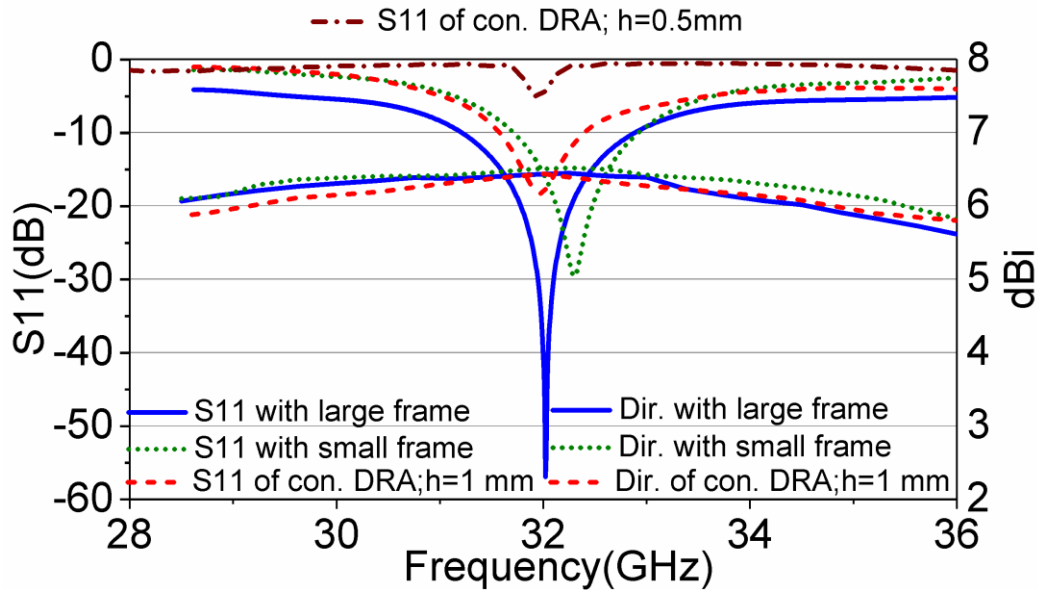
Figure 3.20 Simulated S-parameters and directivity plots for single element GDRA fed through SIW longitudinal slot with small PMMA frame and large PMMA template and comparison to a conventional high permittivity DRA © 2019 IEEE. Reprinted with permission.

**Dir. = Directivity; Con. = Conventional

3.5.3. Fabrication and Measured Results

The high vertical to lateral aspect ratio (in this case 10:1) required for the GDRA grid gaps of 50 μm presents considerable microfabrication challenges. Deep X-ray lithography is utilized for

realizing high quality deep rectangular cavities with lateral dimensions of 200μm×500μm in a 500μm thick PMMA template. The fabrication process is described in detail in Chapter 5. All steps in this process were done at CLS, with deep-XRL exposures performed at the SyLMAND beamline. Scanning electron microscope (SEM) images of prototyped devices are presented in Figure 3.21 for visualizing the excellent side walls and structure quality possible with the deep-XRL and electroforming process. The fabricated GDRA template with feed structure is provided in Figure 3.22. Rectangular markers placed at the top corners of the template and PCB feed circuit are utilized for ensuring the precise microscopic alignment between them. More detailed fabrication process from mask making to sample exposure and development is presented in Chapter 5.

A standard PCB process is used for building the SIW feeding circuit for a single element GDRA prototype on Rogers 6002 substrate with permittivity=2.95 and the substrate thickness of 0.508mm. The GDRA template is bonded to the feedline structures using thin silicon adhesive under the optical microscope. The fabricated prototype is measured using an Agilent vector network analyzer HP8722ES. over the frequency band of 29 to 36 GHz. Figure 3.22 shows the measured reflection coefficients for the GDRA element having an impedance bandwidth of 3.9 GHz centered at 32.25 GHz.

Simulated co/cross pol response for the single element GDRA are presented in Figure 3.23 confirming the broadside radiation pattern with cross-pol levels below -24dB. For a magnetic field fed single element GDRA design, H-field vectors orientation in both slot and GDRA are well matched, thus resulting in low H-cross pol levels, i.e., below -24dB. Furthermore, E-field vectors of the longitudinal slot and the GDRA element are well aligned and result in low E-cross pol levels, i.e., below -22 dB. The radiation behavior of the SIW-fed GDRA element is experimentally characterized through the NSI-spherical measurement system. All E and H-plane radiation patterns are found to be in good agreement with the simulation results. A maximum broadside gain of 6.4dBi is observed at 32.25GHz. The slight variation in the simulated and measured gain values may be due to reduced coupling energy from the slot to GDRA template because of small air gap introduce by the silicon glue. Polar plots for all measured radiation patterns are provided in Figure 3.24. Moreover, maximum gain over the design frequency is also presented in Figure 3.22

confirming good patterns and gain stability across the frequency bandwidth for the fabricated design.
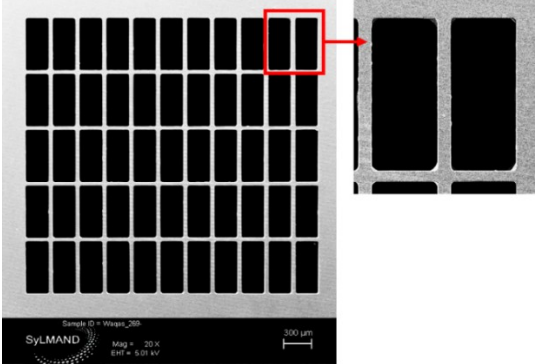
a)
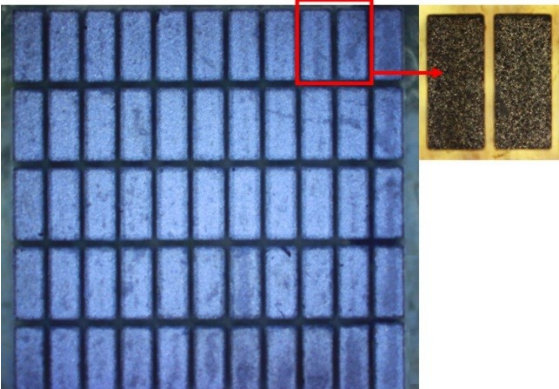
b)
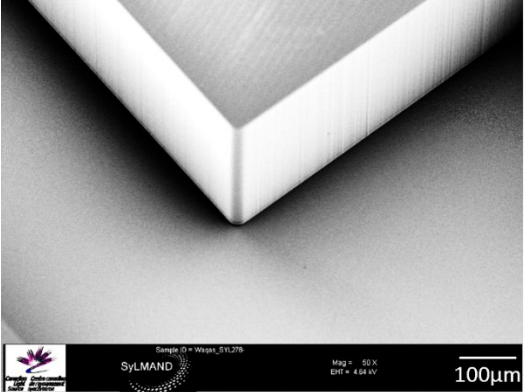
c)

Figure 3.21 a) SEM image of X-ray exposed rectangular cavities in a PMMA template; b) Optical microscope image of nickel-plated cavities; c) SEM image of GDRA array template corner showing vertical side wall quality © 2019 IEEE. Reprinted with permission.
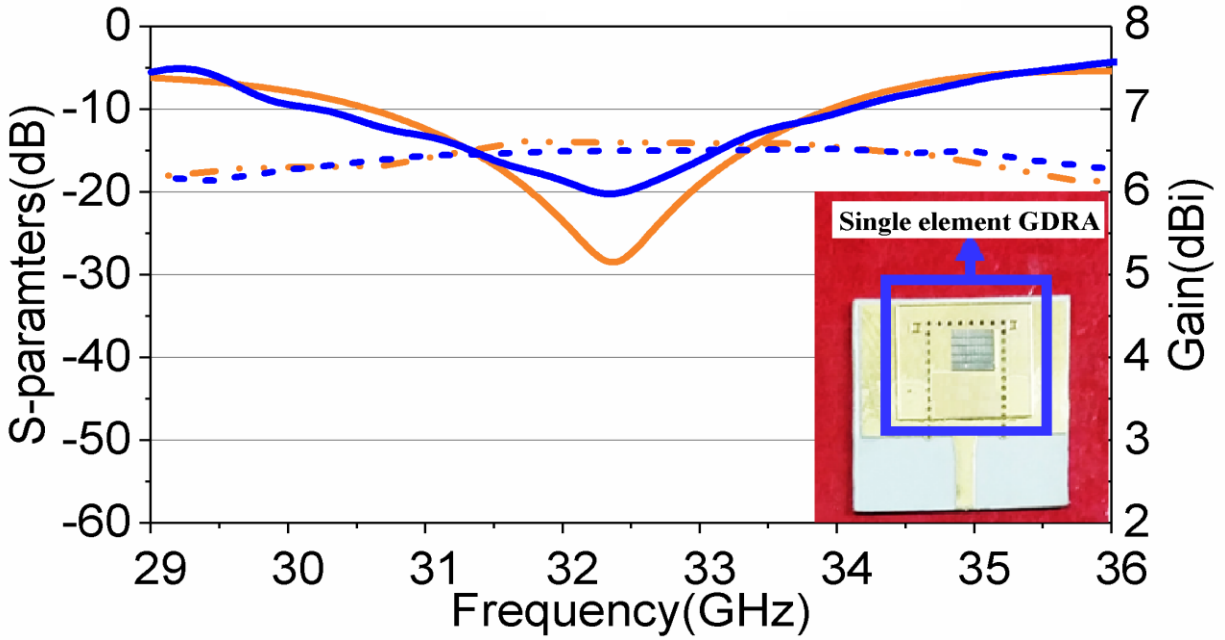
Figure 3.22 Comparison between the simulated and measured S-parameters and gain for the GDRA element © 2019 IEEE. Reprinted with permission.

a) 31 GHz

b) 32 GHz
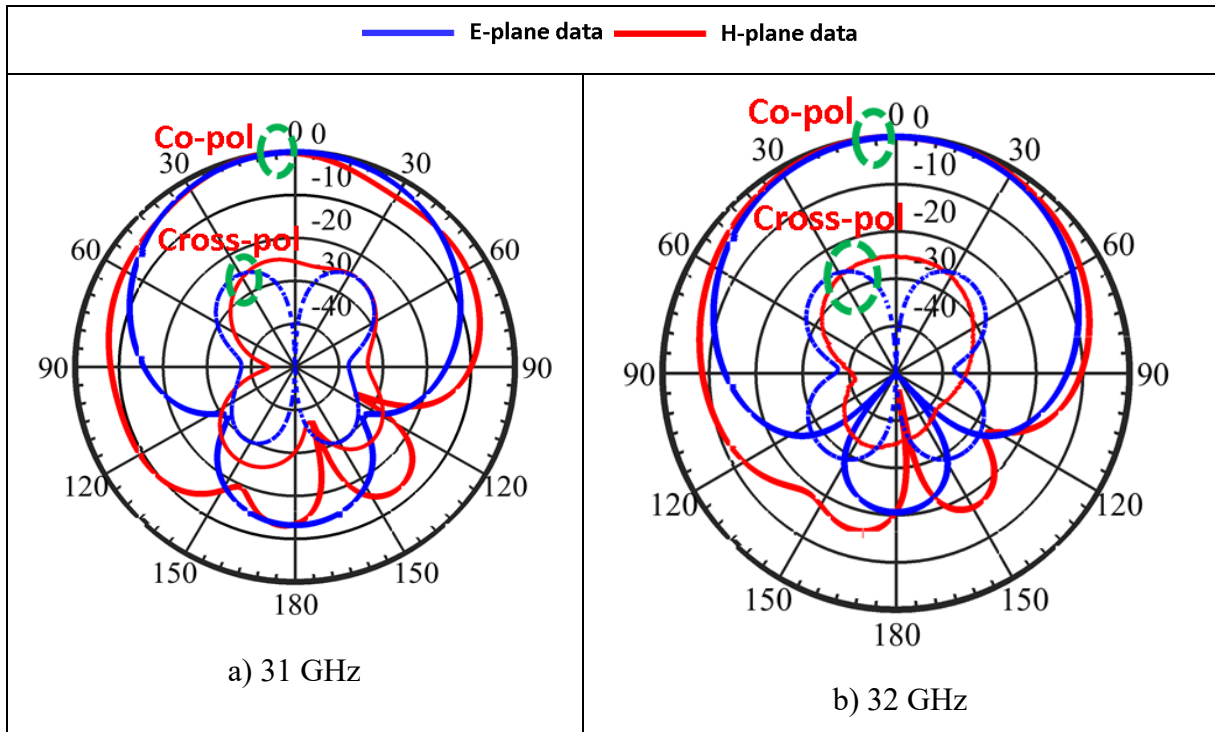
Figure 3.23 Simulated radiation pattern for a single element GDRA
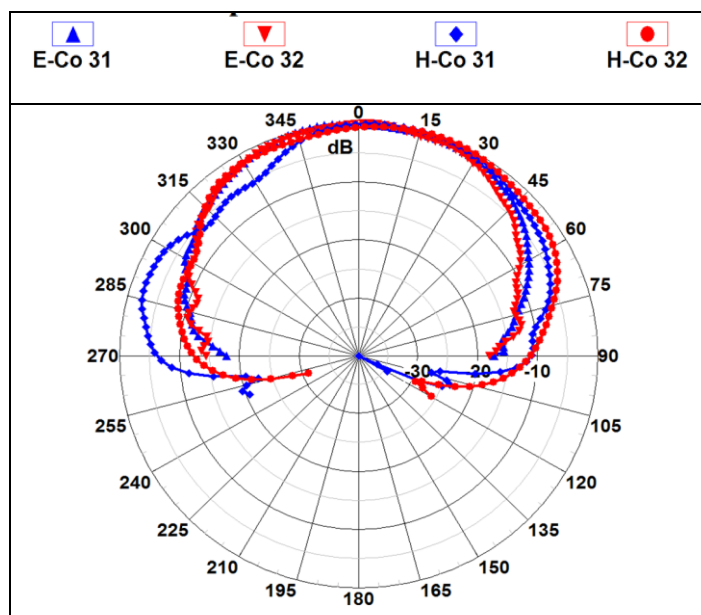
Figure 3.24 Measured radiation pattern for a single element GDRA

3.6. Conclusion

In this chapter, excitation of I-beam and rectangular grid multi-segment GDRAs with two different feeding mechanisms CPW feeding and SIW based longitudinal slot feeding for high frequency mm-wave applications have been investigated and tested. The combination of the underneath feed and the addition of a thin polymer layer with optimized thickness at the base of the metal grid layer has increased the impedance bandwidth up to 16.26%, about 2.71 times larger than the GDRA proposed in [2]. The multi-layer GDRA approach has resulted in the better mode matching at the GDRA and feed-line interface and has enhanced the overall performance characteristics of the previously reported GDRAs.

For rectangular grid GDRAs the effective permittivity of 17 is achieved which is even higher than the I-beam grids (i.e. ϵ_r=14.5) and results in low profile design i.e., height=500 μm and secondly being simpler shape, this has also reduced the fabrication complexity. For both feeding schemes, the effects of various design parameters on the performance of the GDRAs are discussed. The E and H-field vectors inside the GDRA are examined. It is observed that the orientation of field vectors in the feeding region has a substantial effect on the radiation patterns concerning both E and H-field co-pol and cross-pol levels and can be used to enhance the radiation characteristics of the GDRAs. The proposed CPW and SIW longitudinal slot fed GDRAs are found to have the wide-

impedance bandwidth and excellent broadside radiation patterns with very low cross-polarization levels below -18dB in both E and H-planes.

References

[1]   S. Ganguly, "Effect of Variations in Metal Inclusion Geometries on the Performance of Meta-DRAs," M.Sc thesis, University of Saskatchewan, 2015.

[2]   M. T. Aligodarz, D. M. Klymyshyn, A. Rashidian, M. Borner, L. Shafai, and J. Mohr, "Investigations on Photoresist-Based Artificial Dielectrics With Tall-Embedded Metal Grids and Their Resonator Antenna Application," *IEEE Trans. Antennas Propag.*, vol. 63, no. 9, pp. 3826–3838, Sep. 2015.

[3]   X. Chen, T. M. Grzegorczyk, B.-I. Wu, J. Pacheco, and J. A. Kong, "Robust method to retrieve the constitutive effective parameters of metamaterials," *Phys. Rev. E*, vol. 70, no. 1, p. 016608, Jul. 2004.

[4]   R. K Mongia and A. Ittipiboon, "Theoretical and experimental investigations on rectangular dielectric resonator antennas," *IEEE Trans. Antennas Propag.*, vol. 45, no. 9, pp. 1348–1356, 1997.

[5]   R. A. Kranenburg, S. A. Long, and J. T. Williams, "Coplanar waveguide excitation of dielectric resonator antennas," *IEEE Trans. Antennas Propag.*, vol. 39, no. 1, pp. 119–122, 1991.

[6]   R. A. Kranenburg and S. A. Long, "Microstrip transmission line excitation of dielectric resonator antennas," *Electron. Lett.*, vol. 24, no. 18, p. 1156, 1988.

[7]   M. S. Al Salameh, Y. M. Antar, and G. Seguin, "Coplanar-waveguide-fed slot-coupled rectangular dielectric resonator antenna," *IEEE Trans. Antennas Propag.*, vol. 50, no. 10, pp. 1415–1419, Oct. 2002.

[8]   A. Petosa, *Dielectric resonator antenna handbook*. Artech House, 2007.

[9]   W. M. Wahab, D. Busuioc, and S. Safavi-Naeini, "Low Cost Planar Waveguide Technology-Based Dielectric Resonator Antenna (DRA) for Millimeter-Wave Applications: Analysis, Design, and Fabrication," *IEEE Trans. Antennas Propag.*, vol. 58, no. 8, pp. 2499–2507, Aug. 2010.

[10] Y. Gao, Z. Feng, and L. Zhang, "Compact CPW-Fed Dielectric Resonator Antenna With Dual Polarization," *IEEE Antennas Wirel. Propag. Lett.*, vol. 10, pp. 544–547, 2011.

[11] M. S. Al Salameh, Y. M. M. Antar, and G. Seguin, "Coplanar-waveguide-fed slot-coupled rectangular dielectric resonator antenna," *IEEE Trans. Antennas Propag.*, vol. 50, no. 10, pp. 1415–1419, Oct. 2002.

[12] Y.-M. Pan, K. W. Leung, and K.-M. Luk, "Design of the Millimeter-wave Rectangular Dielectric Resonator Antenna Using a Higher-Order Mode," *IEEE Trans. Antennas Propag.*, vol. 59, no. 8, pp. 2780–2788, Aug. 2011.

[13] D. Deslandes, "Design equations for tapered microstrip-to-Substrate Integrated Waveguide transitions," in *2010 IEEE MTT-S International Microwave Symposium*, 2010, pp. 704–707.

[14] M. Abdolhamidi, A. Enayati, M. Shahabadi, and R. F-Dana, "Wideband Single-Layer DC-Decoupled Substrate Integrated Waveguide (SIW) - to - Microstrip Transition Using an Interdigital Configuration," in *2007 Asia-Pacific Microwave Conference*, 2007, pp. 1–4.

Chapter 4 : SIW Feeding Networks for GDRA Array

4.1.   Introduction and Background

Due to its unique properties, substrate integrated waveguide (SIW) is well suited to become a preferred technology in waveguide-based power splitters. A large number of designs have focused on X-band frequencies up to 12 GHz, e.g., a 1×4 Wilkinson power splitter with insertion loss of 8 dB [1], and a 1×8 power splitter with insertion loss of 10.5 dB [2]. Improvements in T and Y junctions can help in bandwidth enhancement [3]. A wide band 16 port SIW power splitter is reported in [4] providing 28 percent frequency bandwidth at 11.75 GHz.

In this chapter[5], a detailed study of high performance, wideband, 3-stage power splitters based on SIW technology is presented. Additionally, an in-depth parametric analysis of various broadband T-junctions such as 1×4 and 1×2 T-junctions is provided for exploring the key design parameters for optimizing performance including wide impedance bandwidth, and low insertion loss at mm-wave frequencies. These building blocks are further cascaded to realize a 1×8 SIW power splitter demonstrated at 24 GHz. Broadband tapered microstrip transitions are used for feeding all designed SIW structures. The optimized microstrip transitions and T-junctions are used to design a broadband, eight-way power splitter with 15dB return loss from 23.0 GHz to 26.4 GHz and simulated phase and amplitude imbalance of ± 2.5º and ± 0.8 dB respectively. A procedure for tuning the positions of SIW inductive posts is also provided for assisting in the design of mm-wave, high performance power splitters. These power distribution networks are used to feed the GDRAs in subsequent chapters.

4.2.   Ultra-Wideband Microstrip to SIW Transition

The key design parameters for SIW were described in Section 2.3.3. A simulation model of the SIW fed through microstrip line transition is presented in Figure 4.1. In this work, Rogers RO6006c substrate with a dielectric constant of 2.94 and 0.762 mm thickness is considered for designing the SIW structures. The equivalent SIW width is found to be A_e = 5mm using A_r = 5.21mm, D = 0.4mm and P = 0.8mm in equation 2.71. The cut-off frequencies for the first and second order TE modes obtained using equation 2.68 are 17.46 GHz and 36.38 GHz, respectively. The chosen SIW

---

geometries ensure that only the fundamental mode TE_{10} propagates in the desired operating band (i.e., 22-26 GHz).

There are several planar techniques available for transitions to an SIW structure. Here a, tapered microstrip transition is discussed and analyzed using a mode matching technique [5]. The main benefits of using this transition include widespread use of microstrip based circuits, large bandwidth covered by this transition and better performance when compared to other coplanar [6] and microstrip transitions [7]. Most importantly, the transition losses are very low. This comes from the fact that the electromagnetic fields in microstrip match closely to the field distribution of SIW. In [8], the microstrip portion is modeled by an equivalent TEM waveguide. The impedance for this model is given by

$$Z_e = \sqrt{\frac{\mu}{\epsilon_0 \epsilon_e} \frac{h}{w_e}} \tag{4.1}$$

h = waveguide height

w_e = width of TEM waveguide

Combining the analytical expressions for microstrip line impedance [9] and the microstrip waveguide model [5] results in

$$Z_e = \sqrt{\frac{\mu}{\epsilon_0 \epsilon_e} \frac{h}{w_e}} = \begin{cases} \dfrac{60}{\sqrt{\epsilon_e}} \ln\left(8\dfrac{h}{w} + 0.25\dfrac{w}{h}\right) & {}^w/_h < 1 \\[4mm] \dfrac{120\pi}{\sqrt{\epsilon_e}\left[\dfrac{w}{h} + 1.393 + 0.667\ln\left(\dfrac{w}{h} + 1.44\right)\right]} & {}^w/_h > 1 \end{cases} \tag{4.2}$$

ϵ_e = Effective permittivity

h = Height of the substrate
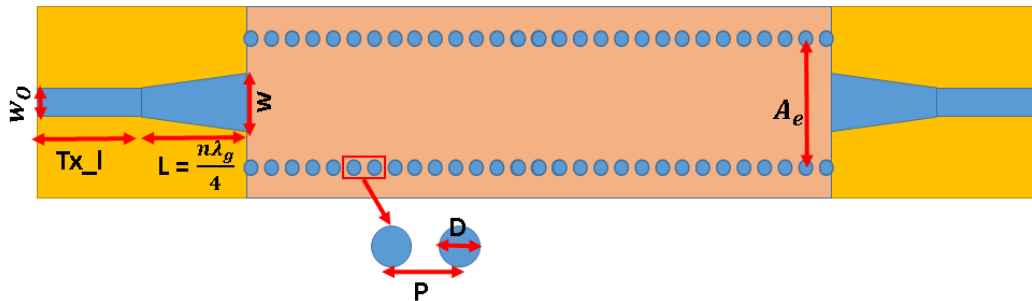
Figure 4.1 Back to back microstrip to SIW transition © 2018 Wiley. Reprinted with permission

Microstrip tapering enables broad impedance bandwidth by effectively transforming the quasi-TEM mode of the microstrip line to the SIW TE mode. The length and width of the tapered section play a vital role in this transition. Analytical expressions for calculating the width of this tapered section mentioned in [8] are used here:

$$\frac{1}{w_e} = \begin{cases} \frac{60}{\eta h} \ln\left(8\frac{h}{w} + 0.25\frac{w}{h}\right) & \text{w}/h < 1 \\ \frac{120\pi}{\eta h \left[\frac{w}{h} + 1.393 + 0.667 ln\left(\frac{w}{h} + 1.44\right)\right]} & \text{w}/h > 1 \end{cases} \tag{4.3}$$

$$\frac{1}{w_e} = \frac{4.38}{A_e} e^{-0.627\frac{\epsilon_r}{\frac{(\epsilon_r+1)}{2} + \frac{(\epsilon_r-1)}{2} + \frac{1}{\sqrt{1+\frac{12h}{w}}}}} \tag{4.4}$$

w = tapering width

A_e= equivalent width of the SIW

w = width of the microstrip line

Equation 4.3 and 4.4 relate the width of the TEM waveguide (w_e) to the microstrip line and to the SIW equivalent width (A_e) respectively. These equations are equated by the mode matching technique i.e. to match mode between the TEM waveguide and SIW waveguide, to find the optimum taper width for the tapered section, during this transition. This width is further tuned through the parametric analysis shown in Figure 4.2a. The length of the tapered section depends on the degree of width discontinuity between the microstrip and SIW. A larger width discontinuity normally requires a longer taper for good mode matching. However, at millimeter-wave frequencies with high permittivity substrates, there is less sensitivity to the width discontinuity and, the required taper length can be relatively short. A quarter wavelength taper at the band center frequency is usually sufficient to achieve a good return loss. The taper length must be selected a multiple of quarter wavelength i.e. $\left(\frac{n\lambda_g}{4}\right)$, to achieve both wide impedance bandwidth and good return loss. This can be visualized by the parametric study of factor "n" provided in Figure 4.2b. The best impedance bandwidth is achieved for n =2 and width of 2.71mm, providing S_{11} below -15 dB from 21 GHz to 29 GHz as depicted in Figure 4.2b. The maximum insertion loss of 0.50 dB is achieved across the band over a 20mm long SIW channel. All design parameters and their values for this

93

transition are listed in Table 4.1. The expression for calculating the guided wavelength is mentioned below.
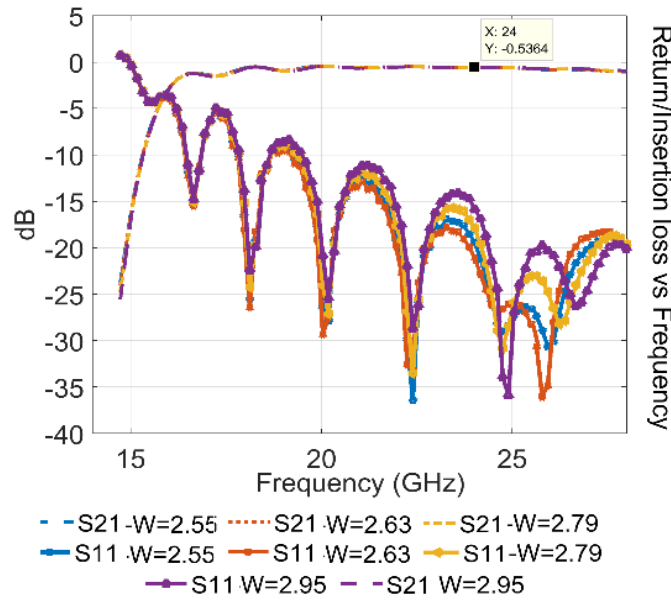
a)
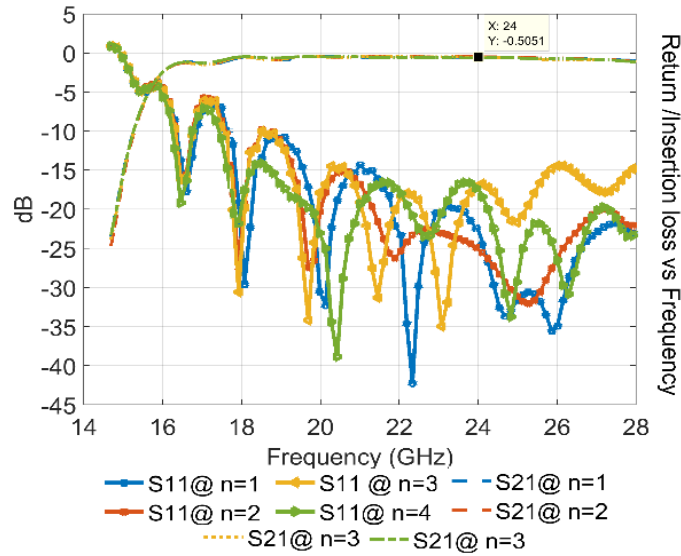
b)

Figure 4.2 a) Parametric study of variable "w" over fixed tapered section length $L = 3.63$ for back to back microstrip transmission line to SIW transition; b) Parametric study of variable "L" over fixed tapered section width $w = 2.95$ for back to back microstrip to SIW transition © 2018 Wiley. Reprinted with permission

$$\lambda_g = \frac{c}{f\sqrt{\varepsilon_r}} \tag{4.5}$$

$$L = \frac{n\lambda_g}{4} \quad n = 1,2,3,4 \dots \tag{4.6}$$

$L = length\ of\ taper\ section$

$f = design\ frequency$

$\varepsilon_r = relative\ permitivity\ of\ dielectric\ material$

Moreover, a comparison between the current and previous developed SIW transitions is also given in Table 4.2.

Table 4.1 SIW design parameters (mm)

Variable	value	Variable	value
f_{design}	24 GHz	f_{cutoff}	17.46 GHz
A_e	5	Tx_l	5.37
A_r	5.21	w	1.95
D	0.4	L	3.63
P	0.8	w	2.95
λg	8.11	Sub_w	10
Sub_l	46		

Table 4.2 Comparison between current and previous developed SIW transitions

Ref:	Proposed	[10]	[11]	[12]	[13]
Type	Microstrip to SIW	GCPW to SIW	Microstrip to SIW	Slot line to SIW	Microstrip to Empty-SIW
B.W (GHz)	21-29	9-11	12-18	18-28	12-18
I. loss(dB)	0.9	0.6	0.78	1.6	1.2
R. loss(dB)	-15	-10	-15	-20	-20

B. W = bandwidth; I. Loss = insertion loss; R. loss = return loss

4.3.   Power Splitter Design

For detailed analysis, the design procedure for the 1×8 power divider is split into four tasks; i) 1×2 input T power splitter, ii) 1×4 T power splitter, iii) 1×2 output T splitter and iv) 1×8 splitter. The overall design of a 1×8 splitter is comprised of four 1×2 T splitters fed through the four output ports of a 1×4 T splitter.

By utilizing the optimized microstrip to SIW transition as discussed in Section 4.2, the design is tuned for best performance with respect to impedance bandwidth and insertion loss. The term impedance bandwidth refers to the range of frequencies for which return loss (S_{11}) is below -10 or -15 dB depending upon the set design goal. All design segments are optimized through parametric analysis for design goal of return loss below -15dB.

4.3.1. One Cross Two Input T Splitter

The simulated design model of the 1×2 input T splitter is presented in Figure 4.3a. The concept of using multiple metallic posts [3] allows a wide degree of design freedom in providing good input impedance match. A group of two metallic posts labeled as "$w1$" is placed at the center of the 1×2 T splitter. These posts extend $\frac{\lambda_g}{4}$ from the common wall of two output ports as shown in Figure 4.4.
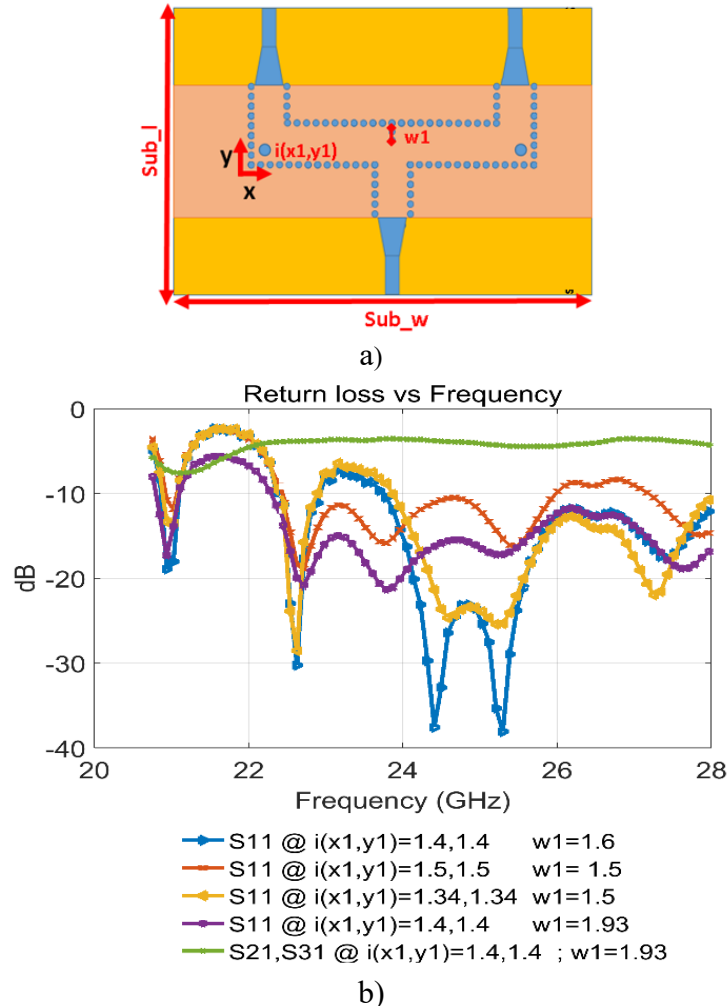

a)

b)

Figure 4.3 a) Geometry of SIW based 1×2 input T junction; b) Simulated S-parameters for 1×2 input T junction © 2018 Wiley. Reprinted with permission

The positions and diameters of these posts are further tuned to provide equal power splitting with good input match over a wide impedance bandwidth. Through parametric study, the diameter of all metallic posts is chosen to be 0.8 mm for minimum input reflection. The frequency of resonance is controlled by tuning the central metallic posts position "$w1$". These posts function similar to the power divider's boundary in a conventional metallic waveguide power divider. The 90-degree corners in SIW as depicted in

Figure 4.3a, are also an important consideration for the multi-way power divider as they add to the reflections at the input port, hence degrading the overall performance. Therefore, two additional inductive posts are placed in the corners, i.e. $i(x1, y1)$ to reduce the effect of discontinuity and minimize these reflections. The diameter and position of these metallic posts greatly affects the input return loss. The inductive posts are initially placed at a distance of $\frac{\lambda_g}{4}$ along the x and y axis away from the corner as suggested in [14], then their positions are tuned to improve the performance. The optimum positions are listed in Table 4.4. The parametric analysis of S-parameters obtained by varying the positions of the inductive posts $i(x1, y1)$ and the common center posts "$w1$" is presented in

Figure 4.3b. A maximum bandwidth of 3.3 GHz from 22.7 GHz to 26 GHz is achieved with (S_{11}) below -15 dB and an average insertion loss of 3.6 dB.

4.3.2. One Cross Four T Splitter

The proposed design for the 1×4 T power splitter is presented in Figure 4.4. It is an extension of the 1×2 T input power splitter, combining three 1×2 T power splitters. Even power distribution is achieved by placing common central metallic posts "$w2$" at the center of both 1×2 T power splitters with a starting gap of $\frac{\lambda_g}{4}$ similar to that shown in Figure 4.4 for "$w1$". The symmetric inductive posts $i(x1, y1), i(x2, y2)$ are placed at the SIW corners thus minimizing the reflection loss and improving the input match. The optimum parameters of the 1×2 T power splitter in the previous section are considered as a starting point for this design. Further tuning of the position of the inductive posts $i(x1, y1), i(x2, y2)$ and the common central metallic posts "$w2$" of the second level 1×2 T power splitters is made through parametric analysis, to achieve both wide impedance bandwidth and minimum input port reflection.
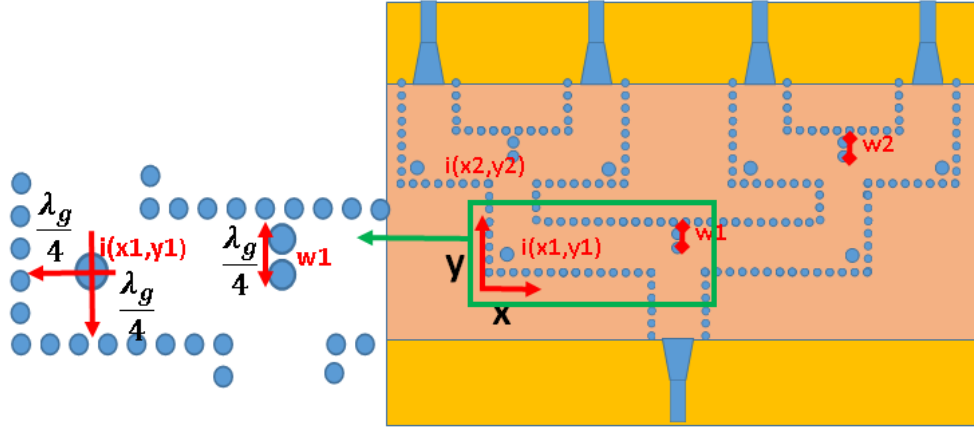
Figure 4.4 Geometry of SIW 1×4 T power splitter © 2018 Wiley. Reprinted with permission

In the first stage, the inductive post position $i(x1, y1)$ is tuned for maximum impedance bandwidth below -10 dB as shown by the green curve in Figure 4.5a. While in the second stage, these results are further improved by tuning both the inductive post position $i(x2, y2)$ and central metallic post "$w2$". This study revealed that the inductive post position $i(x1, y1)$ greatly affects the impedance bandwidth of the splitter whereas input port reflection is more sensitive toward central metallic posts "$w2$". The optimum positions of all inductive posts and common central metallic posts "$w1, w2$" are mentioned in Table 4.4. The parametric study of the S-parameters for both inductive post positions $i(x1, y1)$, $i(x2, y2)$ and the central metallic posts is illustrated in Figure 4.5 to visualize their impact on impedance bandwidth and input reflection. The best design provides a bandwidth of 2.85 GHz from 22.9 GHz to 25.75 GHz with S_{11} below -15 dB and an average insertion loss of 6.78 dB as shown in Figure 4.5b.

4.3.3. One Cross Two Output T Splitter

The simulation model of the 1×2 output T junction required at the output of the 1×8 power splitter is shown in Figure 4.6. The design is tuned to a similar approach in to the 1×2 T power splitter in Section 4.3.1, however here the difference is that the output ports are much closer together. The simulated S-parameters of the 1×2 output T junction are shown in Figure 4.7. The bandwidth of 2.5 GHz from 22.5 GHz to 25 GHz is achieved with S_{11} below -15 dB and an average insertion loss of 3.9 dB. The insertion loss is relatively high, due to extended bent microstrip lines at the output ports which are not inherent to the design but added to create a sufficient space for the 2.4 mm connectors to facilitate measurements, i.e., the distance between two adjacent SIW waveguide channels is 8.3 mm, however, the width of the single 2.4 mm connector is 10 mm.
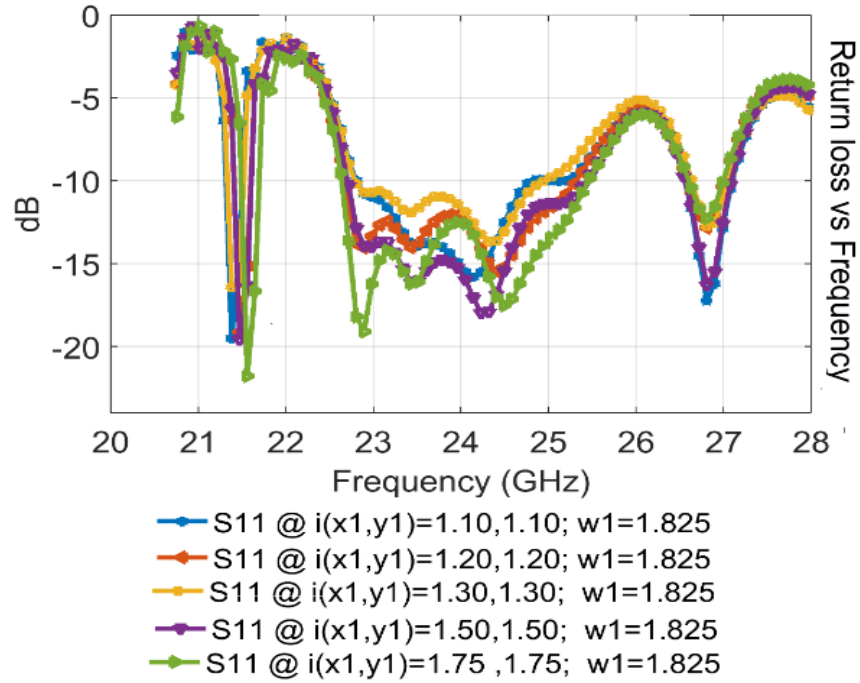
a)
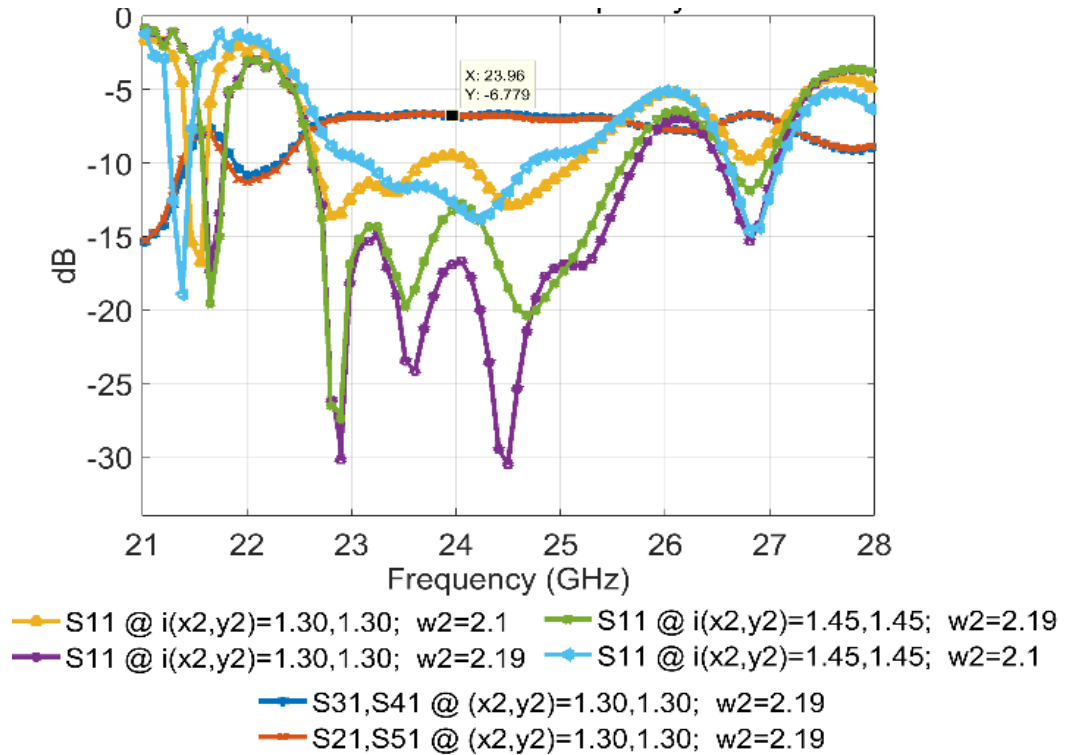
b)

Figure 4.5 a) Parametric study of inductive post position $i(x1, y1)$ for 1×4 T power splitter; b) Parametric study of inductive post position $i(x2, y2)$ and center metallic posts position "$w2$" for 1×4 T power splitter © 2018 Wiley. Reprinted with permission

99
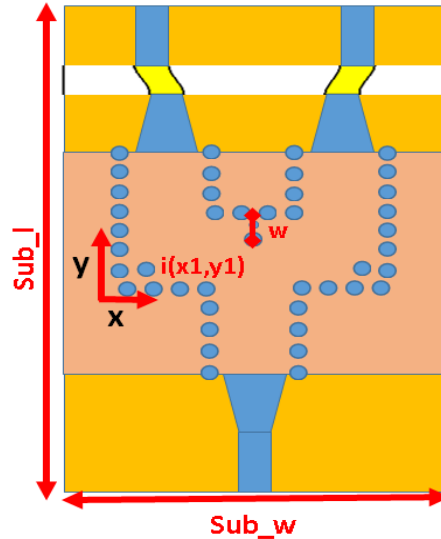
Figure 4.6 Simulation model of 1×2 output T junction with extended microstrip transmission lines © 2018 Wiley. Reprinted with permission

b)
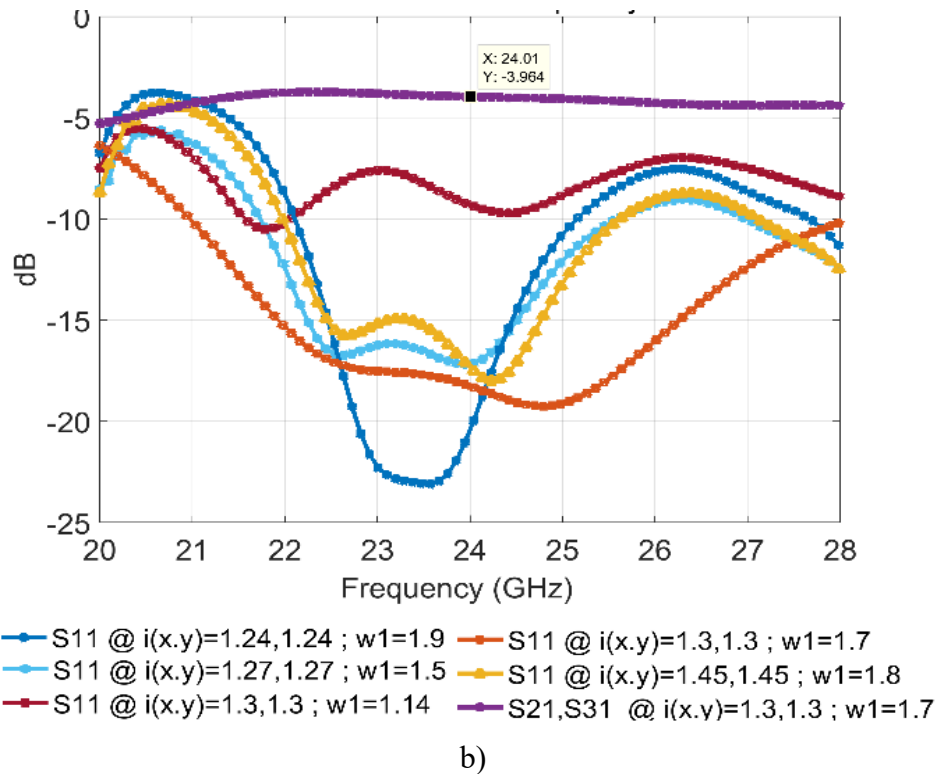
Figure 4.7 Parametric analysis of 1×2 output T junction with extended microstrip transmission lines to facilitate testing © 2018 Wiley. Reprinted with permission

4.3.4. One Cross Eight Power Splitter

The simulated design for the 1×8 power splitter showed in Figure 4.8a, is comprised of a 1×4 T junction and four 1×2 output T junctions. Extensive parametric analysis is performed to remove the mutual interferences of all design segments. The simulated return loss for different parametric

values is shown in Figure 4.8b. The best design with extended bent microstrip lines at the output port has a frequency bandwidth of 3.6 GHz from 22.8 GHz to 26.4GHz, with return loss below -15 dB and average insertion loss of 12 dB across the entire bandwidth.
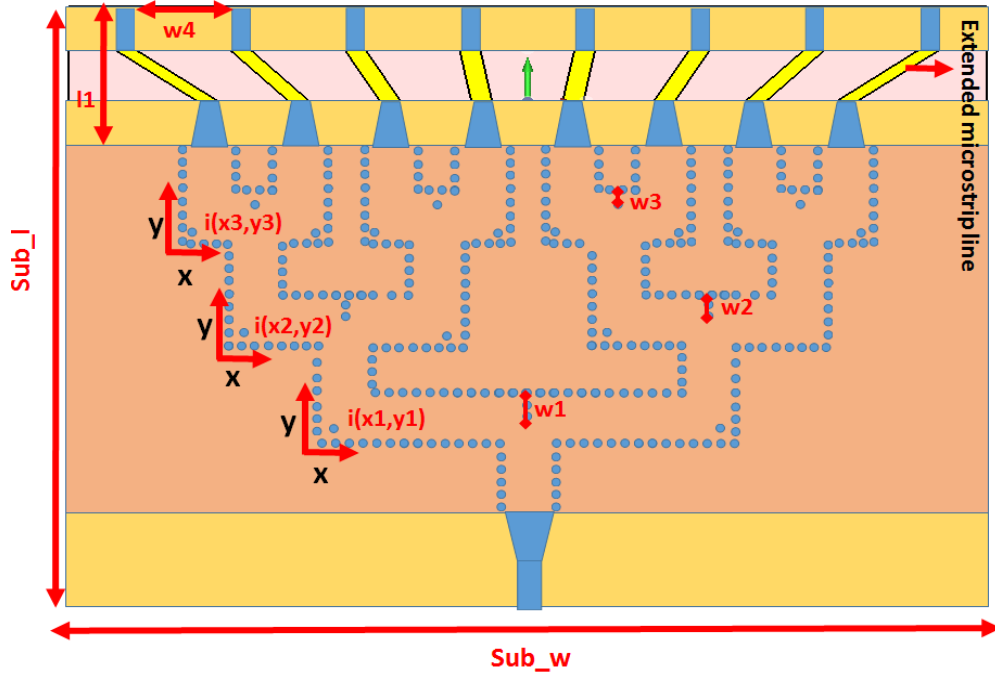
a)
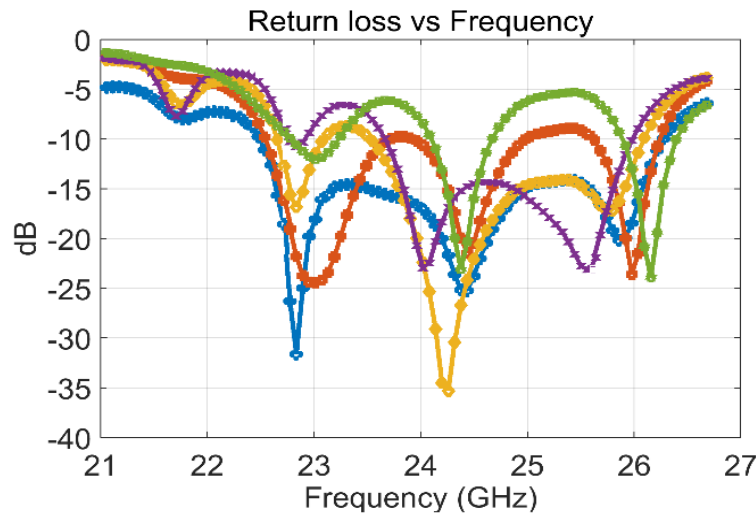
b)

Figure 4.8 a) Geometry of SIW 1×8 power splitter; b) Parametric analysis of return loss for 1×8 power splitter with extended bend microstrip lines © 2018 Wiley. Reprinted with permission

The optimized positions of all inductive post and length of common central metallic posts, i.e., "$w1, w2, w3$" are mentioned in Table 4.4. For all metallic posts, the diameter of 0.8 mm is chosen as it offers minimum reflection at the input port. Most importantly, optimized inductive post positions in terms of guided wavelength are also provided for all design sections as well as the complete 1×8 power splitter, to assist in designing of high-performance mm-wave power splitters. The S_{11} (dB) plot for best design is shown in Figure 4.8, whereas the insertion loss plots are provided in Figure 4.9. The minimum insertion loss at 24 GHz for the extended transmission line design is (10.75±1.4) dB for all 8-output port. This is respectable, considering the ideal 8-way power splitter insertion loss of 9 dB. The extended bent microstrip lines have an average additional 1.75 dB of insertion loss, when compared to the output ports with straight microstrip lines as shown in Figure 4.9. The simulated phase plot, without the extended microstrip lines at each output port, has maximum phase imbalance of $\pm 2.5^{o}$ at 24 GHz as shown in Figure 4.10. A performance comparison between the proposed and some of the previous developed 1×8 power splitters is also given in Table 4.3.
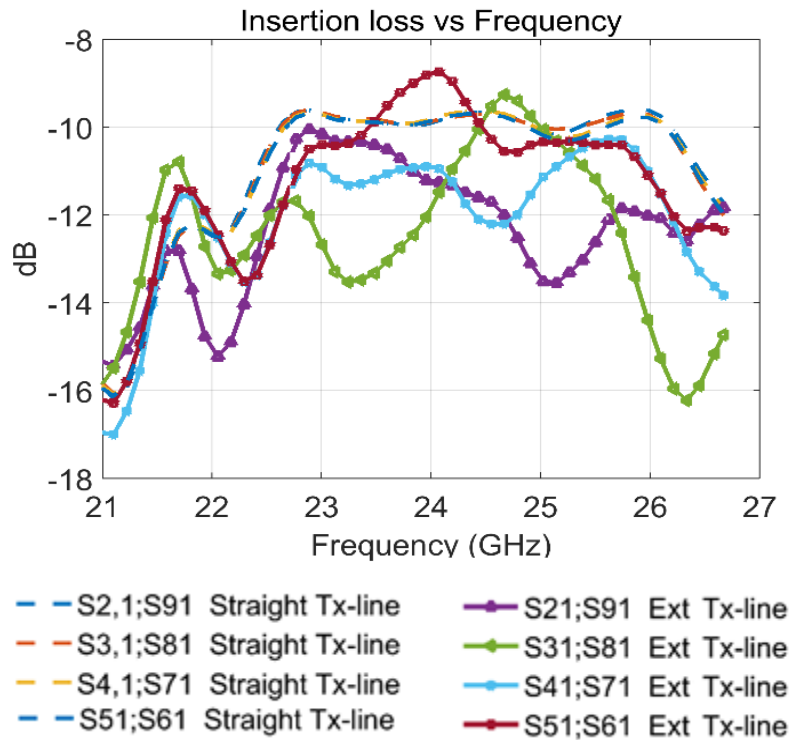
Ext = Extended

Figure 4.9 Insertion loss for 1×8 power splitter, for the case of both non-extended and extended bend microstrip lines © 2018 Wiley. Reprinted with permission

b)
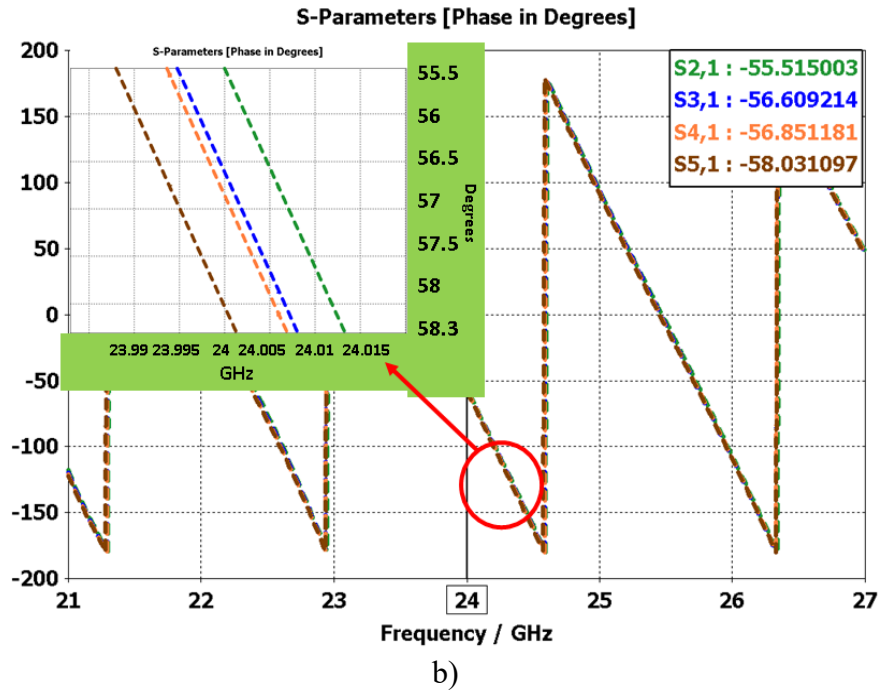
Figure 4.10 Simulated output ports phase for 1×8 power splitter without extended microstrip transmission lines at the output port © 2018 Wiley. Reprinted with permission

Table 4.3 Comparison between proposed 8-way T-splitter and other works

Ref:	Current	[15]	[10]	[4]
Type	SIW	SIW	SIW	SIW
#outputs	8	8	8	16
Frequency-Bandwidth (GHz) S11≤-10 dB	22.6-26.2	8-12	8.5-11.7	10-13.5
Insertion loss(dB)	10.2	10.4	10.8	14.5

To validate the design performance in terms of guided wavelength, the frequency scalability of 1×8 and 1×4 power splitters by a factor of 2 is also displayed in Figure 4.11. The response is quite similar to the preliminary design at the fundamental operating band. The frequency bandwidth is scaled by the same factor from 46 to 50 GHz.
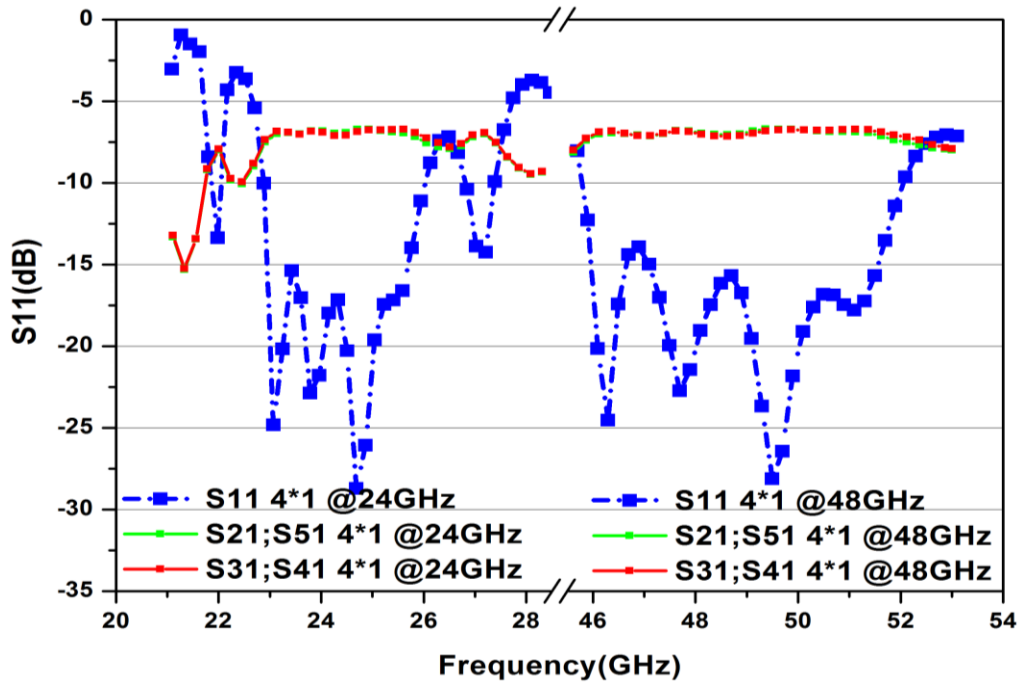
a)
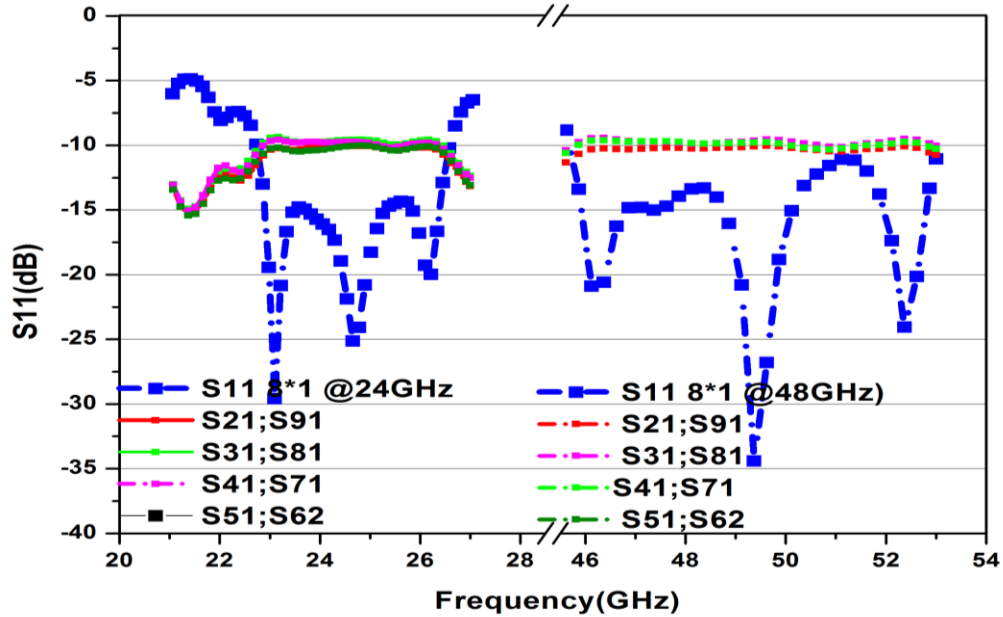
b)

Figure 4.11 Simulated S-parameters for normal and frequency scaled version of a) 1×4; b) 1×8 power splitter © 2018 Wiley. Reprinted with permission

Table 4.4 Optimal design parameters for designing various T power splitters

1 × 2 Input T Junction Parameters (mm)

Sub_l	32		Sub_w	63			
Variables	Initial value	End Value	Iterations	Bandwidth GHz	Goal S_{11}(dB)	Optimal value	λ_g relation in mm
$i(x1,y1)$ post position	1,1	1.5, 1.5	8	22.7-26	≤-15	1.4, 1.4	0.172*λ_g
$w1$	1.5	2	6			1.767	0.217* λ_g

1 × 2 output T Junction Parameters (mm)

Sub_l	32		Sub_w	24			
Variables	Initial value	End Value	Iterations	Bandwidth GHz	S_{11}(dB)	Optimal value	λ_g relation in mm
$i(x1,y1)$ post position	1, 1	2,2	5	22.5-25	≤-15	1.45, 1.45	0.178* λ_g
$w1$	1.5	2.5	5			1.7	0.209* λ_g

1 × 4 T Junction Parameters (mm)

Sub_l	42		Sub_w	63			
Sub_l	Initial value	End Value	Iterations	Bandwidth GHz	S_{11}(dB)	Optimal value	λ_g relation in mm
$i(x1,y1)$ post position	1, 1	1.8, 1.8	8	22.9-25.75	≤-15	1.75, 1.75	0.214* λ_g
$i(x2,y2)$ post position	1, 1	1.4, 1.4	6			1.3, 1.3	0.160* λ_g
$w1$	1.7	2.5, 2.5	5			1.825	0.224* λ_g
$w2$	1.7	2.5,2.5	5			2.19	0.269* λ_g

1 × 8 Power splitter Parameters (mm)

Sub_l	68		Sub_w	52			
$w4$	8.6		$L1$	13.3			
Variables	Initial value	End Value	Iterations	Bandwidth GHz	S_{11}(dB)	Optimal value	λ_g relation in mm
$i(x1,y1)$ post position	1, 1	1.6, 1.6	10	23-26.4	≤-15	1.45, 1.45	0.178* λ_g
$i(x2,y2)$ post position	1, 1	1.4, 1.4	6			1.1, 1.1	0.135* λ_g
$i(x3,y3)$ post position	1, 1	1.4, 1.4	6			1.1, 1.1	0.135* λ_g
$w1$	1.8	3, 3	5			2.8	0.343* λ_g
$w2$	1.8	2.5, 2.5	5			2	0.245* λ_g
$w3$	1	2	5			1.7	0.208* λ_g

4.4. Measured Result and Discussion

To validate the proposed designs, fabrication of all SIW parallel fed power splitters is performed using standard PCB process. All designed structures are realized on Rogers RT-6002 substrate, with

$\in_r = 2.94$, $\tan\delta = 0.0012$ and thickness of 0.762mm. The vias are filled using plated through hole techniques (PTH). The simulated and measured S-parameters for SIW transition and all splitter designs measured are shown in Figure 4.12, Figure 4.13, Figure 4.14, Figure 4.15 and Figure 4.16. The S-parameters are characterized by using Agilent vector network analyzer HP8722ES having operating frequency range of 50 MHz to 40 GHz. The fabricated power dividers and measurement set up is shown in Figure 4.17. 2.4mm connectors are used for S-parameter measurements with all unused ports of the power splitters terminated with 50Ω loads. For the 1×8 power splitter, and the 1×2 T output power splitter, the average insertion losses are found to be 0.8dB and 0.3dB higher than the simulated values. This increased loss is mainly due to the extended lossy microstrip lines at the output ports required to fit the coaxial connectors for testing, and the coaxial connector launch discontinuity, which is not considered in the simulation. The average measured insertion loss for 1×4 T splitter, 1×2 T output splitter, and 1×8 power splitters are 7.2 dB, 4.3 dB and 12.2 dB respectively. More details about the measured results are also provided in Table 4.5.
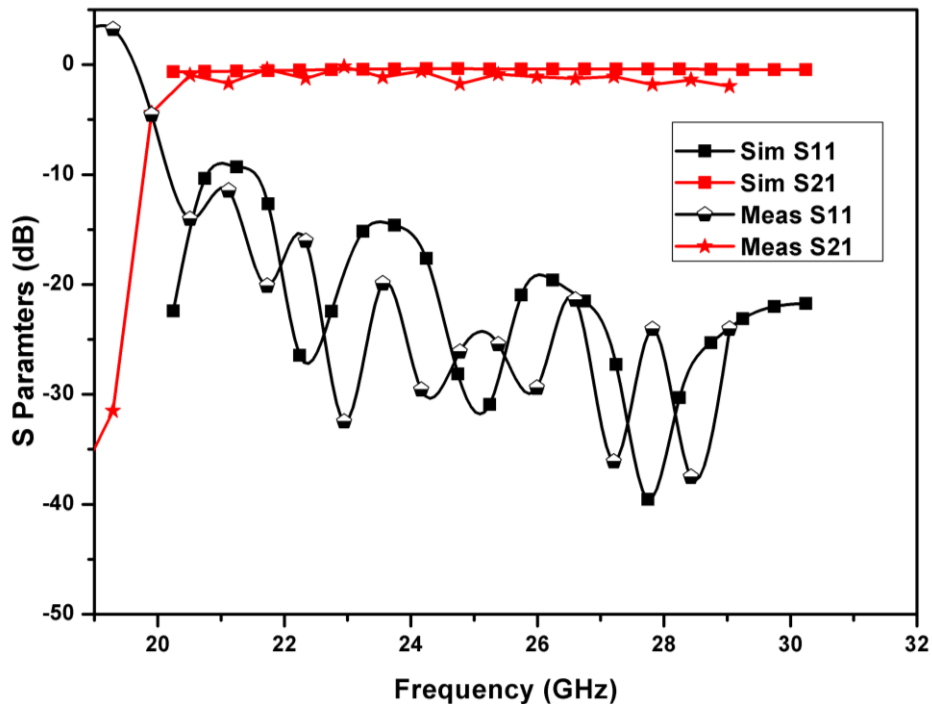
Figure 4.12 Measured and Simulated S parameter results for simple SIW transition © 2018 Wiley. Reprinted with permission © 2018 Wiley. Reprinted with permission
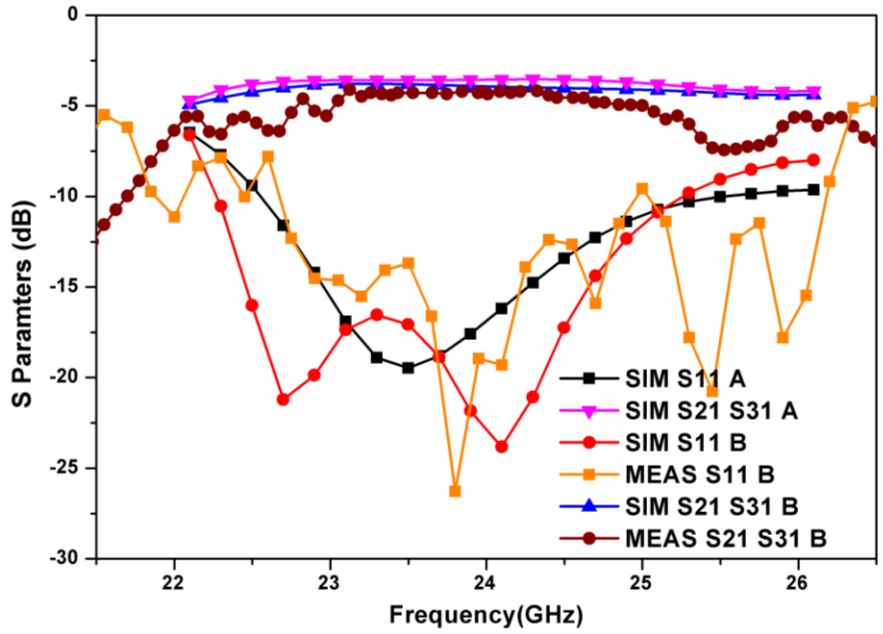
Figure 4.13 Measured and Simulated S parameter results of 1×2 output T power splitter © 2018 Wiley. Reprinted with permission

(*Symbol A represents power splitters without extended transmission lines; Symbol B represents power splitters with extended transmission line)*
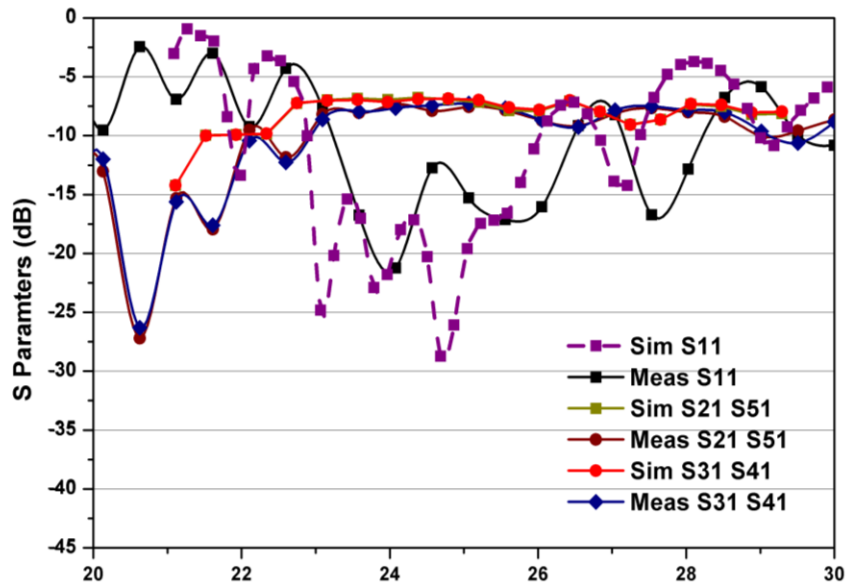
Figure 4.14 Measured and Simulated S parameter results of 1×4 T power splitter © 2018 Wiley. Reprinted with permission
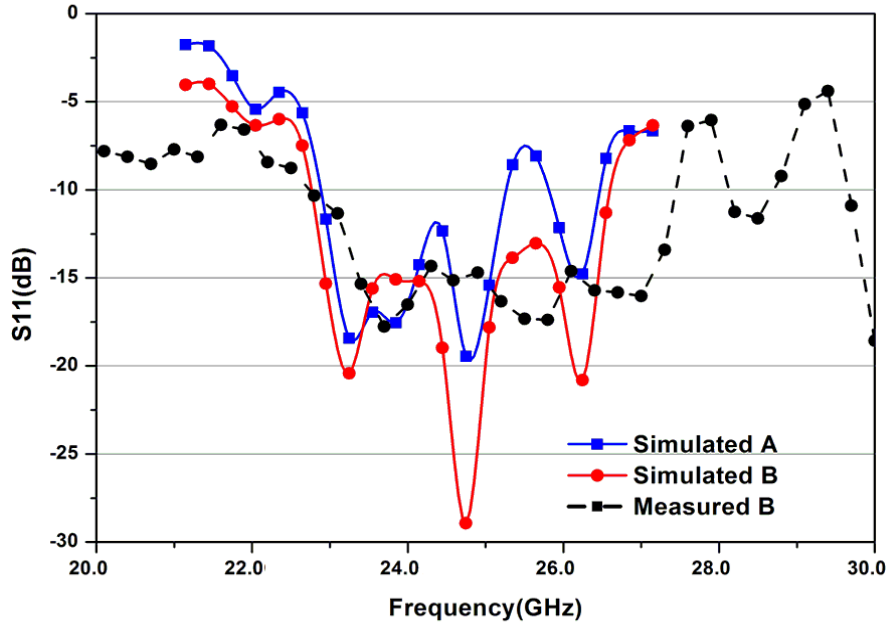
b)

Figure 4.15 Measured and Simulated return loss of 1×8 cross power splitter © 2018 Wiley. Reprinted with permission

(*Symbol A represents power splitters without extended transmission lines; Symbol B represents power splitters with extended transmission line*)
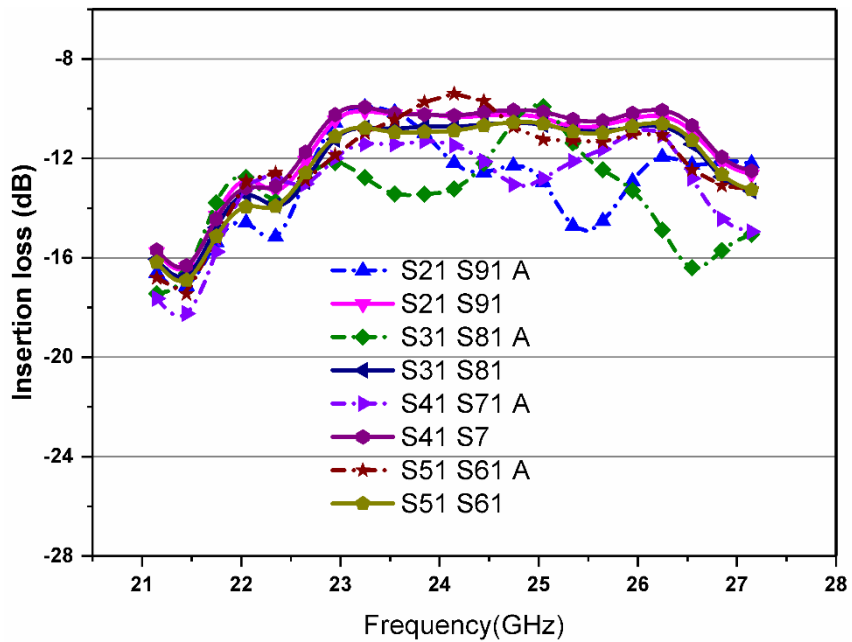
Figure 4.16 Measured and Simulated insertion loss of 1×8 power splitter © 2018 Wiley. Reprinted with permission

(*Symbol A represents power splitters with extended transmission line*)
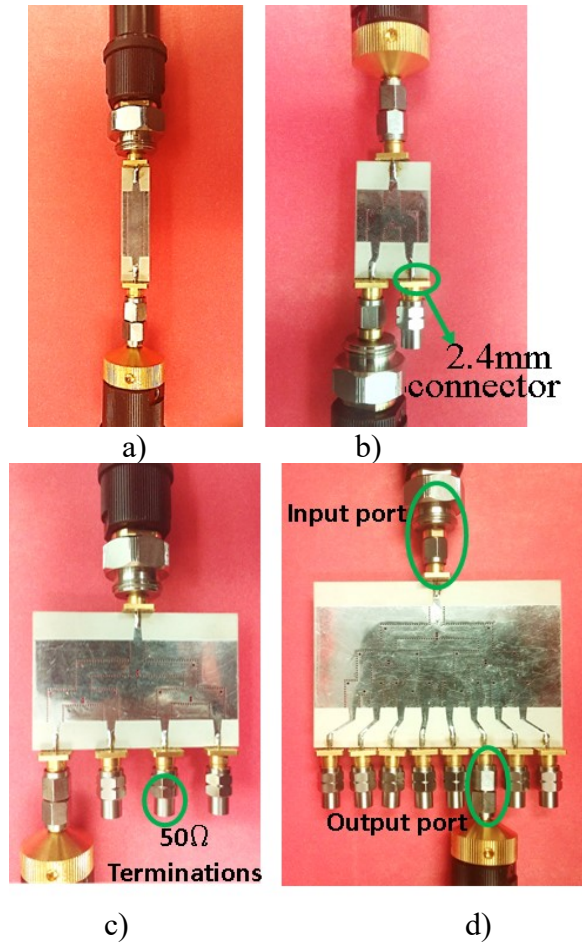
Figure 4.17 Fabricated designs for a) SIW transition; b) 1×2 Y power splitter; c) 1×4 T power splitter; d) 1×8 power splitter © 2018 Wiley. Reprinted with permission

Table 4.5 Measured Results

Component name	Measured parameters in dB @ 24 GHz					
SIW transition	S_{11}	≤-28.3	S_{21}	≤0.9		
1×2-outputT splitter	S_{11}	≤-23	S_{21}; S_{31}	≤4.38 ≤4.38		
1×4-T splitter	S_{11}	≤-21.3	S_{21}; S_{51}	≤7.25 ≤7.25	S_{31}; S_{41}	≤7.25 ≤7.25 .
1×8-T splitter	S_{11}	≤-19.6	S_{21}; S_{91}	≤12.2 ≤12.2	S_{31}; S_{81}	≤12.4 ≤12.4
			S_{41}; S_{71}	≤11.8 ≤11.8 .	S_{51}; S_{61}	≤9.8 ≤9.8 .

4.5. Conclusion

In this chapter, a wideband, 8-way SIW power divider with microstrip line launch is presented. The design is composed of multiple two-stage power dividers. To achieve a wider impedance match, various inductive posts at different locations of T-junctions have been added to minimize the reflections around the corners and smoothing the effect of various discontinuities.

Parametric analysis of the taper width and taper length of the microstrip line is done for improving the transition between the microstrip line and SIW structure. The parametric analysis of various inductive posts positions is also provided to understand the significance of their position and size. All design parameters are tuned for reflection coefficient below -15 dB. For each designed power splitters, guided wavelength relation for various inductive post positions is provided to help in direct designing of high-performance splitters. All simulated designs are validated by prototyping and measurement. The proposed designs are wideband, low profile and can easily be scaled and adapted to realize the GDRA feeds presented in the following chapters.

References

[1]   Y. Yang, C. Zhang, S. Lin, and A. E. Fathy, "Development of an ultra wideband Vivaldi antenna array," in *IEEE Antennas and Propagation Society International Symposium*, 2005, vol. 1A, pp. 606–609.

[2]   R. Kazemi, A. E. Fathy, and R. A. Sadeghzadeh, "Dielectric Rod Antenna Array With Substrate Integrated Waveguide Planar Feed Network for Wideband Applications," *IEEE Trans. Antennas Propag.*, vol. 60, no. 3, pp. 1312–1319, Mar. 2012.

[3]   S. Germain, D. Deslandes, and K. Wu, "Development of substrate integrated waveguide power dividers," in *CCECE-Canadian Conference on Electrical and Computer Engineering*, 2003, vol. 3, pp. 1921–1924.

[4]   Z. Hao *et al.*, "Multiway broadband substrate integrated waveguide (SIW) power divider," in *IEEE Antennas and Propagation Society International Symposium*, 2005, vol. 1A, pp. 639–642.

[5]   K. Gunter, "About the frequency-dependent characteristics of a microstrip-waveguide transition," *Int. J. Electron. Commun.*, vol. 35, pp. 69–71, 1981.

[6]   D. Deslandes and K. Wu, "Analysis and design of current probe transition from grounded

coplanar to substrate integrated rectangular waveguides," *IEEE Trans. Microw. Theory Tech.*, vol. 53, no. 8, pp. 2487–2494, Aug. 2005.

[7]   M. Abdolhamidi, A. Enayati, M. Shahabadi, and R. F Dana, "Wideband Single-Layer DC-Decoupled Substrate Integrated Waveguide (SIW) to Microstrip Transition using an Interdigital Configuration," in *2007 Asia-Pacific Microwave Conference*, 2007, pp. 1–4.

[8]   D. Deslandes, "Design equations for tapered microstrip-to-Substrate Integrated Waveguide transitions," in *IEEE MTT-S International Microwave Symposium*, 2010, pp. 704–707.

[9]   D. M. Pozar, *Microwave engineering*. Wiley, 2012.

[10]   S. Yang, A. Elsherbini, S. Lin, A. E. Fathy, A. Kamel, and H. Elhennawy, "A highly efficient Vivaldi antenna array design on thick substrate and fed by SIW structure with integrated GCPW feed," in *2007 IEEE Antennas and Propagation International Symposium*, 2007, pp. 1985–1988.

[11]   Z. Kordiboroujeni and J. Bornemann, "New Wideband Transition From Microstrip Line to Substrate Integrated Waveguide," *IEEE Trans. Microw. Theory Tech.*, vol. 62, no. 12, pp. 2983–2989, Dec. 2014.

[12]   F. F. He, K. Wu, W. Hong, L. Han, and X. Chen, "A Planar Magic-T Structure Using Substrate Integrated Circuits Concept and its Mixer Applications," *IEEE Trans. Microw. Theory Tech.*, vol. 59, no. 1, pp. 72–79, Jan. 2011.

[13]   H. Esteban, A. Belenguer, J. R. Sanchez, C. Bachiller, and V. E. Boria, "Improved Low Reflection Transition From Microstrip Line to Empty Substrate-Integrated Waveguide," *IEEE Microw. Wirel. Components Lett.*, vol. 27, no. 8, pp. 685–687, Aug. 2017.

[14]   Z. Hao, W. Hong, H. Li, H. Zhang, and K. Wu, "Multiway broadband substrate integrated waveguide (SIW) power divider," in *IEEE Antennas and Propagation Society International Symposium*, 2005, vol. 1A, pp. 639–642.

[15]   R. Kazemi, R. A. Sadeghzadeh, and A. E. Fathy, "Design of a wide band eight-way compact SIW power combiner fed by a low loss GCPW-to-SIW transition," *Prog. Electromagn. Res. C*, vol. 26, pp. 97–110, 2012.

Chapter 5 : Deep X-Ray Lithography Process for Building GDRA Array Layers

5.1.   Introduction

Fabrication of high aspect ratio microstructures and ultra-high precision manufacturing is of great interest in a multitude of applications. Various fields such as robotics, micromechanics, integrated optics and sensors are directly related to this technology. Deep X-ray lithography (DXRL) is one of the unique techniques for obtaining high aspect ratio microstructures (HARMST) with tall vertical sidewalls and optical quality out of Polymethylmethacrylate (PMMA) [1] or SU-8 [2]. DXRL can be combined with electroplating and molding processes and is known by acronym **LIGA**; **LI** for X-ray lithography, **G** for Galvanoformung (German word for galvanic or electroplating) and **A** for Abformung (German word for molding). The use of X-ray lithography in LIGA makes the process highly suitable for producing microstructures with lateral dimensions as small as 200 nm and height of several millimeters [3]. DXRL inherits the advantage of the high degree of collimation of synchrotron radiation light to transfer the mask patterns with ultra-precision into the thick polymer resists. These microstructures can be used as master mold in the subsequent replication steps. The resultant metal, alloy, or plastic products have numerous type of applications [4], [5].

This chapter discusses the deep-X-ray lithography (DXRL) procedure for developing two different low profile GDRA array template layers; i) solid template frame GDRA array layer; ii) strip template frame GDRA array layer. A graphite mask made through precision ultraviolet (UV) laser lithography has been used to expose a 500 μm thick polymethylmethacrylate (PMMA) substrate to realize the GDRAs having micro-structures with an aspect ratio of 10 and high structure quality. The design process flow includes; i) developing X-ray graphite-mask using the UV laser writer, ii) transferring the graphite mask pattern into the 500 μm thick PMMA resist using DXRL; iii) sample development in developer; iv) nickel electroplating the X-ray exposed cavities up to 300 μm to realize the artificial dielectric metal inclusions and lastly, v) dissolving the silicon wafer to extract the final GDRA devices. It is essential to note here that all design steps involved in this fabrication are performed at SyLMAND lab at Canadian Light Source (CLS), Saskatoon. Especially the electroforming of such thick metal structures i.e., 300 μm inside plastic for microwave devices is done for the first time at CLS. The high permittivity GDRA arrays developed

through DXRL provide various advantages over the conventional DRA arrays such as monolithic template frame approach helps in precise alignment between the antenna array elements and the underneath feed structure, wide impedance bandwidth, and stable gain pattern with compact design geometry. The quality of the X-ray mask and developed structures are examined using an optical and a scanning electron microscope (SEM). Moreover, the details of the entire design sequence comprising mask development, sample exposure, sample development, and electroplating are provided.

a)   b)
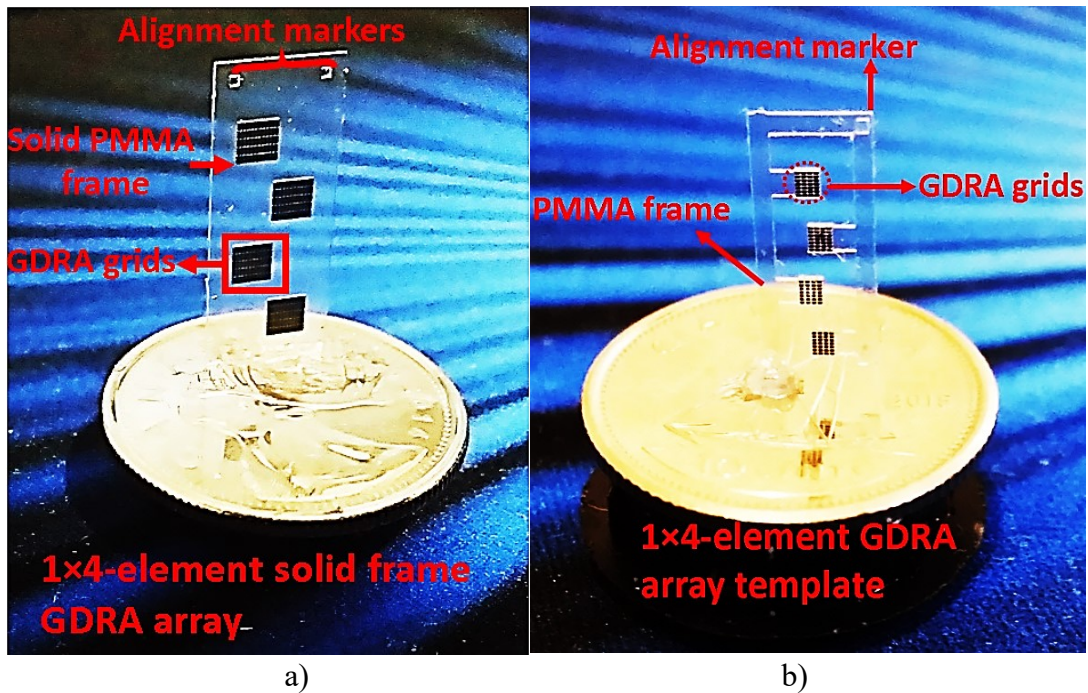
Figure 5.1 a) 4-element solid template frame GDRA array sample; b) 4-element strip template frame GDRA array sample

5.2.   Solid Template Frame vs Strip Template Frame Approach for GDRA Array

A thin monolithic layer of solid template frame GDRA array developed through deep-XRL is shown in Figure 5.1a. It is comprised of a thin layer of polymer PMMA with small groupings of rectangular shaped micro-inclusions as highlighted by *GDRA grids* in Figure 5.1a each of which grouping function as GDRA element. Several of these element clusters in the PMMA frame collectively produce an antenna array effect. This novel solid template frame approach provides various interesting features in comparison to conventional dielectric resonator antennas (DRAs) with large permittivity $\epsilon_r > 15$ such as more compact low-profile antennas. Secondly, the monolithic solid template frame approach facilitates in aligning the individual antenna elements over the feed networks for large antenna arrays, and lastly locally controlling the material

properties such as effective permittivity is possible by using different shape metal inclusions. The second design approach involving a strip template frame layer is shown in Figure 5.1b. The main difference here is the removing the PMMA polymer plastic in-between the adjacent elements of GDRA array to provide high permittivity contrast between the GDRA array adjacent elements to lower the energy coupling through the template frame. Both designs samples are fabricated using a single DXRL graphite mask containing various designs of solid template frame and strip template frame GDRA arrays. Therefore, both design approaches involve the same fabrication sequence from mask to sample development and electroplating. A detailed DXRL fabrication process for both design approaches is presented in Section 5.3. Moreover, the comprehensive electrical performance characterization of designed prototyped devices is demonstrated in Chapter 6 and Chapter 7.

5.3. Fabrication Process
5.3.1. X-Ray Mask Fabrication
A standard X-ray mask is typically comprised of a thin carrier foil of low atomic number material carrying the microfabricated structures of a relatively thick, and high atomic number material [6]. For the carrier foil/membrane materials like titanium (Ti), beryllium (Be), silicon (Si) and compounds having low absorption coefficient, high transparency to X-rays is generally desirable [7], whereas for the absorber structures, materials with high atomic number such as gold are most commonly used. Graphite wafer-based masks that are common for XRL are often low-cost and generally preferred for quick prototyping due to simple fabrication process. Therefore, in this study, a mask made from graphite material was used. The graphite mask offers high X-ray transparency, and low thermal expansion coefficient, which makes it stable for very hard X-rays required for exposing thick resists and allows it to be used for multiple exposures. Moreover, it is physically more rigid and less prone to breaking for multiple exposures then other membranes. Conversely, the graphite masks have also some limitations such as porous surface, side wall striations in the exposed structures and feature sizes restriction to 8μm [8]. However, all of these issues do not greatly impact the required structures for GDRA fabrication. The walls striations as shown in Figure 5.2 are relatively small typically 0.5 to 1μm than compared to GDRA dimensions and hence can easily be ignored and lastly the grids dimensions are much larger than the feature size limitation of 8μm i.e., 50μm is the smallest feature size of the GDRA.
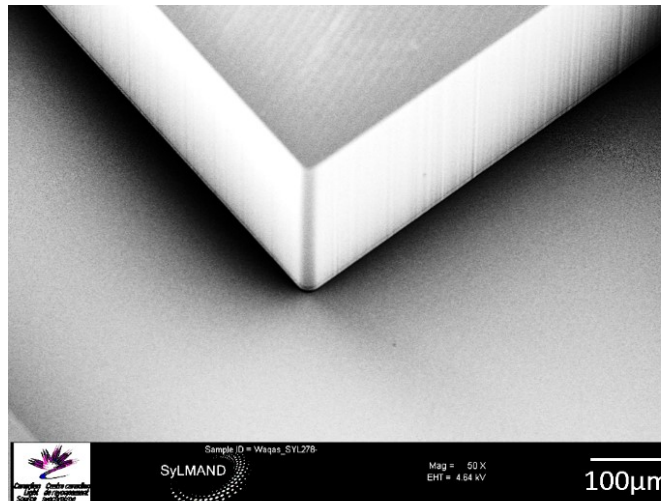
Figure 5.2 SEM image of GDRA array template corner showing vertical side wall quality. Sidewall striations are visible on the upper right-hand sidewall portion.

A two-step mask transfer process has been extensively utilized for producing DXRL masks [9]. The aspect ratio of the intermediate mask is increased in the working XRL mask, providing thicker gold absorbers and resulting in a high contrast mask enabling deep exposures. But the two-step mask fabrication process is costly and time-consuming. Therefore, a single step working mask approach was adapted in this case for a simpler approach for the GDRA arrays, for exposing $500\mu m$ thick PMMA substrate with micro-structures with an aspect ratio of 10. The top surface of the graphite wafer is sealed by layering and flood exposing a thin layer of SU-8 prior to spin coating a thick layer of SU-8 required for writing a design mask image. This thin layer of polymer helps in smoothening the porous surface to avoid absorption of an extra SU-8 polymer into the graphite wafer during the spin coating process. To make the mask the GDRA array pattern is transferred to $50\mu m$ spin coated SU-8 photo resist on the the $250 \mu m$ thick graphite wafer using UV laser lithography. A Heidelberg Instruments DWL 66+ laser writer with a 355nm UV laser and a 10mm write head was used for exposing the GDRA array pattern into SU-8 negative tone photoresist. The irradiated SU-8 cross links and hardens where the polymer is exposed. The remaining polymer was removed by dissolving it in a developer solution. The developed cavities were then electrodeposited with gold to obtain $25\mu m$ gold absorbers to produce a high contrast X-ray mask. Figure 5.3a provides the optical microscope inspection of the single element of the selected GDRA array on a developed graphite mask. The small variation observed between the actual and measured dimensions as summarized in Table 5.2 is caused by diffraction/side wall

slope effect generated during direct writing into $50\mu m$ thick SU-8 resist. Finally, the graphite mask process sequence is presented in Figure 5.3b.
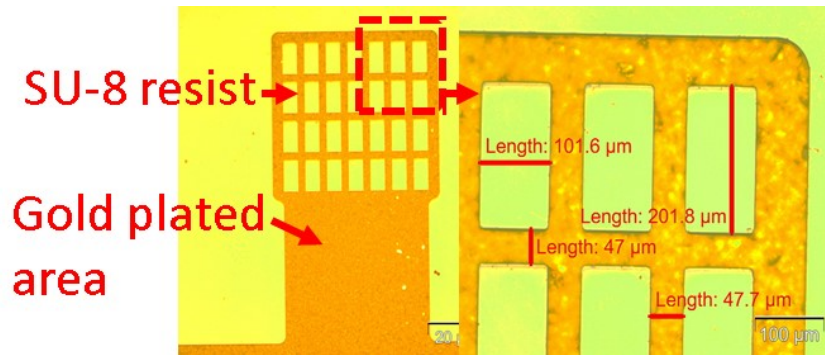
a)

b)

Figure 5.3 a) Optical microscope inspection of the GDRA array element on a graphite mask ; b) Graphite mask process sequence

5.3.2. Sample Exposure

The first step for realizing GDRA arrays is the X-ray exposure of the PMMA resist. A 1.5mm thick PMMA sheet was glued and press-bonded on a sacrificial silicon wafer, coated with a 2.5 μm thick titanium dioxide (TiO$_2$) seed layer to facilitate the electroplating process. The PMMA sample

116

was then fly cut to the height of 0.5 mm and treated with an annealing process to remove the stress from the glue layer introduced during the press bonding process. The graphite mask realized in the preceding section was mounted in the X-ray scanner. A proximity gap of 250 μm was applied between the X-ray mask and the sample exposure to minimize the effect of diffraction, which is the primary contributor to the loss of structural resolution [10]. The X-ray exposure transfers the GDRA array pattern to the PMMA resist to generate the template of the polymer part of the GDRA arrays. Figure 5.4 shows the mask mounted in an X-ray scanner.
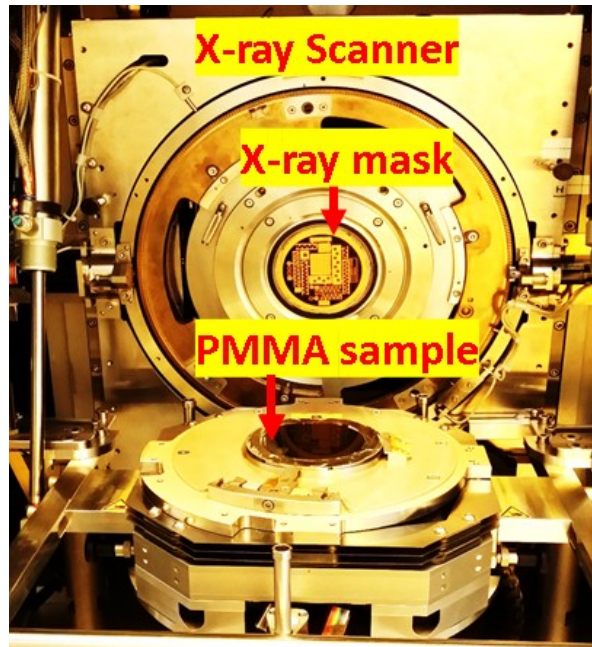
Figure 5.4 X-ray beam scanner with graphite mask and PMMA sample installation (image courtesy of SyLMAND CLS)

Initially, a top to bottom dose ratio of approximately 3:1 with a bottom dose of 3.5 kJ/cm^3 was used for the sample exposure. However, several attempts were made to optimize this dose until the cavities of size $l = 200\ \mu m \times w = 100\ \mu m \times h = 500\ \mu m$ were completely exposed from top to bottom of the resist. A bottom dose value of 4.2 kJ/cm^3 was found to be an appropriate value for complete sample development. The horizontal slits in the beamline were adjusted to limit the X-ray beamwidth to 100 mm, which is the size of the silicon wafer, whereas the vertical slits were kept at 3 mm separation to avoid the X-ray beam vertical height beam spillover within length of the mirrors. i.e., (900 mm) at a low mirror grazing angle of 4 mrad. The lower energy component of the X-ray spectrum is filtered by using 15μm thick aluminum absorber, and the double mirror system tilted an angle of 4 mrad to absorb the higher energy component. The effect of the

absorbers and filters on the power spectrum obtained from the synchrotron radiation source CLS (Canadian Light Source) in Saskatoon (electron energy 2.9 GeV, bending radius 7.1428m) is shown in Figure 5.5. The scanner working chamber is evacuated and then flooded with 100mbar of He to assist in cooling of the mask and substrate. During the exposure, the backside of the wafer sample holder plate was in contact with the thermostatic scanner plate at 19 °C. Moreover, during the experiment, the temperature is monitored using several thermocouples mounted at various points on the scanner. The highest temperature recorded at mask was 27 °C.
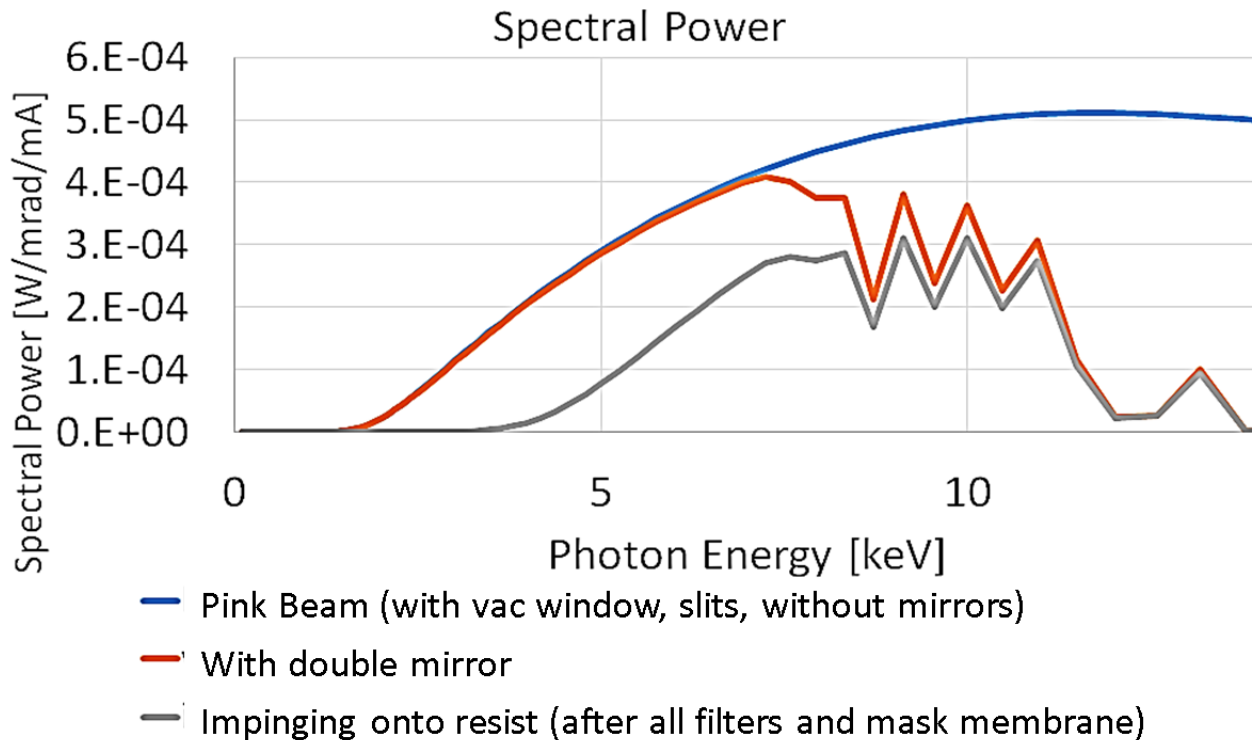
Figure 5.5 Power spectrum from synchrotron radiation source CLS before and after filters and mirror (image courtesy of SyLMAND CLS)

The mask and PMMA substrate surfaces are mounted perpendicular to the synchrotron light beam to avoid any oblique irradiation in the lithography process. During the sample exposure, both the mask and substrate are irradiated by highly intense and collimated synchrotron radiation. The complete and homogeneous dose distribution across the sample is achieved by vertically moving the mask and sample holder through the beam at a constant velocity.

5.3.3. Sample Development

There have been several studies done in XRL [11]–[15] addressing the development of thick irradiated polymers and structures. Some of the critical parameters focused in these studies are the type of the PMMA e.g. crosslinked, non-crosslinked, the developer temperature, the developer type, the synchrotron source (dose rate, mean photon energy), the time between the exposure and the development, the aspect ratio of the microstructures, and the dose deposited which must be taken into account for analyzing the development behavior of any irradiated resist. In the present case, a study on the development of thick resist, i.e., $500\,\mu$m PMMA with different dose distribution supported with stirring and dip development under vacuum has been carried out.

Three samples were exposed and developed at different radiation dose levels for conducting the development study. All three samples are $500\,\mu$m thick. The development was performed immediately after the exposure to utilize the outgassing effect, which increases the transport of PMMA fragments and this effect is not very dominant after a few hours delay between the exposure and development [11]. For comparative study, the same element of the selected GDRA array is considered for all inspections. GG developer [16] was used for performing the development process. Additionally, bath stirring was utilized for enhancing the transport of developer solution into the deep cavities. Several observations were made during the development process. For all samples, at the initialization of the development, a layer of bubbles was noticed on the exposed areas due to the rapid diffusion of the gas. Therefore, each sample was flipped upside down for 15 minutes after an interval of every 2 hours to assist in the release of entrapped gas bubbles and help the flow of fresh developer solution into the small cavities. For all samples, the development process was performed for 15 hours, which is slightly higher than the time normally required for developing exposed resist of same thickness, which is on the order of 10 hours [12]. The main reason for this increased development time is to add an extra safety margin due to the limited transport of the developer solution in small and high aspect ratio cavities, which is not usually incorporated by most of the simulation tools use for estimating the resist development time [17]. The development process for the three samples is summarized in Table 5.1.

At the end of the development process, sample #1 was rinsed with deionized water for inspection. A few residue flakes were observed along the side walls of developed GDRA cavities as shown in Figure 5.6a. Moreover, for a quick development test, the sample was immersed into the nickel-

plating bath to see if plating in all GDRA cavities is initiated, and this plating initiation confirms whether all GDRA cavities are completely developed down to the metal seed layer. Interestingly, all the GDRA cavities were left un-plated in comparison to surrounding large developed areas as shown in Figure 5.6b. The possible reason for the problem is undeveloped residue left inside the deep rectangular cavities, which is difficult to examine under the optical microscope. Therefore, to resolve the issue, sample #2 was exposed with slightly higher bottom dose values, i.e., 4.2 kJ/cm^3 and was processed through similar steps as discussed for sample #1. This time, 16 out of 28 GDRA cavities were plated as shown in Figure 5.6c which confirms the low dose problem for previous sample #1 and secondly in this case, complete development of some of the deep rectangular GDRA cavities. However, still 12 out of 28 cavities were found un-plated. Hence in a further step, sample #3 was exposed with the same dose values as used for sample#2, but with a slightly improved development process. In this case, dip development was performed separately in a vacuum chamber for an hour after every two hours of regular development (i.e., with stirring) in order to assist the evacuation of the gas bubbles trapped inside the deep cavities which prevents the transport of the fresh developer into the cavities, to promote the development process.

Moreover, a plasma descuming [18] was performed to remove any polymer residual layer left along the side walls and masking the plating seed layer surface prohibiting any plating in these areas. During descum process, the developed sample was placed inside the plasma reactor and bombarded with plasma activated oxygen atoms that react vigorously with photoresist at room temperature and hence striping the "organic smear" or thin film of the resist left in developed areas. Finally, a quick plating test was performed to inspect the complete development of the GDRA cavities. Figure 5.6d illustrates the plating initiated in all grid cavities, which validates the significance of the vacuum dip development in enhancing the developer transport into the deep micro-structures and the descum procedure for removing any residual flakes along the GDRA cavities sidewalls and the plating surface of the wafer.

To visualize the structure side wall quality, the SEM images of a 4-element strip frame GDRA array is presented in Figure 5.7. The side walls for GDRA array were found to be quite smooth and vertical. A small striation visible in Figure 5.7b along the sidewalls is the characteristic of the graphite mask [8].
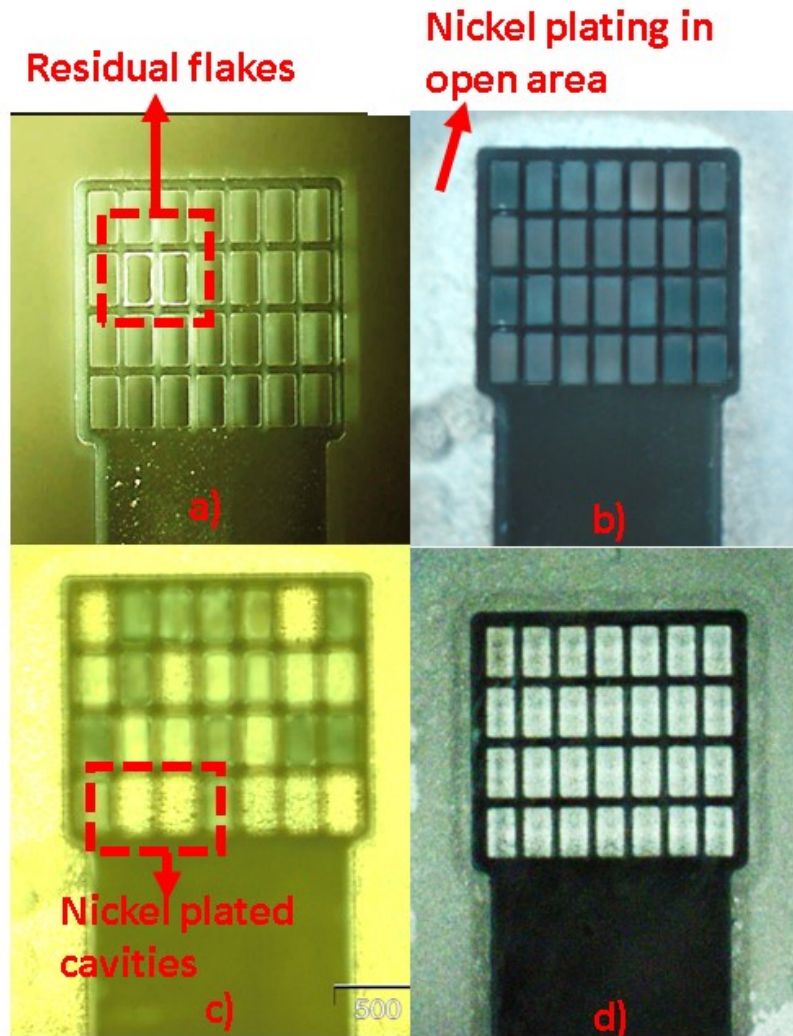
Figure 5.6 Different attempts of the exposure and development process with 3 different samples

Table 5.1 Result of studies related to development of PMMA in high aspect ratio structures

Sample #	Bottom dose (kJ/cm^3)	Development time (hours)	Development condition	Plating test comments
1	3.5	15	Stirring 21 ºC; No vacuum	None of the cavities was plated
2	4.2	15	Stirring 21 ºC; No vacuum	Only a few cavities were plated
3	4.2	15	Stirring 21 ºC; 1-hour dip development in vacuum after every two hours of normal development operation.	All cavities were plated
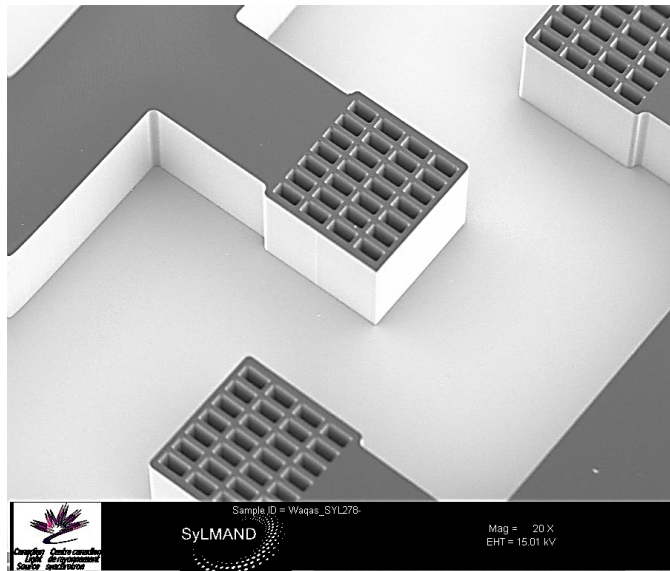
a)
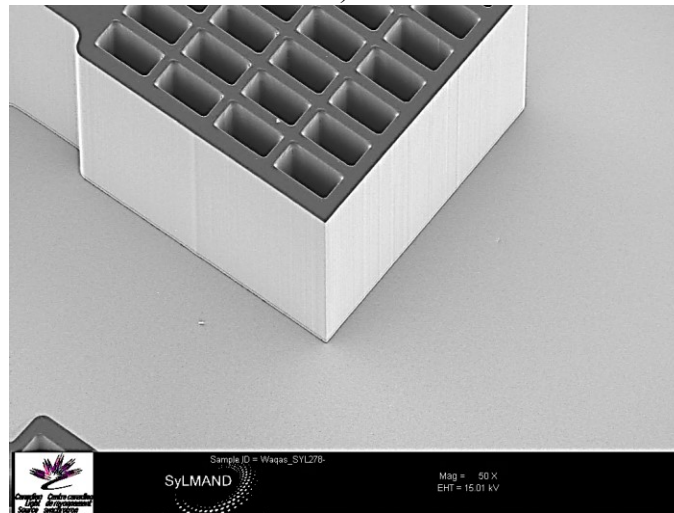
b)

Figure 5.7 a); b) SEM imaging of 4-element GDRA array sample (image courtesy of SyLMAND CLS)

5.4. Electroforming and Structure Releasing

Micro electroforming allows a variety of metal and metal alloys to be utilized for the fabrication of microstructure produce by DXRL. However, the best-known processes are the electroforming of nickel where a metallic nickel layer is being deposited from a chloride-less sulfamate electrolyte, and the electro-deposition of the gold [19]. Other materials, being less frequently used are copper, nickel-cobalt alloy, zinc, and pure iron. Electroforming can provide high dimensional precision, precise reproduction of the surface details i.e., typically fine details of 0.01 μm, production of complex shapes and thin wall components with an extensive range of sizes [20],

122

[21]. However, it also has certain limitations like long deposition time, material restriction, and non-uniform thickness, which may hinder its use as a viable production process [22]. The requirements on the electrodeposition process for defect-free microstructures are high such as the electrolyte should be very pure and free from any kind of impurities like dust or anodic mud, which could possibly cause the formation of hydrogen bubbles that locally inhibit the metal deposition.

In the present case, DisChem nickel plating solution [23] is used for plating PMMA based GDRA deep microstructures through electroforming. The important physical operating parameters for nickel electroforming include the nickel anode for the source of nickel ions, the wafer sample holder, which acts as a cathode, and sulfamate nickel as a conductive electrolyte for transporting nickel ions from anode to cathode. Other processing parameters to control electroforming are the plating solution composition, pH, temperature, additive, and impurity [24].

Above all current density management is the most critical factor for controlling the electrodeposition process for two main reasons. Firstly, it controls the rate of the metal deposition and secondly it must be controlled within the correct operating range to achieve good deposit quality with uniform appearance and free from burning. The actual thickness of nickel at any point on the surface of the cathode depends on the current density at that point i.e., how the current is distributed over the surface of the structure being plated. Specially for nickel electroforming, the current distribution is largely determined by geometric factors such as shape of the cavity to be electroplated, relative placement of the cathode with respect to the anode, and the dimension of the system. In most of the cases, except the simplest shape to be electroplated have prominent surfaces nearer to anode than recessed areas, a uniform thick nickel coating is difficult to achieve. The current density in prominent/open surface areas is greater due to the shorter anode to cathode distance and lower resistance to the current flow. Conversely, recessed areas like the small cavities being further away from the anode and restricted in opening will have less current density because of increased resistance to the current flow. This evidently means, that the plating in the prominent areas will be faster than the recessed ones. Because of the large geometrical influence on the current density at localized areas in the case of nickel electroforming, current distribution is virtually the same as the metal distribution. Thus, auxiliary anode and shields can be used effectively for achieving the uniform thickness over the target surface [20].
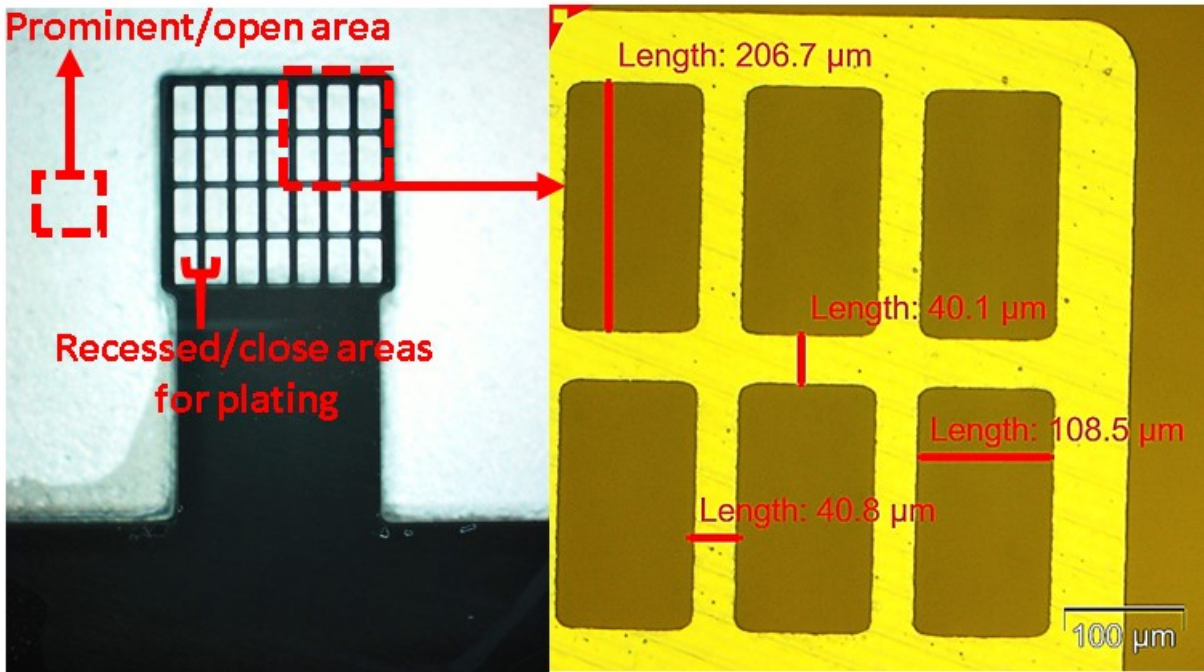
Figure 5.8 Fully nickel plated GDRA element (image courtesy by SyLMAND CLS)

Nickel ions are dissolved in electrolyte and carried and deposited at cathode by DC current operation. The distance selected between anode and cathode was 5cm. On the basis of the calculated plated area, a DC current of 0.22 amperes is chosen to achieve current density of 8mA/cm^2, which is slightly less than the typical requirement of 10mA/cm^2 to attain low internal stress for producing flat plated surfaces [23]. Additionally, the pH of the plating bath was adjusted to 3.72 for achieving optimal plating speed [23]. With the selected plating rate of 0.15 μm/min, the plating height of 300 μm is realized in 28 hours which is comparable to an estimated time of 33.2 hours. The plating thickness in the sample is monitored regularly after every 4 hours using an optical microscope. The plating rate at the center of the wafer was observed faster than the side areas due to the high electric flux density between the parallel faces of anode and cathode. Similarly, the plating rate in prominent surfaces as shown in Figure 5.8 was noticed higher than in recessed small cavities due to large current distribution. This validates the fact that the amount of metal deposit on the surface of any object being plated is proportional to the current that reaches the surface. Consequently, the electrodeposited coating is relatively thick in open/prominent areas and relatively thin in recessed areas. Moreover, to avoid the over-plating at prominent areas the wafer was shielded with PMMA masking tape during sample plating.
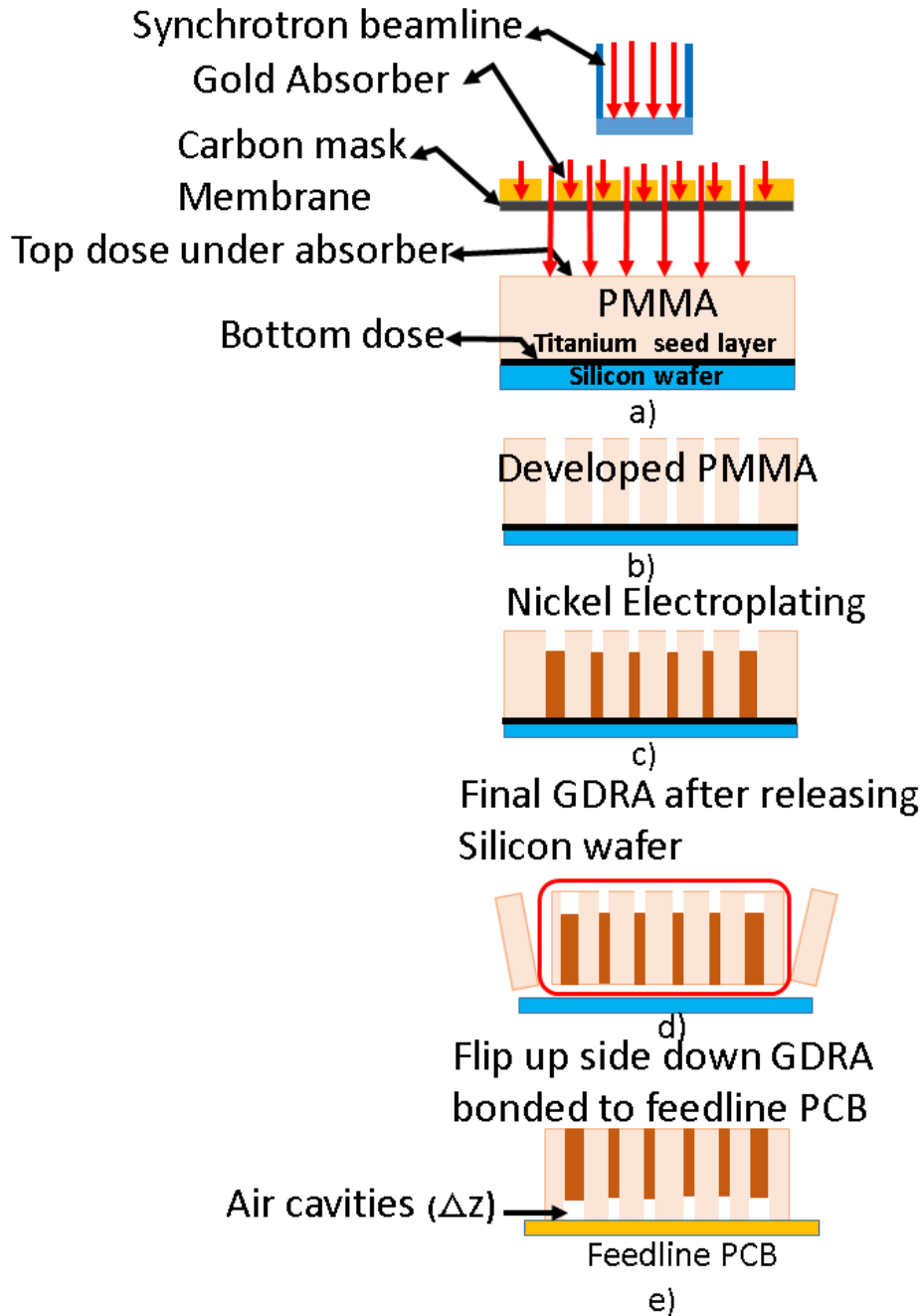
Figure 5.9 Schematic illustration of the GDRA array fabrication using DXRL

The top microscopic view of fully plated cavities in a GDRA array element are presented in Figure 5.8. All cavities are successfully plated with maximum height variation of 50 μm. A complete schematic illustration of the GDRA array fabrication using DXRL is presented in Figure 5.9. The geometry of a single element strip frame GDRA along with design variables is presented in Figure 5.10. Moreover, the comparison between the structural dimensions from mask to plated structures is summarized in Table 5.2. The inclusion x and y gap variations between the graphite mask and

electroplated structures could be the result of various fabrication factors like reduced mask contrast as a result of multiple X-ray exposures, diffraction effect due to large proximity gap of 250 μm in our case which reduces the design features resolution, thermal/ heat load effect due to large dose distribution on the top surface of the PMMA substrate during deep-XRL exposures which tends to increase the expected size of the exposed cavities and consequently reducing the adjacent cavities spacing or the inclusion gaps, secondary dose deposition in areas close to the gold absorbers, and the sample over development due to large development time.
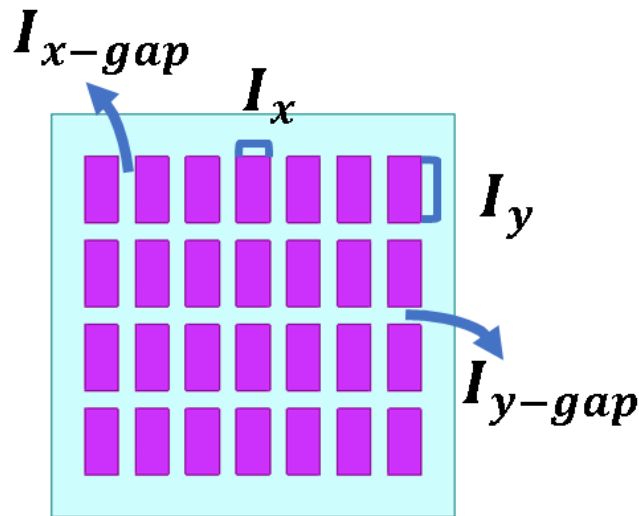

Figure 5.10 Geometry of single element GDRA along with design variables

Table 5.2 Comparison between the GDRA element actual dimensions, on graphite mask and on an electroplated sample.

GDRA sample	Inclusion-width(μm) I_x	Inclusion-length(μm) I_y	Inclusion-x gap(μm) I_{x-gap}	Inclusion- y-gap(μm) I_{y-gap}
Actual dimension	100	200	50	50
On mask	101.6	201.8	47.7	47
On plated sample	108.5	206.7	38	41.1

After finishing the electrodeposition process, the DXRL developed structures are released by dissolving the silicon wafer in KOH bath at 60 ºC and the titanium seed layer by applying Hydrofluoric acid (HF). Finally, the fabricated devices are manually extracted by delicately detaching them from large surrounding plated areas as shown in Figure 5.11. During the process, each GDRA sample is carefully pressed outward from the nickel frame and hence separated from
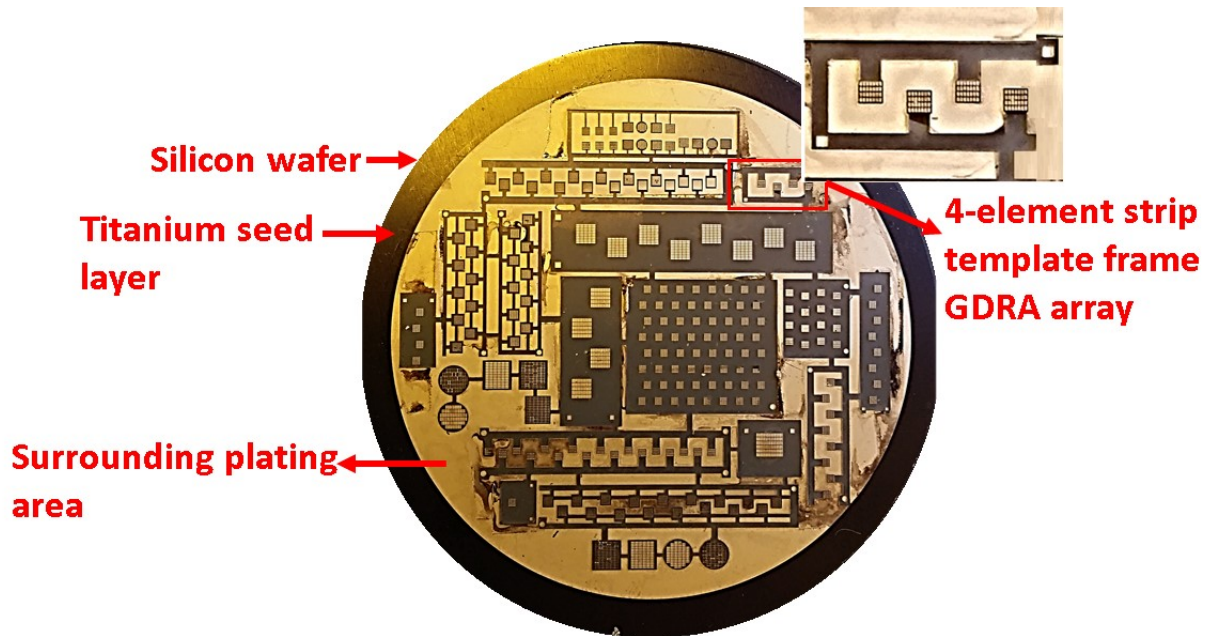
the large metallic surrounding area.

Figure 5.11 Nickel plated sample wafer

5.5. Conclusion

In summary, an X-ray lithographic procedure for fabricating GDRA array template for millimeter-wave application has been presented. A graphite mask built through UV-lithography is utilized for exposing 500 μm thick PMMA substrate using deep-XRL. Different design stages from mask fabrication to sample exposure, development and electroforming are investigated. Performing dip development in the vacuum chamber is found to have significant impact on the development of high aspect ratio irradiated PMMA microstructures by enhancing the fluid transport into the deep cavities. The design performance of both solid template frame and strip template frame GDRA array layers fabricated using DXRL is characterized in Chapter 6 and Chapter 7.

References

[1] E. W. Becker, W. Ehrfeld, P. Hagmann, A. Maner, and D. Münchmeyer, "Fabrication of microstructures with high aspect ratios and great structural heights by synchrotron radiation lithography, galvanoforming, and plastic moulding (LIGA process)," *Microelectron. Eng.*, vol. 4, no. 1, pp. 35–56, May 1986.

[2] L. Singleton *et al.*, "Deep X-ray lithography with the SU-8 resist," *Proc. SPIE, Emerging Lithographic Technologies,* vol. 4343, pp. 182–192, Aug. 2001.

[3]   E. W. Becker *et al.*, "Production of separation-nozzle systems for uranium enrichment by a combination of X-ray lithography and galvanoplastics," *Sci. Nat.*, vol. 69, no. 11, pp. 520–523, Nov. 1982.

[4]   W. Ehrfeld, "The LIGA Process for Microsystems," in *Micro System Technologies 90*, Berlin, Heidelberg: Springer Berlin Heidelberg, 1990, pp. 521–528.

[5]   A. Rogner, J. Eicher, D. Munchmeyer, R.-P. Peters, and J. Mohr, "The LIGA technique-what are the new opportunities," *J. Micromechanics Microengineering*, vol. 2, no. 3, pp. 133–140, Sept. 1992.

[6]   S. Stadler, I. Derhalli, and C. G. Khan Malek, "Cost-effective mask fabrication on Kapton membrane for deep X-ray lithography," *Proc. SPIE, Microlithography and Metrology in Micromachining III*, vol. 3225, pp. 102–108, Sept. 1997.

[7]   C. K. Malek, K. H. Jackson, W. D. Bonivert, and J. Hruby, "Masks for high aspect ratio X-ray lithography," *J. Micromechanics Microengineering*, vol. 6, no. 2, pp. 228–235, June. 1996.

[8]   Y. M. Desta, G. Aigeldinger, K. J. Zanca, P. J. Coane, J. Goettert, and M. C. Murphy, "Fabrication of graphite masks for deep and ultradeep x-ray lithography," *Proc. SPIE, Materials and Device Characterization in Micromachining III*, vol. 4175, p. 122, Aug. 2000.

[9]   W. Ehrfeld, W. Glashauser, D. Münchmeyer, and W. Schelb, "Mask making for synchrotron radiation lithography," *Microelectron. Eng.*, vol. 5, no. 1–4, pp. 463–470, Dec. 1986.

[10]   K. Early, M. L. Schattenburg, D. B. Olster, M. I. Shepard, and H. I. Smith, "Diffraction in proximity X-ray lithography: Comparing theory and experiment for gratings, lines, and spaces," *Microelectron. Eng.*, vol. 17, no. 1–4, pp. 149–152, Mar. 1992.

[11]   P. Meyer, A. El-Kholi, and J. Schulz, "Investigations of the development rate of irradiated PMMA microstructures in deep X-ray lithography," *Microelectron. Eng.*, vol. 63, no. 4, pp. 319–328, Sep. 2002.

[12]   F. J. Pantenburg, S. Achenbach, and J. Mohr, "Influence of developer temperature and resist

material on the structure quality in deep X-ray lithography," *Journal of Vacuum Science & Technology B: Microelectronics and Nanometer Structures Processing, Measurement, and Phenomena,* vol. 16, no. 6, p. 3547, 1998.

[13]   M. X. Tan *et al.*, "PMMA development studies using various synchrotron sources and exposure conditions," *Proc. SPIE, Materials and Device Characterization in Micromachining,* vol. 3512, p. 262, Sept. 1998.

[14]   P. Meyer, A. El-Kholi, J. Mohr, C. Cremers, F. Bouamrane, and S. Megtert, "Development behavior of irradiated foils and microstructures," *Proc. SPIE 3874, Micromachining and Microfabrication Process Technology*, vol. 3874, pp. 312–320, Aug. 1999.

[15]   Y. Hirai, S. Hafizovic, N. Matsuzuka, J. G. Korvink, and O. Tabata, "Validation of X-ray Lithography and Development Simulation System for Moving Mask Deep r-Ray Lithography," *J. Microelectromechanical Syst.*, vol. 15, no. 1, pp. 159–168, Feb. 2006.

[16]   W. Glashauser and G. Ghica, Ger. Pat. 3039110, 1982.

[17]   S. Achenbach, G. Wells, and C. Shen, "Characterization of the surface contamination of deep X-ray lithography mirrors exposed to synchrotron radiation," *J. Synchrotron Radiat.*, vol. 25, no. 3, pp. 729–737, May 2018.

[18]   J. Brcka, "AXIC Application report Photoresist stripping," *Axic X-ray and Plasma equipment,* California, 1996.

[19]   J. A. McGeough, M. C. Leu, K. P. Rajurkar, A. K. M. De Silva, and Q. Liu, "Electroforming Process and Application to Micro/Macro Manufacturing," *CIRP Ann.*, vol. 50, no. 2, pp. 499–514, Jan. 2001.

[20]   M. J. Sole, "Electroforming: Methods, materials, and merchandise," *JOM*, vol. 46, no. 6, pp. 29–35, Jun. 1994.

[21]   M. S. Hussain, "Electroforming a process for macro/nano manufacturing," *Int. J. Nanomanuf.*, vol. 6, no. 1/2/3/4, p. 324, 2010.

[22]   S. Watson, "Modern Electroforming," *Trans. IMF*, vol. 67, no. 1, pp. 89–94, Jan. 1989.

[23]   "Chemistry, Relationships and Trouble Shooting of Optical Media Electroforming Baths

Introduction to Optical Media Stamper Electroforming," *DisChem, Inc.*, 2018. https://www.discheminc.com/uploads/3/4/4/2/34425361/efmp2908_chemistry_and_relatio nships_in_sn_baths.pdf

[24] P. Hernández *et al.*, "Electroforming Applied to Manufacturing of Microcomponents," *Procedia Eng.*, vol. 132, pp. 655–662, Jan. 2015.

Chapter 6 : Low Profile Artificial Grid Dielectric Resonator Antenna (GDRA) Arrays for K_a band Applications

6.1. Introduction

This chapter[6] presents wideband solid template frame grid artificial dielectric resonator antenna (GDRA) arrays at 32 GHz for mm-wave applications. Rather than simply manually assembling individual GDRA elements in an array structure, the entire GDRA array is realized as a thin monolithic polymer layer with all the GDRA elements embedded inside, removing the requirement to assemble and align individual GDRA elements to the feed structure. The antenna array is comprised of a GDRA layer and a substrate integrated waveguide feeding layer. The GDRA array layer is built by embedding thin rectangular metal grid structures in low permittivity dielectric polymethyl methacrylate (PMMA) using a deep-X-ray lithography (DXRL) and electroforming process as described in Chapter 5. The rectangular metallic inclusions significantly increase the effective permittivity of the base material in this case up to 17 by creating high electric flux density regions inside. Low loss SIW feeding with longitudinal slots is utilized to excite the GDRA array layer. A 200μm thin perforated layer of PMMA realized between the rectangular grid structures and the SIW feedlines avoids shorting the metal inclusions to the excitation slots, while improving broadband energy coupling to the GDRA layer. Four element (1×4) and eight element (1×8) GDRA arrays have been fabricated and measured.

6.2. SIW Series Slot Fed GDRA Array

The single element GDRA design with solid template frame and an effective permittivity of 17 as described in Chapter 3, Section 3.5 is used here for building monolithic solid template layer 4-element and 8-element GDRA arrays.

6.2.1. 4-Element Standing Wave Slot Fed GDRA Array

The exploded view of the 4-element GDRA array, series fed through an SIW feeding mechanism is provided in Figure 6.1. Non-resonant longitudinal slots [1], [2] are offset a certain distance from center to provide power control of the excitation amplitude for each element. Also, the slots are used alternatively in opposite sides of the waveguide, which due to the current phase inversion

---

provides in-phase excitation of the alternate array elements [3], resulting in a more compact array structure. The critical design parameters are the slot offset (d_n) from center, the slot gap ($slot\_gap$), and the distance between the last slot and SIW short-circuited wall (W_{sc}). The SIW dimensions, slot length (sl_lg) and the intermediate layer thickness ($\triangle z$) are the same as in Section 3.5 and Table 3.5. The distance W_{sc} is initially set to $\lambda_g /4$ [4] and then further tuned to improve the input reflection coefficient and standing wave phase at the excitation slots.
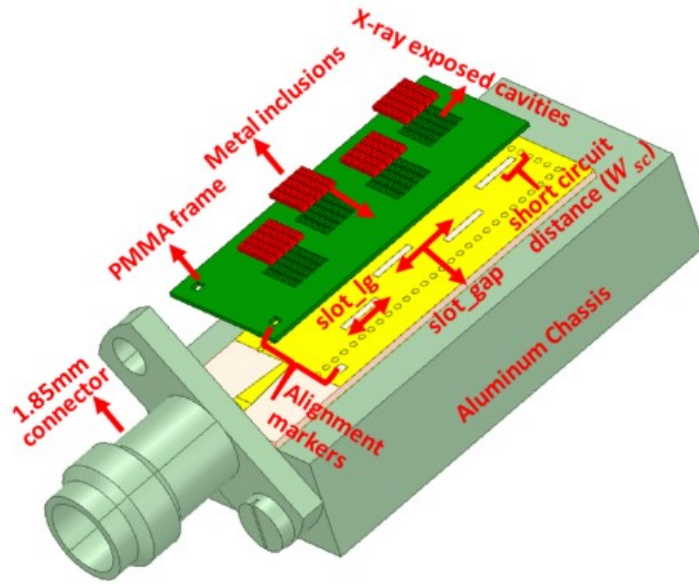

Figure 6.1 Simulation design for 4-element series fed GDRA array © 2019 IEEE. Reprinted with permission.

A narrow slot cut longitudinally into the broadside of the waveguide interrupts x-directed current as shown in Figure 6.2. This interruption in the surface currents causes E-fields inside the slot which act as an excitation source. A slot close to the centerline of the waveguide is near the open circuit point and disrupts a minor amount of current. Conversely, a slot moved from the centerline in the x-direction toward the sides of the waveguide causes large disruption in surface current, and induces strong E-fields across the slot, and high coupling to the antenna layer. Figure 6.2b provides the instantaneous current density on the broad surface of the waveguide for TE_{10} mode, which confirms that the current density is minimum at the center of the waveguide and then increases toward the outer edge of the broadside walls. This increasing energy transfer with slot x-direction position can be used to control power distribution across each antenna element for tailoring the array radiation pattern [5]. In the present study, uniform power distribution [6] across the slots is

132

considered for the 4-element GDRA array. In other words, all slots are placed at the same offset from the center of the SIW channel. The value of the uniform displacement is calculated by expressions [7]–[9] given below:

$$d_n = \frac{a}{\pi} \sqrt{\sin^{-1} \frac{1}{(N*G)}} \tag{6.1}$$

$$G = 2.09 \times \frac{a}{b} \times \frac{\lambda_g}{\lambda_0} \times \left[\cos(0.464\pi \times \frac{\lambda_g}{\lambda_0}) - \cos 0.464\pi \right]^2 \tag{6.2}$$

where a is the SIW width, b is the height of the substrate, N is the number of array elements, G is the normalized slot conductance and λ_g, λ_o are the free space and the guided wavelengths at the design frequency. For $\lambda_g = 8.4$mm in Equation 6.2, d_n is calculated to be 1.2mm.

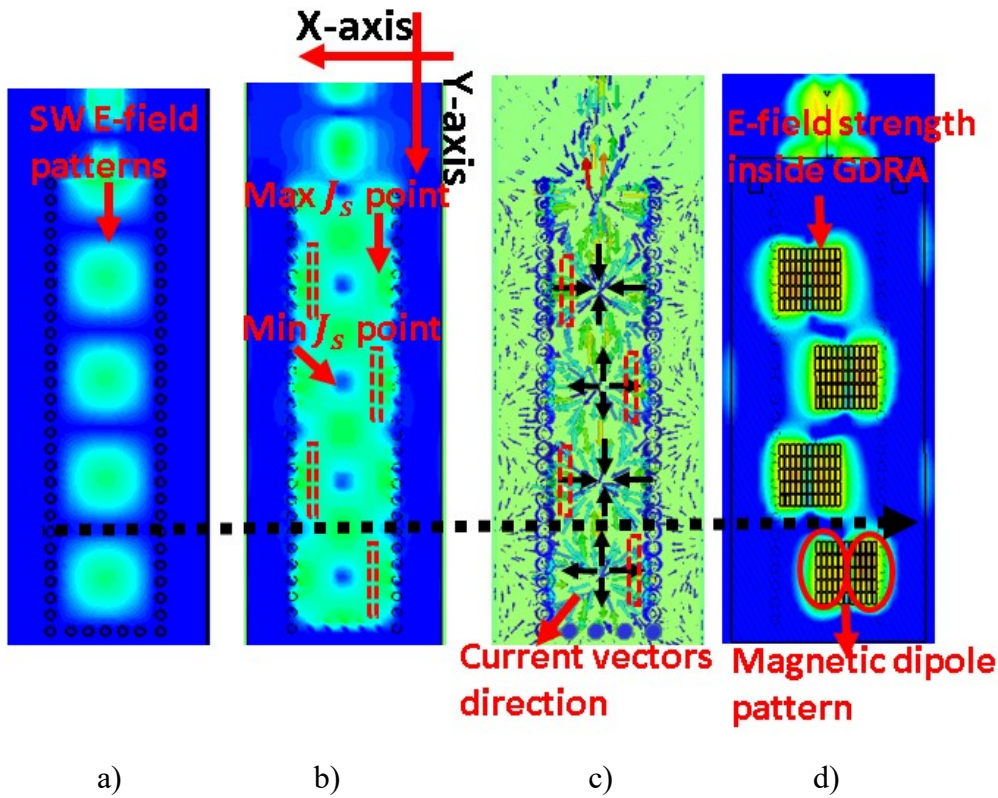

a)   b)   c)   d)

Figure 6.2 a) E-field standing wave pattern in unloaded SIW; b) Current density pattern in unloaded SIW (slots shown for information with $\frac{\lambda_g}{2}$ spacing); c) sketch of the current vectors in unloaded SIW; d) SIW E-field intensity plot in the PMMA template for the 4-element GDRA array © 2019 IEEE. Reprinted with permission.

Due to the current phase inversion shown in Figure 6.2c, slots placed at $\frac{\lambda_g}{2}$ and on opposite sides of the waveguide centerline will be in phase ensuring that all GDRA array elements are fed constructively, producing an antenna array effect.

This slot spacing is also a critical factor in controlling the beamwidth of the array. Element spacing less than $\lambda_g/2$ results in a wider beamwidth, whereas spacing greater than $\lambda_g/2$ offers more compact beamwidth, but with grating lobes in the visible region of the pattern [10]. Moreover, the E-fields of each GDRA element resemble a magnetic dipole-like pattern, similar to a conventional DRA as shown in Figure 6.2d. Therefore, it is expected to generate a similar radiation pattern.
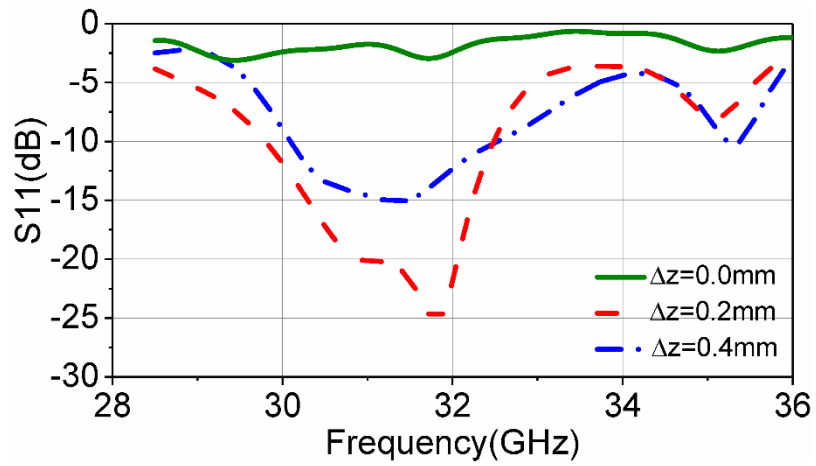
6.2.1.1.   Effect of Intermediate Layer Thickness

GDRAs fed through direct slot contact under the PMMA template can be problematic since the metal grids can short to the feed structures resulting in unpredictable performance, and abrupt impedance variations across the frequency band as shown by the red curve in Figure 6.3a.To avoid this, an intermediate perforated polymer dielectric layer (Δz) is introduced at the GDRA and feeding slot interface. A parametric study of the variable Δz is conducted for a fixed metal grid height ($I_z = 0.3$mm), to analyze its impact on the input impedance and the reflection coefficient of the 4-element GDRA array. Based on the S-parameters provided in Figure 6.3b, at $\Delta z = 0$, there is hardly any energy coupled into the GDRA elements and the shorted GDRA metal grids behave as a reflective surface positioned on top of the longitudinal slots [11]. As the intermediate layer thickness Δz is increased, the input impedance can be adjusted closer to system impedance, improving energy coupling and gain, and increasing impedance bandwidth of the GDRA array as shown in Figure 6.3.
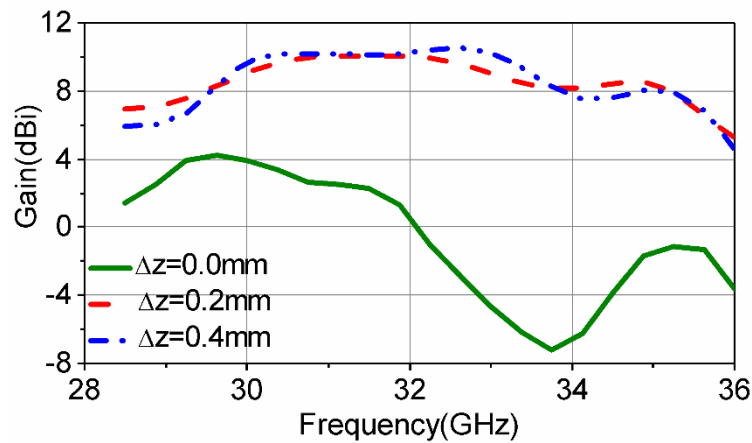
An intermediate layer thickness of $\Delta z = 0.2$mm provides good performance and is chosen for the sample designs. For instance, a -10dB bandwidth of 2.65 GHz centered at 31.2 GHz with peak gain of 10.2 dBi is obtained. This design methodology results in a type of multi-segment resonator structure, where the bottom layer is the lower permittivity intermediate layer and the top layer is the higher permittivity GDRA template. The arrangement has similar effects, particularly in increasing the impedance bandwidth, as with the conventional multi-segment DRA [12].

134
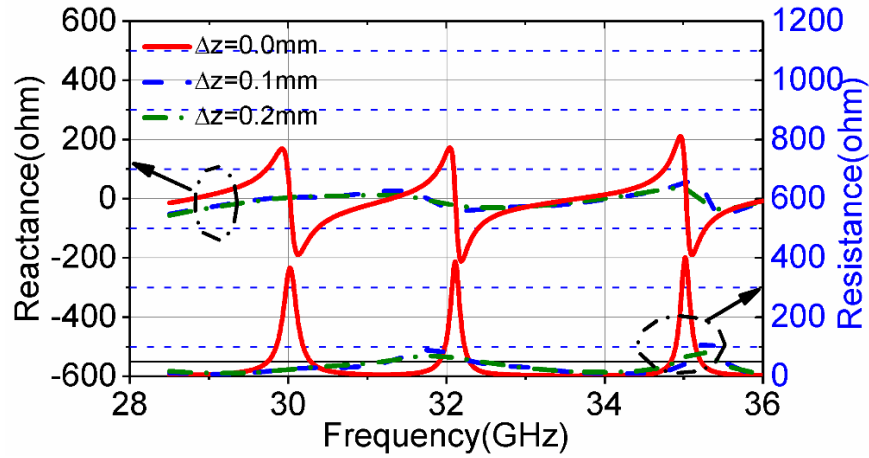
Figure 6.3 Parametric study of the intermediate layer thickness Δz for 4-element GDRA template over a) input impedance variation; b) S-parameters impedance bandwidth; c) Gain performance © 2019 IEEE. Reprinted with permission.

6.2.1.2. Effect of Metal Height

The resonance frequency of the GDRA array can be controlled through the embedded metal grid height (I_z) inside the PMMA template, as shown in Figure 6.4a. Increasing the height of the grid I_z from 0.3 mm to 0.8 mm results in a 6.4% downward shift in the frequency resonance from 31.8 GHz to 29.36 GHz. The gain also improves with increasing grid height, which tends to promote more directed broadside radiation patterns, as shown in Figure 6.4b. This enhancement is also similar to conventional DRAs, where low profile DRAs with height $< \lambda_g/2$ can suffer from low gain due to suboptimal mode excitation. Moreover, Figure 6.4a confirms the non-resonant behavior without the intermediate layer, and also the non-resonant behavior of the slots alone without the multi-segment GDRA layers.
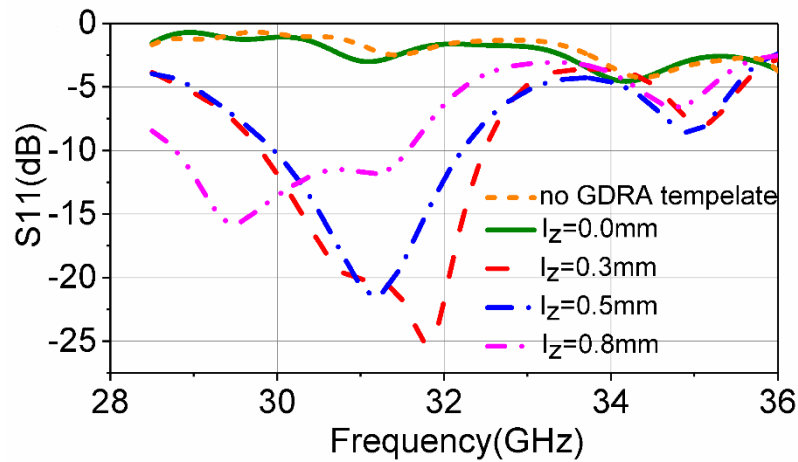
a)
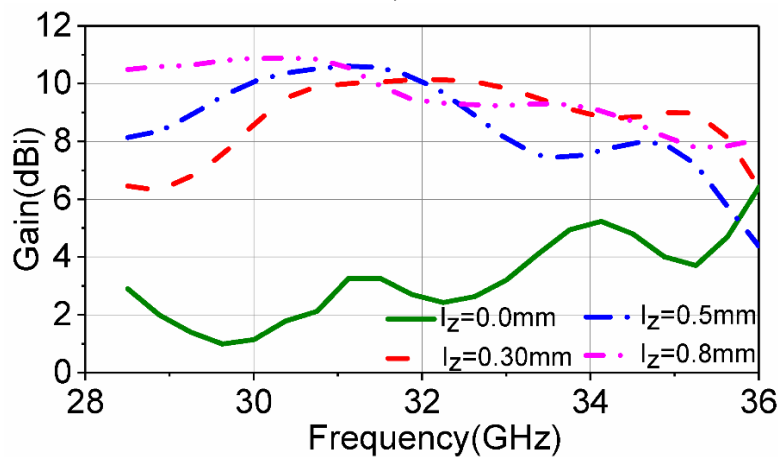
b)

Figure 6.4 Effect of grid inclusion height on 4-element GDRA array: a) impedance bandwidth; b) gain © 2019 IEEE. Reprinted with permission.

6.2.1.3.   Mutual Coupling between Adjacent Elements

Mutual coupling between adjacent GDRA elements is an important factor in array performance, affecting the gain, impedance bandwidth, and efficiency [13], [14]. Two back-to-back embedded GDRA elements are fed through separate feeds to determine the mutual coupling as shown in Figure 6.5, for different template permittivities. As shown in Figure6.6a, the mutual coupling increases by about 3 dB by increasing the template permittivity from 2.5 to 4.2, while the resonant frequency and impedance bandwidth decrease due to an overall increase in the GDRA effective permittivity. Moreover, the increased mutual coupling between adjacent array elements degrades the radiation efficiency, as shown in Figure6.6b. The higher permittivity template frame results in less permittivity contrast between the adjacent GDRAs and consequently more energy flows between the neighboring GDRAs through the template frame as the energy remains more confined in high permittivity dielectric materials.
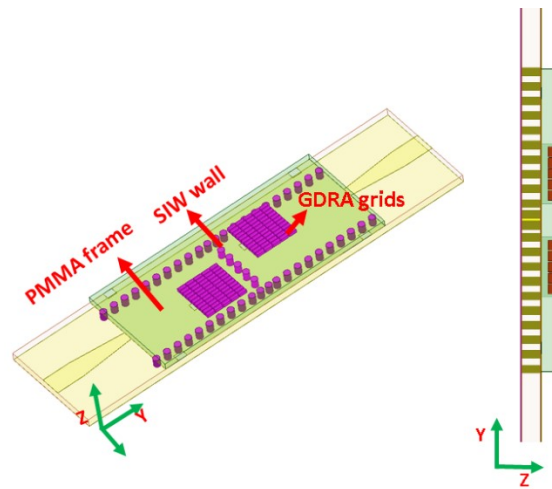

Figure 6.5 Simulation model for adjacent element mutual coupling of embedded GDRA elements © 2019 IEEE. Reprinted with permission.

6.3.   8-Element Standing Wave Slot Fed GDRA Array

An 8-element SIW series fed GDRA array shown in Figure 6.7 is constructed using the same approach as for the 4-element design. Design parameters including the slot length, the slot gap, and the intermediate layer thickness (Δz) remain the same, and uniform slot offsets are determined using Equations (6.1) and (6.2).

Simulated results for an optimized design are presented in Figure 6.8, demonstrating a 10-dB impedance bandwidth of 5.3 GHz from 29.0 to 34.3 GHz, and maximum realized gain of 12.13 dBi.
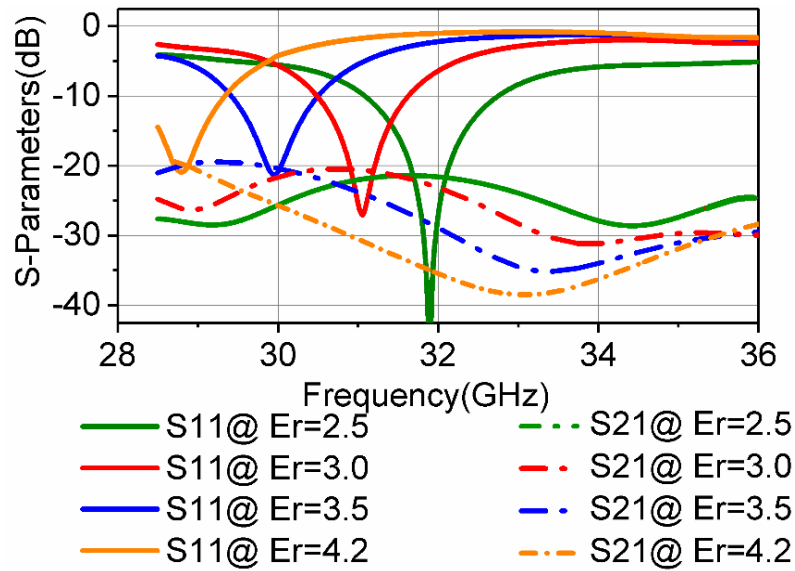
a)
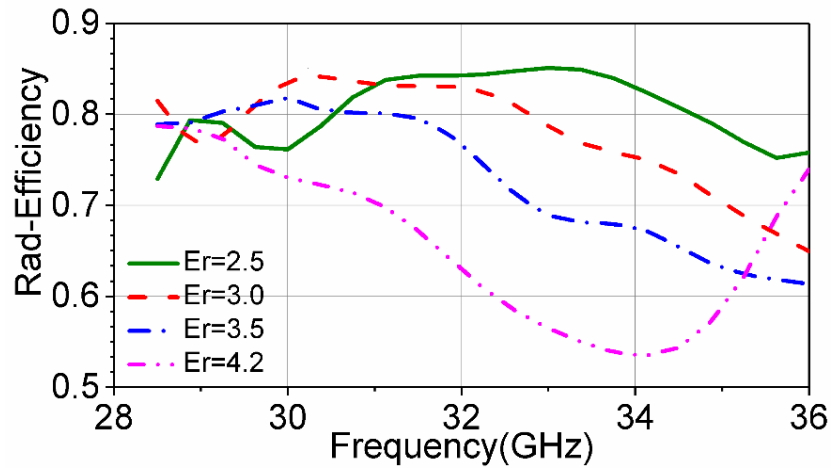
b)

Figure 6.6 a) Effect of template permittivity on mutual coupling and resonance frequency of the GDRA; b) Effect of template permittivity on GDRA radiation efficiency © 2019 IEEE. Reprinted with permission.
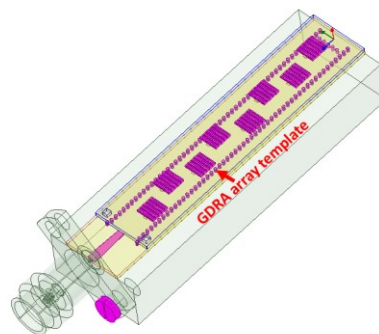

Figure 6.7 Simulation design for 8-element GDRA array © 2019 IEEE. Reprinted with permission.
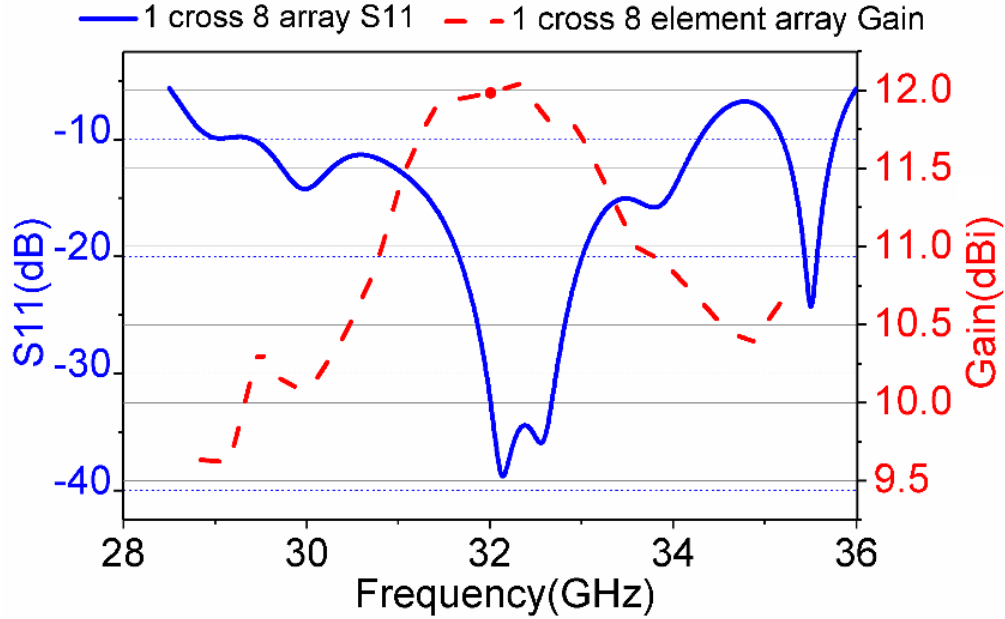
Figure 6.8 Simulated S_{11} and gain for 8-element embedded GDRA array © 2019 IEEE. Reprinted with permission.

6.4. Fabrication and Measurement

The solid template frame fabrication approach as discussed in Chapter 5 is utilized for realizing the series-fed GDRA arrays.

A standard PCB process is used for building the SIW feeding circuits for all designed prototypes on Rogers 6002 substrate with permittivity of 2.95 and a substrate thickness of 0.508 mm. For all circuits, input microstrip lines are excited through two-hole flange mount V-type connectors with customized aluminum chassis as shown in Figure 6.9. All GDRA array templates are bonded under an optical microscope to the feedline structures using a layer of thin silicone adhesive. The S-parameters of the fabricated prototypes are measured over the frequency band of 28 to 36 GHz. All reflection coefficients measured using Agilent vector network analyzer HP8722ES having operating frequency range of 50 MHz to 40 GHz are presented in Figure 6.10a, depicting 4-element, and 8-element SIW series slot fed GDRA arrays with a measured impedance bandwidth of 4.4 GHz from 30.8-35.20 GHz and 5.95 GHz from 29.25-35.20 GHz respectively. However, a frequency offset of 1 GHz is noticed between the simulated and measured results. The reason for this affect is the grid height (I_z) variations produce during the metallization process. The average grid height (I_z) measured at different locations in the template frames for both 4-element and 8-element GDRA arrays is found to be 0.25 mm instead of the simulated value of 0.3mm. Therefore, a separate comparison between the simulated and measured return loss for a grid height I_z=0.25

mm is also provided in Figure 6.10b, which validates the close resemblance between the simulated and measured results. The measured and simulated bandwidth comparison is summarized in Table 6.1.

Simulated and measured co- polarization and cross-polarization responses for 4-element and 8-element GDRA array configurations are illustrated in Figure 6.11 and Figure 6.12 with the maximum broadside gain of 10.2 dBi and 12.13 dBi and cross-pol levels of -25 dB and -22 dB respectively. For a 4-element and 8-element GDRA array, all GDRAs are fed by E-fields in the longitudinal slots in the broadside wall of the SIW. Since the E-cross pol levels are low i.e., below -22 dB, this indicates that the E-field vectors of each slot and GDRA elements are well aligned.

Table 6.1 Comparison between simulated and measured return loss (dB)

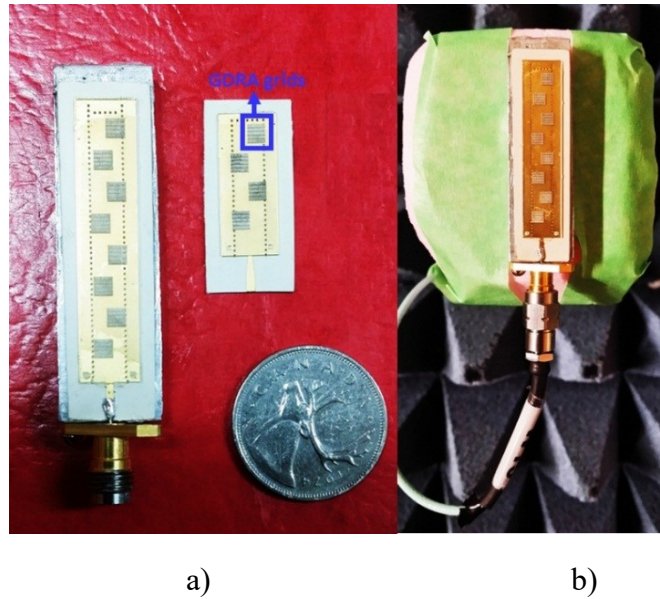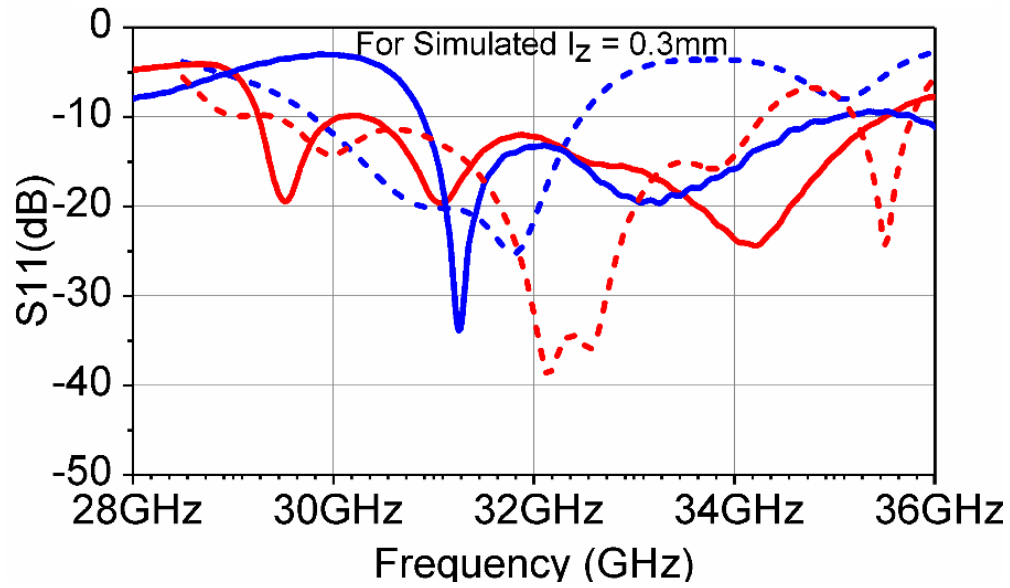| Design	Simulated S_{11}(dB)≤-10 in GHz for I_z= 0.25	Measured S_{11}(dB)≤-10 in GHz	Measured %Bandwidth ≤-10 dB
4-element GDRA array	30.70-33.5	30.80-35.20	13.33%
8-element GDRA array	29.35-35.50	29.25- 35.20	18.46%

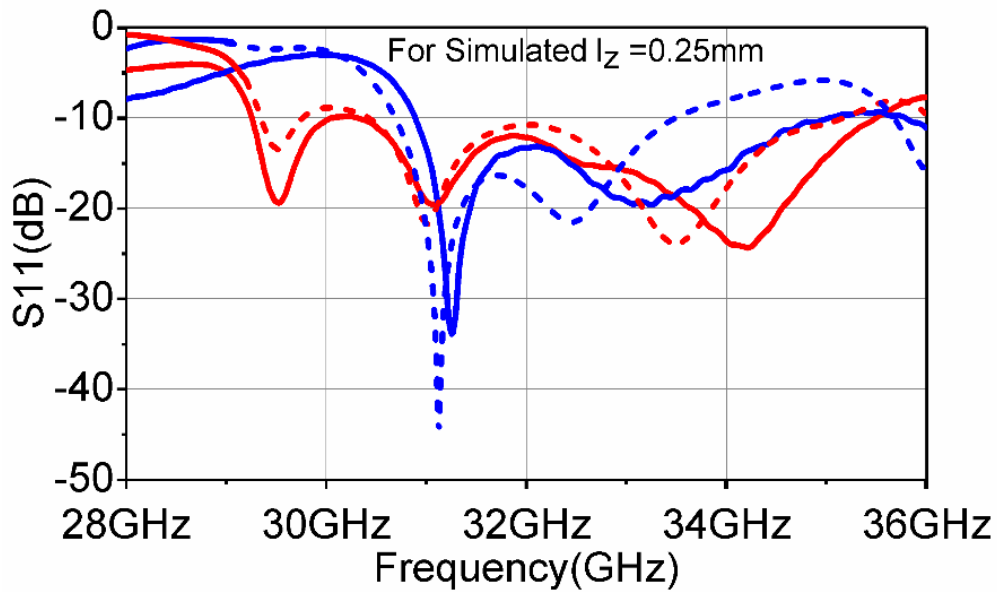a)   b)

Figure 6.9 a) 8-element and 4-element GDRA prototypes; b) 8-element GDRA array mounted on the AUT stage of the spherical measurement system © 2019 IEEE. Reprinted with permission.

Figure 6.10 Simulated and measured S-parameters comparisons for 4-element and 8-element GDRA array: a) for I_z= 0.3 mm; b) for I_z= 0.25 © 2019 IEEE. Reprinted with permission.

The radiation behavior of all antenna prototypes is experimentally characterized through the NSI-700S spherical measurement system. For a 4-element design, the maximum measured broadside gain of 10.05 dBi is observed at 32 GHz. Whereas, for 8-element array design, a maximum far-field gain of 12.02 dB is observed at 32 GHz. The slight variation in the simulated and measured

gain values may be due to reduced coupling energy from the slot to GDRA template because of a small air gap introduced by the silicone glue. Most of the E and H-plane radiation patterns as shown in Figure 6.11 and Figure 6.12 are found to be in good agreement with the simulation results.
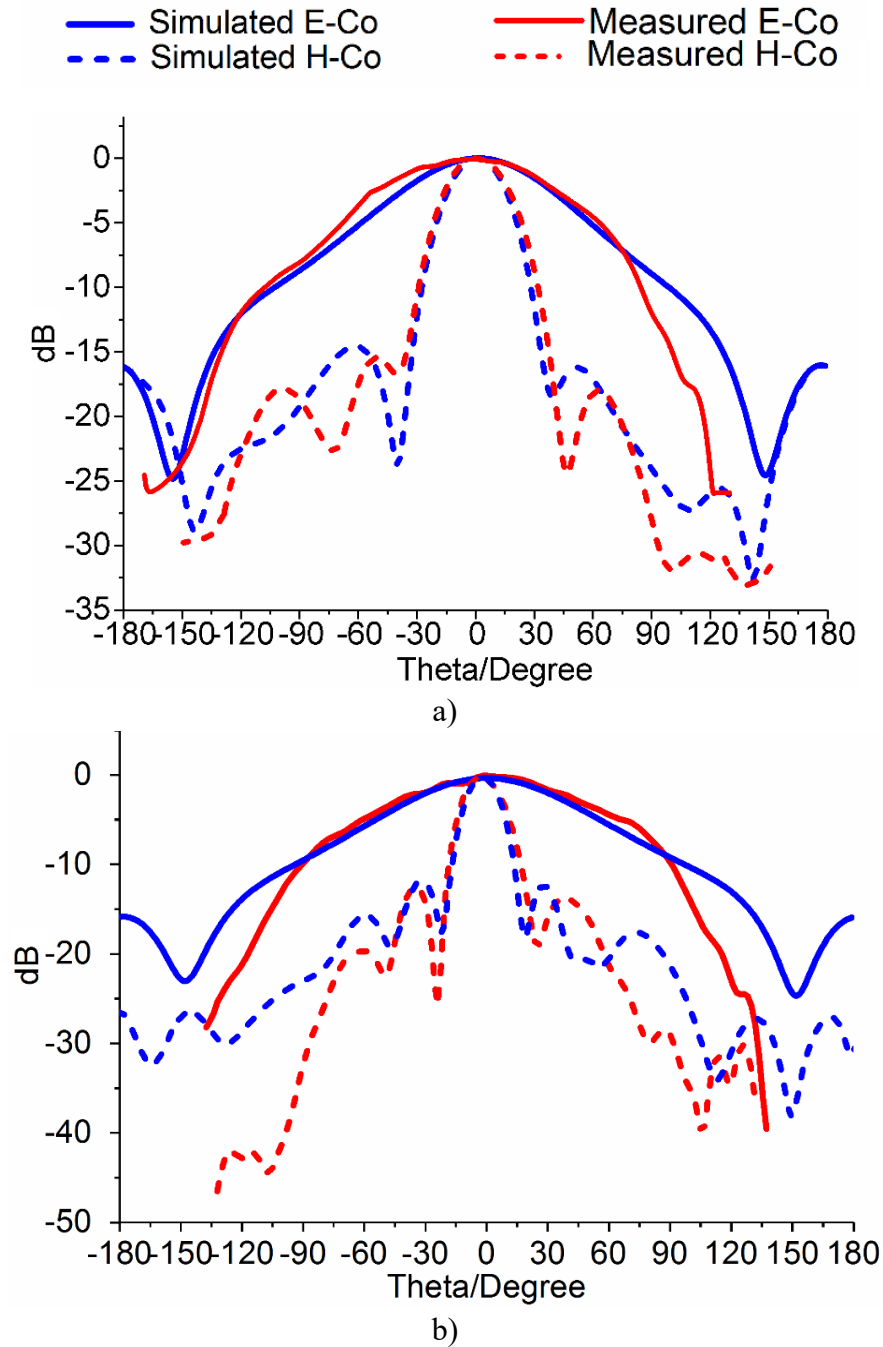

Figure 6.11 Simulated and measured radiation patterns: a) 4-element GDRA array co-pol; b) 8-element GDRA array co-pol © 2019 IEEE. Reprinted with permission.
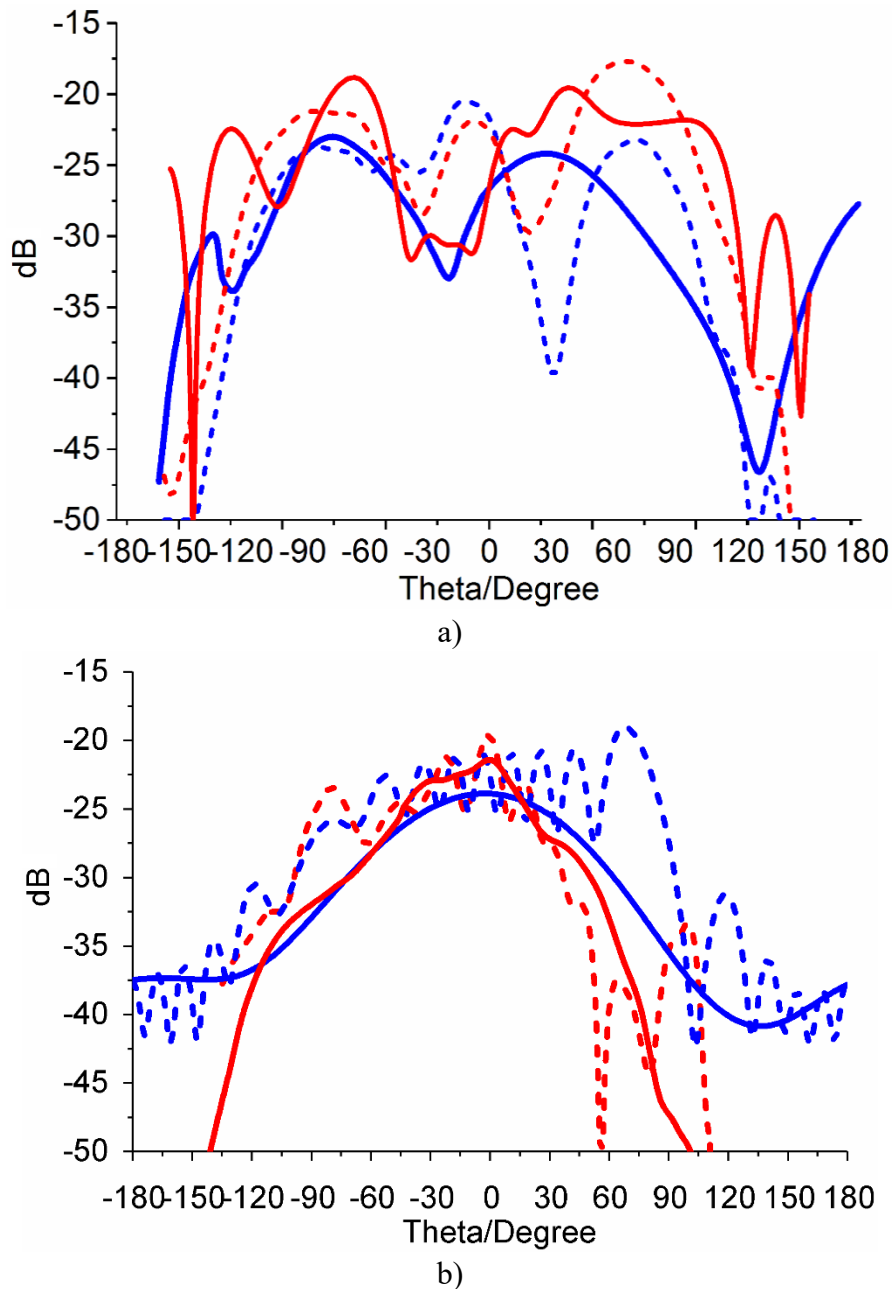
Figure 6.12 Simulated and measured radiation patterns: a) 4-element GDRA array cross-pol; b) 8-element GDRA array cross-pol © 2019 IEEE. Reprinted with permission.

The maximum gain over the design frequency bandwidth presented in Figure 6.13, confirms the gain stability across the bandwidth for all fabricated designs. Moreover, the radiation efficiency measured by comparing the realized gain and directivity ratio is also provided in Figure 6.14. The maximum radiation efficiency of 76.4% is achieved for 8-element GDRA array, validating the GDRA array as a high efficiency antenna at mm-wave frequencies.
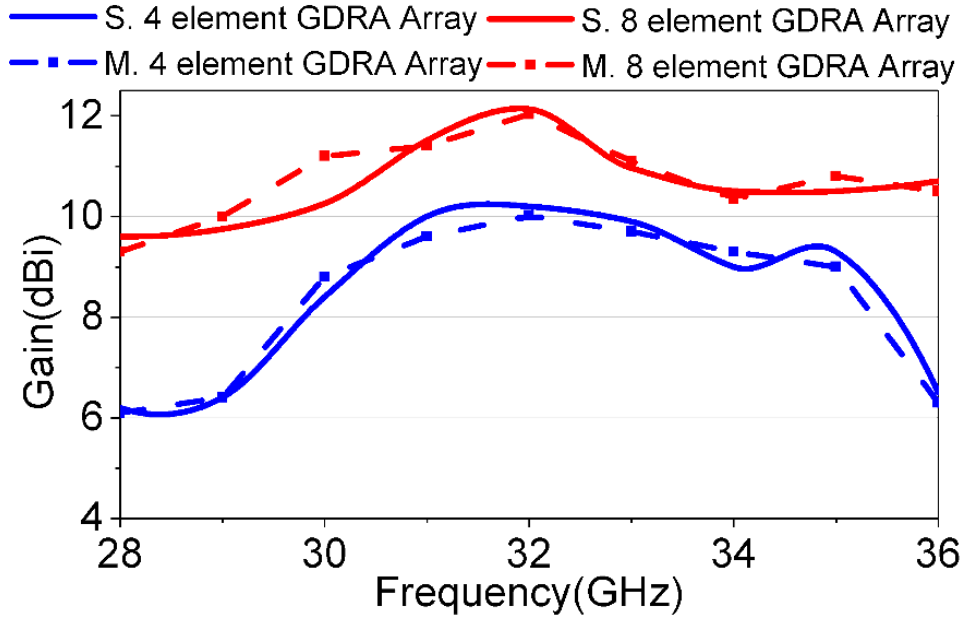
143

Figure 6.13 Simulated and measured gain comparison for 4-element GDRA array, and 8-element GDRA array © 2019 IEEE. Reprinted with permission.

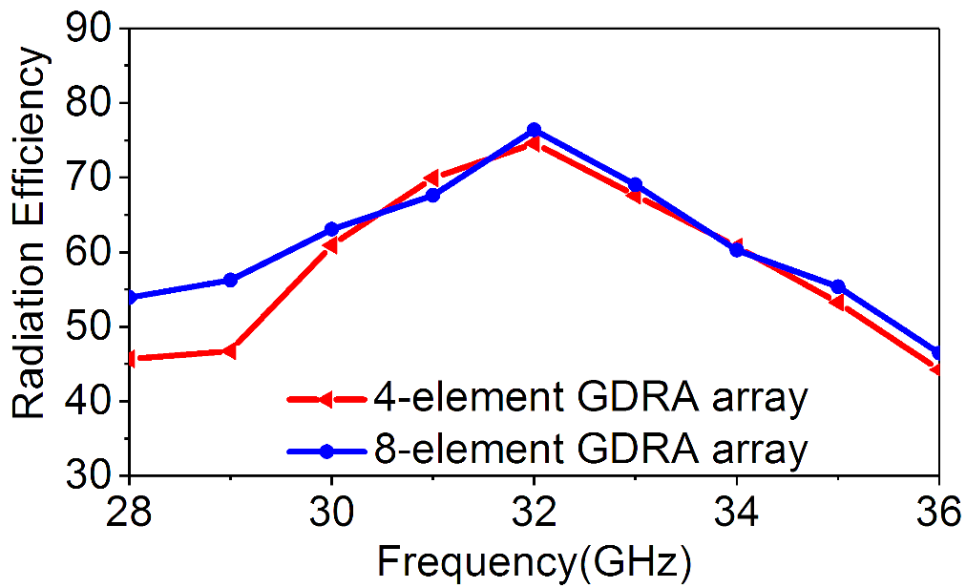Figure 6.14 Measured radiation efficiency for 4-element and 8-elment GDRA array © 2019 IEEE. Reprinted with permission.

6.5.   Conclusion

In this chapter, the potential of the artificial grid DRAs (GDRAs) as an antenna array has been demonstrated. The utilization of the GDRA elements in a single monolithic solid PMMA template array has resulted in a wide-band and an efficient high-gain mm-wave antenna (i.e., radiation

efficiency of 76.4%). The multi-layer GDRA approach provides a more versatile slot feed excitation in contrast to simple narrow band microstrip feeding.

The 8-element array covers a maximum impedance bandwidth of 5.95 GHz from 29.3-35.20 GHz, and has a peak broadside realized gain of 12 dBi. Good agreement between the simulated and measured results endorses them an attractive alternative candidate to conventional dielectric resonator arrays for mm-wave applications. In the next Chapter, this template approach is extended to 2D arrays.

References

[1] K. Gong, X. H. Hu, P. Hu, B. J. Deng, and Y. C. Tu, "A Series-Fed Linear Substrate-Integrated Dielectric Resonator Antenna Array for Millimeter-Wave Applications," *Int. J. Antennas Propag.*, vol. 2018, pp. 1–6, Apr. 2018.

[2] P. Abdulla, Y. K. Singh, and A. Chakrabarty, "Coupling enhancement of waveguide-fed dielectric resonator antenna," *Microw. Opt. Technol. Lett.*, vol. 53, no. 4, pp. 769–770, Apr. 2011.

[3] W. M. Wahab, D. Busuioc, and S. S-Naeini, "Millimeter-Wave High Radiation Efficiency Planar Waveguide Series-Fed Dielectric Resonator Antenna (DRA) Array: Analysis, Design, and Measurements," *IEEE Trans. Antennas Propag.*, vol. 59, no. 8, pp. 2834–2843, Aug. 2011.

[4] W. M. Wahab, D. Busuioc, and S. S-Naeini, "Low Cost Planar Waveguide Technology-Based Dielectric Resonator Antenna (DRA) for Millimeter-Wave Applications: Analysis, Design, and Fabrication," *IEEE Trans. Antennas Propag.*, vol. 58, no. 8, pp. 2499–2507, Aug. 2010.

[5] H. J. Visser, *Array and phased array antenna basics*. Wiley, 2005.

[6] H. M. El Misilmani, M. Al-Husseini, and K. Y. Kabalan, "Design of Slotted Waveguide Antennas with Low Sidelobes for High Power Microwave Applications," Prog. Electromagn. Res. C, vol. 56, pp. 15–28, 2015.

[7] W. Coburn *et al.*, "A Slotted-Waveguide Array for High-Power Microwave Transmission," , Army Research Laboratory, 2001.

[8]   A. F. Stevenson, "Theory of Slots in Rectangular Wave-Guides," *J. Appl. Phys.*, vol. 19, no. 1, pp. 24–38, Jan. 1948.

[9]   K. L. Hung and H. T Chou, "A design of slotted waveguide antenna array operated at X-band," in *2010 IEEE International Conference on Wireless Information Technology and Systems*, 2010, pp. 1–4.

[10]   R. C. Hansen, *Phased array antennas*. Wiley, 2009.

[11]   W. Mazhar, D. M. Klymyshyn, M. T. Aligodarz, S. Ganguly, A. A. Qureshi, and M. Boerner, "CPW fed grid dielectric resonator antennas with enhanced gain and bandwidth," *Int. J. RF Microw. Comput. Eng.*, vol. 29, no. 3, p. e21639, Mar. 2019.

[12]   A. Petosa, N. Simons, R. Siushansian, A. Ittipiboon, and M. Cuhaci, "Design and analysis of multisegment dielectric resonator antennas," *IEEE Trans. Antennas Propag.*, vol. 48, no. 5, pp. 738–742, May 2000.

[13]   A. Ludwig, "Mutual coupling, gain and directivity of an array of two identical antennas," *IEEE Trans. Antennas Propag.*, vol. 24, no. 6, pp. 837–841, Nov. 1976.

[14]   I. Gupta and A. Ksienski, "Effect of mutual coupling on the performance of adaptive arrays," *IEEE Trans. Antennas Propag.*, vol. 31, no. 5, pp. 785–791, Sep. 1983.

Chapter 7 : 60 GHz Substrate Integrated Waveguide fed Monolithic Grid Dielectric Resonator Antenna Arrays

7.1.   Introduction

In this chapter[7] the two different design approaches for building artificial grid dielectric resonator antenna (GDRA) arrays are used to demonstrate larger array possibilities at much higher mm-wave frequencies. The arrays are integrated with longitudinal slot-fed substrate integrated waveguide (SIW) networks and demonstrated at 60 GHz (V-band) for wideband and high gain applications. For both approaches, the effective permittivity of a 500μm thick, low permittivity polymethyl methacrylate (PMMA) substrate is locally increased by up to 22.4 by embedding groups of micro-sized rectangular metal inclusions, each group functioning as antenna elements and collectively functioning as an antenna array.

In the first approach, the monolithic solid template frame GDRA array approach as discussed in Chapter 5 Figure is used to demonstrate two large 2-dimensional (2D) planar GDRA arrays while providing precise inter-element spacing. This also represents a more complicated SIW feed network, combining the series fed concept of Chapter 6, with the parallel feed distribution of Chapter 4. GDRA prototypes with 4×4 and 8×8 array elements are fabricated and tested at 60 GHz.
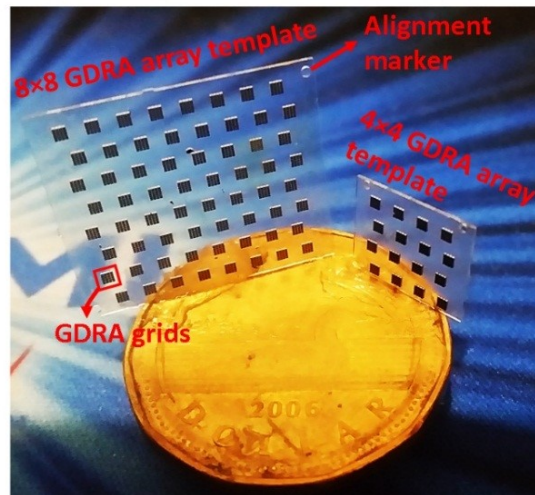

Figure 7.1 4×4 and 8×8 monolithic 60 GHz GDRA array layers © 2019 IEEE. Reprinted with permission.

---

[7] Details including some textual material, some illustrations and some tabular material in Section 7.2-7.6 are published in "W. Mazhar, D. Klymyshyn, G. Wells, A. A Qureshi, and, M. Jacobs "60 GHz Substrate Integrated Waveguide Fed Monolithic Grid Dielectric Resonator Antenna Arrays" *IEEE antennas and wireless propagation letters*, *vol. 18, no. 06, April 2019* © 2019 IEEE . Reprinted with permission.

In the second approach, a monolithic strip frame template based GDRA array as described in Chapter 5 is developed to reduce the inter-element mutual coupling between the array adjacent elements through the template frame. For a comparative analysis, S-parameters, gain and radiation efficiency of both design approaches; SIW fed 4-element monolithic solid template frame and the strip template frame GDRA array are provided.

7.2. Design and Concept for 60 GHz Solid Template Frame GDRA Arrays

Large 2D 60 GHz SIW fed GDRA arrays are fed through SIW based T-junction power splitters similar to those discussed in Chapter 4. Simulations are conducted with the aid of ANSYS HFSS and CST Microwave Studio. All GDRA array layers are fabricated using deep X-ray lithography (DXRL) with metal electroplating, whereas the feed circuits are built through standard printed circuit board (PCB) technology on Rogers CLTE-XT substrate with relative permittivity of 2.95 and thickness of 0.25mm.

7.2.1. Effective Permittivity Estimation

The permittivity estimation method described in Section 3.2.1 is used to retrieve the constitutive parameters of the current grid dielectric material. All design variables for this study are provided in Figure 7.2 and Table 7.1. The retrieved effective permittivity of the test material along with refractive index η and impedance z are shown in Figure 7.3a, and Figure 7.3b. An effective permittivity of 22.4 is realized with inclusion dimensions of 0.2×0.1×0.3 mm ($l{\times}w{\times}h$), and grid separation of 0.05 mm. Moreover, the material loss tangent (tanδ) of 0.003 is estimated at 60 GHz by using the ratio of the imaginary ($\varepsilon'' = 0.07$) and real part ($\varepsilon' = 22.4$) of the effective permittivity presented in Figure 7.3.
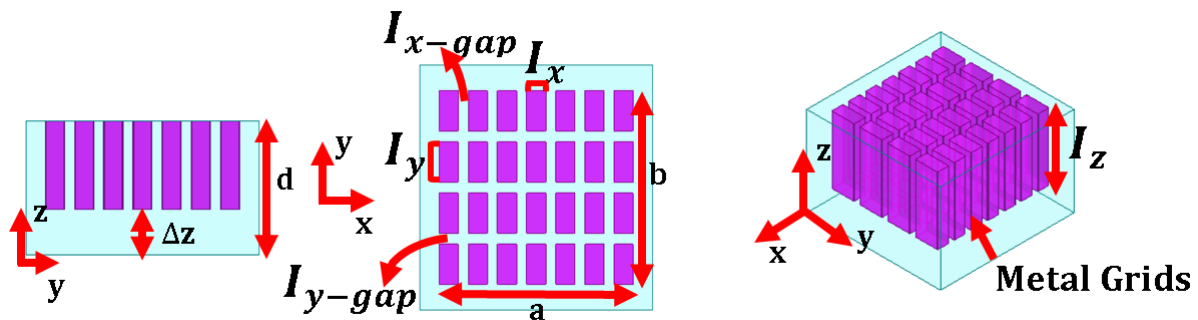

Figure 7.2 Design model of single GDRA element © 2019 IEEE. Reprinted with permission.

Table 7.1 Design variables for a single GDRA element

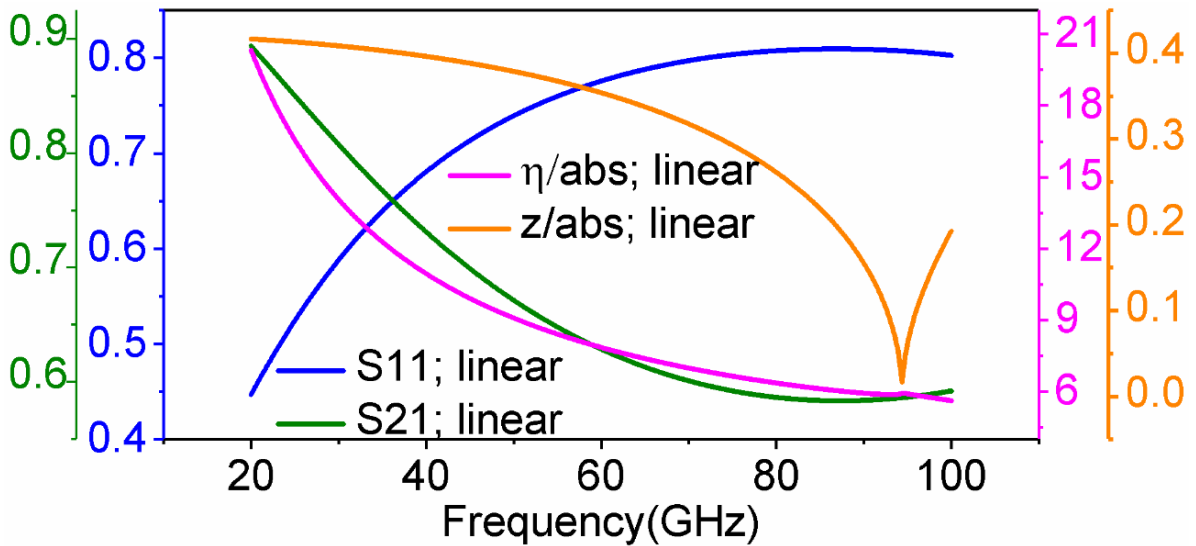| Parmaters	Symbol	Values(mm)
GDRA-width	b	0.90
GDRA length	a	0.90
GDRA height	d	0.05
Inclusion x-gap	I_{x-gap}	0.05
Inclusion y-gap	I_{y-gap}	0.05
Inclusion-width	I_x	0.20
Inclusion-length	I_y	0.10
Inclusion-height	I_h	0.30
Inclusion-offset	Δz	0.20
No of grids along x and y-axis		7×4

Figure 7.3a Simulated reflection and transmission coefficients along with refractive index and impedance of the GDRA sample © 2019 IEEE. Reprinted with permission
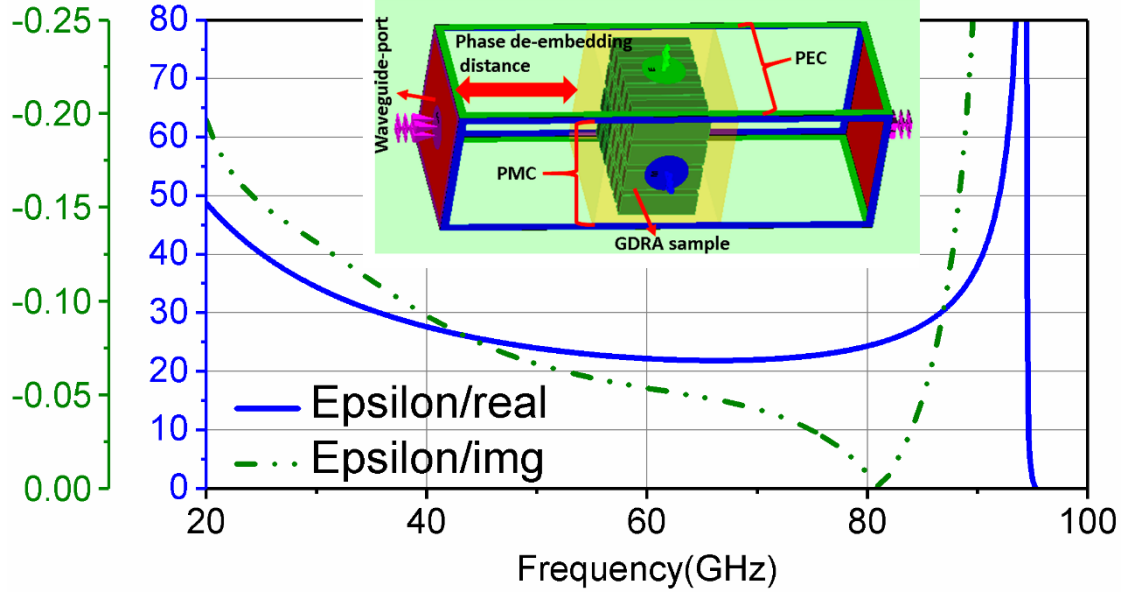
149

Figure 7.3b Real and imaginary permittivity of the GDRA sample © 2019 IEEE. Reprinted with permission

7.2.2. SIW Fed Single GDRA Element Design

It is essential to characterize the design performance of the single GDRA element prior to designing multichannel SIW fed GDRA arrays. Therefore, a single GDRA element fed by SIW based longitudinal slot feed technique is evaluated in this section. An SIW width of 2.3mm is considered. The critical design parameters for this study are the slot length "S_lg", the slot width "S_wd", and the slot position "Sc_W"are shown in Table 7.2. The coupling slot length "S_lg" is kept in the proximity of "$\lambda_g/2$" at a center frequency to avoid the slot resonance, whereas the slot width $= 0.3$mm$<\lambda_g/10$ is used to avoid high cross pol levels during the GDRA excitation process. The slot position "Sc_W" is initially considered at "$\lambda_g/4$", which corresponds to a maximum standing wave field intensity (maximum coupling) in the channel as shown in Figure 7.4a.

The dimensions for the single GDRA element are estimated by using the transcendental equation mentioned in Section 2.4.2.1. The variables a, b and d are the length, width, and height of the GDRA. For simplicity, the variables a and b are kept almost the same i.e., square GDRA, whereas d is 0.5mm thick for achieving the low profile GDRA design. By inserting equation (2.80), (2.81) and equation (2.82) along with the design frequency $f_o = 60$ GHz, and an estimated bulk grid dielectric material permittivity $\varepsilon_r = 22.4$ in equation (2.90) and solving it for variable a gives a; $b = 0.90$ mm. The single GDRA element design model with above calculated dimensions fed by an SIW based longitudinal slot is presented in Figure 7.4a. The simulated gain and S-parameters

150

are provided in Figure 7.4b with the frequency resonance at 60 GHz validating the estimated permittivity of 22.4 and the working principle of the GDRAs.

Figure 7.4b also compares the GDRA element to a conventional DRA of the same height with permittivity of 22.4 and dimensions of 1.0×1.0×0.5 mm (l×w×h). The return loss (S_{11}) of the matched classical DRA is very narrow band, while the GDRA provides a 10-dB impedance bandwidth of 4.6 GHz. This demonstrates the superior performance of the GDRA over the conventional DRA for low-profile and wideband mm-wave applications. An E-field plot of the GDRA element (Figure 7.4c) resembles a magnetic dipole-like pattern, where the red areas indicate local high electric flux density regions for producing a large effective permittivity. Moreover, Figure 7.4b shows a simulated peak realized gain of 7.9 dBi, with radiation efficiency of 95% (shown later in Figure 7.20), demonstrating the excellent radiation characteristics of the GDRA element.
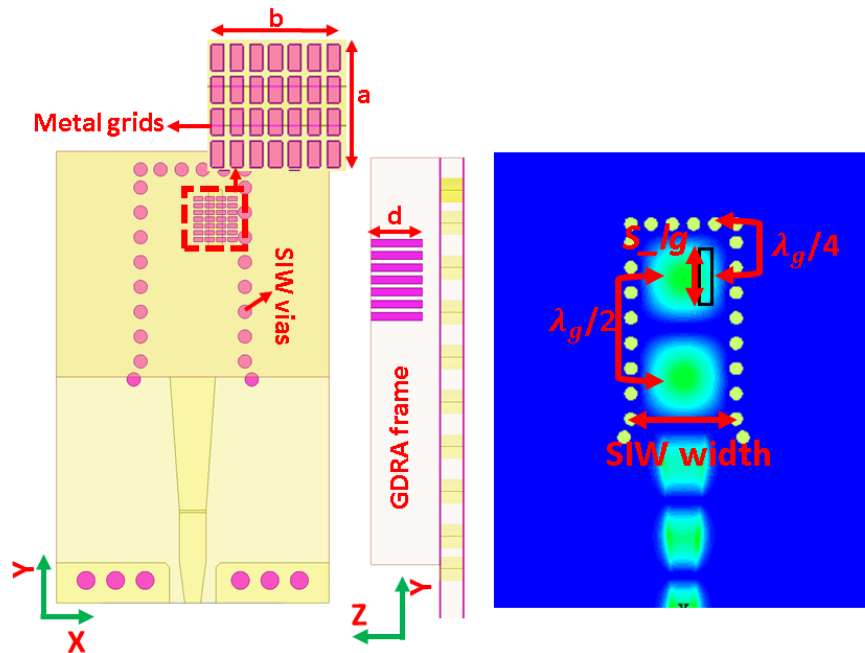

Figure 7.4a Simulated model for single GDRA element fed by SIW based longitudinal slot plus slot placement in an SIW channel for max- E field coupling © 2019 IEEE. Reprinted with permission.
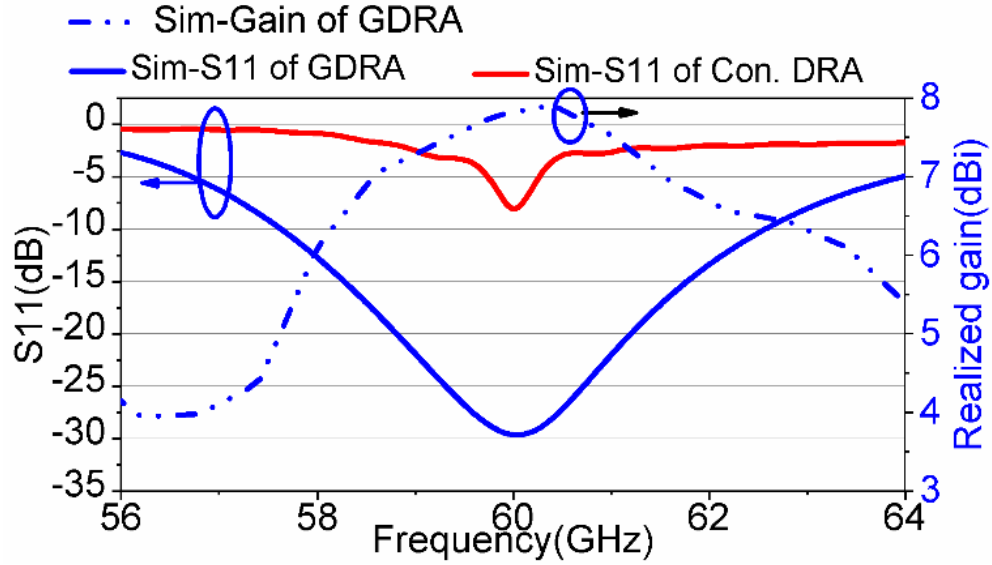
Figure 7.4b Electric field intensity inside GDRA © 2019 IEEE. Reprinted with permission.
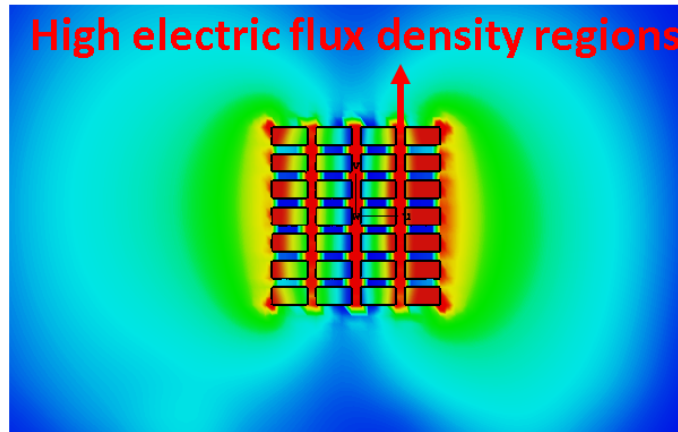

Figure 7.4c Simulated S-parameters and gain plot for single longitudinal slot fed GDRA element © 2019 IEEE. Reprinted with permission.

Table 7.2   1×4, 1×8 element GDRA subarray design parameters

Parameters	Value	Parameters	Value
SIW width	2.3mm	vias pitch	0.5mm
via_rad	0.15mm	slot-length	1 mm
slot-width	0.3mm	slot-gap	2.2mm
Tx-w	0.6mm	slot position	1.05mm

7.3. Subarray Design

The GDRA subarrays are series fed through non-resonant longitudinal slots entrenched in a standing wave SIW channel in a similar manner as described in detailed in Chapter 6.

Single channel $1 \times n$ element GDRA subarrays are shown in Figure 7.5 for operation in the frequency band of 58 to 62 GHz, where $n = 4$ and 8. In both 1×4 and 1×8 subarrays, the key design parameters such as PMMA frame thickness, rectangular inclusions size (i.e., length, width, height), and inclusion x and y-axis spacing are kept the same as used for the single GDRA element shown in Table 7.1 and Table 7.2.
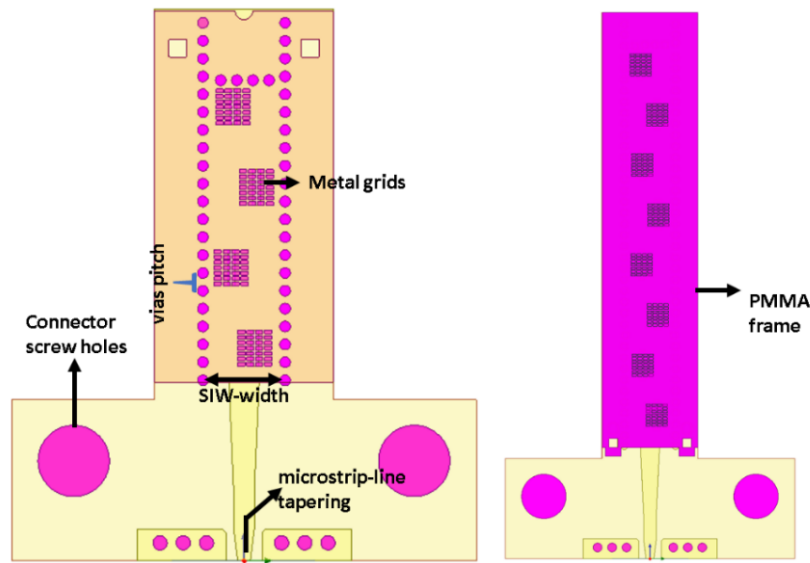

Figure 7.5 Simulation design for a) 1×4 element GDRA subarray; b) 1×8 element GDRA subarray

A thin layer of a PMMA, i.e., 200µm is placed between SIW feed and actual GDRA template to aid the slot coupling as explained previously.

The slot offsets are different in both subarrays for conducting a low side lobes study. The slot offset for 1×4 subarray with uniform aperture distribution [1] is calculated by using expression 6.1 and 6.2 as described previously. For $\lambda_g = 4.7$ and $\lambda_0 = 5mm$ in the equation 6.2, d_n comes out to be 0.38 mm. In the 1×4 subarray, the same value of the offset is used for all four slots to provide a uniform excitation.

For the 1×8 element subarray, the GDRA slot offsets are computed by applying the Taylor distribution [2] procedure with a minimum side lobe level (SLL) requirement of -25dB. The design equations [3] used for this aperture distribution are listed below:

$$d_n = \frac{a}{\pi} \sin^{-1} \sqrt{\frac{g_n}{(2.09 \times \frac{\lambda_g}{\lambda_0} cos^2(\frac{\pi\lambda_0}{2\lambda_g})}} \tag{7.1}$$

$$g_n = \frac{c_n}{\sum_{n=1}^{N} c_n} \tag{7.2}$$

$$n = 1,2 \dots .8; \tag{7.3}$$

where d_n is the slot offset, c_n is the Taylor amplitude coefficients, a is the width of the SIW, and N is the number of the slots. The computed slot offsets are provided in Table 7.3, which are further scaled to improve the impedance bandwidth and gain of the 1×8 GDRA array at the expense of slightly higher side lobe levels, i.e., -18 dB. It is observed that both impedance bandwidth and gain are improved by increasing the number of GDRA elements fed through the coupling slots. For a 4-element GDRA subarray an impedance bandwidth of 5 GHz (i.e., from 58 to 63 GHz) with a peak gain of 10.8 dBi and the radiation efficiency of more than 85% is achieved across the frequency band. Whereas for the 8-element GDRA subarray, a 10-dB impedance bandwidth of 5.5 GHz from 57 to 62.5 GHz and a peak broadside gain of 13.53 dBi is achieved. The simulated results for both subarrays are provided in Figure 7.6. Moreover, both SIW fed GDRA subarrays are terminated in a short circuit, i.e., at a quarter wavelength away from the center of the last slot to avoid any impedance disturbance and to excite each GDRA at the peak of the standing wave in the SIW channel [4]. For both subarrays, the impedance bandwidth is wide enough covering the entire 7 GHz ISM band at 60 GHz. These subarrays results are next used to demonstrate two-dimensional (2D) antenna arrays: i) 4×4 element GDRA array; and ii) 8×8 element GDRA array.
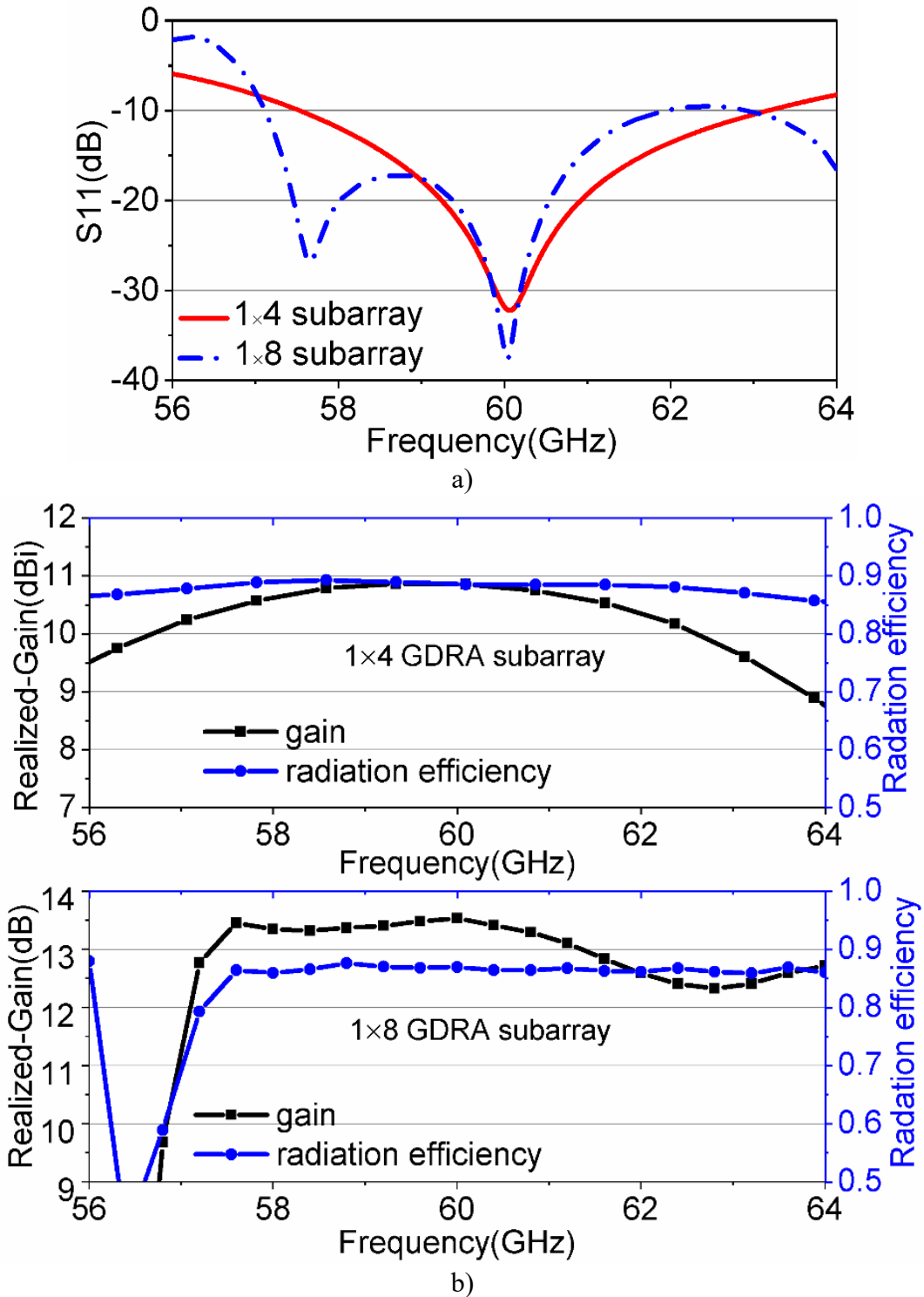
Figure 7.6 a) Simulated S-parameters for 1×4 and 1×8 GDRA subarrays; b) Simulated realized gain and radiation efficiency for 1×4 and 1×8 GDRA arrays

Table 7.3 Computed slot displacement for -25dB SLL Taylor excitation coefficients

| c_n	$d_n(mm)$	Improved d_n (mm)
0.423	0.3059	0.823
0.5929	0.3814	0.7102
0.8343	0.4594	0.8593
1	0.5014	0.9407
1	0.5014	0.9407
0.8343	0.4594	0.8593
0.5929	0.3814	0.7102
0.423	0.3059	0.458

7.4.   SIW Power Dividers

The SIW power distribution network required here is very similar in concept to that presented in Chapter 4, though scaled for 60 GHz. The main difference here is the rounded corners and SIW wall vias adjustment at the microstrip line to SIW transition which improve the S-parameters performance at 60 GHz.
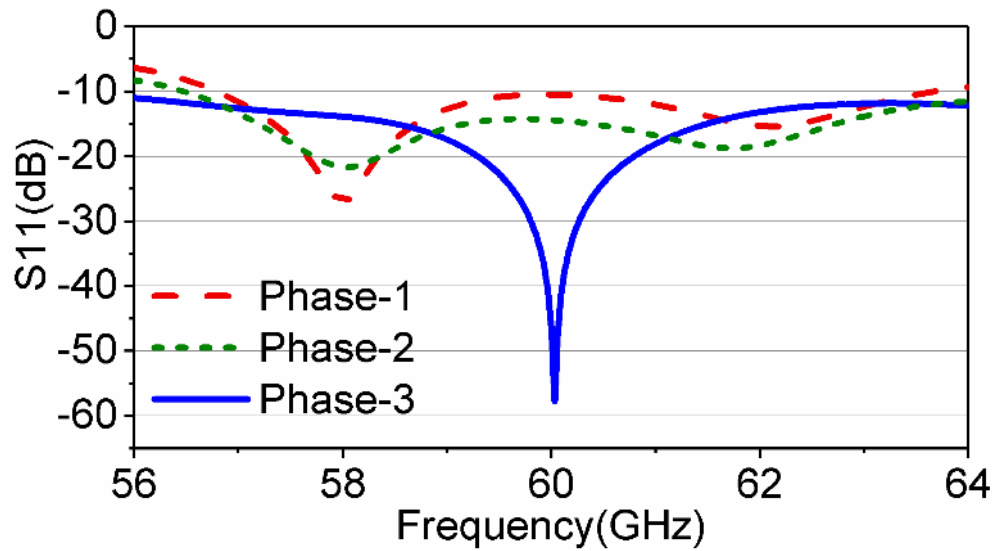
7.4.1. 1×4 Power Divider

A two-stage conventional T-power splitter made through SIW technology is shown in Figure 7.7a. A metallic via acting as an inductive post [5] is normally required at the right-angle corner of each stage of T-splitter for impedance matching. However, in this case, it is observed that these inductive posts cause an additional signal dispersion when added at the output stage of the splitter. Therefore, no inductive posts are used at the splitter output stage right angle corners as shown in phase-3 of Figure 7.7a.

The right-angle bends of the T-splitter are replaced with the rounded corners to help the fluid signal propagation and minimize the reflections arising from the sharp discontinuity. Moreover, it is observed that the SIW width shown by the variable "a_m" in phase-3 is found to have a substantial impact on the return loss of 1×4 power splitter. A slight increase in the width improves the return loss up to -10 dB by enhancing mode matching between the TEM waveguide and TE SIW. Figure 7.7b depicts the simulated S-parameters response for the different design phases of the 1×4 power splitter. A10-dB impedance bandwidth of 10 GHz centered at 60 GHz is achieved with phase and

amplitude imbalance of 0.02dB and 0.2º (shown in Figure 7.7c). In summary, the proposed 1×4 SIW power divider has 3 design phases: 1) designing a power divider with 90-degree bends and with output inductive posts; 2) integrating curved bends and removing output corner inductive posts for reducing the corner reflections and phase compensation; and 3) using mode matching for enhancing the impedance bandwidth and improving return loss. All three design phases are illustrated in Figure 7.7a.
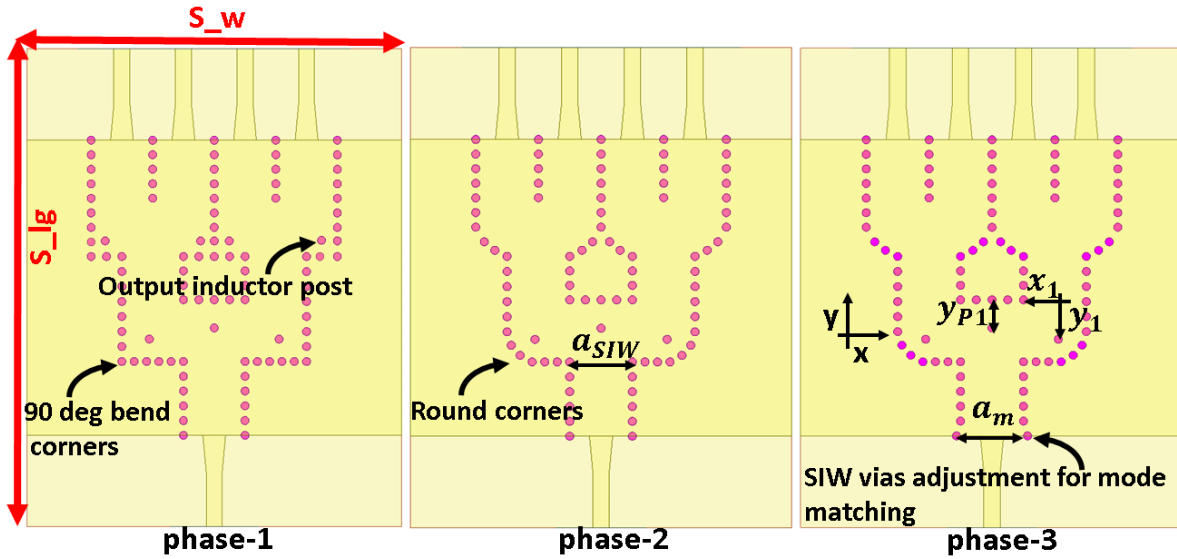
a)

b)

Figure 7.7 a) Simulated design model for 1×4 SIW power splitter; b) Simulated S-parameters for 3-different design phases of 1×4 SIW power splitter
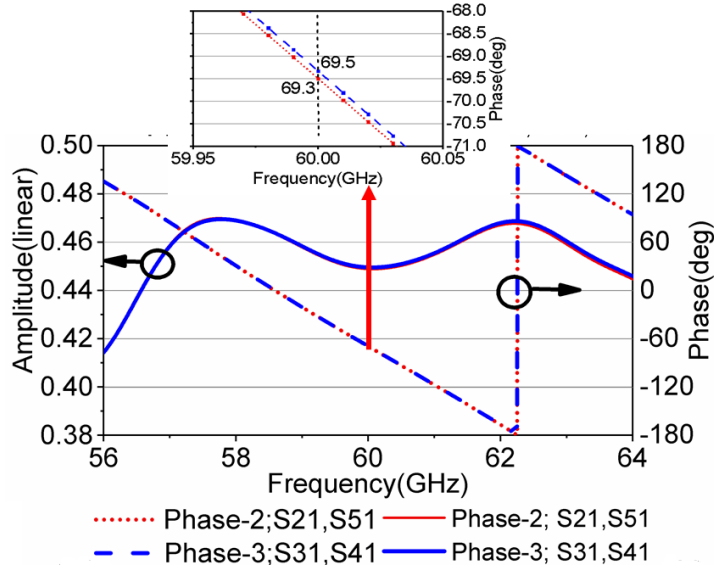
Figure 7.7c Simulated amplitude and phase imbalance for the 1×4 power splitter

7.4.2. 1×8 Power Divider

Figure 7.8 demonstrates the design geometry for a 3-stage, 1×8 equal SIW power splitter, which is symmetrical around the centerline.
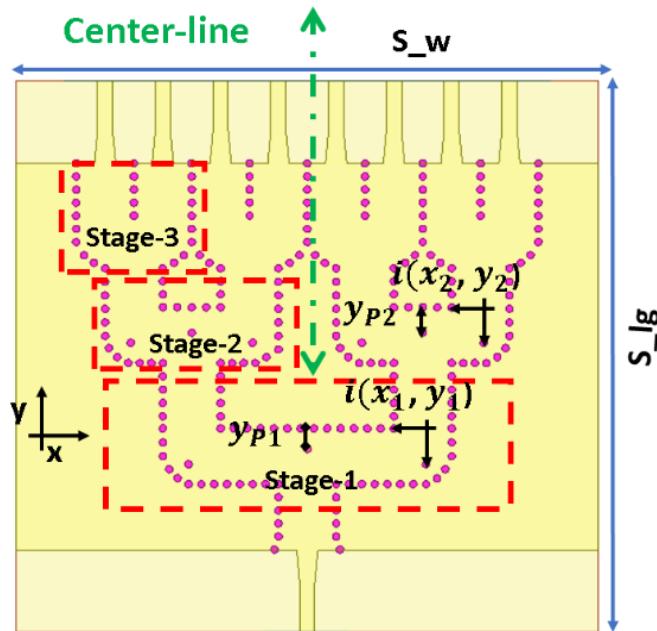

Figure 7.8 Simulated design model for 1×8 SIW power splitter

The same design strategy as discussed in Section 7.4.1 is employed for building this design. The simulated S-parameters presented in Figure 7.9a show that all three design stages of the divider have good impedance matching characteristics and wideband performance. The detailed values of

all optimized parameters are listed in Table 7.4. Figure 7.9b shows the output response of the final 1×8 SIW feeding network with an impedance bandwidth of 8 GHz from 57 GHz to 64 GHz within $S_{11} \leq$ -15 dB. Secondly, it also illustrates the improvement in the return loss with and without mode matching as discussed in Section 7.4.1. An amplitude and phase imbalance of ± 0.7 dB and ± 2.2º is achieved for the current design as shown in Figure 7.9c. Moreover, an average insertion loss of -10dB (i.e., 0.315 in linear) is realized from an input to the output port, which validates the low loss characteristic of the SIW.
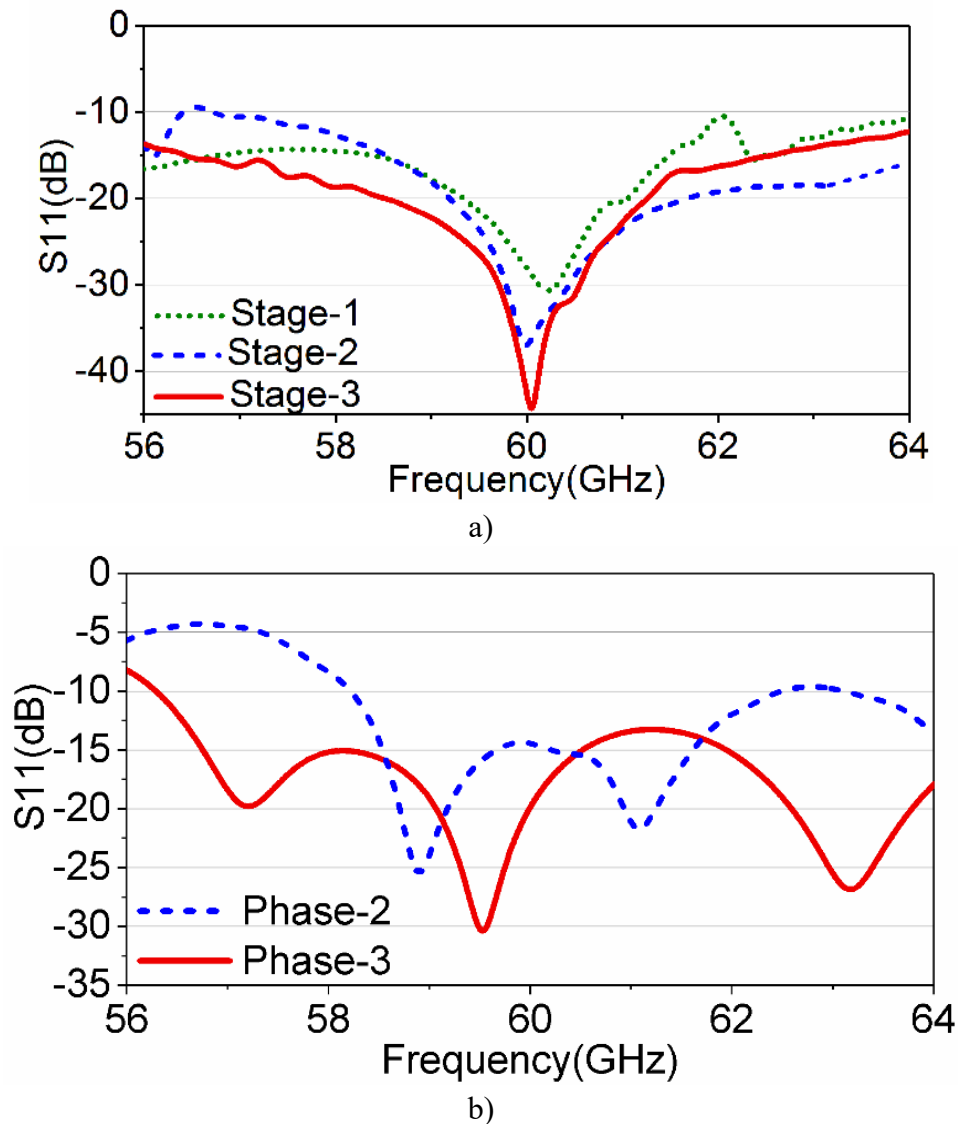

a)

b)

Figure 7.9 a) Simulated S-parameters for different design stages of 1×8 SIW power splitter; b) Simulated S-parameters for 1×8 SIW power splitter;
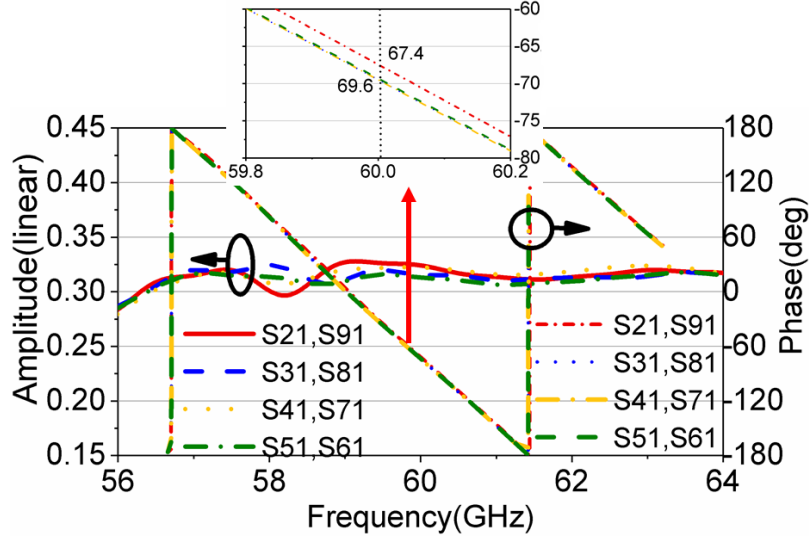
Figure 7.9c Simulated amplitude and phase imbalance for 1×8 the power splitter

TABLE 7.4 1×4 AND 1×8 SIW POWER SPLITTER DESIGN PARAMETERS (MM)

1×4 SIW power splitter			
$i(x_1y_1)$	1.125; 0.90	y_{P1}	1.10
a_m	2.60	a_{siw}	2.30
S_lg	18.1	S_wd	14
1×8 SIW power splitter			
$i(x_1, y_1)$	1.025; 0.82	$i(x_2, y_2)$	1.025; 0.85
y_{P1}	0.90	y_{P2}	0.85
S_lg	23.4	S_wd	23.1

7.5.   Array Design

Based on the subarray configurations discussed in Section 7.3, two GDRA arrays with wide impedance bandwidth and high gain performance are demonstrated in this Section.

7.5.1. 4×4-Element SIW Fed GDRA Array

The design geometry of the 4×4 GDRA array is provided in Figure 7.10. A 1×4 equal SIW power splitter presented in Section 7.4.1 is utilized for feeding this array. The impedance bandwidth of the array is dependent on both subarray and power splitter performance. Therefore, both are tuned separately for the best performance before their integration. The final tuning is made by adjusting the SIW-power splitter inductive posts $i(x_iy_j)$ to remove the mutual interference between two

160

design segments [6]. A microstrip line with tapered transformer is used for launching the signal into the SIW based power splitter. All design parameters for the 4×4 GDRA array are provided in Table 7.2. Additionally, uniform aperture distribution is utilized for computing the slot offsets. A simulated 10-dB input impedance bandwidth of 5.5 GHz from 57 to 62.5 GHz and maximum simulated realized gain of 16.1 dBi is achieved as shown in Figure 7.11 and Figure 7.13 respectively. Furthermore, an average simulated radiation efficiency of 82% is achieved across the design bandwidth as illustrated in Figure 7.20.
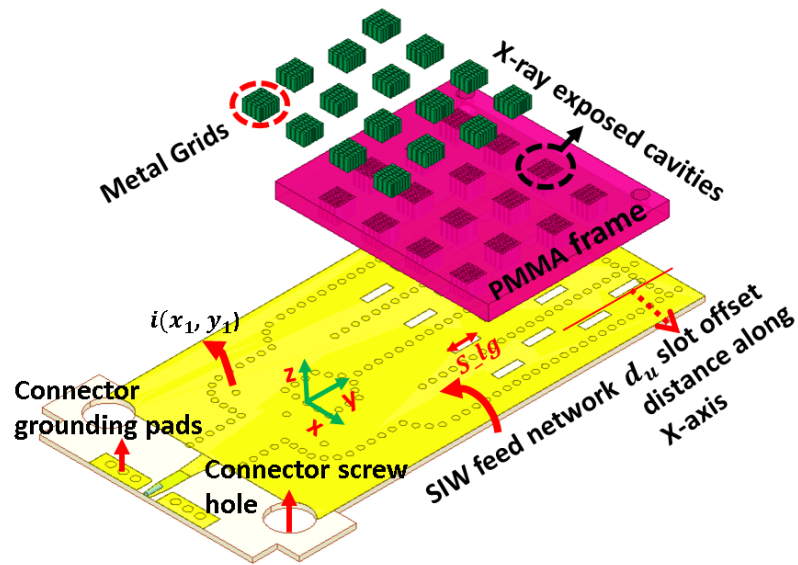

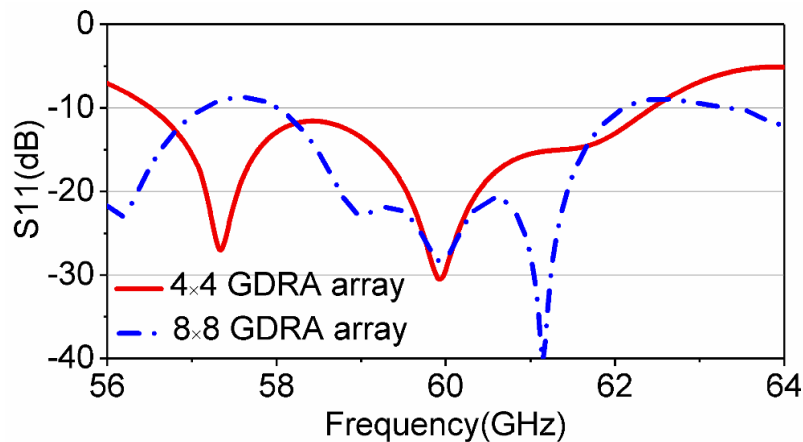Figure 7.10 Exploded design model of 4×4 GDRA array © 2019 IEEE. Reprinted with permission.

Figure 7.11 Simulated S-parameters for 4×4 and 8×8 GDRA array

7.5.2. 8×8-Element SIW Fed GDRA Array

The design model of the 8×8 GDRA array structure is presented in Figure 7.12, showing the 1×8 power splitter and 1×8 GDRA subarrays comprising the monolithic 8×8 array layer. All GDRA

array elements are fed through longitudinal slots patterned on the top surface conductor of the SIW feeding network. In this design, a Taylor aperture distribution is used with the slot offset (d_n) values shown in Table 7.3. The first slot y-axis offset i.e., y_{offset} as shown in Figure 7.12 and SIW power splitter inductive posts offsets $i(x_i, y_j)$ are the critical parameters for tuning the array performance. The simulated S-parameters, gain, radiation patterns, and radiation efficiency are provided in Figure 7.11, Figure 7.13, Figure 7.19 and Figure 7.20. A bandwidth of 3.7 GHz from 58.5 to 62.2 GHz is observed with maximum broadside gain of 20.1 dBi and an average radiation efficiency of 77%. The simulated H-plane side-lobe levels are below -22dB as shown in Figure 7.19c, close to the expected -25 dB from Taylor distribution and confirming the slot offset design.
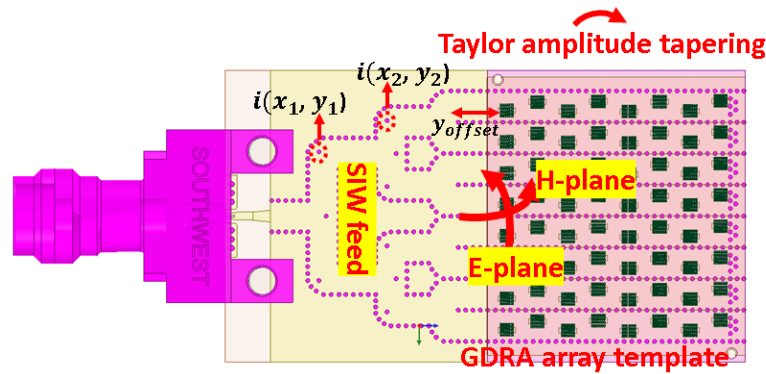

Figure 7.12 Design model for 8×8 GDRA array © 2019 IEEE. Reprinted with permission.
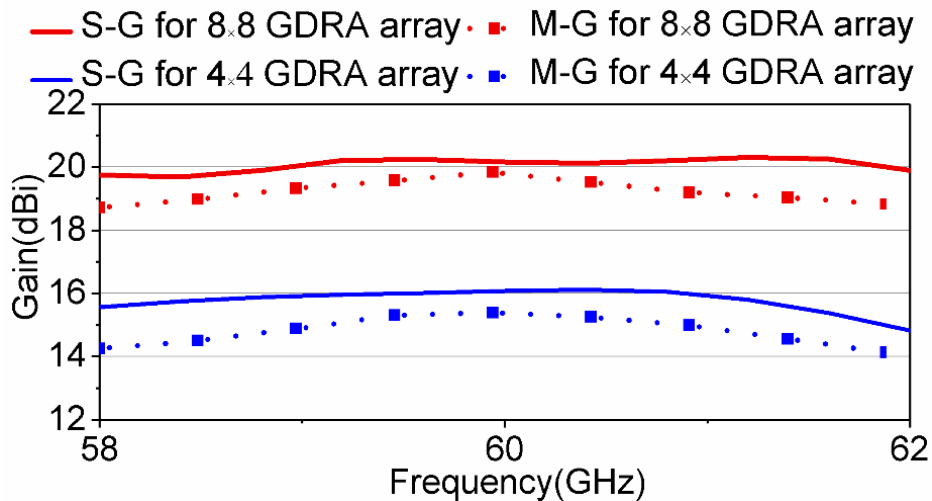

Figure 7.13 Simulated and measured realized gain for 4×4 and 8×8 GDRA array © 2019 IEEE. Reprinted with permission.
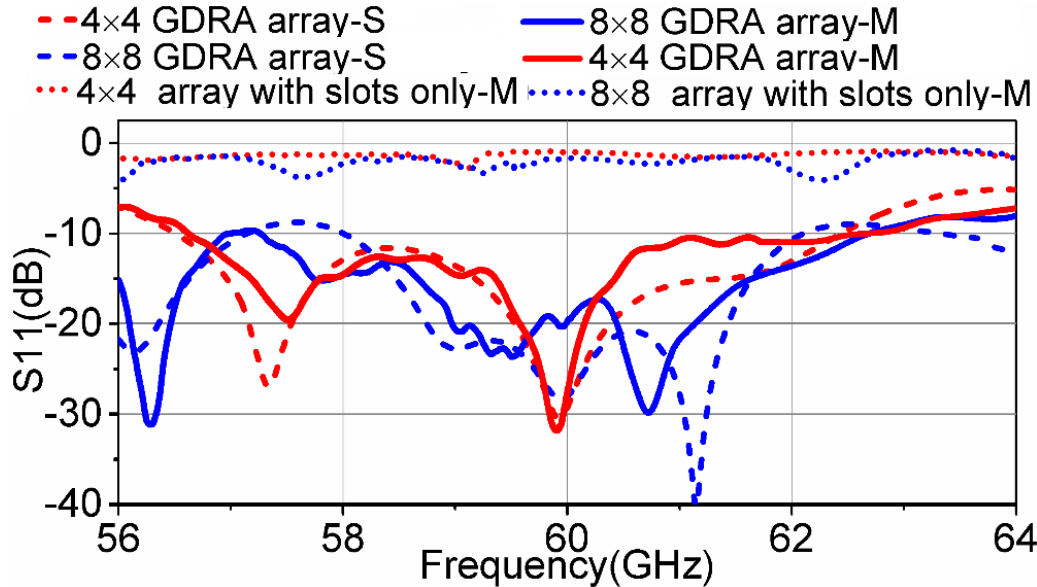
Figure 7.14 Simulated and measured S-parameters comparison for 4×4 and 8×8 fed GDRA array prototypes (S=Simulated; M=Measured) © 2019 IEEE. Reprinted with permission.

7.6.   Fabrication and Measurement

The solid template frame GDRA layers with embedded metal inclusions are fabricated using deep X-ray lithography with metal electroplating, as described in Chapter 5. High quality, tall rectangular cavities with lateral dimensions of 100 μm× 200 μm are exposed and developed in a 500 μm thick polymethyl methacrylate (PMMA) layer bonded to a sacrificial silicon wafer. Figure 7.15 provides an SEM image of the exposed PMMA template showing one of the GDRA elements of a sample array, and the deep cavities for electroplated metal inclusions. The figure also demonstrates the high-quality smooth and vertical side walls typical of deep X-ray lithography. These cavities are then electroplated in nickel up to 300 μm using electroforming. Figure 7.1 shows different GDRA array layers released after dissolving the silicon wafer in a KOH solution. In each array layer, small markers are placed at the corners for the microscopic alignment with the underlying feed layer.

Complete assembled fabricated prototypes are shown in Figure 7.16. GDRA array layers are aligned under a microscope and bonded to the feed layers for measurement. Figure 7.14 depicts the comparison between the simulated and measured return loss of the GDRA arrays from 56 GHz to 64 GHz, which are summarized in Table 7.5. Measured impedance bandwidths of 10.4% and 12.0% are realized for 4×4 and 8×8 GDRA array prototypes using R&S vector network analyzer ZVA 67 having operating frequency range of 10 MHz to 67 GHz. Figure 7.14 also shows the return

163

loss for the feed layer alone without the GDRA layer, confirming that the SIW-based longitudinal slots are non-resonant.

Table 7.5 Measured vs. Simulated S_{11}(dB) results comparison

Design	Simulated $S_{11}\leq$-10dB (GHz)	Measured $S_{11}\leq$-10dB (GHz)
4×4 GDRA array	57.0 to 62.5	56.5-63.0
8×8 GDRA array	58.5 to 62.2	55.0-62.0

Figure 7.15 a) SEM image of the exposed PMMA demonstrating the side wall and structure quality © 2019 IEEE. Reprinted with permission.
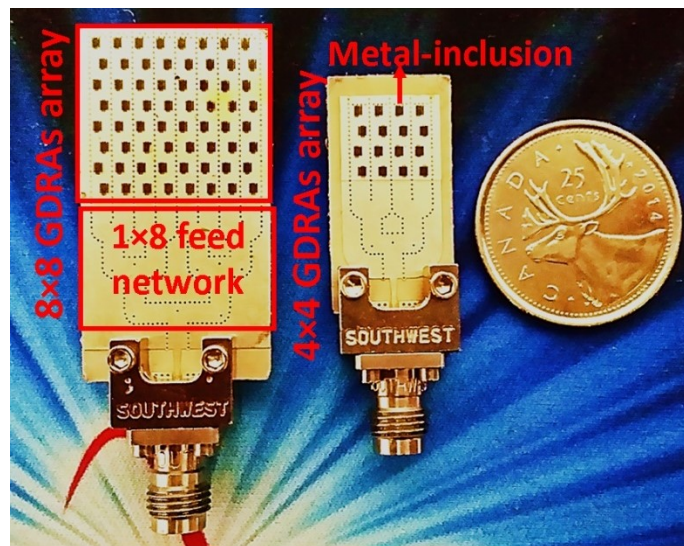

Figure 7.16 Fabricated prototypes for 4×4, and 8×8 GDRA arrays © 2019 IEEE. Reprinted with permission.

The simulated and measured normalized radiation patterns for 4×4 and 8×8 GDRA array prototypes at 60 GHz in both E-plane and H-plane are provided in Figure 7.17, Figure 7.18 and Figure 7.19. The measured realized gain shown in Figure 7.13 is stable over the broadband impedance bandwidth, with peak values of 15.2 dBi for the 4×4 array and 19.4 dBi for the 8×8 array. Discrepancies between the simulated and measured gains are mainly due to launch mismatch losses and the air-gap variations between the array and feed layers affecting coupling, which are somewhat sensitive and difficult to control and model at 60 GHz. Figure 7.19d shows the sidelobe levels of -20dB for 8×8 GDRA array, which are quite close to simulated levels of -22dB. Both arrays have excellent polarization properties, with cross polarization below -20dB. Moreover, the measured radiation efficiency determined by comparing the realized gain and directivity ratio is also provided in Figure 20. The measured radiation efficiency of 73% achieved for the 4×4 GDRA array, is less than the simulated efficiency of 82%, but still respectable given the additional losses in the launch and large feed structure which make characterization of the GDRA layer performance at 60 GHz difficult. With further refinement in the feed network, the potential for the GDRA array as a high efficiency antenna at 60 GHz is promising, considering the efficiency of the SIW slot-fed GDRA element can approach 95% (shown in Figure 20).
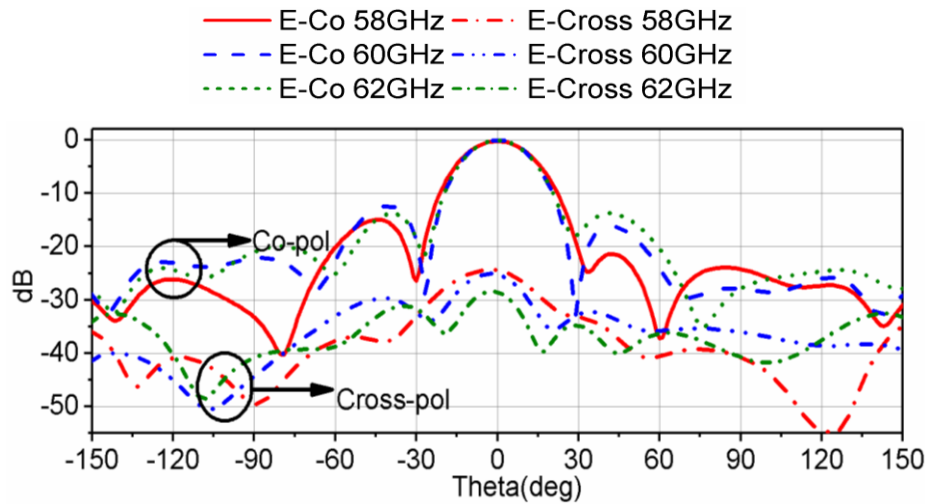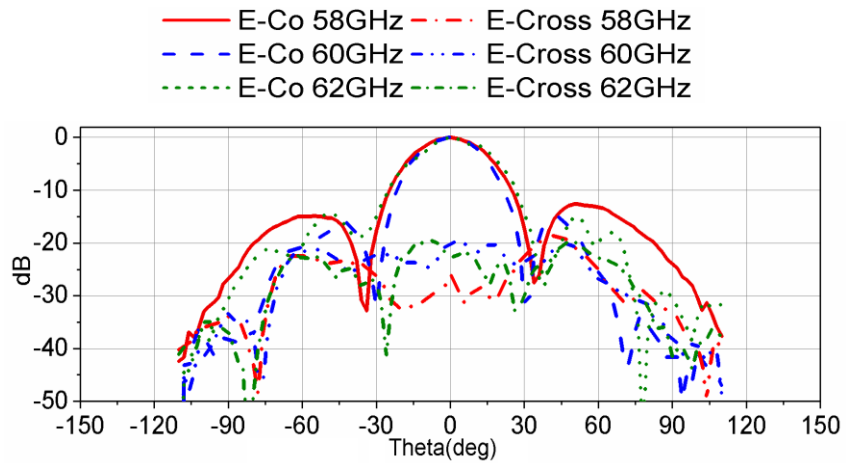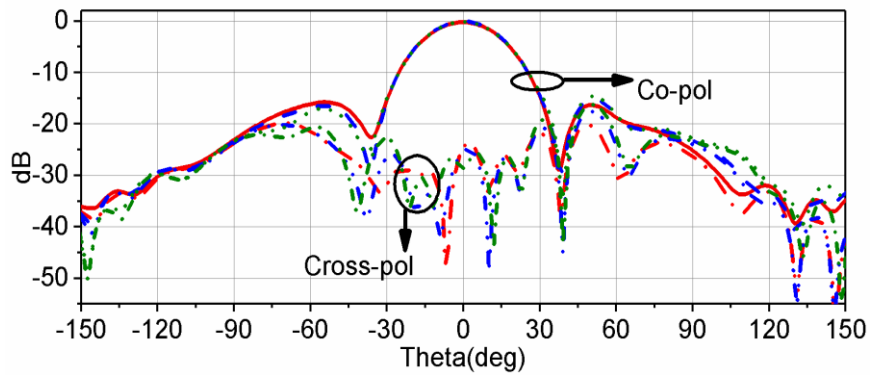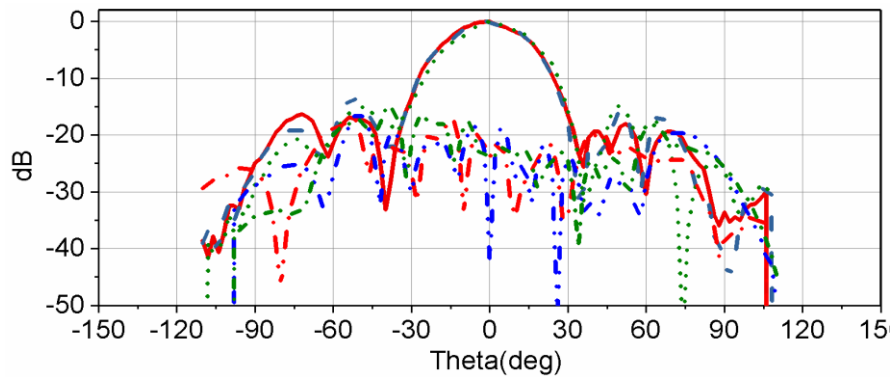

Figure 7.17 Simulated E-plane co/cross pol plots for 4×4 GDRA array

a) Measured E-plane co/cross pol plots for 4×4 GDRA array

b) Simulated H-plane co/cross pol plots for 4×4 GDRA array

c) Measured H-plane co/cross pol plots for 4×4 GDRA array

Figure 7.18 Simulated and measured radiation pattern for 4×4 GDRA arrays

a) Simulated E-plane co/cross pol plots for 8×8 GDRA array

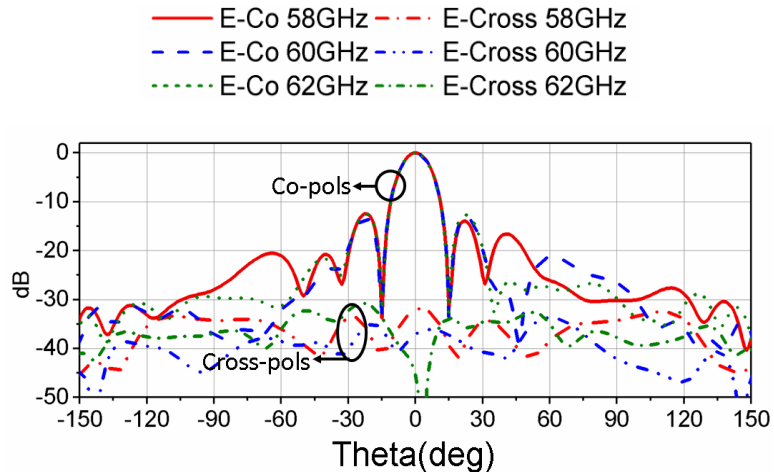b) Measured E- plane co/cross pol plots for 8×8 GDRA array

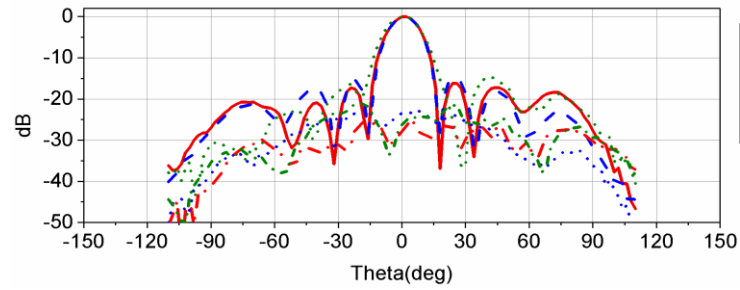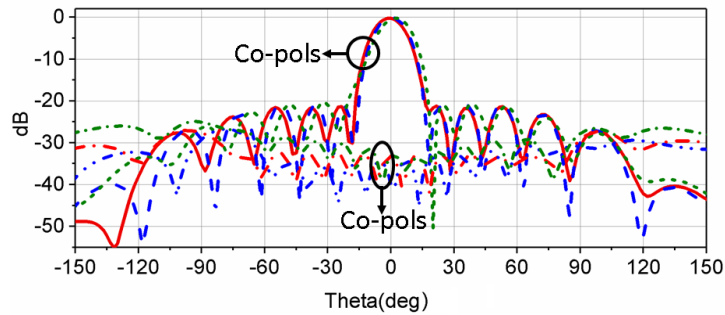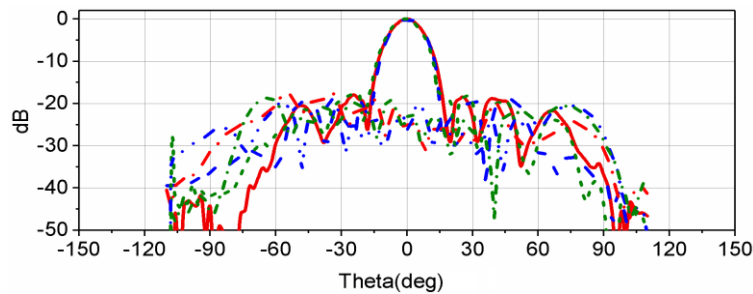c) Simulated H- plane co/cross pol plots for 8×8 GDRA array

d) Measured H- plane co/cross pol plots for 8×8 GDRA array

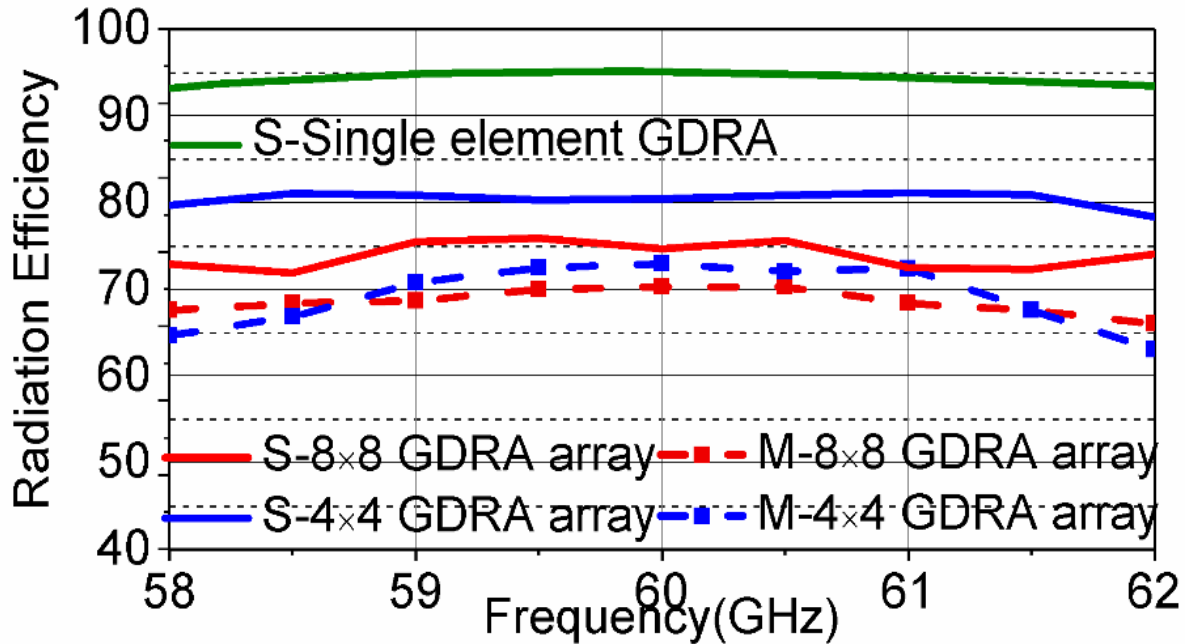Figure 7.19 Simulated and measured radiation pattern for 8×8 GDRA arrays

Figure 7.20 Simulated and measured radiation efficiency for 4×4 and 8×8 GDRA array (**S-G= Simulated gain; M-G= Measured gain © 2019 IEEE. Reprinted with permission.

7.7. Strip Template Frame GDRA Array

The monolithic solid template frame approach allows GDRA assembly in large arrays in a simple monolithic layer reasonable bandwidth and gain performance. However, this can be further improved by using a strip template frame approach as discussed in Chapter 5, which helps in lowering the inter-element mutual coupling between the adjacent elements or energy carried through the template frame, by removing portion of the template layer. But this is only an example cut out frame pattern to disrupting the fields between the adjacent GDRAs, other pattern might produce different results. A fabricated sample of 4-element strip frame GDRA array is tested for an impedance bandwidth and radiation pattern performance. A wide impedance bandwidth of 5 GHz from 58 GHz to 63 GHz and broadside radiation pattern with a peak gain of 10.8 dBi is achieved.

7.7.1. Design Concept

The simulated design model for a 4-element strip template frame GDRA array is shown in Figure 7.21. Most of the design parameters are similar to those described for solid template frame GDRA arrays in Section 7.2.
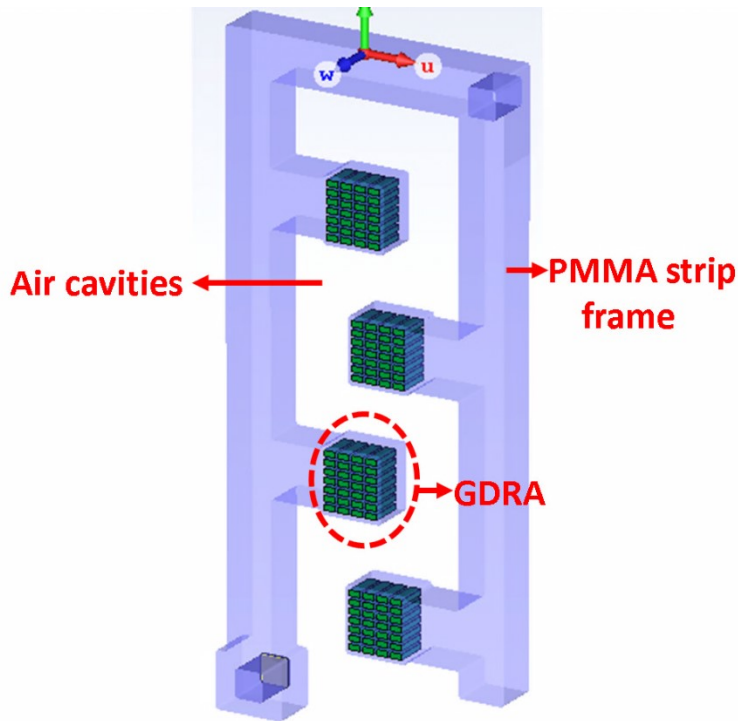
Figure 7.21 Design model of a 4-element strip template frame GDRA array

7.7.2. 4-Element Strip Template Frame and Solid Template frame GDRA Array Comparison

The exploded view of 4-element template frame GDRA array fed by SIW feeding mechanism is shown in Figure 7.22. The critical SIW and slot feeding design parameters are the same as used in Section 7.2.2. In comparison to the solid template frame approach, the strip template frame approach provides better permittivity contrast between adjacent GDRA elements as a result less amount of energy flow between them. A similar effect is also demonstrated in Section 6.2.1.3 which showed increased mutual coupling for high permittivity solid template frame approach. For visualizing the mutual coupling [7], [8] effect between the GDRA array adjacent elements for both solid template frame and strip template frame cases, the simulated E-field patterns in the template frames are provided in Figure 7.23. This reduced mutual coupling between the GDRA array adjacent elements improves the impedance bandwidth, gain and radiation efficiency of the GDRA array. These are illustrated by the simulated S-parameters, gain and radiation efficiency comparison for both strip template frame and solid template frame approaches as provided in Figure 7.24, Figure 7.25, and Figure 7.26 respectively. Moreover, a performance comparison between the simulation results for solid template frame and strip template frame is summarized in

Table 7.6. It is observed that the solid template frame approach results in a slight lowering of the resonant frequency and the reason for this effect is that the solid template frame approach increases the overall effective volume of the GDRA. i.e., large template areas in GDRA surroundings.

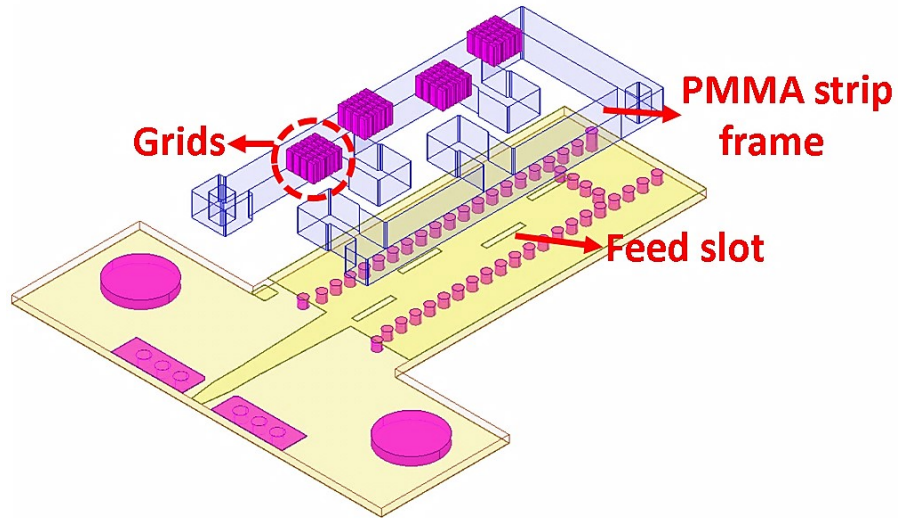Figure 7.22 Exploded design model of SIW fed 1×4 element strip template frame GDRA array
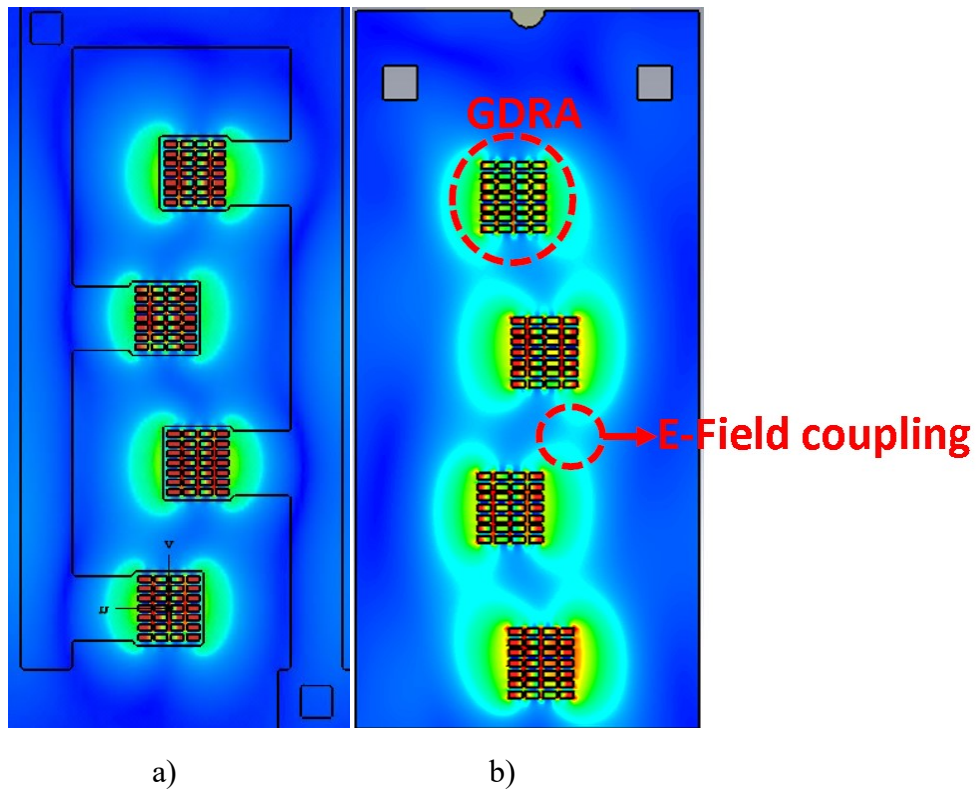

a)   b)

Figure 7.23 Simulated E-field coupling comparison for a) strip frame; b) solid template frame GDRA array
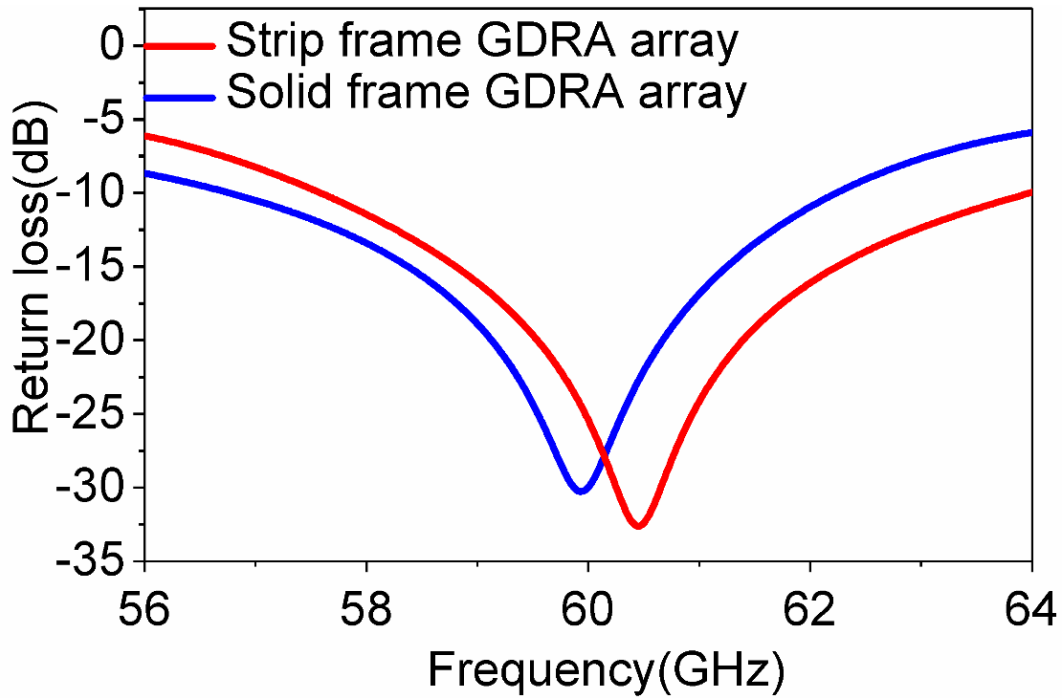
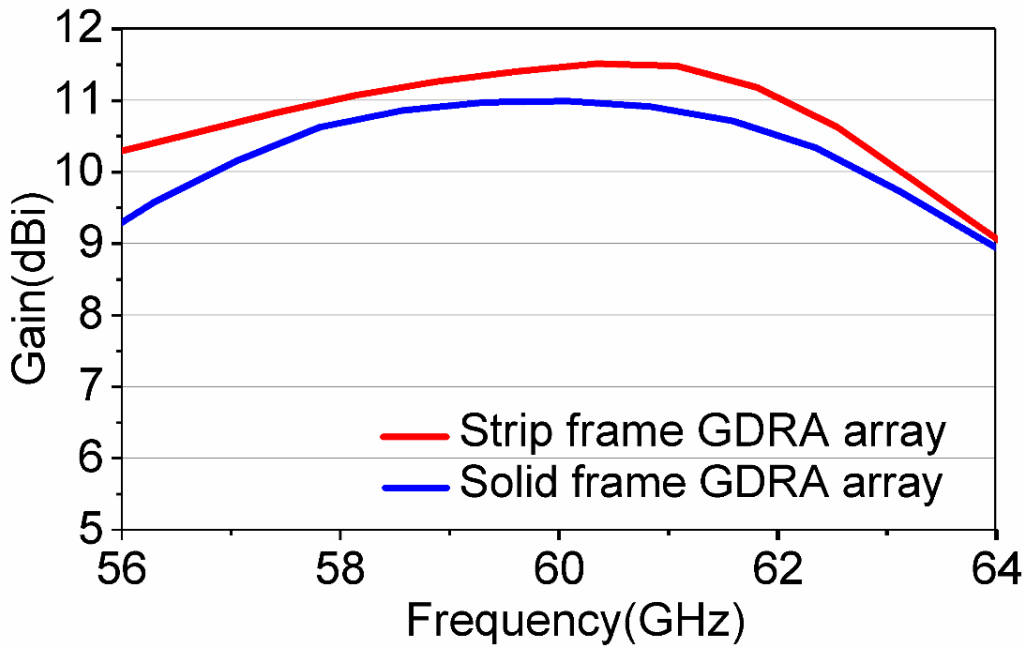Figure 7.24 Simulated S-parameters comparison for strip frame and solid template frame GDRA array

Figure 7.25 Simulated gain comparison for strip frame and solid template frame GDRA array

171
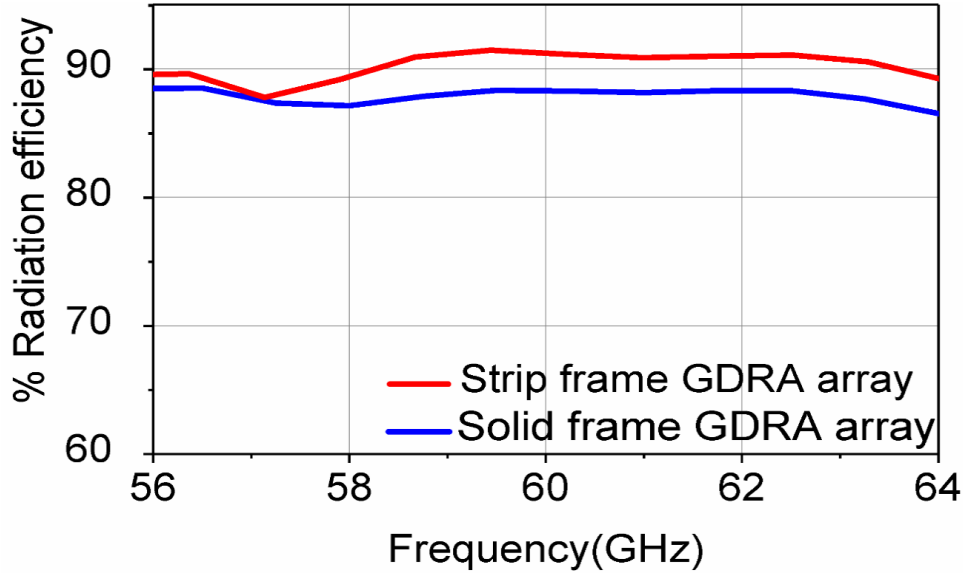
Figure 7.26 Simulated radiation efficiency comparison for strip frame and solid template frame GDRA array

Table 7.6 Simulation results comparison for GDRA strip template frame approach and solid template frame approach

Performance parameters	4 element strip template frame GDRA array	4 element solid template frame GDRA array
Impedance bandwidth (GHz)	6.3	5.35
Max. gain	11.5	11
Max. radiation efficiency	92%	88%

7.7.3. Fabrication and Measurement

A complete description for the fabrication of 4-element strip template frame GDRA array is presented in Chapter 5. For antenna performance, a 4-element GDRA array template is excited through a longitudinal coupling slot placed in substrate integrated waveguide (SIW). The SIW feed circuit is built through standard printed circuit board (PCB) technology on Rogers CLTE-XT substrate with relative permittivity of 2.95 and the thickness of 0.254mm. Figure 7.27 shows the 4-element strip template frame GDRA array integrated with SIW feed circuit.

A measured frequency response of the selected GDRA array is illustrated in Figure 7.28. The return loss for slot only case (feedline without the GDRA array) is found close to -5 dB, which confirms the non-resonance behavior of the SIW feed slots. In contrast, for slot loaded GDRA array, an impedance bandwidth of 5 GHz is realized below -10dB from 58 GHz 63 GHz, proving the fact that radiation is explicitly coming from the GDRA array template.

172

Finally, the radiation performance of the 4-element GDRAs array is characterized by using NSI-spherical measurement system. A maximum broadside far-field gain of 10.9 dB as shown in Figure 7.29 is observed at 60 GHz. The slight variation in the simulated and measured gain values may be due to reduced coupling energy from the slot to GDRAs array template because of a small air gap introduced by the silicone adhesive. The E-Co and H-Co-plane plot provided in Figure 7.30. confirms the directive array patterns. Moreover, the E-Cross and H-Cross pol are found below -20 dB which endorse the good polarization property of the designed GDRA array.

Figure 7.27 SIW fed 4-element strip template frame GDRA array prototype
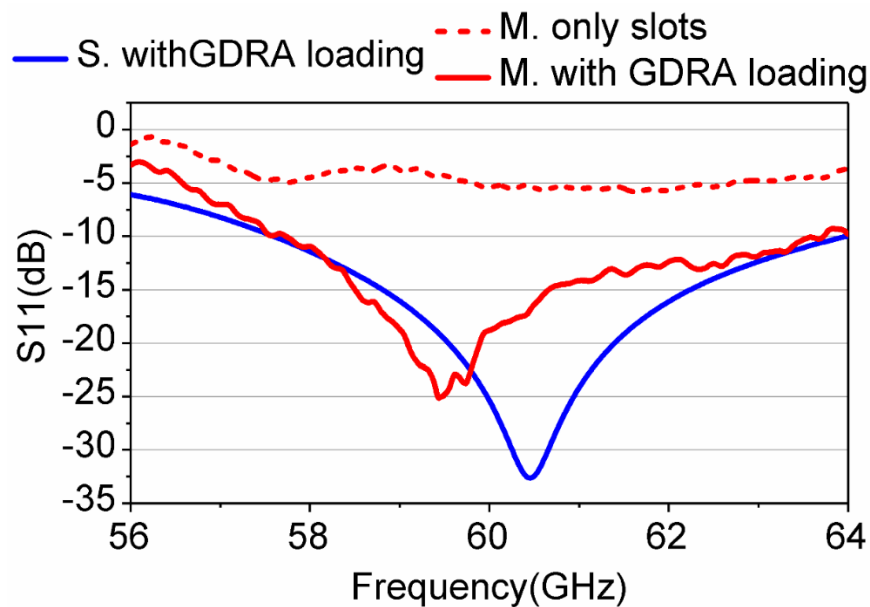

Figure 7.28 Simulated and measured return loss for 4-element strip template frame GDRA array (*S.= Simulated; M.= measured)
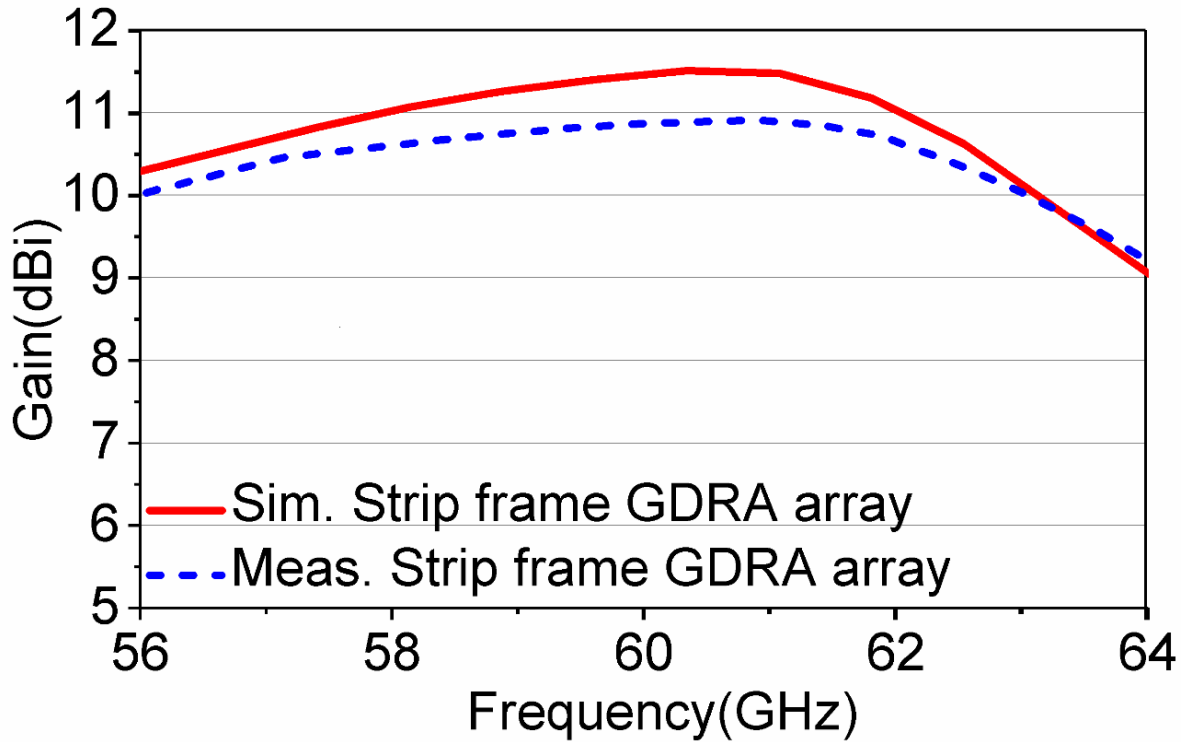
Figure 7.29 Simulated and measured gain plot for 4-element strip template frame GDRA array (*Sim. =Simulated; Meas.= measured)
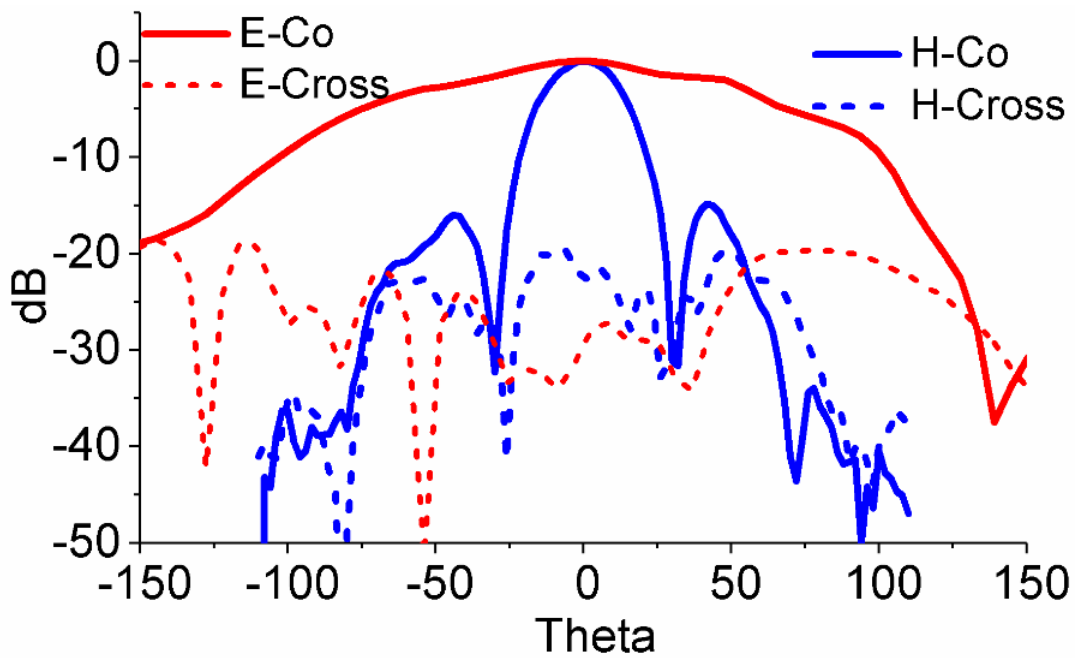

Figure 7.30 Measured radiation pattern for 4-elements GDRA array sample

174

7.8. Conclusion

Two different GDRA arrays approaches excited through SIW signal distribution and longitudinal slot feeding have been demonstrated with large impedance bandwidth and high gain at 60 GHz. In the first design approach, low-loss broadband T-power splitters with swept corners are interfaced to the 4×4 and 8×8 solid template frame GDRA array layers through slot feeding and have resulted in a wide-band and an efficient high-gain mm-wave antennas (i.e., with measured radiation efficiency of 73%). Measurements of the 4×4 and 8×8 solid template frame GDRA arrays confirm large peak broadside gains of 15.2 dBi and 19.4 dBi, respectively. Broadband measured impedance bandwidths in the range of 10%, 12% are readily obtained, as are stable radiation patterns with low side-lobe levels and low cross-polarization.

For the second design approach, a 4-element strip template frame GDRA array integrated with an SIW feed network is designed and compared with the solid template frame GDRA array. A strip template frame GDRA design is found to have superior impedance bandwidth, gain and radiation efficiency due to reduced mutual coupling between the array adjacent elements. A fabricated sample of 4-element strip template frame GDRA fed by SIW feed mechanism has demonstrated a wide impedance bandwidth of 5 GHz from 58 GHz to 63 GHz and broadside radiation pattern with a peak gain of 10.9 dBi.

References

[1]   H. M. El Misilmani, M. Al-Husseini, and K. Y. Kabalan, "Design of slotted waveguide antennas with low sidelobes for high power microwave applications," *Prog. Electromagn. Res. C*, vol. 56, pp. 15–28, 2015.

[2]   C. A. Balanis, *Antenna theory : analysis and design*. Wiley, 2016.

[3]   H. J. Visser, *Array and phased array antenna basics*. Wiley, 2005.

[4]   W. M. Abdel-Wahab, D. Busuioc, and S. Safavi-Naeini, "Millimeter-Wave High Radiation Efficiency Planar Waveguide Series-Fed Dielectric Resonator Antenna (DRA) Array: Analysis, Design, and Measurements," *IEEE Trans. Antennas Propag.*, vol. 59, no. 8, pp. 2834–2843, Aug. 2011.

[5]   J. Hirokawa, K. Sakurai, M. Ando, and N. Goto, "An analysis of a waveguide T junction with an inductive post," *IEEE Trans. Microw. Theory Tech.*, vol. 39, no. 3, pp. 563–566,

Mar. 1991.

[6] S.-J. Park, D.-H. Shin, and S.-O. Park, "Low Side-Lobe Substrate-Integrated-Waveguide Antenna Array Using Broadband Unequal Feeding Network for Millimeter-Wave Handset Device," *IEEE Trans. Antennas Propag.*, vol. 64, no. 3, pp. 923–932, Mar. 2016.

[7] I. Gupta and A. Ksienski, "Effect of mutual coupling on the performance of adaptive arrays," *IEEE Trans. Antennas Propag.*, vol. 31, no. 5, pp. 785–791, Sep. 1983.

[8] A. Ludwig, "Mutual coupling, gain and directivity of an array of two identical antennas," *IEEE Trans. Antennas Propag.*, vol. 24, no. 6, pp. 837–841, Nov. 1976.

Chapter 8 : Conclusion and Future Directions

Mobile communication is one of the major technological innovations in the era of modern history. The increasing popularity of the smartphones and other mobile computing devices has made mobile communications indispensable for 5 billion people. The unprecedented growth of mobile data has been continuously pushing wireless communication systems towards mm-wave frequencies for improved air-interference capacity and wideband frequency operation. Unused wideband frequency spectrums available at 28 GHz and 60 GHz are the potential wireless channel for future broadband wireless systems such as HD video, mm-wave imaging, 5G cellular phones, autonomous cars, and the IEEE 802.11ad Wi-Gig technology as the sub 6 GHz is highly congested by current wireless applications.

Antennas are an essential front-end component in mm-wave communication systems and typically a bottleneck to realizing effective consumer devices requiring high performance, compact size and low-cost materials. Conventional printed metal antennas such patch antennas are not as viable at mm-wave frequencies due to reduced radiation efficiency caused by high conductor and radiation losses. Secondly their narrow impedance bandwidth makes them undesirable for future emerging broadband applications.

Considering the above limitations, alternatives for designing high performance mm-wave antennas are required. One approach to address these issues is to develop mm-wave antennas using artificial metal gridded dielectrics, that can provide high radiation efficiency and gain in a low-profile device. Accomplishing similar performance in high permittivity ceramic devices is difficult for large and complicated arrays due to a lack of a viable batch fabrication process. Therefore, the GDRA antennas could be a potential candidate for the future mm-wave applications.

8.1. Thesis Summary

This thesis develops innovative artificial grid dielectric resonator antennas (GDRAs) and GDRA arrays for mm-wave applications using DXRL.

Several solutions to improve the previously explored GDRAs performance are proposed. These include the implementation of a multi-layer GDRA integrated with coplanar feedlines to enhance the energy coupling and feed versatility. A detailed discussion of two different types of CPW techniques successfully integrated with the GDRA elements with wide impedance bandwidth and

high gain performance is provided. A new monolithic single element solid template frame GDRA element with rectangular inclusions is designed and investigated. This structural approach improves the performance of the previous GDRA element in term of increased effective permittivity, while making them feasible for incorporation in large GDRA arrays.

Effective feeding of the GDRA arrays is an important aspect of the thesis. A complete design procedure for building 4-port and 8-port SIW power splitters at 24 GHz and 60 GHz along with in-depth simulation analysis involved is provided.

A fabrication procedure for building two different GDRA array layers using deep X-ray lithography (DXRL) is presented. Different design stages from X-ray mask fabrication, exposing thick PMMA templates, sample development and electroforming and the challenges encountered during these stages are discussed in detail. The resulting devices/antenna structures are examined under an optical microscope and scanning electron microscope (SEM).

A novel approach for constructing monolithic solid template frame GDRA arrays is provided. A PMMA based solid template frame is used to develop monolithic single channel series fed GDRA arrays at 32 GHz. All GDRA arrays are fed by longitudinal slots placed in the SIW channels. Complete design and analysis with in-depth parametric study is provided.

The concept of the single-channel series feed monolithic GDRA sub-array is further extended to multi-channel 2D 4×4 and 8×8 GDRA arrays at 60 GHz. In this case, 1×4, and 1×8 element series fed GDRA subarrays are integrated with 4-port and 8-port SIW power splitters for realizing 4×4 and 8×8 GDRAs arrays. Additionally, the design performance of two different 1×4 GDRA array approaches with solid template frame layer and with the strip template frame layer is compared. For all fabricated devices simulated, and measured results are illustrated and compared.

8.2.   Conclusion and Contributions

The scope of this Ph.D. dissertation is focused on studying novel grid dielectric resonator antennas (GDRAs) as a single element as well as for a large scale 2-dimensional antenna arrays for millimeter-wave applications using different planar feeding techniques. The salient features of the research conducted under this thesis are listed below:

1) Enhancing the performance parameters and feed versatility of the previously explored single element GDRAs for wideband and high gain applications. Feed techniques other than microstrip line such as GCPW, CPW, and SIW are successfully developed and tested.

2) Developing a wideband SIW based eight-way power splitter for mm-wave applications. In-depth parametric analysis of different design stages such as T-splitters and Y-splitters along with their design variables and their relations based on guided wavelength is provided. The proposed design offers an impedance bandwidth of 3.4 GHz from 23.0 GHz to 26.4 GHz with 15dB return loss and phase and amplitude imbalance of $\pm\, 2.5^o$ and $\pm\, 0.8$ dB respectively.

3) The GDRAs with rectangular grid structures are successfully developed in comparison to previously investigated I-beam inclusions. This new design approach has reduced the structural complexity and has enhanced the effective permittivity of the PMMA up to 22.4 by creating higher electric flux density regions.

4) For the first time GDRAs involving complete DXRL procedure with two different approaches are developed at SyLMAND. The difference in two approaches is the removing of the PMMA polymer plastic in-between the adjacent elements of GDRA array in second approach to provide high permittivity contrast between the GDRA array adjacent elements to lower the energy coupling through the template frame and hence improving the overall performance of the GDRA array in comparison to the solid template frame approach.

5) A solid PMMA template approach is developed to implement the integration of the GDRA elements into the antenna arrays. The proposed design procedure has helped to mitigate the problem of GDRAs alignment over the feed networks especially for large 2-dimensional antenna arrays.

6) 1×4, and 1×8 element series fed GDRA arrays with solid template frames are developed at 32 GHz. A detailed design description of the different aspects of the GDRA array layer including the effect of the frame thickness, the effect of the frame permittivity, the effect of the mutual coupling, the effect of inclusions height and their excitation and integration with SIW feeding mechanism is provided. The measured impedance bandwidth of 29-34.5 GHz with broadside gain of 11.9 dBi is achieved at 33GHz.

7) 60 GHz 2D SIW fed 4×4, and 8×8 element monolithic GDRA arrays are designed and fabricated. Effective permittivity of 22.4 is achieved by embedding thin rectangular micro-

inclusions in a low permittivity polymer PMMA. A measured impedance bandwidth of 5.5 GHz from 56.5 to 62 GHz and 7 GHz from 55 GHz to 62 GHz is realized for 4×4 and 8×8 GDRA array. Additionally, both GDRA arrays have stable radiation pattern with broadside gain of 15dBi and 19.8dBi respectively.

This research has demonstrated the potential of GDRAs as a low-profile, high permittivity high performance resonator antenna, which could be very attractive for future compact millimeter-wave antennas. A solid monolithic template frame approach allows easy and precise assembly of large 2D planar GDRA arrays. The tiny embedded grid structures have allowed the successful excitation of the comparatively low profile GDRA design which is not realizable in similar size conventional DRAs. Moreover, the proposed single element high permittivity GDRA design which is the fundamental building element for large planar GDRA arrays has outperformed the similar size high permittivity conventional DRA design in both the percentage bandwidth and the directivity. The major contributions of the work are the low profile, multilayer GDRA concept, a monolithic template frame approach which is scalable for large GDRA arrays and SIW feed incorporation with GDRAs at 32 GHz and 60 GHz. All these contributions are recognized in IEEE Transactions on Antennas and Propagation ("*Low profile artificial grid dielectric resonator antenna arrays for mm-wave applications", vol. 67, no. 07, 2019*) and IEEE Antennas and Wireless Propagation Letters (*60 GHz Substrate Integrated Waveguide Fed Monolithic Grid Dielectric Resonator Antenna Arrays, 2019*).

8.3. Future Work
Following are the recommendation for the further enhancement and development of grid dielectric resonator antennas (GDRAs).

1) Currently, the cost of designing GDRAs are high due to the direct X-ray lithography process. Other alternatives are required to be studied to lower the design cost of the GDRAs. For instance, one approach is to build certain type of GDRAs made up of SU-8 polymer template using UV-lithography. This could be advantageous in term of building much thicker and higher aspect ratios structures with small exposure dose as the SU-8 negative tone resist is 2000 times more sensitive than the PMMA positive tone resist. Secondly, the SU-8 resist has a permittivity value of 3.5 which is 1.4 times larger than the PMMA resist i.e. 2.5, and this may also further increase the effective permittivity of the

GDRAs. Another approach is to use XRL to fabricate master tooling for low-cost polymer replication.

2) The higher order mode characterization in the GDRAs is complicated and still requires further study which could be very useful in controlling impedance and pattern bandwidth of the low profile GDRAs.

3) The concept presented of low profile GDRAs, i.e. 0.5mm can be further extended to thin-film GDRAs which could be very attractive for Antenna on chips (AoC) and Antenna in the package (AiP) applications. Secondly, they could be directly fabricated by using UV laser lithography only.

4) Until now most of the grid structures embedded in the GDRAs i.e., I-beam or rectangular grids are meant to enhance the electric response or effective permittivity of the GDRAs. However, one other approach is to use ring types structures to produce rotational currents and to see the effect on the effective permeability of the GDRA.